SEARCH FOR SUPERSYMMETRY IN DIJET AND MULTIJET CHANNELS AND SOFT QCD MEASUREMENTS USING THE ATLAS DETECTOR AT THE LARGE HADRON COLLIDER

by

RISHIRAJ PRAVAHAN

Presented to the Faculty of the Graduate School of
The University of Texas at Arlington in Partial Fulfillment
of the Requirements
for the Degree of

DOCTOR OF PHILOSOPHY

THE UNIVERSITY OF TEXAS AT ARLINGTON
DECEMBER 2010

To, Ma and the memory of Papa for all the support and love...

ACKNOWLEDGEMENTS

I would first and foremost like to thank my committee for their time and patience. Specially, Dr Kaushik De my advisor, for presenting me with the opportunity and the encouragement to work in a marvelous project like CERN. If it were not for Dr De, I will not be in high energy physics. He has been an inspiration, a guide and a friend through the beginning of my undergraduate to the end of my doctorate. I owe my academic career to Dr De.

Secondly, I would like to thank Dr Amir Farbin for shaping me into a high energy physicist. My early years at CERN involved working with hardware and shifts at the detector and a slow and painful process of getting used to the machinery of the HEP experimental and computational world. Dr Farbin, even when he was not a professor at UTA but a colleague at CERN took me under his wings. He taught me most of the experimental high energy physics and computing I know. Other than being an outstanding academic mentor he has been a friend, a guide and an endless supplier of free espresso, the lifeblood of graduate students. I thank him for all of it.

I would also like to thank all the other members of the UTA group, specially Dr Edward Sarkisyan-Grinbaum for working with me on the minimum-bias paper and teaching me soft QCD, Dr Giulio Usai for guiding me through many calibration and detector level analyses as well as the photon-jet study, Dr Alden Stradling and Dr Mark Sosebee for a lot of computational and technical assistance.

Next I would like to take this opportunity to thank all my family and friends who have helped through my life to achieve a dream. I cannot with words explain the deep pain I feel of not having my father around to witness my success. In his absence

I must share my joy and gratitude with my mother. Their influence in my life has made me achieve my goal. My grandparents, Sri Chitta Bhusan Dasgupta and Smt. Malati Dasgupta for living a life that inspired me to strive for excellence in thought and action. My uncle Mr Pradip Dasgupta for lending me all his physics books and showing me that one can be inspired by physics at any level and at any age.

I could not have been able to finish my work and goals without the support of the many close friends I have been lucky to have had in my life. First among them is Ima-Karina Narvaez, my girlfriend who I met my first year in Geneva. Through the past five years we have grown together. Her support in my life and work is indispensable.

My friends, Robert Angelopoulos and his wife LaShea Angelopoulos have been the most generous, thoughtful and familial support I could ever expect from anyone. They made me feel I have always had a home in Arlington, every time I have had to come to Texas. Sharing their house, their car, their life with me as if I was part of the nuclear family.

My friendship with Roger Begrich has transcended family ties. He has been there through the best of times and through the worst of times, holding my hand, literally. I would not have made it without his practical yet wise world view. His influence in my life and my work is enormous. Moving to a new country and adjusting to a new culture, language and settling down is difficult. When I moved to Geneva, Roger's parents, Rainer Begrich and Traudl Begrich and sister Annette Begrich helped me feel right at home with all the help expected from a family. A special thanks to Annette for driving down from Basel to look for an apartment for me in Geneva, a formidable assignment!

I want to thank Jake Livesay for asking me to 'calm down' when I needed to, Mustafa Amin for hours of physics problem solving together, Alysa Benefield for going out of her way to support and help me, Neeraj Tulshan for the great road trips since 1987, Amael Paillex for the wonderful lake Leman barbecues and finally all my friends in India, Switzerland and the United States for being there for me in tough and easy times.

I would also like to thank all the faculty I have taken classes from and learned a great deal from at UTA. I want to thank the members of SUSY working group, the Direct photon working group, and the Minimum bias working groups at ATLAS for helping me collaborate my work.

Finally, I would like to thank the thousands of physicists, engineers and technicians from across the globe who had worked numerous hours to build the Large Hadron Collider and the ATLAS experiment. Their laborious contribution towards a greater understanding of physics is enormous. I feel I owe a great deal to all those who build and commissioned the experiments, so students like I can learn about and explore the fundamentals of the building blocks of our Universe.

November 19, 2010

ABSTRACT

SEARCH FOR SUPERSYMMETRY IN DIJET AND MULTIJET CHANNELS AND SOFT QCD MEASUREMENTS USING THE ATLAS DETECTOR AT THE LARGE HADRON COLLIDER

RISHIRAJ PRAVAHAN, Ph.D.

The University of Texas at Arlington, 2010

Supervising Professor: Kaushik De

The ATLAS experiment at the CERN Large Hadron Collider (LHC) has collected a substantial amount of data to understand the Standard Model of particle physics at higher than previous center of mass energy available and to explore new physics beyond the Standard Model. This dissertation describes observations of charged particle multiplicity distributions in 7 TeV and 900 GeV data as well as searches for new physics with a signature of high energy jets and missing transverse energy using the first few months of data available at the LHC.

Multiplicity distributions of charged particle tracks, one of the first observables in high energy collisions were made for a center of mass energy, $\sqrt{s} = 900$ GeV as well as 7 TeV proton-proton collision data. Such distributions help to understand multi-particle production processes. One of the predicted features of multiplicity distribution and its moments is KNO scaling which implies that the shape and moments of the scaled multiplicity distribution is independent of the center-of-mass energy. Although a clear violation of KNO scaling is not observed within the error limits,

an indication of such violation is noted. Different models of hadro-production to describe multiplicity distributions are also studied. The Negative Binomial Distribution (NBD) is an often used distribution modeling multiplicity distributions. It has been observed that NBD is satisfied in different types of collisions and over wide range of energies and it was observed that not only the full-phase-space multiplicity distribution can be successfully fitted by the NBD but also the distribution within central pseudo-rapidity intervals. Based on these findings, the model of cluster (or clan) cascading type has been proposed. Although, a good NBD fit can be obtained, it is observed for hadronic interactions that the presence of two weighted NBD or Double NBD (DNBD) components, one corresponding to soft production and the other to semi-hard one (mini-jets) seems to fit the data better for broad pseudo-rapidity ranges. It was found that the soft component follows KNO scaling while the semi-hard component does not. The proton-proton collision data at LHC has been analyzed to test the NBD and DNBD parametrization and test the energy dependence of the fitted parameters.

It is well understood that the Standard model of Particle physics in incomplete. Our knowledge of cosmology also leaves several crucial questions unanswered, one of them being the composition of the dark matter that has been indirectly observed through astronomical observations. The primary objectives for constructing the Large Hadron Collider has been to solve these problems through the discovery of the Higgs particle and to find new physics processes that predict the production of massive non-interacting stable particles. Searches of such new physics producing heavy stable particles in its final state has been performed. Finding such signals would provide direct observation of a dark matter candidate particle. The exclusive event topology of two high energy jets and missing transverse energy has been explored to perform the

above search, using ATLAS detector data. A summary of results of these preliminary searches in comparison with theoretical predictions has been presented.

In order to understand and discriminate any new physics, a clear and coherent understanding of the detector response is crucial. Moreover, a detailed knowledge of the behavior of known standard model phenomena is required. A detailed description of the ATLAS detector and several important calibration techniques is discussed and their results summarized. Estimates of Standard Model physics, contributing to irreducible backgrounds to dark matter searches is presented in detail. One such physics process constituting an irreducible background is the production of the Z boson decaying into two neutrinos (ν) with associated jets. The observation of these events directly from data is an impossible task due to the non-interacting nature of the neutrinos. An estimate of the production cross section of these process is estimated using observations of photon (γ) plus jet events and theoretical predictions. Estimated numbers for the γ plus 2,3,4 and more associated jets production with uncertainties has been summarized.

TABLE OF CONTENTS

LIST OF FIGURES

LIST OF TABLES

CHAPTER 1

INTRODUCTION

1.1 Introduction

Human being is a curious creature. It is this curiosity that drives him to investigate everything around him and understand underlying causes for things to be the way they are. What differentiates this investigation from that of the 'curious cat' is his ability to experiment and deduce from his observations. From Heron of Alexandria Galileo, Newton to Michelson and Morley, men have found ways to investigate and understand the basic workings of nature. In the face of things, the mechanical puppets of Heron, Galileo's telescope, Newton's prisms or Michelson-Morley's apparatus has little to do with real world applications and may seem to be simply amusing. This process of creating instruments that enable us to investigate and utilize nature in completely new ways, pushing completely new frontiers of knowledge, has enabled us to be where we are today in terms of civilization.

The beginning of the twentieth century witnessed the greatest revolution in our understanding of nature. The initial understanding of relativity theory and quantum mechanics was extended to formulate quantum field theory and by the end of the century we had an experimentally valid theory of the origin of the universe as well as of particles and fields at the subatomic level. These theories although valid are not complete. Many mysteries within these theories remain unsolved and many questions beyond these theories remain unanswered.

To gain a better understanding of nature beyond the present, the Large Hadron Collider (LHC) was commissioned at the European Center for Nuclear Research

Figure 1.1. Aerial view of the LHC facilities.

(CERN) in Geneva, Switzerland (Fig. 1.1) by governments and scientists from all over the world. A particle collider is the perfect instrument to recreate conditions of early universe as well as producing unknown particles and fields to investigate their properties.

This dissertation describes the physics motivations behind the building of the LHC, a description of the machine and the detector experiments, as well as some early physics results from the ATLAS (A Toroidal Large Hadron Collider Apparatus) detector.

1.2 The Large Hadron Collider

The Large Hadron Collider is a particle accelerator that accelerates protons and lead ions up-to a center of mass energy of 14 TeV, where 1 TeV $= 10^{12} \times 1.6 \times$

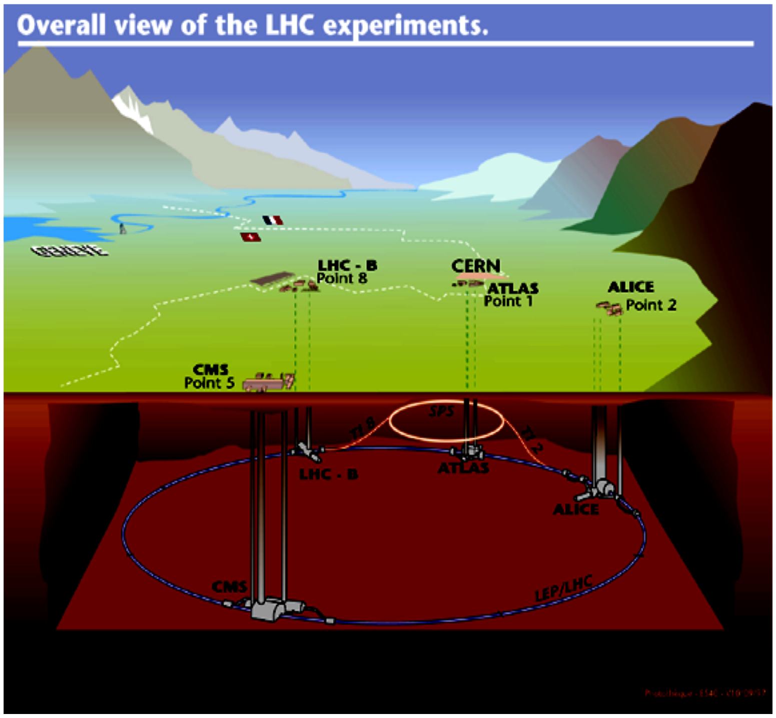

Figure 1.2. Schematic view of the LHC experiments.

10^{-19} Joules [?] [1]. It has four collision points, with a detector at each of these points to record the collisions. The LHC detectors are, ATLAS (A Toroidal Large Hadron Collider ApparatuS), CMS (Compact Muon Solenoid), LHCb (Large Hadron Collider beauty) and ALICE (A Large Ion Collider Experiment), Out of these, the ATLAS and CMS detectors are general purpose high luminosity detectors. ALICE is specialized for detecting physics from the heavy Pb ion collisions, LHCb studies beauty physics. There are associated experiments like TOTEM (TOTal Elastic and diffractive cross section Measurement) and LHCf (Large Hadron Collider forward) which studies forward particles i.e. particles along the original beam, measuring proton size, monitoring LHC luminosity and, simulating cosmic rays for experiments, respectively.

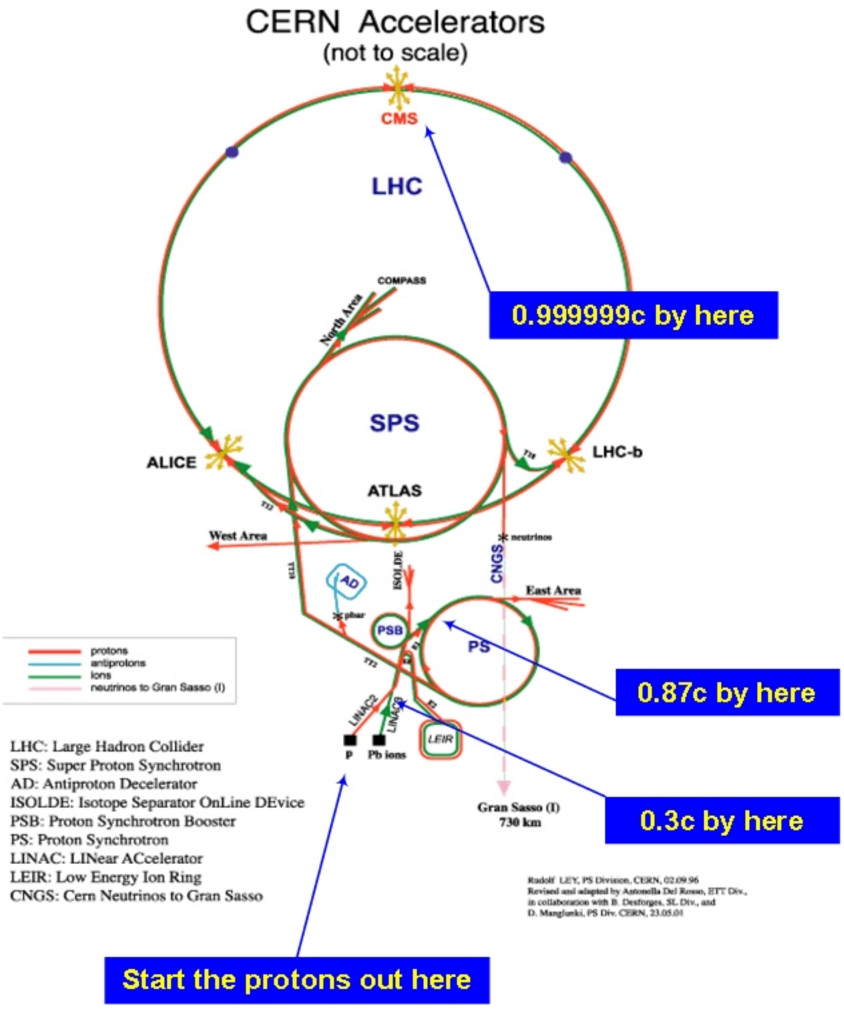

Rudolf LEY, PS Division, CERN, 02.09.96
Revised and adapted by Antonella Del Rosso, ETT Div.,
in collaboration with B. Desforges, SL Div., and
D. Manglunki, PS Div. CERN, 23.05.01

Figure 1.3. The beam injection system.

1.2.1 LHC at the energy frontier

The LHC is designed to operate at a maximum energy of 7 TeV per beam [2]. The 100m underground tunnel where the LHC is located is 26.659 km in circumference. The force on a charges particle moving in a magnetic field is given by

$$\vec{F} = q.(\vec{E} + \vec{v} \times \vec{B}) \tag{1.1}$$

To accelerate a proton to a momentum of 7 TeV/c, where c is the velocity of light, and the magnetic field is perpendicular to the momentum one needs

$$\begin{aligned} mv^2/R &= e_0 v B \\ B &= \frac{p}{e_0 . R} \end{aligned} \tag{1.2}$$

with e_0, B, R, p being the proton charge, the magnetic field, the radius of curvature and momentum of the proton respectively. Thus a dipole magnetic field of 8.33 Teslas is used to keep the protons circulating in the LHC beam pipes. Moreover, since the LHC collides protons head on with protons, two beam pipes with equal but opposing magnetic fields are required to keep the beams in orbit. Magnetic fields of such large values are obtained using superconductors. The magnetic fields are thus susceptible to heat loads and thus beam losses during operation.

The acceleration to the 7 TeV energy is not achieved in a single step. Figure 1.3 shows the many steps in which the protons and the ions are accelerated to nominal energy in the LHC complex. The acceleration is done using electric fields that are fed into radio-frequency cavities operating at 400 MHz, composed of 8 superconducting cavities per beam, with a peak voltage of 16 MVolts. The radio-frequency voltage also imparts bunch structure to the beams. Other than the dipoles accelerating the beams, there are quadrupole magnets that focus the beams. One quadrupole magnet can act as a converging lens to focus the beams in one plane while diverging it in a perpendicular plane. Thus a series of quadrupole magnets are used to keep the beam focused. Multiple-corrector magnets are also used to correct trajectories of particles with high amplitude. The LHC houses a total of 1232 dipole magnets and 392 quadrupole magnets, and a total of 9593 magnets, with the dipole magnets operating at a temperature of 1.9 K (-271.3 C). Table 1.1 summarizes the important LHC parameters.[2] [1]

Table 1.1. LHC parameters

Quantity	number
Circumference	26659 m
Nominal energy of protons	7 TeV
Nominal energy of ions	2.76 TeV per nucleon
Design luminosity	$10^{34} cm^{-2} s{-}1$
Dipole Operating Temperature	1.9 K
Number of magnets	9593
Number of main dipoles	1232
number of main quadrupole	392
Number of RF cavities	8 per beam
Peak magnetic dipole field	8.33 T
Minimum distance between bunches	7 m
Number of bunches per proton beam	2808
Number of protons per bunch	1.1×10^{11}
Number of turns per second	11245
Number of collisions per second	600 million

1.2.2 LHC at the luminosity frontier

High energy physics observations are normalized by counting the number of events for any given physics process. The probability of an event is given by the cross section (σ) of the process. One can theoretically calculate the cross section of a physics process. The number of events is given by

$$N_{event} = L\sigma_{event} \tag{1.3}$$

where σ_{event} is the cross section for the physics event and L the luminosity of the machine. The luminosity is given by,

$$L = \frac{kN^2 f}{4\pi\sigma_x^*\sigma_y^*} \tag{1.4}$$

where k is the number of bunches, N the number of protons per bunch, f the revolution frequency, and σ_x^* and σ_y^* are the horizontal and vertical beam sizes respectively. The σ_i^* can be written as,

$$\sigma_y^* = \sqrt{\beta^*/\epsilon} \tag{1.5}$$

with β^* characterizing the beam envelope and ϵ the phase space volume occupied by the beam. Looking at equation 1.4 one can see that increasing k and N/ϵ while decreasing β^* increases the overall luminosity of the machine. It is also evident from equation 1.4 that the luminosity of the machine cannot remain constant over time and must have a lifetime. The calculated net luminosity lifetime of the LHC is given as,

$$\tau_L = 14.9h \tag{1.6}$$

The integrated luminosity over one run is given by,

$$L_{int} = L_0 \tau_L (1 - e^{-T_{run}/\tau_L}) \tag{1.7}$$

where T_{run} is the total time of the run, and L_0 the luminosity at the beginning of the run. Using this one calculates a total of 80 fb^{-1} to 120 fb^{-1} of data assuming 200 days of running at 15 hours per luminosity lifetime at the maximum instantaneous luminosity achievable.

1.3 The ATLAS detector

The ATLAS experiment is the largest detector experiment at the LHC. It is a general purpose detector that is roughly cylindrical in shape with a length of 46m and a diameter of 25m weighing 7000 tons. As an experiment, it is a collaboration of 3000 scientists from 37 countries and 173 different universities and laboratories. The purpose of ATLAS is to record the results of the collisions of protons from the LHC at the center of the detector and analyze the signature so obtained towards discovery of missing Standard Model pieces, like the Higgs Boson as well as to look for physics beyond the Standard Model of particle physics.[3] [4] [5]

1.3.1 The ATLAS Coordinate System

The ATLAS detector being cylindrical in shape and symmetry beckons the use of a cylindrical coordinate system. The beam line naturally lends itself as the axis of the cylindrical system, which in rectangular coordinates is denoted as the z-axis. The detector has two schematic sides, 'A' and 'C' corresponding to the positive and the negative of the z-axis. The detector is symmetric in the azimuthal angle ϕ. The plane of $z = 0$ is called the transverse plane, and projection of physical quantities in this plane are referred to as 'transverse' quantities.

The momentum Lorentz vector p_μ in rectangular coordinates can be written as,

$$p_\mu = (p_x, p_y, p_z, E) \tag{1.8}$$

However, in this system only p_x and p_y are Lorentz invariant. If θ is defined to be the angle relative to the z-axis, a quantity 'rapidity' can be defined as,

$$y \equiv \frac{1}{2} \ln \left(\frac{E + p_z}{E - p_z} \right) = \frac{1}{2} \ln \left(\frac{1 + \beta \cos\theta}{1 - \beta \cos\theta} \right) \tag{1.9}$$

with $\beta = p/E$. One can further define 'pseudo-rapidity' as,

$$\eta \equiv \frac{1}{2} \ln \left(\frac{1 + \cos\theta}{1 - \cos\theta} \right) = - \ln \tan \left(\frac{\theta}{2} \right) \tag{1.10}$$

Using equations. 1.9 and 1.11 one can show that,

$$\beta \tanh(\eta) = \tanh(y) \tag{1.11}$$

The pseudo-rapidity or η is used extensively in ATLAS as a coordinate and will be referred to for detector as well as physics measurements.

1.3.2 Design of the ATLAS detector

The ATLAS detector has five different physical components each specializing in a specific ability to detect different particles coming from the collision. [3] [5] [6] These are the Inner Detector, the Liquid Argon calorimeter, the Tile Calorimeter, the Muon Spectrometer and the Magnet system. Figure 1.4 shows the various parts of the ATLAS detector. The yellow part at the center of the detector is the Inner Detector, the green is the Liquid Argon Calorimeter, orange the Tile Calorimeter, blue the Muon Spectrometer and gray the Magnet system.

1.3.2.1 The Inner Detector

The ATLAS inner detector is designed to measure particle tracks with excellent precision. It comprises of a silicon pixel detector at its innermost, then the semiconductor tracker (SCT) and the transition radiation tracker at its outermost layer, all covering a pseudo-rapidity $|\eta| < 2.5$ in a solenoidal magnetic field of 2 Tesla. [7]

The pixel detector provides the ability to recognize patterns for tracks near the point of collision. It is also used to recognize secondary vertexes resulting from decay of short lived particles after collisions. The pixel detector is nearest to the beam and it is also designed for optimal impact parameter resolution for secondary decays. It consists of 1744 modules with 80 million channels within a cylinder of length 1.4m and

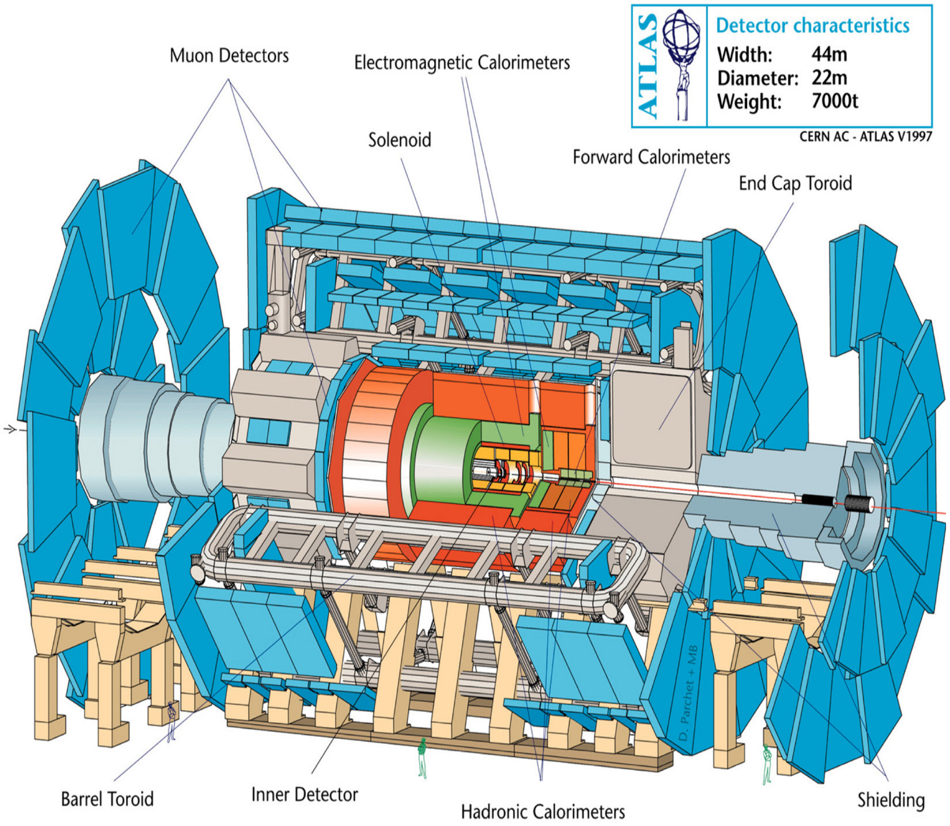

Figure 1.4. Overview of the ATLAS detector experiment.

diameter 0.5m. The modules are assembled from silicon wafers 16.4mm by 60.8mm with 46080 pixels.

The next layer is the SCT. It consists of modules built with 2 pairs of identical, single-sided silicon micro-strips sensors glued back to back using pyrolitic graphite, a thermal dissipator. Each module has 1536 channels giving a high level of granularity. It provides a very precise measurement of momentum, impact parameter, vertex as well as ability for pattern recognition.

The Transition Radiation Tracker is a straw detector consisting of straws that are 4mm in diameter with sense wires in isolated gas envelopes. It is used to separate electrons from other charged particles by employing Xenon gas to detect transition

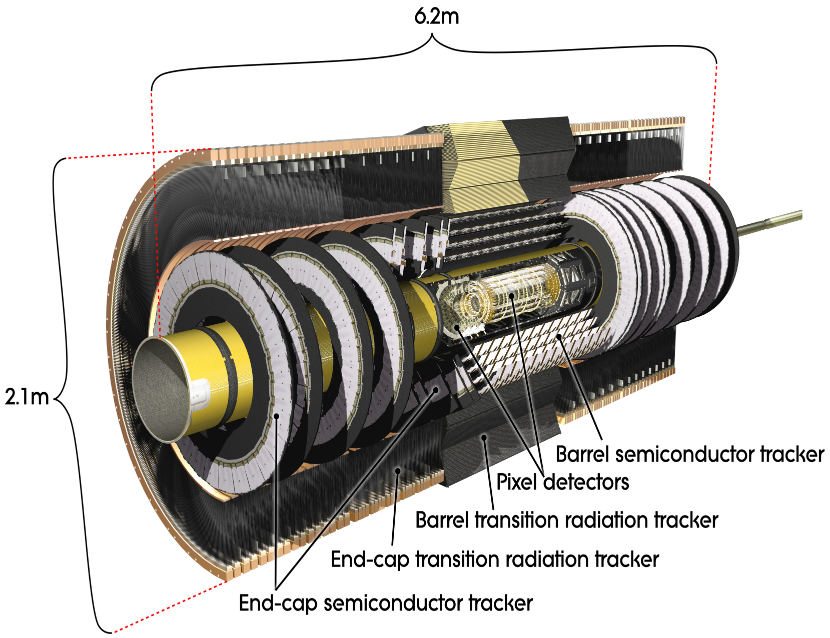

Figure 1.5. 3-Dimensional computer generated image of the Inner Detector.

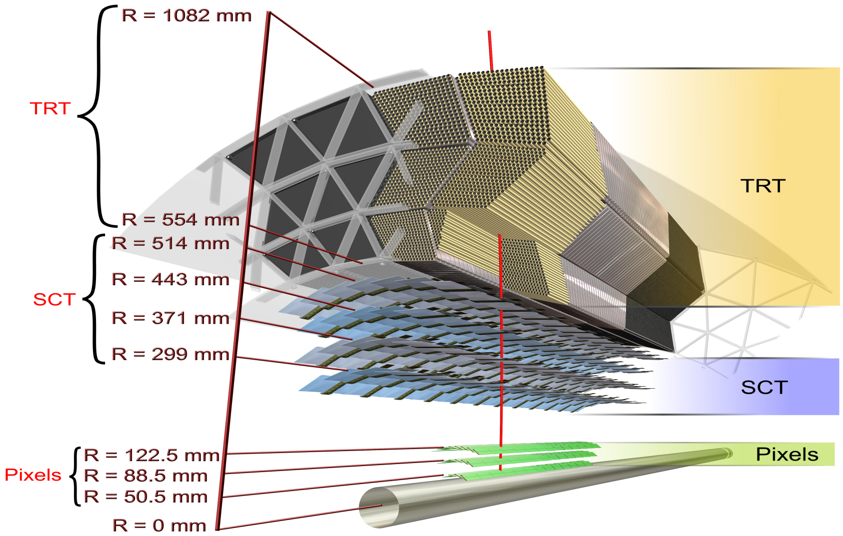

Figure 1.6. Schematic representation of the Inner Detector.

radiation photons emitted by the electrons between the straws. There are a total of 420000 electronic channels each channel providing drift time measurements with a spatial resolution of 170 μm per straw, and two independent thresholds allowing the detector to discriminate between tracking and TRT hits.

The inner detector is pivotal in tracking measurements. In chapter 3, early measurements of charged track multiplicity using tracks from minimum bias data are reported.

1.3.2.2 The Liquid Argon Calorimeter

The Liquid Argon Calorimeter (LAr) is part of the Calorimetry system in ATLAS. It is designed specifically to trigger on and give precise measurements of photons, electrons, jets, and missing transverse energy. The LAr consists of the 'barrel' region with $|\eta| < 1.475$ the 'end cap' region with $1.375 < |\eta| < 3.2$, the hadronic end-cap (HEC) region with $1.5 < |\eta| < 3.2$, and the forward calorimeter (FCAL) region with $3.1 < |\eta| < 4.9$ as shown in Fig. 1.7 schematically. The detectors themselves are located within three different cryostats with liquid argon as the active material. [8]

The LAr also has an accordion geometry to maximize coverage in ϕ without having cracks for services. The accordion geometry of the liquid argon calorimeter leads to a very uniform performance in linearity and resolution as a function of ϕ. The barrel consists of two half barrels made up of 1024 such accordion shaped absorbers and covering $0 < |\eta| < 1.475$ and $-1.475 < |\eta| < 0.$ regions respectively. Figure 1.8 shows the details of the LAr barrel. The four parts can be seen as the presampler, consisting of only liquid argon without absorption layer used to correct for energy loss in the inner detector. The second part is the 'first sampling' with a depth of 4.3 radiation lengths and $\Delta\eta \times \Delta\phi = 0.0031 \times 0.098$ giving it excellent resolution. The next layer is the 'second sampling' extending to 16 radiation lengths with strips of

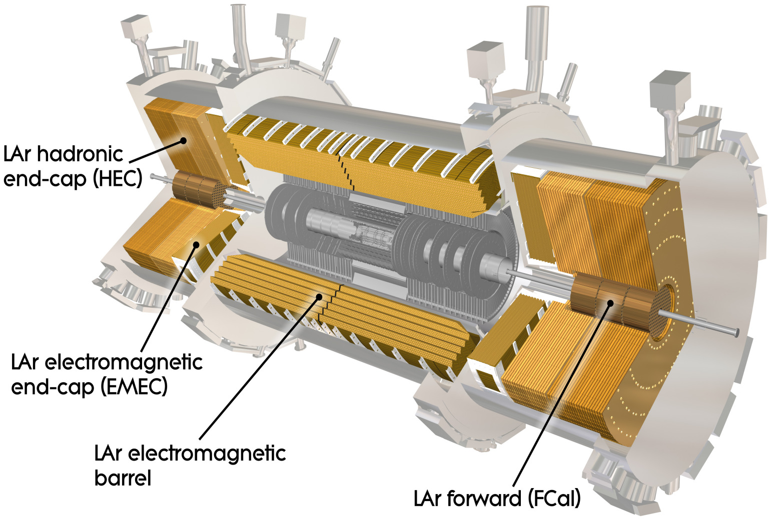

Figure 1.7. The Liquid Argon Calorimeter.

$\Delta\eta \times \Delta\phi = 0.0245 \times 0.0245$, making it radially long enough to fully contain clusters of energy below 50 GeV. The last part is the 'third sampling' with larger cell sizes.

1.3.2.3 The Tile Calorimeter

The Tile Calorimeter (TileCal) is the hadronic calorimeter for ATLAS enveloping the LAr Calorimeter. It is divided into the barrel and the extended barrels, with the barrel covering $|\eta| < 1.0$ and the extended barrels covering the range of $0.8 < |\eta| < 1.7$. It is a non compensating sampling calorimeter with steel as absorber material and scintillating tiles as the active material. The central barrel is 5.8 m in length whereas the extended barrels are 2.6 m in length each shaped like a hollow cylinder of inner radius of 2.28 m and an outer radius of 4.25 m allowing a depth of 7.4λ interaction lengths. Each of the barrel and extended barrel consists of 64 modules divided in $\delta\phi \approx 0.1$ covering from $-\pi$ to π in azimuth. [9] [10]

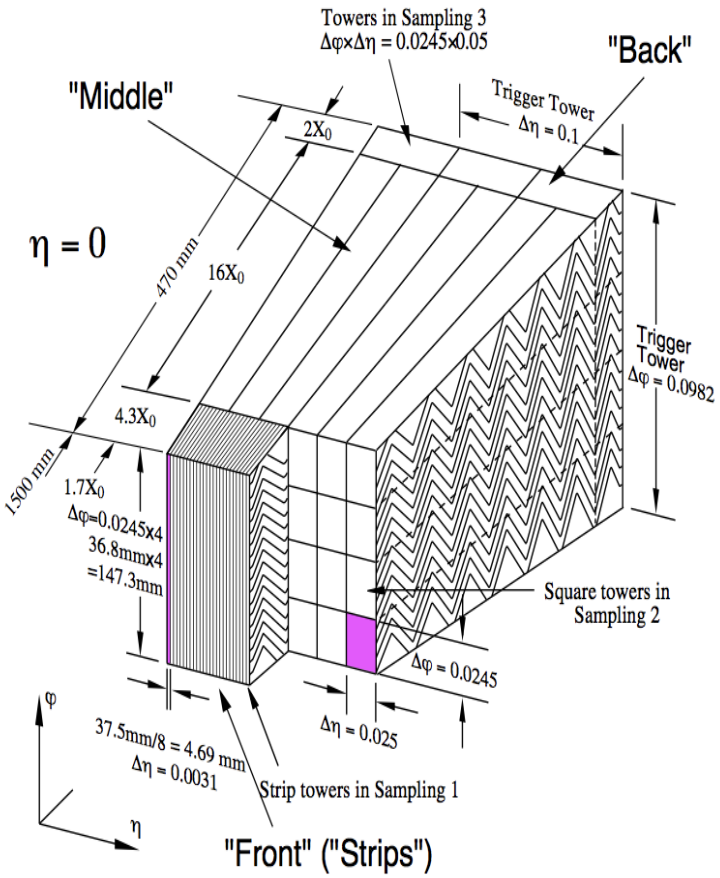

Figure 1.8. The structure of the Liquid Argon Calorimeter.

The modules of the TileCal consist of steel plates and scintillating material inter spaced parallel to the beam pipe. At the end of a hadronic shower slower moving charged particles have velocities isotropically distributed as in a gas. This makes it possible to have the plates parallel to the direction of the incoming particles. Figure 1.9 shows a schematic view of a TileCal module. In the magnified view one can see the placing of the steel and scintillator plates. Wavelength shifting optical fibers are attached to the radial edges of the scintillator plates, shown in 1.9. These fibers are grouped together and coupled to a photomultiplier tube in the radial end of the

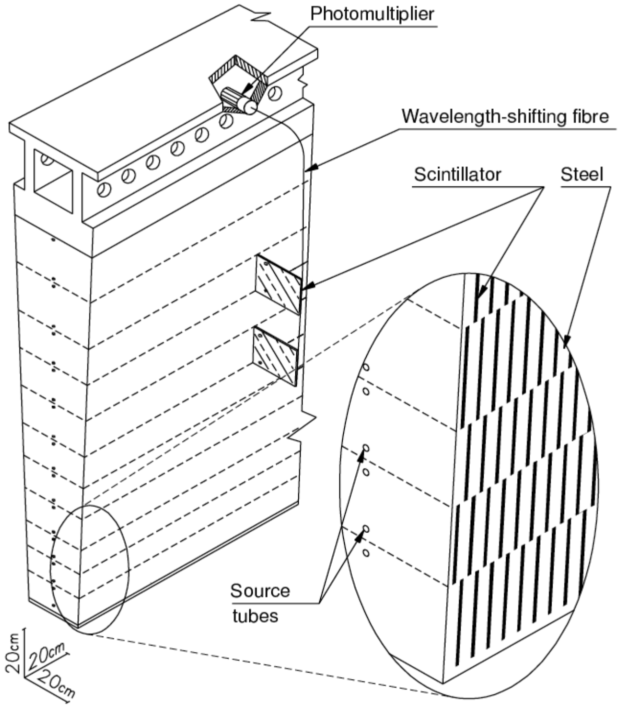

Figure 1.9. Schematic view of the Tile Calorimeter.

module where the electronic drawers are located. The Intermediate Tile Calorimeter (ITC) a part of the Tile Calorimeter that is located in between the main barrel and the extended barrels is designed specifically to compensate for energy loss due to dead material between the barrel and the extended barrels. A more detailed description of the TileCal and the ITC with its calibration system will be given in chapter three.

1.3.2.4 The Muon System

The muon spectrometer is the outermost part of the ATLAS detector covering charged particles, mainly muons, that escape beyond the calorimeter system with a coverage of $|\eta| < 2.7$ and can also trigger on them. [11] Charged particles of momenta 3 GeV to 3 TeV can be measured with good momentum resolution and charge identification.

The muon system consists of four chamber sub systems and the toroidal magnets. The Monitored Drift Tubes (MDT) and the Cathode Strip Chambers (CSC) form the precision -measurement tracking chambers whereas the Resistive Plate Chambers (RPC) and the Thin Gap Chambers(TGC) are for triggering. The muon chambers in the barrel form three concentric cylindrical shapes about the beam axis at radii 5m, 7.5 m and 10 m respectively. Large wheels perpendicular to the beam axis cover the end cap regions at distances of 7.4 m, 10.8 m, 14 m,and 21.5 m from the interaction point. Figures 1.10 and 1.11 shows the cross section views of the muon system along the plane perpendicular to the beam axis and parallel to the beam axis respectively. Three concentric cylindrical layers of eight large and small chambers arranged around the toroid magnets are shown in fig 1.10. The three layer system results in the three points necessary to construct a trajectory. In fig 1.11 schematic muon tracks are shown in dashed lines traversing typically three muon stations. The muon chambers are constructed to have a momentum and mass resolution of 1% as well as position resolution of 50 μm. The toroid magnets deliver a magnetic field of $\tilde{0}$.5T perpendicular to the trajectory of the charged particle.

1.3.3 The ATLAS Trigger System

It is of paramount importance that a detector system be equipped with a well functioning trigger system.[12] The LHC is designed to deliver around 600 billion collisions per second. It is physically impossible to record all the collisions and analyze the data because of its sheer volume. Thus the trigger system plays the very important role of identifying ‘events’ of interest when high transverse momentum muons, photons, electrons, τ-leptons, jets or high missing or total transverse momentum is

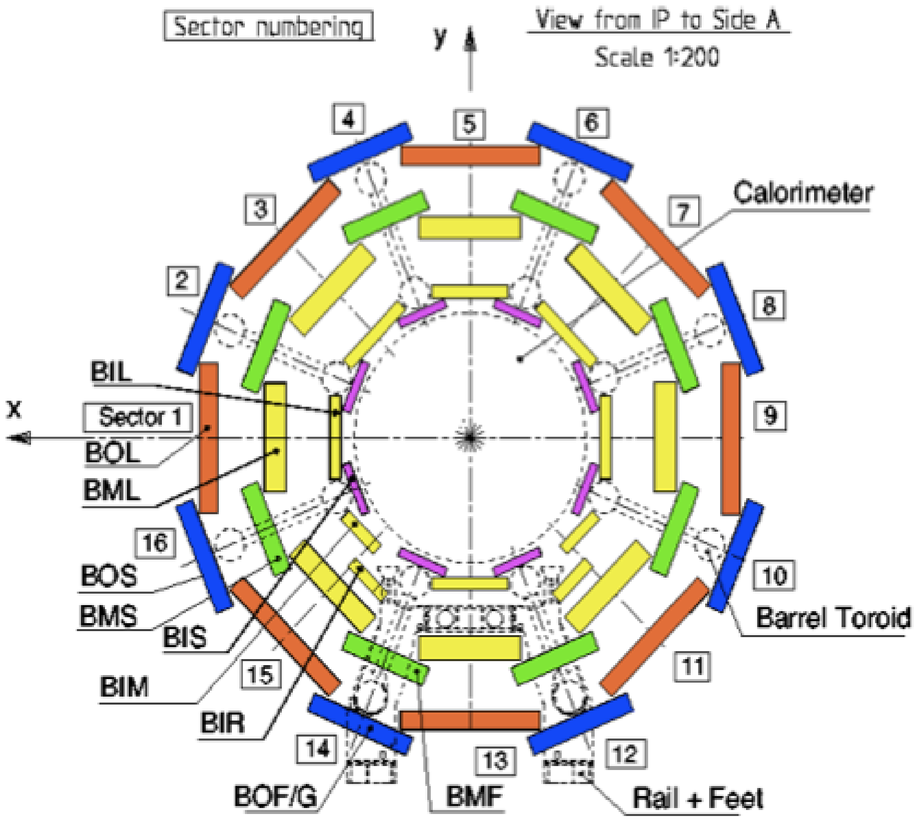

Figure 1.10. X-Y Cross-section in schematic view of the muon system.

present. The trigger and data acquisition systems (TDAQ) consists of logical blocks in every subsection of the detector. The trigger system itself can be subdivided into three levels. The Level 1 (L1) of trigger system can make a decision in less than 2.5 μs on the data that is buffered by the data acquisition system, reducing the rate to about 75 kHz. The Level 2 (L2) and Event Filter (EF) trigger system brings the rate down to 200 Hz with an average even size of 1.3 MB. Once an event is selected the data is moved to the permanent storage at CERN computing facility. The data acquisition system facilitates this movement of data as well as monitors and controls the proper

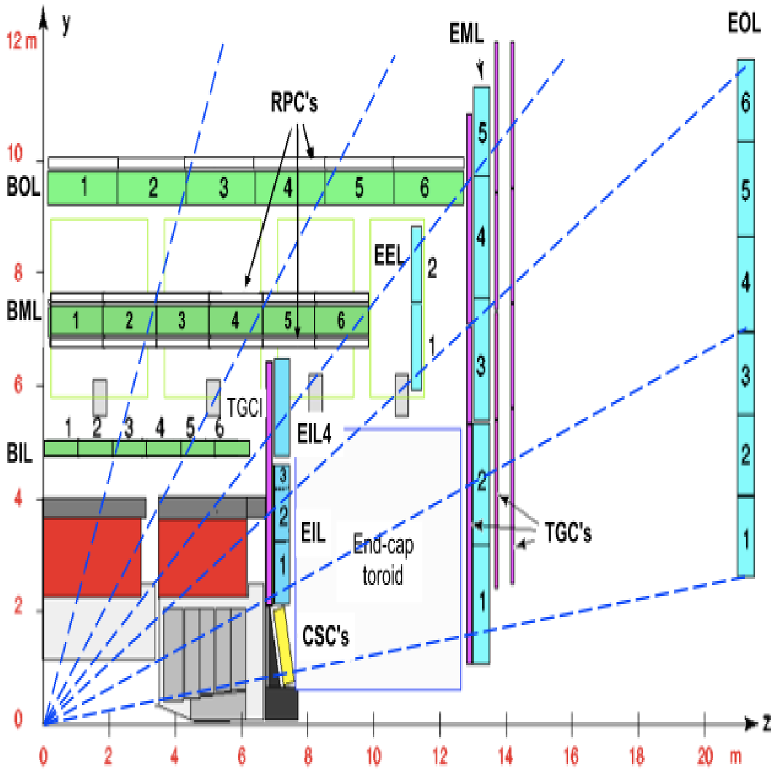

Figure 1.11. Y-Z Cross section schematic view of the muon system.

functioning of the various hardware and software components of the detector. In this sense the TDAQ system can be considered to be the ‘brain’ of the ATLAS detector.

1.3.4 ATLAS Simulation and Reconstruction

The ATLAS detector environment can be simulated using Monte Carlo techniques.[13] A general purpose Monte Carlo program for ATLAS named GEANT4 [14] is used for simulating various physics processes within the ATLAS detector. Either data from LHC proton collisions or simulated by GEANT is then reconstructed by the ATLAS reconstruction software and the ‘raw data’ or ‘hits’ are eventually transformed into physics objects. The main framework that encompasses all the software components of ATLAS is called ATHENA (ref). ATHENA is an object oriented framework consisting of Tools, Services and Data Objects, all communicating via a common StoreGate service. It is written in C++ and consists of Python scripts, or JobOptions, that are used to configure specific Tools and Algorithms. [15]

Figure 1.12 shows a flow chart of the ATLAS software chain. It begins with the generation of events using various Monte Carlo event generators. Commonly used event generators in ATLAS are PYTHIA [16], HERWIG [17], ALPGEN [18], ISAJET [19] and other MC@NLO [20]. The event generators like PYTHIA or HERWIG generate matrix elements describing specific linear order partonic interactions and add initial and final state radiative processes. Some generators like ALPGEN or other MC@NLO generators only produce matrix elements at linear as well as next to linear orders with detailed information and evolution of color and flavor structures. For these PYTHIA or HERWIG is used for simulating the hadronic final states.

Once events are generated the output is used for the ATLAS detector simulation using GEANT. The GEANT program knows about the geometry and materials of the ATLAS detector and models the interaction of particles with this material, while managing all the hits and tracks that can be produced. It also constructs a 'true' trajectory and interaction that is used in the Monte Carlo for many studies requiring understanding of the detector and its material. It also is equipped with a database for simulating of all possible decays of particles and nuclei, through electromagnetic, hadronic as well as optical processes. All visible and invisible energy deposits are also accounted for. A fast, not so detailed, simulator known as ATLFAST(II) is also used in ATLAS to approximately simulate the detector. Although not as detailed as GEANT, ATLFAST has the advantage of being lightweight and covers both simulation and reconstruction in a single step and thus is suitable for quick test studies.

The next step in data processing is Reconstruction. From this step onward the software is identical for LHC data or simulation. In this step either real signals from the many detector components or digitized GEANT hits are converted into physics objects like jets, electron, photons, muons etc. with the use of reconstruction algorithm. Details of reconstruction algorithms for various objects of interest will be presented in the subsequent chapters. More than one reconstruction algorithm is available and often used to reconstruct each physics object. The data at this point is converted into a very structured format with detailed information pertaining to each object stored in a 'container' and is called Event Summary Data or ESD. A ESD contains about 500 kBytes of information per event. The ESD is further reduced in size by only retaining the essential summary of the event without detailed information about detector related quantities, into an Analysis Object Data or AOD. A typical AOD contains about 100 kBytes per event. Most physics analyses are started at the AOD level.

Although not part of the ATLAS software system, ROOT [21] is a physics analysis software written in C++ that is used widely in ATLAS. It is lightweight and can be used with any computer operating system, to perform simple to complicated analysis. Another software package named SPyRoot, written in PYTHON uses ROOT within a framework of object oriented physics analysis code. Most of the analysis for this dissertation has been performed using the SPyRoot framework.

1.3.5 The ATLAS Computing System

One of the most crucial components of ATLAS is its Computing System. The ATLAS computing system consists of the main computing infrastructure at CERN and the ATLAS Distributed Computing system. [15] All data from the detector is written into tapes in the CERN CASTOR system. The CERN system is the first part of the multi tiered GRID computing infrastructure. The data from CERN, Tier 0 is distributed real time to Tier 1 systems all over the world. The Tier 0 facility receives raw data from the DAQ systems and performs the first reconstruction of this 'raw' data. ATLAS is designed to produce around 15 Petabytes of data per annum to be used by many thousand scientists all over the world. The Grid infrastructure ensures quick and easy access to data as well as extensive CPU power at the scientists' disposal. All Tier 1 computing centers receive data from the Tier 0 around the clock and distributes reconstructed data (ESDs and AODs) to Tier 2 facilities. Tier 2 facilities provide computing power as well as data to users. Moreover, these in turn distribute data to Tier 3 facilities that consist of small clusters in universities or personal computers. Some universities like the University of Texas at Arlington has both Tier2 and Tier3 facilities available for data processing. The computing GRID not only makes analyses of ATLAS data feasible it also facilitates the participation of a global scientific community in performing the analysis towards the greater goal of discovering new physics.

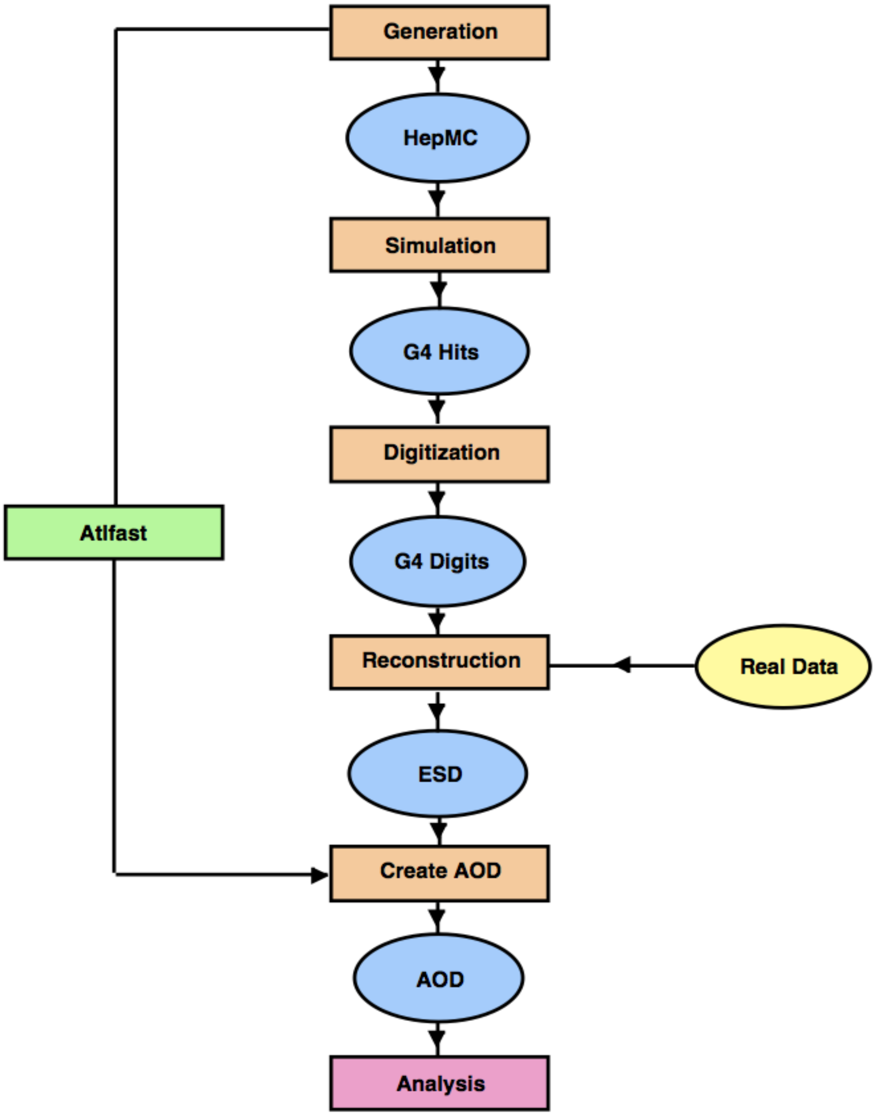

Figure 1.12. The ATLAS Software Chain.

CHAPTER 2

THEORETICAL BACKGROUND

2.1 Introduction

This chapter will provide summary of the necessary theories that are essential for understanding the physics of the LHC. A brief introduction to the Standard model will be given followed by the theoretical predictions of the physics that lies beyond the standard model. The goal is not to summarize all of theoretical physics, an impossible task in one chapter, but to elucidate the background required in the understanding of the subsequent chapters.

2.1.1 The Standard Model of Particle Physics

The Standard Model of Particle Physics as the the name suggests is a model that describes all of the known physics of matter and its interactions in a compact form. [**?**] It aims to describe the four known fundamental forces within the framework of gauge theories. However, this is only possible for electromagnetic, weak and strong forces with gravitational gauge theory being incomplete. Moreover, the origin of mass in the theory is via the Higgs mechanism, although this is yet not experimentally observed. One of the primary reasons for constructing the LHC was to look for the quanta of the Higgs field known as the Higgs boson. A more detailed description on the Higgs mechanism and the search for it at ATLAS is presented subsequently.

According to the Standard Model all known fundamental particles can be classified into two categories. The first being a fermion and the second a boson, both named after physicists who described the statistical behavior of these particles in

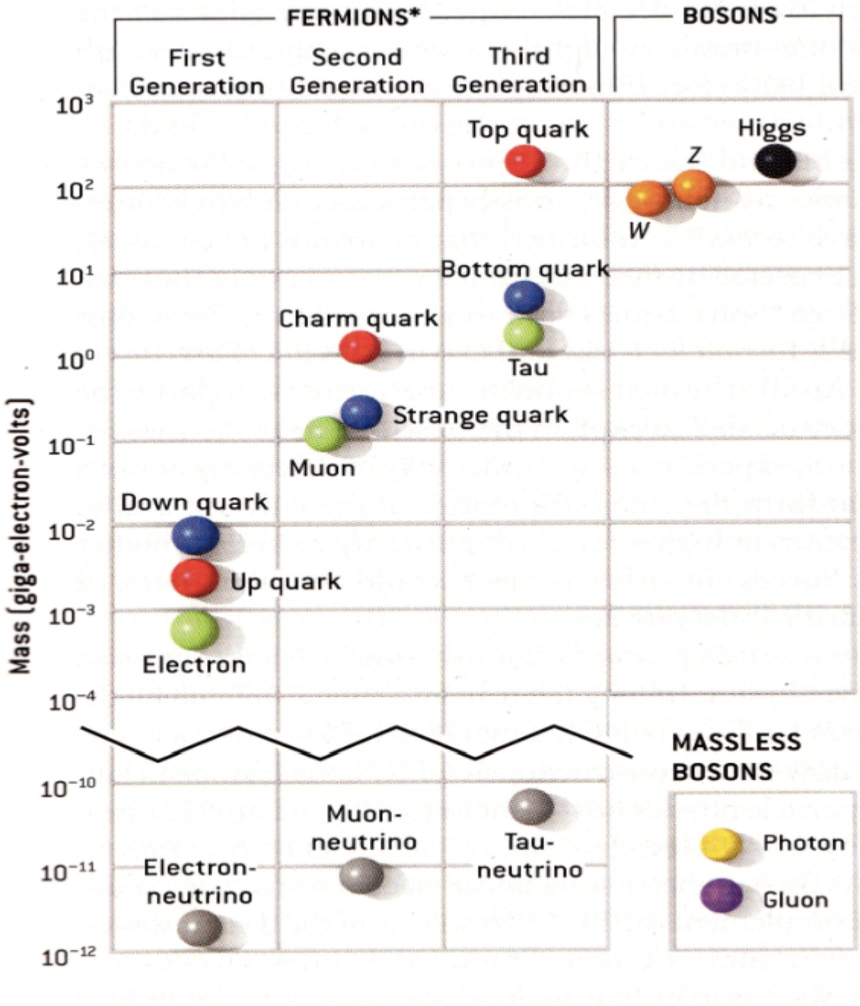

Figure 2.1. Summary of Standard Model Particles and Properties.

an ensemble. Fermions are characterized by multiples of half-integer spins while the bosons carry multiples of integer spins and the spin the particles carry govern their interactions in large systems.

As in fig. 2.1 the two main columns separate the fermions and the bosons. In addition to this, the fermions are classified into two categories, that of quarks and leptons. Each quark has a corresponding lepton in its 'generation' where the different 'generations' are distinguished primarily by their mass range. The leptons also have a corresponding neutrino associated with them. All the quarks, leptons in the three generations have been discovered. Quarks can carry fractional charges ($-1/3$ or $2/3$) without violating any conservation of charge as they cannot be observed in isolation from other quarks. In addition to electric charges, so far referred to simply as ‘charge’, particles that interact via the strong force also carry a ‘color-charge’. The color-charge is not related to any optical properties but merely refer to the conserved quantity emerging out of the symmetries of the gauge fields that mediate the strong interactions. The color-charge can be red, green or blue with corresponding anti-red and anti-green and anti-blue. Quarks must combine to form mesons, a combination of a quark and an anti-quark, or baryons, combinations of three quarks, such that an integer charge as well as a color of ‘white’ is obtained. Particles formed by quarks are collectively referred to as hadrons. For example the proton is a hadron which is a baryon composed of two Up quarks and one Down quark, adding up to a charge of $+1$ and a color of 0 or white. [22]

All known matter is composed of quarks and leptons along with their respective anti-particles that carry equal but opposite charges, all held together by the interaction between them via the exchange of gauge bosons.

The gauge bosons are the force carriers. Since the Standard Model is a gauge theory, each force field in it has an associated gauge boson, also referred to as the ’force-carriers’. This is because these bosons are exchanged among the corresponding fermions during interactions. The theory of Quantum Electro Dynamics (QED), describes the interaction of electrically charged particles like that between the electron and the positron via the exchange of the photon, the gauge boson for QED. Similarly according to the theory of Weak Interaction, there are two gauge boson for the weak interaction the Z^0 and $W^{\pm}$. In one of most significant achievements of theoretical physics in the later part of the twentieth century is the unification of the theory of

QED with Weak interactions into what is known as the Electro-Weak theory. This theory was shown to be renormalizable, a theoretical requirement for a gauge theory to be free of infinities, and is now well tested experimentally. However, one of the more puzzling facts of the Electro-Weak theory is that the Z^0 and the $W^{\pm}$ are substantially massive. In the following sections the origin of this mass,and essentially any mass, via the Higgs mechanism will be explored.

Another step towards understanding the fundamentals of particles and interaction was the formulation of Quantum Chromo Dynamics or QCD, the 'chromo' referring to the color-charges carried by the quarks. Once it was understood that gauge theories emerge out of their corresponding space-time symmetries or in more technical terms each gauge theory is associated with a Lie group, it was a matter of some innovative mathematics and tedious experimental searches to discover quarks and gluons and understand the composition of particles such as the proton and the neutron. The force carrier or the gauge boson for QCD is called the gluon. Figure 2.2 shows the basic Feynman diagrams for the exchange processes of bosons among leptons for interactions.

Through QCD we have come to understand the very building blocks of nature as we observe it everyday. The discovery of the six quarks and understanding of their interactions has been the task and accomplishments of the particle accelerator and detectors until now. However, QCD itself is not very well understood in low energy boundaries. In the realm of particles with a few mega electron volts or less of energy one applies effective theoretical models based on non-perturbative and lattice based calculations. Such calculations are approximate at best.[**?**]

The Standard Model is thus a collection of consistent rules and laws belonging to Electro-Weak theory and QCD valid in the realm of high energy physics. It is evident that the Standard Model is consistent with present experimental observations but is

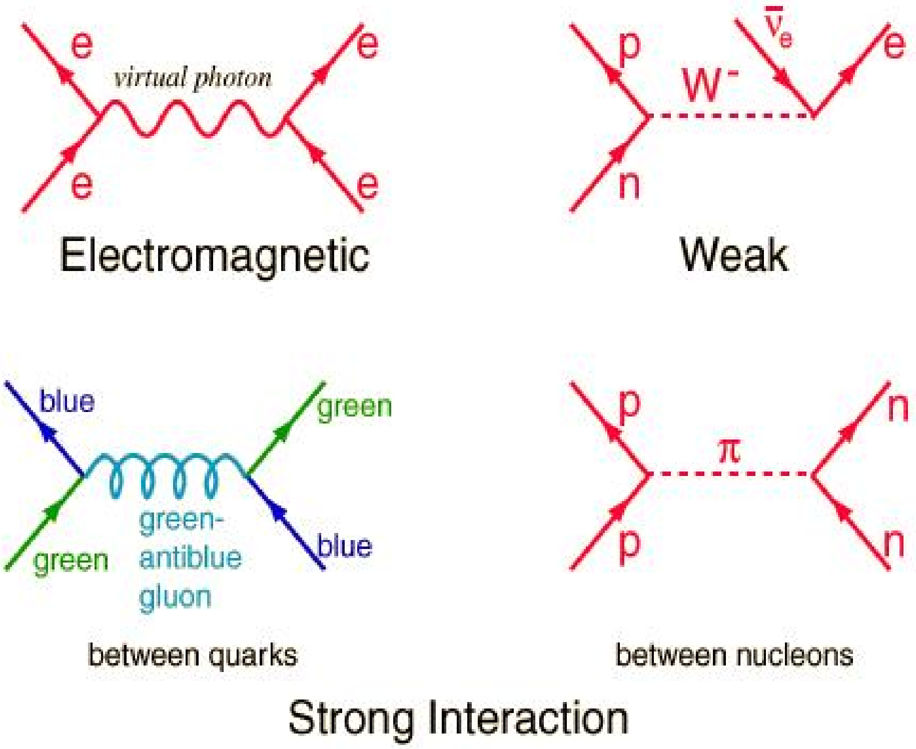

Figure 2.2. Feynman diagrams showing leptons exchanging gauge bosons.

incomplete in its ability to describe all sub atomic phenomenon. Other than being incomplete in terms of knowing the origin of mass or interaction at low energies, the Standard Model has been remarkably successful in predicting an explaining all observed phenomenon in high energy physics.

2.1.2 Big Bang and Cosmology

The goal of physics is to explain all observed phenomenon. A theory capable of explaining all phenomenon must incorporate gravity. No renormalizable gauge theory of gravity that can be experimentally verified is known as of this writing. There is also an extensive theory of cosmology based on the geometric theory of gravity or General Relativity. The cosmological theory of Big Bang based on General Relativity gives an accepted and observationally verified [23] [24] view of the origin of the universe. Big Bang theory postulates a beginning for the universe from a single point of singularity, like a ‘point’ in the Cartesian plane. Right after the Big Bang the universe started expanding at a rapid rate. Along with this expansion came the decoupling of the forces of gravity and the other three. In figure 2.3 a diagram of this evolution is shown. It is postulated that at one time in the history of the universe the forces of gravity, strong, weak and electromagnetism were one and the same. This necessitates the existence of a theory of gravity that is valid at the plank scale ($\sim 1.6 \times 10^{-35}$m) defined by using the following formula

$$L_P = (hG/2\pi c^3)^{1/2} \tag{2.1}$$

which denotes the length scale at which gravity and the other forces need to be unified, a scale when the size of the universe was that big. Other than the major problems with finding a gauge theory that intertwines gravitational, strong and electro-weak forces, several other cosmological observations still remain unsolved. One of them is the fact that the known baryonic matter in the universe constitutes only 4.6% of the total matter in the universe, resulting in a matter density of 1 proton per 4 cubic meter of space. [23] This opens the question, as to what constitutes the rest of the 96% of the universe. The Standard Model so far is unable to explain this phenomenon.

The following sections will deal with elucidating two pivotal unanswered problems associated with our current knowledge of physics. The accepted theoretical solutions to these problems will be presented, followed by how these solutions can be verified by the ATLAS experiment.

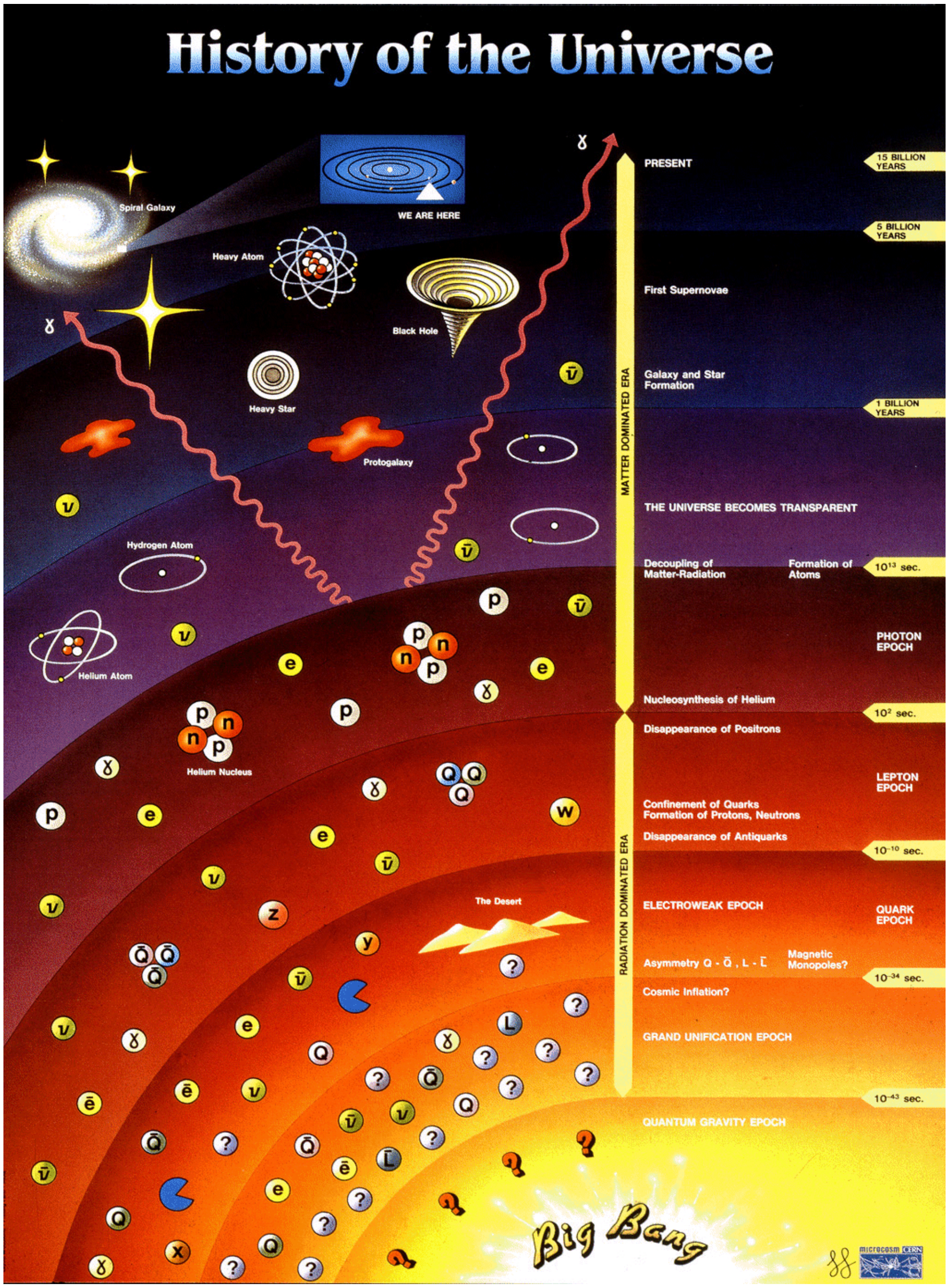

Figure 2.3. Cartoon depiction of the time evolution of the universe.

2.2 Standard Model and The Higgs Mechanism

The standard model is a $SU_3 \bigotimes SU_2 \bigotimes U_1$ Yang-Mill's [25] gauge theory, with the first two groups being non-Abelian. One of the primary restrictions on formulating any Yang-Mil's theories is the condition of Renormalizability. This forces the Standard model Lagrangian to have no explicit mass terms.

2.2.1 The Standard Model Lagrangian

The electroweak theory is based on the $SU_2 \bigotimes U_1$ group, with its Lagrangian given as [25] [26],

$$\mathcal{L}_{SU_2 \bigotimes U_1} = \mathcal{L}_{gauge} + \mathcal{L}_{\phi} + \mathcal{L}_{f} + \mathcal{L}_{Yukawa} \tag{2.2}$$

Where the gauge part is given as,

$$\mathcal{L}_{gauge} = -\frac{1}{4} F^i_{\mu\nu} F^{\mu\nu i} - \frac{1}{4} B_{\mu\nu} B^{\mu\nu} \tag{2.3}$$

with,

$$\begin{aligned} B_{\mu\nu} &= \delta_\mu B_\nu - \delta_\nu B_\mu \\ F_{\mu\nu} &= \delta_\mu W^i_{nu} - \delta_\nu W^i_\mu - g\epsilon_{ijk} W^j_\mu W^k_\nu \end{aligned} \tag{2.4}$$

the $W^i_\mu, i = 1, 2, 3$ and B_μ being representations of SU_2 and U_1 gauge fields, g the SU_2 coupling. The photon, γ and the Z^0 bosons are the mixed states of the B and the W_3 fields. The next term in the Lagrangian in (2.2) is the scalar term given by,

$$\mathcal{L}_{\phi} = -(D^\mu \phi)^\dagger D_\mu \phi - V(\phi) \tag{2.5}$$

with, $\phi = \binom{\phi^+}{\phi^0}$ a complex scalar Higgs field with $V(\phi)$ the Higgs potential, given by,

$$V(\phi) = +\mu^2\phi^\dagger\phi + \lambda(\phi^\dagger\phi)^2 \tag{2.6}$$

that is needed to generate mass for the physical gauge bosons in electroweak theory while preserving $SU_2 \bigotimes U_1$ invariance and renormalizability. The next term in (2.2) is the fermionic term given by,

$$\mathcal{L}_\phi = \sum_{m=1}^{F}(\bar{q}^0_{mL} i\not{D} q^0_{mL} + \bar{l}^0_{mL} i\not{D} l^0_{mL} + \bar{u}^0_{mR} i\not{D} u^0_{mR} + \bar{d}^0_{mR} i\not{D} d^0_{mR} + \bar{e}^0_{mR} i\not{D} e^0_{mR}) \tag{2.7}$$

with $F \geq 3$ as the number of families. The L, R represent the left and right handed chiral property of the wave function. The left handed quarks, $q^0_{mL} = \binom{u^0_m}{d^0_m}_L$ and leptons, $l^0_{mL} = \binom{\nu^0_m}{e^0_m}_L$ are represented as doublets whereas the right handed representations u^0_{mR}, d^0_{mR},e^0_{mR} are singlets. This is also in accordance with the observation that right handed neutrinos or left handed anti-neutrinos are not observed in Nature. The Yukawa term in (2.2) can be written as,

$$\mathcal{L}_\phi = -\sum_{m,n=1}^{F}([\Gamma^u_{mn}\bar{q}^0_{mL}\tilde{\phi}u^0_{mR} + \Gamma^d_{mn}\bar{q}^0_{mL}\phi d^0_{nR} + \Gamma^e_{mn}\bar{l}^0_{mn}\tilde{\phi}e^0_{nR}] + H.C. \tag{2.8}$$

with the Γ_{mn} matrices give the coupling between the Higgs field and the different flavors of quarks (m) and leptons (n) and the H.C denoting the hermitian conjugate of the first term.

The QCD part of the Lagrangian, corresponding to SU_3 symmetry is given as,

$$\mathcal{L}_{SU_3} = -\frac{1}{4}\mathcal{F}^i_{\mu\nu}\mathcal{F}^{\mu\nu i} + \sum_r \bar{q}_{r\alpha} i\not{D}^\alpha_\beta q^\beta_r \tag{2.9}$$

with,

$$\mathcal{F}^i_{\mu\nu} = \delta_\mu G^i_\nu - \delta_\nu G^i_\mu - g_s f_{ijk} G^j_\mu G^k_\nu \tag{2.10}$$

being the gluon field tensor with G^i_μ , $i = 1, \cdots, 8$ and f_{ijk} the structure constants denoted in the irreducible representations of the SU_3 group. The direct sum of the $\mathcal{L}_{SU_3}$ and $\mathcal{L}_{SU_2 \bigotimes U_1}$ yields the $SU_3 \bigotimes SU_2 \bigotimes U_1$ symmetric standard model Lagrangian.

2.2.2 Spontaneous Symmetry Breaking and Goldstone Theorem

For a general quantum field theory with a Lagrangian $\mathcal{L}_0$ one can write a general variation of $\mathcal{L}_0$ as [25] [27] [28],

$$\delta\mathcal{L}_0 = (\delta_\mu \alpha^a)\mathcal{J}^{\mu a} \tag{2.11}$$

where $\mathcal{J}^{\mu a}$ is a vector operator derived from the fields of $\mathcal{L}_0$. From the variational principle one has the following identity,

$$\delta_\mu \mathcal{J}^{\mu a} = 0 \tag{2.12}$$

with the $\mathcal{J}^{\mu a}$ identified as the Noether currents of the global gauge symmetry. Adding a non-Abelian gauge field term to the Lagrangian $\mathcal{L}_0$ yields a locally symmetric Lagrangian of the form,

$$\mathcal{L} = \mathcal{L}_0 - gA^a_\mu \mathcal{J}^{\mu a} + \mathcal{O}(A^2) \tag{2.13}$$

Equation (2.12) guaranties that the matrix elements involving the first two terms in (2.13) are computable using the $\mathcal{J}^{\mu a}$ currents of the original theory with $\mathcal{L}_0$ [25] Now if the global symmetry of the $\mathcal{L}_0$ is spontaneously broken (due to any mechanism), one can identify Goldstone bosons that can be created by action of the charge Q^a, the charge corresponding to the current $\mathcal{J}^{\mu a}$ on the vacuum state. Then, one can write,

$$< 0|\mathcal{J}^{\mu a}(x)|\pi_k(p) >= -ip^\mu F_k^a e^{-ipx} \tag{2.14}$$

where p is the on-shell momentum and the $|\pi_k(p) >$, one such Goldstone boson states. Now, one can again use, (2.12) to take the derivative of (2.14) and write,

$$\begin{aligned} \delta_\mu < 0|\mathcal{J}^{\mu a}(x)|\pi_k(p) > &= p^2 F_k^a e^{-ipx} \\ &= 0 \end{aligned} \tag{2.15}$$

Two things are clear from the above equation. Firstly when F_k^a have non-zero terms, i.e. when the symmetry is broken, this matrix connects the currents of the unbroken symmetry with the Goldstone bosons of the broken symmetry. Also, since equation (2.15) implies that $p^2 = 0$ the Goldstone boson must be mass-less, a proof of the Goldstone theorem.

The Goldstone theorem is vital for the study of broken symmetries in nature. And more often than not one encounters more broken than preserved symmetries. The observation of the pion mass being much less than the proton mass is understood in light of viewing the pion as the Goldstone boson emerging out of the spontaneous breaking of chiral symmetry.[28]

It is then a matter of exercise to see the effect of spontaneous symmetry breaking of the gauge symmetry of $SU_3 \bigotimes SU_2 \bigotimes U_1$ electroweak theory. The following sub section describes the effects of spontaneous electroweak symmetry breaking and the the capture of the Goldstone bosons by the gauge fields to obtain masses also, known as the Higgs mechanism.

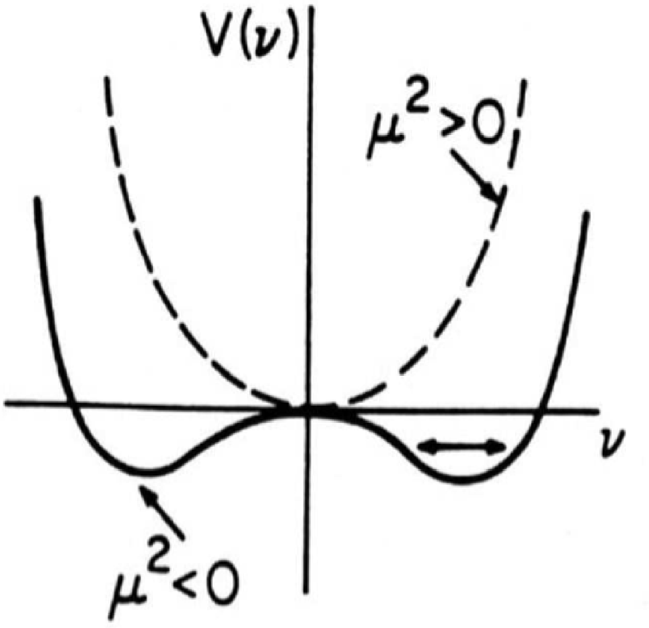

Figure 2.4. The Higgs potential V(v) for $\mu^2 > 0$ and $\mu^2 < 0$.

2.2.3 The Higgs Mechanism

As the weak interaction is short-ranged and weak, the mediating gauge bosons cannot be mass-less. A solution for assigning mass to the gage boson would be to include explicit mass terms in the electroweak Lagrangian. However this will make the theory non-renormalizable and hence unphysical. The solution is to break the gauge invariance of the theory spontaneously. This results in the fact that the lowest energy state is not gauge symmetric and the gauge bosons acquire masses by acquiring the longitudinal degree of freedom of the Goldstone boson. One can say that the mass-less gauge bosons ‘eat’ the Goldstone boson and become massive. [28]

One can write the potential in equation (2.6) in terms of a complex vector $v =< 0|\phi|0 >= constant$ such that $V(\phi) \to V(v)$ gives the minimum energy. One can write the Higgs potential as,

$$\phi = \begin{pmatrix} \phi^+ \\ \phi^0 \end{pmatrix} = \begin{pmatrix} \frac{1}{\sqrt{2}}(\phi_1 - i\phi_2) \\ \frac{1}{\sqrt{2}}(\phi_3 - i\phi_4) \end{pmatrix} \tag{2.16}$$

with, $\phi_i = \phi_i^\dagger$. On choosing the axes such that, $< 0|\phi_i|0 >= 0$ for $i = 1, 2, 4$ and $< 0|\phi_3|0 >= v$ one can rewrite equation (2.17) as,

$$V(v) = \frac{1}{2}\mu^2\nu^2 + \frac{1}{4}\lambda\nu^4 \tag{2.17}$$

Upon minimizing equation (2.17) with respect to v two cases arise. First if $\mu^2 > 0$ the minimum is at $v = 0$. This is the state when the potential is symmetric for $SU_2 \bigotimes U_1$. For the case where $\mu^2 < 0$, see figure (2.4), the solution can be found as $v = (-\mu^2/\lambda)^{1/2}$ at the minimum. Now representing the field as, $\phi \to \frac{1}{\sqrt{2}}\binom{0}{v}$ and using the gauge covariant derivative,

$$D_\mu\phi = (\delta_\mu + ig\frac{\tau^i}{2}W_\mu^i + \frac{ig'}{2}B_\mu)\phi \tag{2.18}$$

one gets the following expression,

$$\begin{aligned} (D_\mu\phi)^\dagger D_\mu\phi &= \frac{1}{2}(0\ v)[\frac{g}{2}\tau^i W_\mu^i + \frac{g'}{2}B_\mu]^2\begin{pmatrix} 0 \\ v \end{pmatrix} + Higgs(K, G) && (2.19) \\ &= M_W^2 W^{+\mu}W_\mu^- + \frac{M_Z^2}{2}Z_\mu^\mu + Higgs(K, G) && (2.20) \end{aligned}$$

where the $Higgs(K, G)$ are the kinetic and gauge terms for the physical Higgs particle. The second line of equation (2.19) show the mass terms associated with the gauge bosons due to spontaneous breaking of gauge symmetry. Defining $\theta_W \equiv g'/g$ the gauge boson terms can be written as,

$$\begin{aligned} W^{\pm} &= \frac{1}{\sqrt{2}}(W^1 \mp iW^2) \\ Z &= -\sin\theta_W B + \cos\theta_W W^3 \\ A &= \cos\theta_W B + \sin\theta_W W^3 \end{aligned} \qquad (2.21)$$

with the corresponding masses given as,

$$\begin{aligned} M_W &= \frac{gv}{2} \\ M_Z &= \sqrt{g^2 + g'^2}\frac{v}{2} = \frac{M_W}{cos\theta_W} \\ M_A &= 0 \end{aligned} \qquad (2.22)$$

the photon indeed turning out to be mass-less. One can calculate the weak scale at $v = 2M_W/g \approx 246 GeV$. Finally, one can write the Higgs potential after symmetry breaking as,

$$V(\phi) = -\frac{\mu^4}{4\lambda} - \mu^2 H^2 + \lambda\nu H^3 + \frac{\lambda}{4}H^4 \qquad (2.23)$$

with the quanta being the Higgs boson with a mass of $M_H = \sqrt{2\lambda}v$. The Higgs coupling λ is unknown and thus the Higgs mass is only constrained by indirect experimental observations. One of the primary goals of the LHC is to observe the Higgs boson. As discussed above it is an essential ingredient for the Standard Model to work. With the Higgs closely related to the weak scale it has a widely accepted mass upper cut of 1 TeV. This also makes it a prime candidate for being observed at ATLAS given enough luminosity.

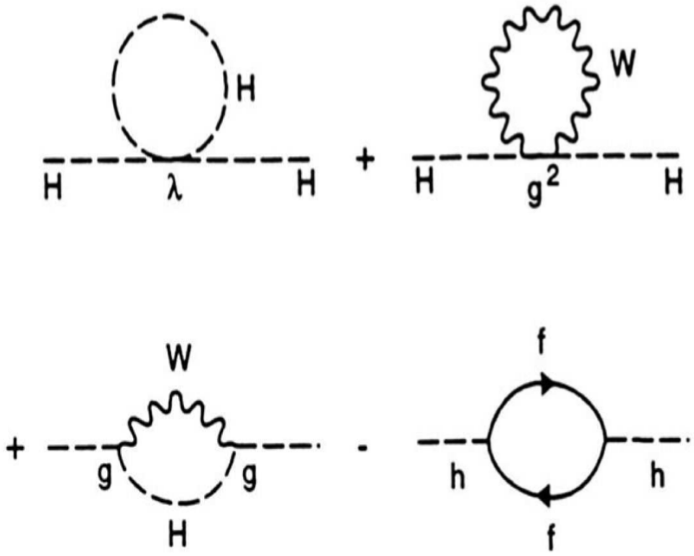

Figure 2.5. Loop Corrections to the Bare Higgs Mass.

2.2.4 The Higgs Hierarchy Problem

Although naturalness and finite mass requirements require the Higgs mass to be in the electroweak scale, loop (Feynman) diagrams as shown in figure (**??**fig:2-5) adds quadratically divergent terms to the Higgs mass. So, the mass now becomes,

$$M_H^2 = (M_H^2)_{bare} + \mathcal{O}(\lambda, g^2, h^2)\Lambda^2 \tag{2.24}$$

where Λ is a next theoretical scale. Given that Λ cannot be an ultraviolet cutoff at near weak scale, since Standard Model must be embedded in a higher theory incorporating Gravity at the Plank's Scale, the Higgs mass in equation (2.19) becomes infinite or too large. This is the Higgs Hierarchy problem ailing the Standard Model. One simple solution comes from the assumption of New Physics, that can 'cancel' these tree level loop diagrams exactly. Such a new theory is Supersymmetry. [29]

2.3 Supersymmetry

Supersymmetry (SUSY) refers to a new type of symmetry between bosons and fermions. For every fermionic field in the Standard Model, SUSY predicts that there is a partner bosonic field and vice-verse. [15] This prediction as a result of extending Poincare symmetry increases the number of particles to twice what we know today. The partners of the fermions are bosons with the same name with a prefixed ‘s’ e.g. the electron’s partner is named (s)electron whereas, the bosons have partners with a suffixed ‘ino’ e.g. the gluon’s partner is the glu‘ino’. Other than doubling the number of animals in the particle zoo SUSY also solves several problems associated with the Standard Model, including the Higgs hierarchy problem as well as naturally yields a Dark Matter candidate. In the following sub section a very brief theoretical overview of SUSY is presented. A more detailed phenomenological study of SUSY in ATLAS and results from the ATLAS data is presented in chapters 5 and 6.

2.3.1 Introduction to SUSY

The Standard Model is invariant under the transformations of the Poincare group. The algebra of the Poincare group determine the basic laws within the Standard Model which are invariant under Lorentz transformations as well as translations. The Lorentz’s transformations are generated by generalized angular momentum operators $M^{\rho\sigma}$ while translations are generated by the four momentum P^{ρ} as shown below [30],

$$\begin{aligned} P^{\rho} &= i\delta^{\rho} \\ M^{\rho\sigma} &= i(x^{\rho}\delta^{\sigma} - x^{\sigma}\delta^{\rho}) + \frac{i}{4}[\gamma^{\rho}, \gamma^{\sigma}] \end{aligned} \tag{2.25}$$

Using $[x^\rho, P^\sigma] = -ig^{\rho\sigma}$ where $g^{\rho\sigma}$ is the metric tensor, the commutation relations of the Poincare algebra can be written as follows,

$$\begin{aligned}
[P^\rho, P^\sigma] &= 0 \\
[P^\rho, M^{\rho\sigma}] &= i(g^{\rho\nu}P^\sigma - g^{\rho\sigma}P^\nu) \\
[M^{\mu\nu}, M^{\rho\sigma}] &= -i(g^{\mu\rho}M^{\nu\sigma} + g^{\nu\sigma}M^{\mu\rho} - g^{\mu\sigma}M^{\nu\rho} - g^{\nu\rho}M^{\mu\sigma}) \qquad (2.26)
\end{aligned}$$

This algebra can be extended according to the Coleman-Mandula no-go theorem to incorporate all further symmetries compatible with interacting relativistic quantum field theories by taking direct products with algebras representing internal symmetries. However, the only possible way to extend the symmetries of the Poincare group without running afoul of the no-go theorem is by introducing non-bosonic generators in the theory. [30]

Fermionic operators in a given theory will change the spin of the fields. Thus if Q_α is a fermionic generator we get,

$$\begin{aligned}
Q_\alpha|boson> &= |fermion>_\alpha \\
Q_\alpha|fermion>^\alpha &= |boson> \qquad (2.27)
\end{aligned}$$

Introduction of one such fermionic operator Q_α gives the simplest N=1 supersymmetric algebra. The commutation relationships can be written as,

$$[Q_\alpha, P^\rho] = 0 \qquad (2.28)$$

$$\{Q^i_\alpha, Q^{\dagger j}_\beta\} = 2\delta^{ij}\sigma^\rho_{\alpha\beta}P_\rho \qquad (2.29)$$

$$[M^{\rho\sigma}, Q_\alpha] = -i(\sigma^{\rho\sigma})^\beta_\alpha Q_\beta \qquad (2.30)$$

$$\{Q_\alpha, Q_\beta\} = 0 \qquad (2.31)$$

with the fermionic operators having anti-commutation whereas the boson commutation relationships. The simplest Standard Model incorporating SUSY is called Minimally Supersymmetric Standard Model (MSSM). The table in figure (2.1) shows the chiral supermultiplets in the MSSM.[31]

Table 2.1. Summary of the Chiral Supermultiplets in the MSSM

Name	Spin 0	Spin 1/2	SU(3) x SU(2) x U(1)
squarks, quarks	$\tilde{Q} = (\widetilde{(u)}_L, \tilde{d}_L)$	$Q = (u_L, d_L)$	$(3, 2, 1/6)$
	$\tilde{u}^*_R$	$\tilde{u}_R$	$(\bar{3}, 1, -2/3)$
	$\tilde{d}^*_R$	$\tilde{d}_R$	$(\bar{3}, 1, 1/3)$
sleptons, leptons	$\tilde{L} = (n\tilde{u}, \widetilde{(e)}_L)$	$L = (\nu, e_L)$	(1,2.-1/2)
	$\tilde{e}^*_R$	$\tilde{e}_R$	(1,1,1)
Higgs, Higgsinos	$H_u = (H^+_u, H^0_u)$	$\tilde{H}_u = (\tilde{H}^+_u, \tilde{H}^0_u)$	(1,2,1/2)
	$H_d = (H^0_d, H^-_d)$	$\tilde{H}_d = (\tilde{H}^0_d, \tilde{H}^-_d)$	(1,2,1/2)

The vector multiplets in the MSSM is summarized in (2.2). In the case of the Higgs the physical Higgs bosons are h, H, A and $H^\pm$ and the binos and winos mix with the Higgsinos to give four neutralinos ($\tilde{\chi}^0_i$) and two charginos ($\tilde{\chi}^\pm_i$)

Table 2.2. Summary of the Vector supermultiplets in the MSSM

Names	Spin 1/2	Spin 1	SU(3) x SU(2) x U(1)
gluino,gluon	$\tilde{g}$	g	$(8, 1, 0)$
wino, W's	$\tilde{W}^\pm, \tilde{W}^0$	$W^\pm, W^0$	(1,3,0)
bino, B	$\tilde{B}$	B	(1,1,1)

Even though Supersymmetry looks like a wonderful and plausible extension to the Standard Model, no bosonic electron or the selectron is observed in nature. Thus if SUSY must exist in nature it must be spontaneously broken.

2.3.2 SUSY solves the Higgs Hierarchy problem

The Standard Model as in equation (2.24) contains loop diagram in the mass calculation of the Higgs, resulting in the Higgs hierarchy problem. In a Supersymmetric Standard Model we will have the vacuum state with zero momentum, $P^i|0>=0$, also being supersymmetric, giving,

$$Q_\alpha|0>=Q^\dagger_\beta|0>=0 \tag{2.32}$$

This can be combined with the fermionic anti commutator of equation (2.30) to give the simple expression,

$$<0|H|0>=0 \tag{2.33}$$

It is clear from equation (2.33) that the fermionic fields giving negative contributions to the vacuum's energy cancels the bosonic field's' positive contribution. In a supersymmetric theory the fermionic and the bosonic contributions cancel exactly in all orders of perturbation theory. [25] This in turn also solves the issue of Higgs divergent mass and hierarchy problem.

2.3.3 SUSY gives a Dark Matter Candidate

The Cosmic Background Explorer (COBE) [24] and the Wilkinson Microwave Anisotropy Probe (WMAP) has provided definitive measures of the flat geometrical structure and the total matter content of the universe by measuring the microwave background fluctuation spectrum. These experiments have also measured the proportion of baryonic matter, dark matter and dark energy and is shown in figure (2.6) as pie charts. Weakly interacting cold dark matter constitutes 23% of the total matter in the universe. There is also strong evidence from observation of gravitational lensing and galactic dynamics that a bulk of the matter of galaxies is invisible. The

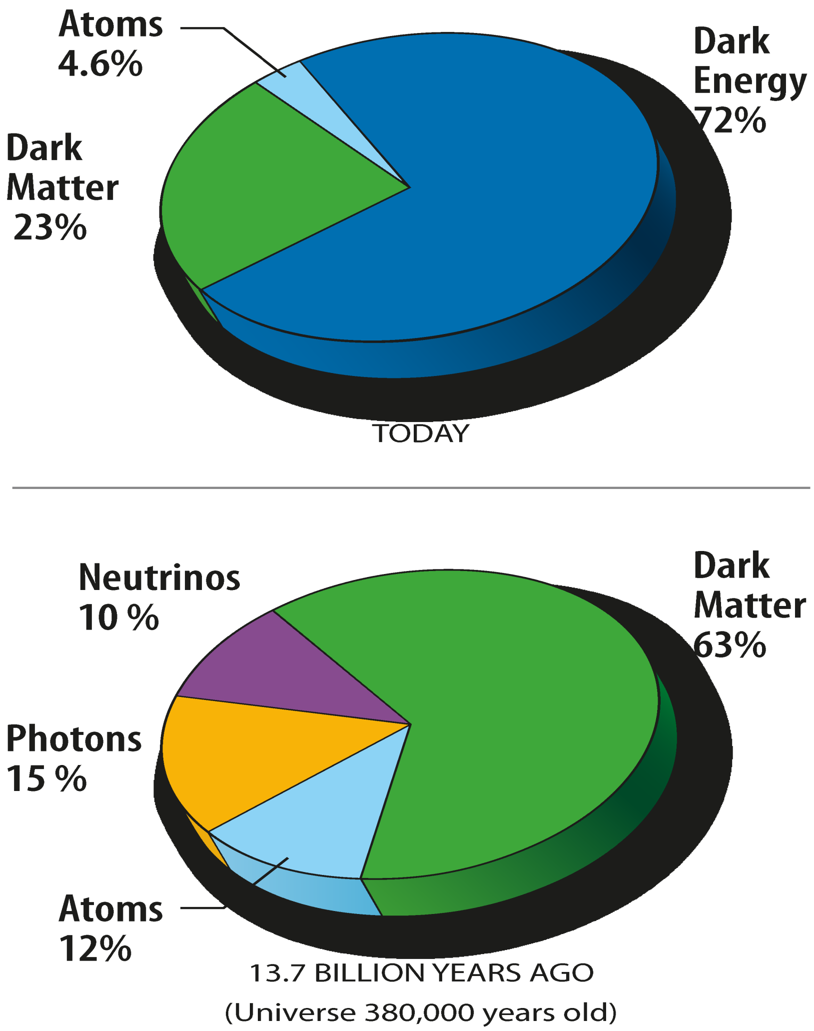

Figure 2.6. Matter Content of the universe.

Standard model as it stands can only provide neutrinos as candidate for dark matter, but WMAP observations also rule out this possibility. The question remains as to what constitutes the dark matter in the universe.

Returning again to the concept of symmetry breaking it is expected that SUSY is broken spontaneously. But knowing that all spontaneously broken symmetries produce a Goldstone boson one may ask as to what happens if SUSY is broken spontaneously. Given that the generators of SUSY are Grassman objects, i.e. objects belonging to the Grassman algebra with anti-commutation rules, instead of a bosonic state a fermionic zero state is produced. This is called the Goldstino. Presence of this Goldstino requires that only the Higgs break the Supersymmetry.[32] This in turn leads to divergent mass sum rules.

The solution is to break SUSY in a hidden sector and transmit the effects via some messenger fields. One can have mediation via gravity e.g. in MSura or via the gauges. Each of these symmetry breaking mechanisms also assume certain properties of the parameters of MSSM at a Grand Unified or Plank scale. This results in different expected mass spectra for the sfermions and their decays.

Unlike in the Standard Model, supersymmetric theories may not conserve baryon or lepton numbers. This leads to predictions of weak scale proton decays that are not observed. As a solution for this a new invariance named R-parity is introduced. It is written as,

$$R = (-1)^{3(B-L)+2S} \tag{2.34}$$

where B, L and S stand for baryon number, lepton number and spin. This gives $R = +1$ for standard model particles and $R = -1$ for all SUSY particles. This has the consequence that SUSY particles are produced in pairs and given R-parity conservation the lightest SUSY particle is unable to decay into a Standard Model particle and is hence stable.

This lightest supersymmetric particle (LSP) makes for a perfect candidate for dark matter.

2.4 New physics beyond Standard Model

It is clear that Standard Model is not complete. The Higgs is as yet undiscovered and within itself there are many unsolved problems and questions. Thus it is near certain that the Standard Model is not a final theory but a building block. The Higgs mechanism as well as SUSY are just one of the ways of solving the problems. There are many alternatives to the Higgs mechanism and to candidate new physics. Many of these require theories that are in extra dimensions and most of them not yet accessible even to the LHC and must be verified later if nature happens to be in accordance.[15]

However, whatever the theory might be, the searches for new physics in ATLAS are capable of finding the evidence of such physics be it SUSY or something else. It is expected that the new physics is not too far from the weak scale, thus probing this new physics at ATLAS is the first step towards a better understanding of the working of the universe.

CHAPTER 3

DETECTOR CALIBRATION AND PERFORMANCE

3.1 Introduction

Before recording the LHC data the ATLAS detector was calibrated and tested for physics performance. This chapter briefly describes the calibration of each part of the ATLAS detector and its performance in reconstructing physics objects. Special emphasis is given to the calibration of the Tile Calorimeter and the Intermediate Tile calorimeter as it constituted a significant part of the the authors contribution towards ATLAS during non-data taking periods of the LHC. Brief overview of jets and missing transverse energy performance as well as photon performance is also presented. The first is important towards understanding signatures of Supersymmetry as described in subsequent chapters and the latter towards the method of estimating the standard model background for SUSY, also a significant part of the author's contribution, described in subsequent chapters.

3.2 Inner Detector and Tracking

The ATLAS inner detector as already discussed in chapter one has the acceptance of $|\eta| < 2.5$ in pseudorapidity and full coverage in ϕ. [7] The nominal transverse momentum resolution of the detector is $\sigma_{p_T}/p_T = 0.05\% \times p_T$ and a transverse impact parameter resolution of 10 μm for high momentum particles.

Calibration of each of the parts of the inner detector was performed using cosmic ray data as well as early LHC runs. A detailed description of the latest calibrations are presented in reference[1]

Before the commencement of the LHC beam in 2009 the inner detector was calibrated with all thresholds adjusted to give good uniformity and response. The noise was well within specification and the timing of components of the detector had a precision of 1-2 ns. The silicon detectors showed an intrinsic efficiency of 100% while the transition radiation tracker had efficiencies of 97.2±0.5%. The impact parameter resolution in the transverse and longitudinal directions were measured to be 22.1±0.9 μm and 112±4 μm respectively. The relative momentum resolution was measured to be $\sigma_p/p = (4.83 \pm 0.16) \times 10^{-4} GeV^{-1} p_T$. The ATLAS inner detector was fully operational and provided high quality tracking before LHC collisions started.

Track with low momenta ($p_T \sim 50 MeV$) are used towards the analysis of multiplicities of charged particles presented in chapter four.

3.3 Liquid Argon Calorimeter

The liquid argon calorimeter, described in chapter one, was calibrated using cosmic muon data as well as LHC beam data. The level 1 trigger energy computations as well as all the timing of the electronics were verified. The uniformity of the calorimeter was tested and agreement between collected data and Monte Carlo in the shower shape variables were verified. A detailed description of the Liquid Argon Calorimeter calibration and performance with data is provided in [8]

Photons reconstructed using primarily the liquid argon calorimeter is used in the study towards estimating the Z + Jets background estimate from the exclusive photon distributions, as described in chapter six.

3.4 Muon Spectrometer

It is important to measure muons with good precision in ATLAS as many physics processes have signals that require high transverse momentum muons in their final state. A description of the ATLAS muon chambers and their functionalities has been presented in chapter one. Muons are identified and reconstructed in ATLAS within a pseudorapidity range of 2.7 and a transverse momentum range of up to 1 TeV with a precision of 10% [33]. Muons are reconstructed as 'standalone' or 'combined', where the standalone muon is reconstructed in the muon chambers by asking for track segments in the bending plane. At least two track segments are required in two different muon stations for a muon track candidate to be formed in the three dimensional magnetic field. The parameters of a muon track,p_T, η, ϕ, and the distance to the point of closest approach to the beam axis is measured from muon spectrometer track fits and account for about 3 GeV of energy loss due to multiple scattering. The combined muon is reconstructed by using the standalone information as described above with the tracking information from the inner detector. A χ^2 fit of the match between the inner detector and the muon chamber tracks is performed with the two sets of track parameters weighted by their covariance matrix. The final track parameter is given as a statistical combination of the parameters obtained by the muon chambers and the inner detector.

Although muons are not explicitly used towards any analysis in this document for the multi-jet zero lepton study of Supersymmetry in chapter five the requirement of zero-leptons is made by vetoing reconstructed combined muons in the event.

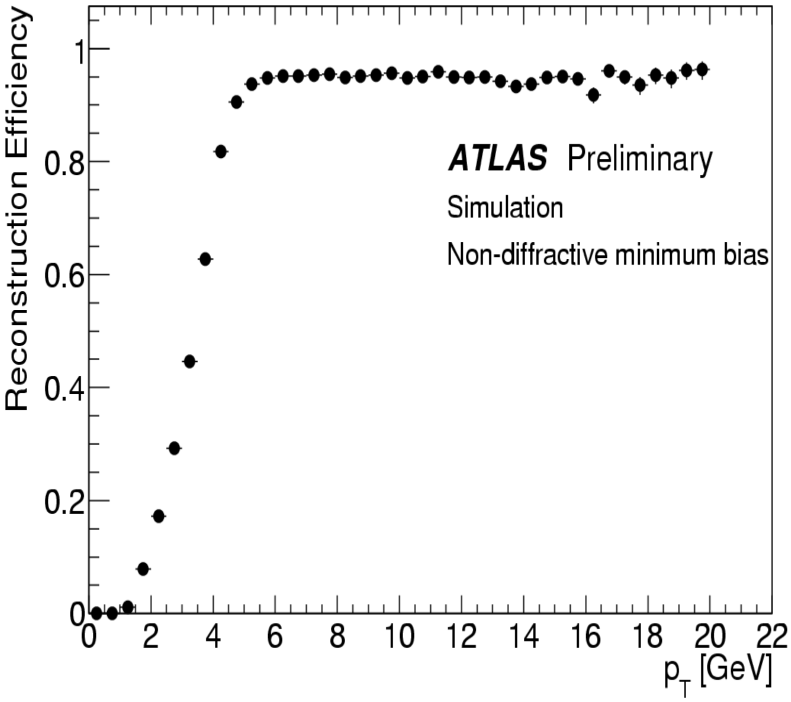

Figure 3.1. Muon reconstruction efficiency as a function of muon transverse momentum.

3.5 Tile Calorimeter and ITC Calibration

The Tile Calorimeter is part of the hadronic calorimeter of ATLAS and has been described in chapter one. The hadronic calorimeter gives the energy of jets as well as estimates of the missing energy in an event. The response of single particles has been studied extensively and reported.Ref[TDR, tile pubnote] The non-compensating nature of the calorimeter requires a energy scale correction to estimate the hadronic scale from the electromagnetic scale. These corrections are based on Monte Carlo studies that have been finely tuned to data obtained in test-beam studies before the commissioning of the detector.

A detailed study of jet energy scale and resolution has been performed using early ATLAS data. Jets [34] [35] as well as the performance of missing energy has been reported [36]. The performance of jets and missing transverse energy is directly related to the calibration of the ATLAS tile calorimeter. The Tile Calorimeter needs to be calibrated correctly to convert the calorimeter signals measured in pC to the global electromagnetic scale and the associated uncertainty. The calibrations require the detector response to be linear in ϕ and η and measure the timing between collision and signal detection and maintain this time stability. There are three primary calibration systems built into the Tile Calorimeter. The charge injection system (CIS) has the functionality of calibrating the front end electronic gains. The laser system monitors the gains and responses of the photomultiplier tubes. The Cs system consists of a radioactive source of γ that travels along the detector Z-coordinate through every single scintillating tile in the calorimeter. This system is used to test and correct the uniformity of response of the different modules by adjusting the high voltages of the photo multiplier tubes as well as establish the EM scale for the response of TileCal modules.

3.5.1 Commissioning the Intermediate Tile Calorimeter

A schematic view of the tile calorimeter cells and rows are shown in figure 3.2. The Intermediate Tile calorimeter (ITC) is the part of the extended barrel lying in the region of $0.8 < |\eta| < 1.6$ on the face of the extended barrel within the 680 mm wide region between the barrel and the extended barrel.[15] [37]

The region $0.8 < |\eta| < 0.9$ consists of a 311 mm thick steel-scintillator stack, similar in the design to the standard Tile Calorimeter modules. Between $0.9 < |\eta| < 1.0$, the stack is 96 mm wide. The combined $0.8 < |\eta| < 1.0$ region of the ITC is called the plug. Between, $1.0 < |\eta| < 1.6$, the ITC consists of scintillator only due to severe space constraints. The scintillators between $1.0 < |\eta| < 1.2$ are called gap scintillators, while those between $1.2 < |\eta| < 1.6$ are called crack scintillators. The

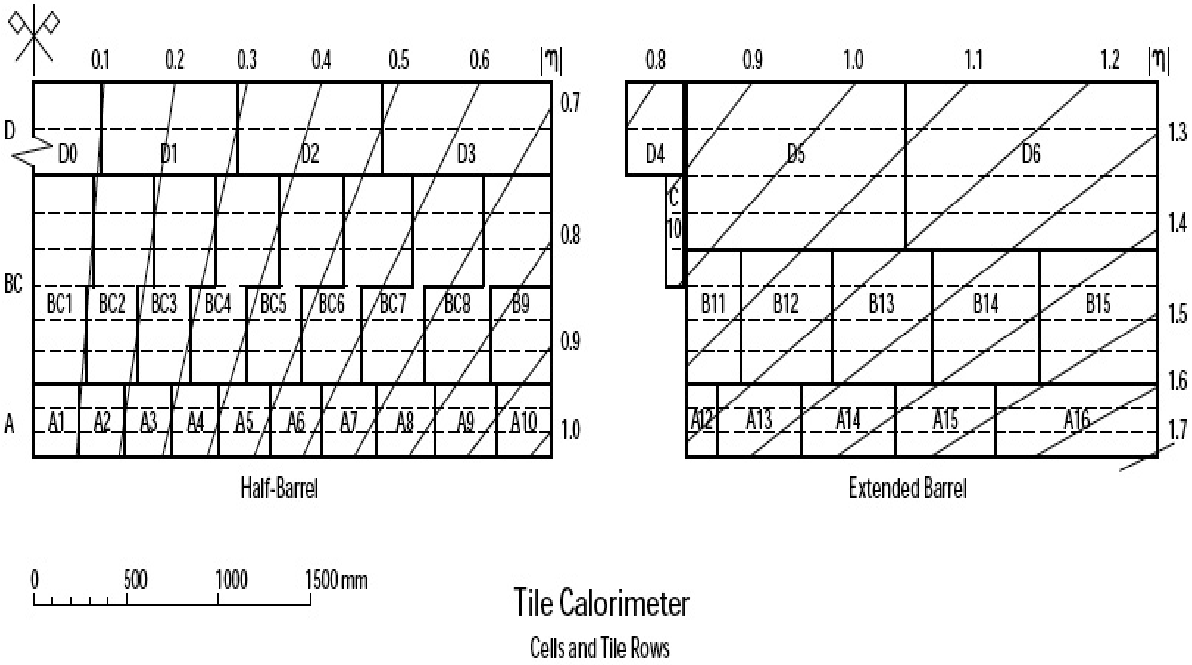

Figure 3.2. Schematic of Tile Calorimeter Cells and Rows.

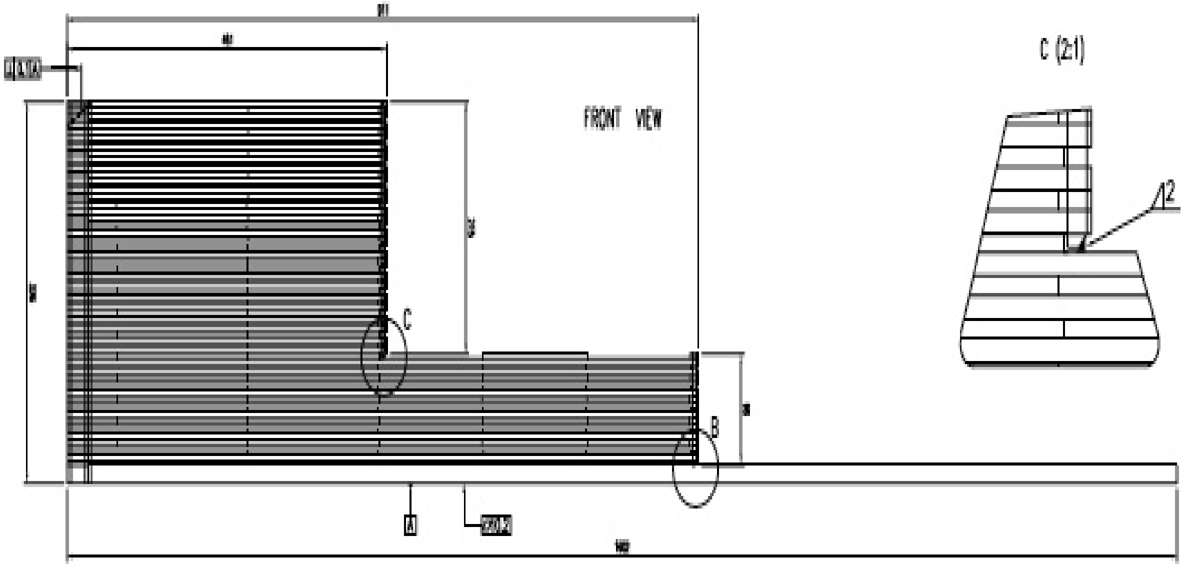

Figure 3.3. Transverse View of an ITC Module.

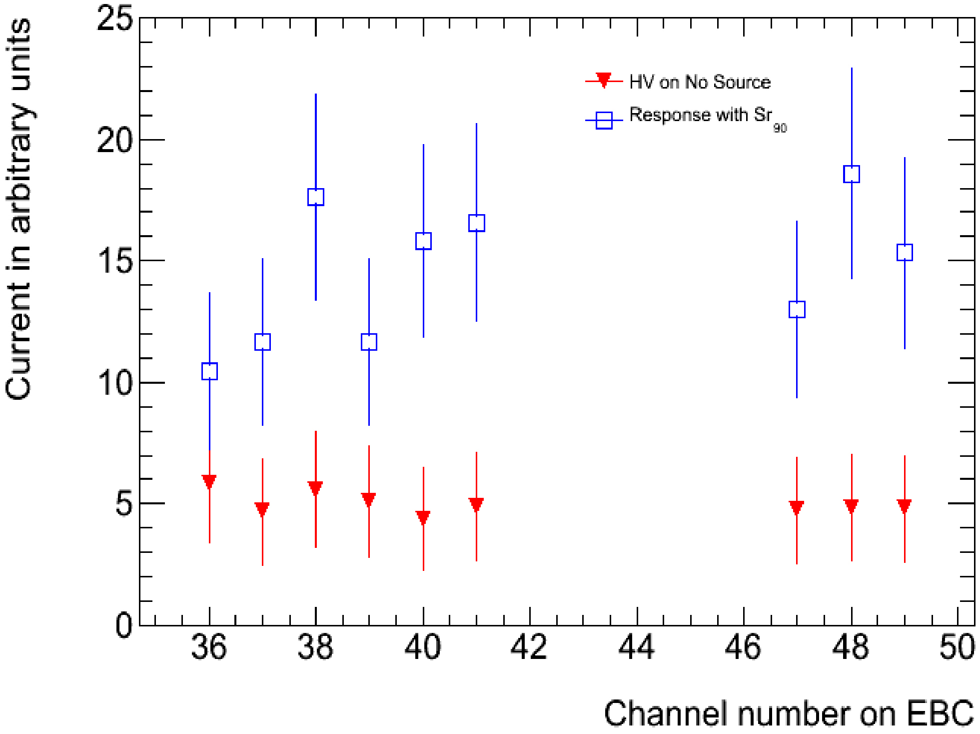

Figure 3.4. Response of select ITC modules to Sr^{90} source.

geometry of the ITC was chosen to provide maximum calorimetry (and shielding) in the vicinity of the electronics boxes and services in this region of the ATLAS detector. Figure 3.3 shows the structure of a typical ITC module.

The installation and preliminary testing of the ITC was performed in the summer of 2006. A β or electron source of Strontium 90 was used to test the response of ITC cells. Higher than usual noise in each cell was investigated and hardware problems like broken fibers or problems with the electronics were fixed. A sample result of this very preliminary study of the ITC is shown in figure 3.4. The blue marks show the normalized response of the corresponding photomultiplier tube, in terms of current in the presence of the Sr90 source. The red points show the pedestal values recorded by the PMTs without the source present. A clear response to the electrons is evident from the plot. This study constituted the first test of the ITC response in the ATLAS cavern.

3.5.2 Calibrating the Intermediate Tile Calorimeter

The Cs calibration system is designed to calibrate all of the Tile Calorimeter including the ITC. [38] The Cs system uses a Cs_{γ}^{137} source with the photon energy $E_{\gamma} = 0.662$ MeV, a half life of 30.2 years with activity of 9 mCi. Due to the shape and position of the ITC the method used towards calibrating the rest of the Tile Calorimeter cells did not produce accurate calibration for the ITC. The response of the Cs system is fitted offline with the following function,

$$F(x) = A\left(\alpha \times e^{-\frac{(x-x_0)^2}{2\sigma^2}} + (1-\alpha) \times e^{-\frac{x-x_0}{\lambda}}\right) \tag{3.1}$$

Figure 3.5 shows the response of a A-B cell from the main barrel to the Cs source compared to the response of the cell C10 in the ITC. The fit using equation 3.1 of sums of Gaussian and exponential for each cell can be fitted to the long barrel cell but because of the tail on the right the fit fails for the ITC cell. The origin of the tail lies in the fact that the Cs source travels out of the cell on the edge of the extended barrel but continues to scintillate the cell as no iron-plate is placed in this face of the extended barrel as in the other face.

A new method to calibrate the ITC improved the calibration for the ‘plug’ cells as well as calibrated the cells E1 and E2 comprising of only sheets of scintillating material. [39] The new method calculates a signal response for the full range of the signal with a fixed value for threshold, that is determined for the cell when no source is present at the vicinity of the cell. Figure 3.6 shows the difference in response of the E1 cell (scintillator) before, shown in blue, and after, shown in red, the calibration was

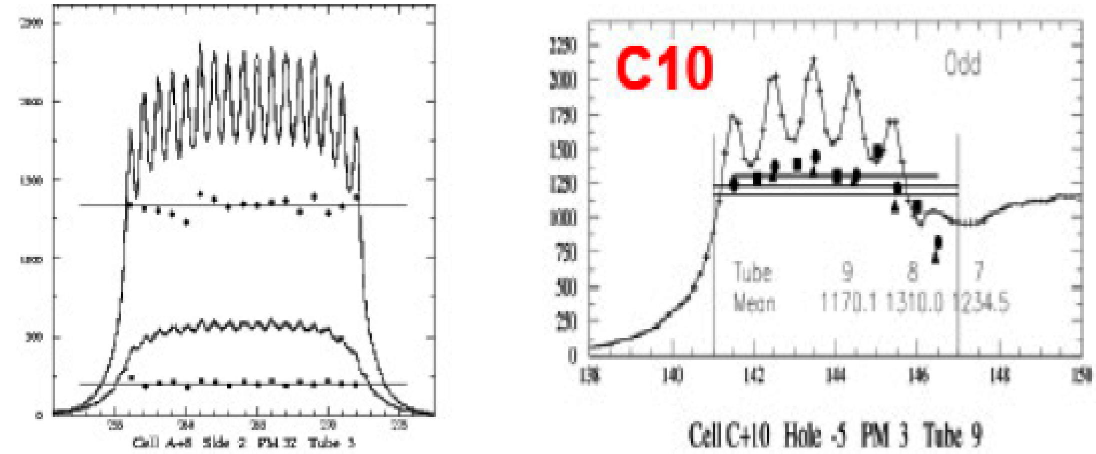

(a) Response of a regular cell to Cs

(b) Response of an ITC cell to Cs

Figure 3.5. Response of tile barrel and ITC cell to Cs^{137} source.

performed. Figure 3.7 shows the total response for all the E1 cells for the extended barrel side C before and after calibration. This method can be used to calibrate all the cells in the ϕ coordinate as no estimate of leakage is performed from adjacent cells. An independent method of calibrating the cells in η using cosmic ray muons were also developed. The response of the cosmic rays were directly correlated to the response of the Cs system for the ITC cells. Figure 3.7 shows the direct linear correlation between the cell response with cosmic against the cell response for the Cs system. Using the above correlation, all ITC cells were calibrated to yield uniform response in ϕ as well as η. The new calibration constants are used for the reprocessing of all ATLAS data in September 2010.

The calibration of the ITC results in a more uniform response for jets as well as missing transverse energy, the two most crucial components of a di-jet, multi-jet with associated missing energy search for SUSY in ATLAS. This search has been detailed in chapter five.

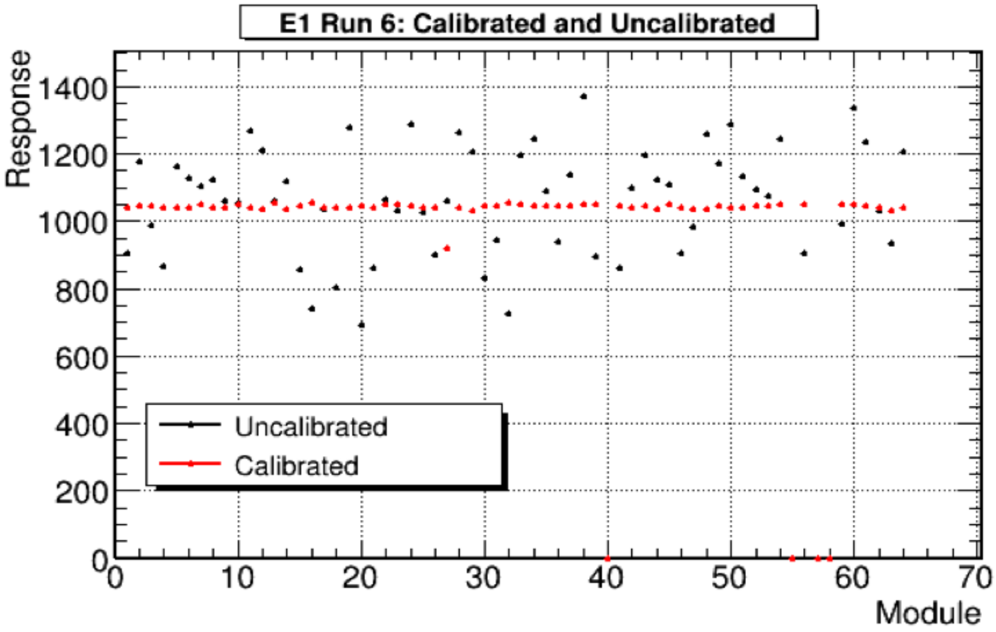

Figure 3.6. Response for cell E1 before and after calibration per module.

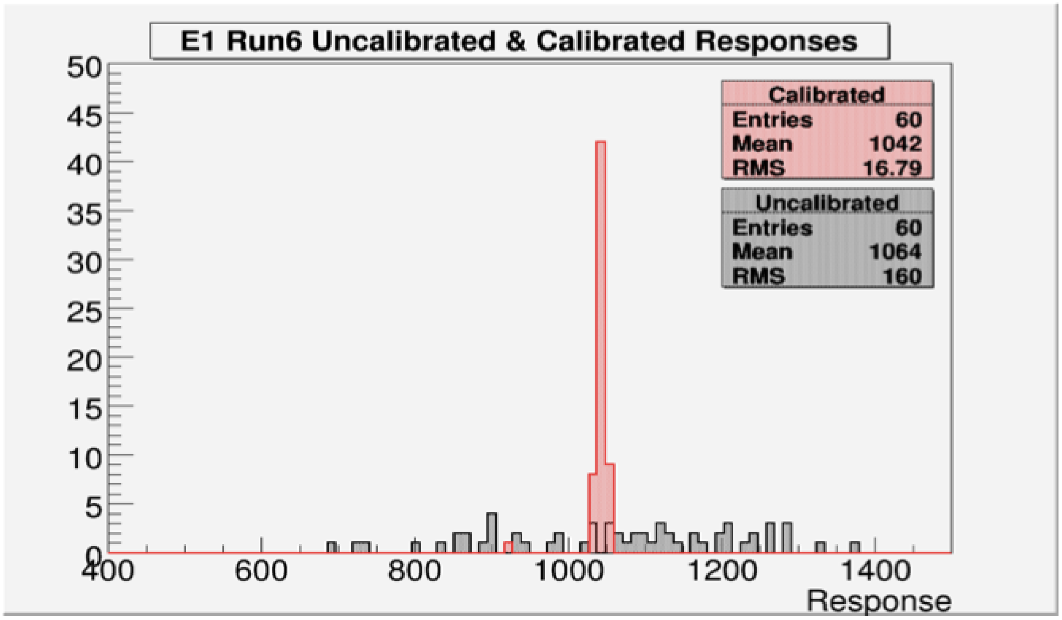

Figure 3.7. Response of cell E1 for all calibrated and uncalibrated modules.

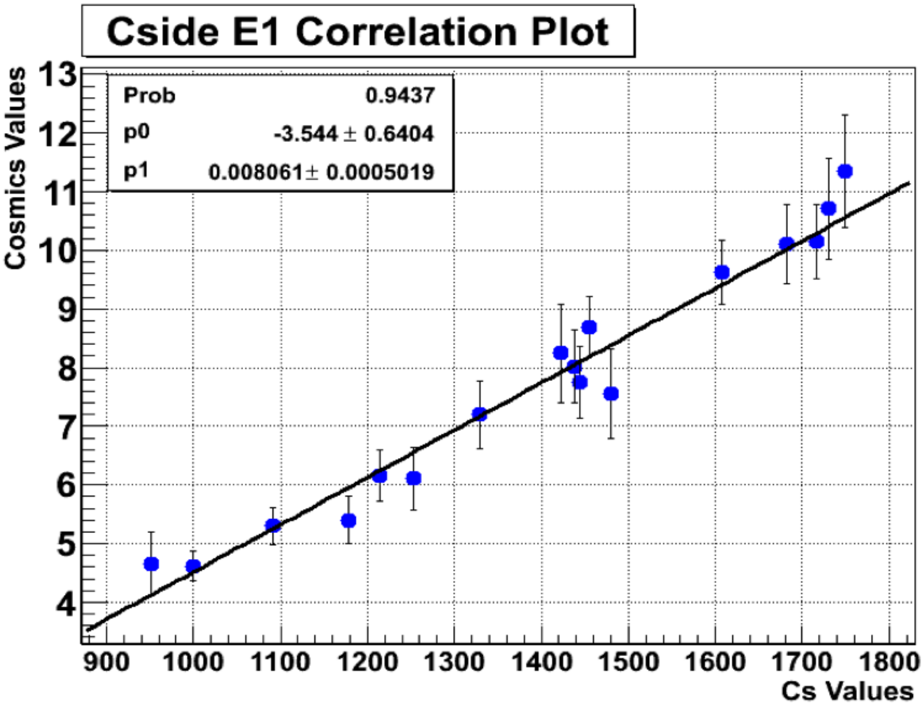

Figure 3.8. Correlation of response of the Cs system and cosmic muons.

CHAPTER 4

SOFT QCD MEASUREMENTS

4.1 Introduction

The first Standard Model physics measurement at ATLAS involves low energy quantum chromo dynamics effects. These low energy or soft interactions result when the constituents of the proton interact diffractively while the protons themselves retain most of the initial momenta. [40] [41] Such events are termed as ‘minimum bias’. One of the first measurements of minimum bias physics is the charged particle multiplicity distribution. [42] In this chapter the analysis to obtain charged particle distributions in ATLAS will be described, along with investigations about the properties of these distribution. First a brief overview of the background theoretical and experimental results are presented.

4.2 Review of Soft QCD Measurements

Although QCD is successful in explaining phenomenon resulting from high energy interactions, the coupling constant α_s for QCD becomes large, approaching 1 as the interaction energy becomes small (~ 0.5 GeV). [41] This make perturbative QCD non-predictive for lower energies as higher order terms in the interactions cannot be neglected. The high momentum transfer involved in the hard scattering process producing heavy particles and their decay products are well modeled in QCD. In contrast the soft partonic interactions of hadronic physics is not well understood with various theories describing different parts without an overall underlying structure. Moreover, minimum bias interactions constitute a dominant process for hadronic interactions and understanding it will be pivotal towards understanding underlying processes and the total cross of the *pp* collisions.

4.2.1 Soft QCD and Diffractive Collisions

The total cross section of a *pp* collision can be written in general as

$$\mathcal{L}\sigma_{total} = N_{elastic} + N_{inelastic} \tag{4.1}$$

along with the Optical Theorem given by,

$$\mathcal{L}\sigma_{total} = \frac{16\pi}{1+p^2}\frac{dN_{elastic}}{dt}|_{t=0} \tag{4.2}$$

where the second, inelastic term in equation (4.1) can be broken down into the following parts consisting of non-diffractive (nd), single diffractive (sd) and double diffractive (dd) components.

$$\sigma_{inelastic}(\sqrt{s}) = \sigma_{nd}(\sqrt{nd}) + \sigma_{sd}(\sqrt{s}) + \sigma_{dd}(\sqrt{s}) \tag{4.3}$$

Figure 4.1 shows the different interaction processes between two partons and the distribution of charges particles in the $\eta - \phi$ phase space. In the case of elastic scattering the protons stay intact while a color singlet given by equation (4.4) is exchanged.

$$\frac{(r\bar{r} + b\bar{b} + g\bar{g})}{\sqrt{3}} \tag{4.4}$$

For the elastic case the separation in the $\eta - \phi$ space is maximum. In the single and the double diffractive case one or both of the protons get exited to a color singlet state of higher mass which decay to give a cascade of (charged) particles. The particles

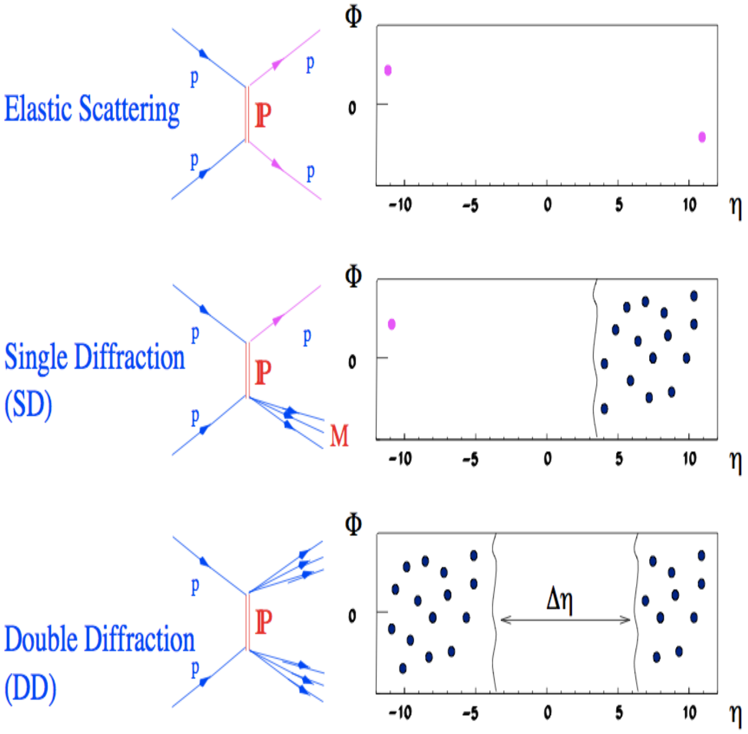

Figure 4.1. Schematics of diffractive process classes..

as shown in 4.1 exhibit a rapidity gap in the $\eta - \phi$ phase space. Minimum bias events are chosen using trigger such that, least bias is present in the selection of the events. A random trigger though ideal is inefficient for instantaneous luminosities $<$ $10^30cm^{-1}s^{-1}$ and a combination of high level triggers is employed in event selections. [ref 2: Expected Performance of the ATLAS Experiment].

Average charged multiplicity distribution, and particle pseudo-rapidity density and transverse momentum spectrum are the first and simplest measurements that can be performed using minimum bias events. Two Monte Carlo generators, PYTHIA [Ref, T. Sjostrand, S. Mrenna, and P. Skands. Pythia 6.4 Physics and Manual. JHEP, 05:026, 2006.) and PHOJET (ref R. Engel. Z. Phys. C, 66:203, 1995.) are used to predict the the pseudorapidity as well as transverse momentum spectrum of

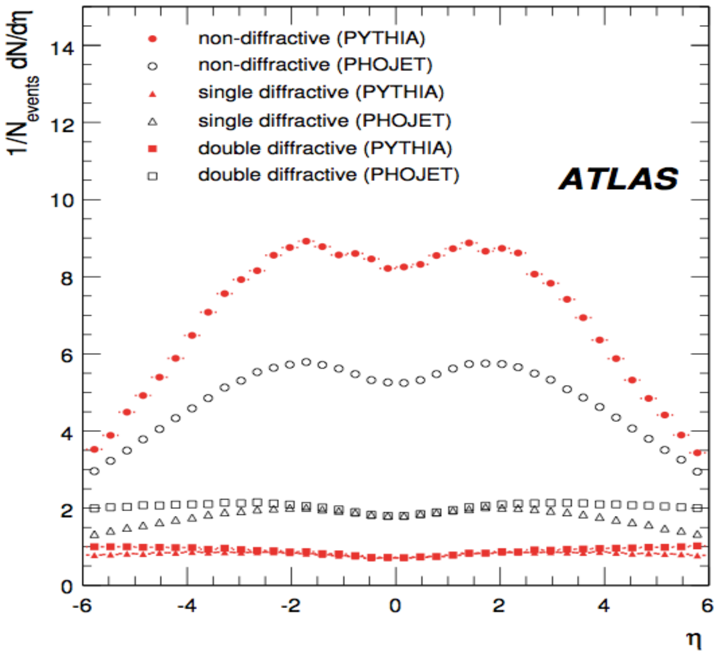

Figure 4.2. Pseudorapidity distributions for charged particles generated by PYTHIA and PHOJET.

the charged particle in ATLAS. The pseudorapidity distribution is shown in figure (4.2) and the transverse momentum distribution for both PYTHIA and PHOJET is shown in figure (4.3) respectively. The Monte Carlo generators incorporate known theoretical models as well as experimental results from previous collider experiments to generated charged particles. In ATLAS, these distributions depend on the trigger selection and fiducial cuts in pseudorapidity with corrections for the trigger and selection efficiencies made on the data.

4.2.2 Scaling Properties of Multiplicity Distributions

The probability $P(n)$ of producing n charged particles independently is given by the Poisson distribution and depends on the underlying production mechanism. Deviations from the Poisson distribution indicate presence of particle correlations.

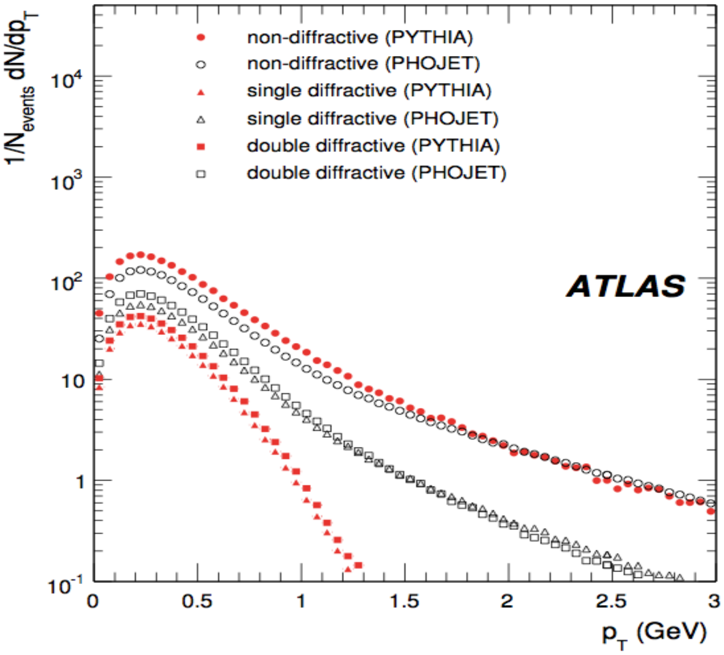

Figure 4.3. Transverse momentum distributions for charged particles generated by PYTHIA and PHOJET.

Multiplicity measurements convey information about the particle production mechanism and differential measurements provide details of these properties. The models of particle production are based on QCD and phenomenological components based on non-perturbative soft scale physics. It is observed in *pp* collisions that Poisson distribution is not followed. Koba, Nielsen, and Olesen (KNO) theoretically derived that multiplicity distributions must follow a universal scaling at high energies.

The idea for KNO scaling was based on Feynman scaling. Feynman postulated that the total number of particles with a given mass and transverse momentump_T, per longitudinal momentum p_z is given by,

$$\frac{dN}{dp_z} \approx \frac{1}{E(p_z)} \tag{4.5}$$

With the (relativistic) energy E of the particle is given by,

$$E = \sqrt{m^2 + p_T^2 + p_Z^2} \tag{4.6}$$

the probability of finding a particle i with mass m and momenta p_T and p_Z at an energy $W = \sqrt{s}/2$ is given by,

$$P_i(W) = f_i(p_T, x_F)\frac{dp_Z}{E}d^2p_T \tag{4.7}$$

where the ratio, $x_F = p_z/W$ and is called 'Feynman-x'. Feynman scaling hypothesizes that f_i becomes independent of W for high $\sqrt{s}$. Integrating equation 4.5 and using experimental inputs to factorize the left hand side, one obtains,

$$< N >= \int_{-1}^{1} f_i(x_f)\frac{dX_F}{\sqrt{x_F^2 + \frac{m_T^2}{W^2}}} \tag{4.8}$$

Approximating m_T with $< p_T >$ and integration yields, $< N >\propto \ln W \propto \ln\sqrt{s}$. Assuming equation 4.8 KNO scaling is derived by taking the moment,

$$< n(n-1)\ldots(n-q+1) >= \int f^{(q)}(x_1, p_{T,1}; \ldots; x_q, p_{T,q})\frac{dp_{z,1}}{E_1}dp_{T,1}^2 \ldots \frac{dp_{z,q}}{E_q}dp_{T,q}^2 \tag{4.9}$$

Substituting $< n >\propto \ln s$ the multiplicity distribution $P(n)$ follows the following scaling,

$$P(n) = \frac{1}{< n >}\Psi\left(\frac{n}{< n >}\right) \tag{4.10}$$

up to leading order in $(\ln s)$. KNO scaling occurs naturally in self similar, scale-invariant phenomenon. The function $\Psi\left(\frac{n}{<n>}\right)$ is same for all energies for a given reaction type.

4.3 Minimum Bias Measurements in ATLAS

The first measurements performed with the ATLAS data involved multiplicity distributions of charged particles with low transverse momentum. [43] Distributions were obtained for both $\sqrt{s} = 0.9TeV$ and $\sqrt{s} = 7TeV$ center of mass energies. The kinematic range of particles under consideration was in the range of $|\eta| < 2.5$ and $p_T > 0.5GeV$

4.3.1 Trigger and Event Selection

ATLAS is equipped with Beam Pickup Timing devices (BPTX) attached to the LHC beam pipes ±175m from the nominal interaction point and Minimum Bias Trigger Scintillators (MBTS) mounted on the extended barrels over the end-cap of the liquid argon calorimeter cryostats. Both of these systems constitute the Minimum Bias trigger at level 1 (L1). The MBTS trigger configuration required at least on hit above threshold on either side ($\pm z$) of the detector. Events were selected to have,

- passed L1 MBTS trigger
- all inner detector sub-systems at nominal conditions
- one primary vertex
- only one primary interaction per bunch crossing or pile-up veto
- at least one ‘good track’ in the event

while a ‘good track’ was defined according to the following criteria,

- $p_T > 0.5$ GeV
- at least one Pixel and one SCT hits
- the transverse parameter with respect to the primary vertex $|d_0| < 1.5$ mm
- the longitudinal impact parameter with respect to the primary vertex $|Z_0| \sin\theta < 1.5$ mm

After the above selections 326201 events with 1863622 selected tracks were used for the $\sqrt{s} = 0.9$ TeV analysis whereas 369673 events with 3769168 selected tracks were used for $\sqrt{s} = 7$ TeV analysis.

4.3.2 Background Estimation

The two primary sources of background towards this analysis was cosmic ray events that got recorded by the L1 MBTS trigger, and beam induced backgrounds. The cosmic background was estimated from previous cosmic ray studies and were determined to be a fraction of 10^{-6} of the total number of recorded events. Beam induced backgrounds are easily rejected by the primary vertex requirement and a fraction of 10^{-4} of the events were estimated to be from such sources.

4.3.3 Efficiencies and Corrections

The various selection of tracks and events have associated efficiencies. It is important to accurately determine and correct for these efficiencies to obtain the 'true' number of tracks that were produced in the collision.

4.3.3.1 Trigger Efficiency

An independent data sample was used to determine the trigger efficiency of the MBTS. A control trigger consisting of a separate level 1 Beam Pickup Timing Device trigger was used to obtain inelastic interactions using inner detector requirements of 6 Pixel clusters and 6 SCT hits at level 2 and at least one reconstructed track with $p_T > 0.2$ GeV at event filter. The efficiency $\epsilon_{trig}(n_{sel}^{BS})$ is given as function of the number of tracks (n_{sel}^{BS}) that pass all the selection criteria except the impact parameter cut along with passing a $|d_0| < 4$ mm cut. The trigger efficiency for this analysis was 100% with respect to the offline selections and were independent of p_T, η,

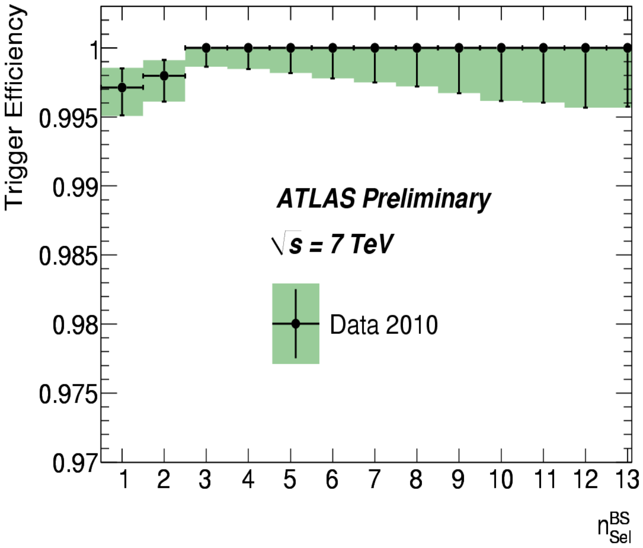

Figure 4.4. Trigger efficiency as a function of n_{sel}^{BS}.

and ϕ. Figure 4.4 shows the dependence of trigger efficiency on the track multiplicity in 7 TeV data. For multiplicities less than 3 the efficiencies are slightly lower than 100% however for higher values the efficiency is 100%.

4.3.3.2 Vertex Reconstruction Efficiency

The vertex reconstruction efficiency was calculated by using the ratio of the number of triggered events with a vertex and the total number of triggered events. The vertex reconstruction efficiency was found to be independent of p_T and only decreased for $n_{sel}^{BS} = 1$ for large values of η. Figure 4.5 shows the vertex reconstruction efficiency(ϵ_{vtx}) as a function of the n_{sel}^{BS}.

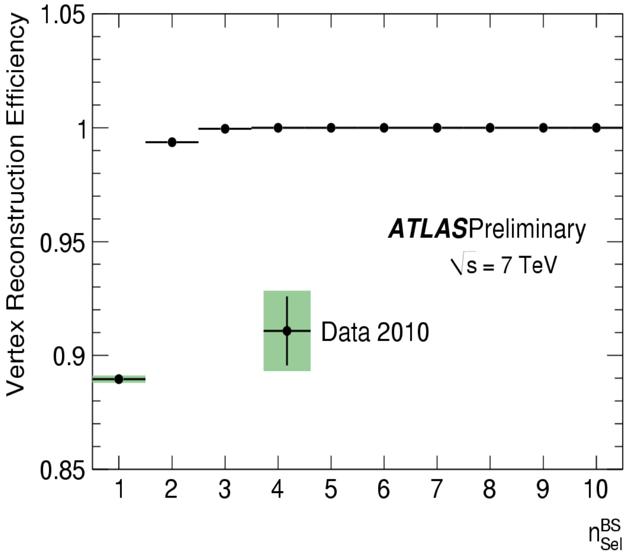

Figure 4.5. Vertex reconstruction efficiency as a function of n_{sel}^{BS}.

4.3.3.3 Track Reconstruction Efficiency

The track reconstruction efficiency for the analyses were obtained in each bin of p_T and η using Monte Carlo simulations of charged tracks. The track-reconstruction efficiency in a given bin of p_T and η is given by,

$$\epsilon(p_T, \eta) = \frac{N_{Reco}^{Matched}(p_T, \eta)}{N_{gen}(p_T, \eta)} \tag{4.11}$$

where $N_{Reco}^{Matched}$ is the number of reconstructed tracks in the bin within a cone of $\Delta R = \sqrt{(\Delta\phi)^2 + (\Delta\eta)^2} < 0.05$ of a generated particle. N_{gen} is the number of generated particles in that bin. Figures 4.6 and 4.7 show the track reconstruction efficiency as a function of η and p_T respectively for 7 TeV data.

An event by event weight is used to correct for the trigger and vertex efficiencies. A weight given by,

$$w_{ev}(n_{sel}^{BS}) = \frac{1}{\epsilon_{trig}} \times \frac{1}{\epsilon_{vtx}} \tag{4.12}$$

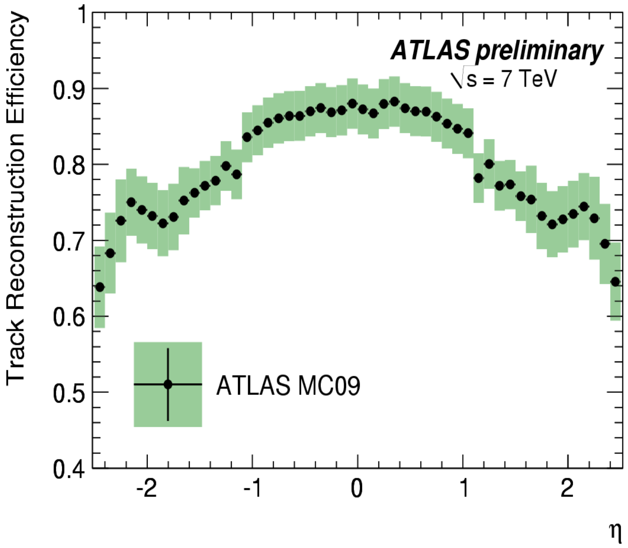

Figure 4.6. Track reconstruction efficiency as a function of η.

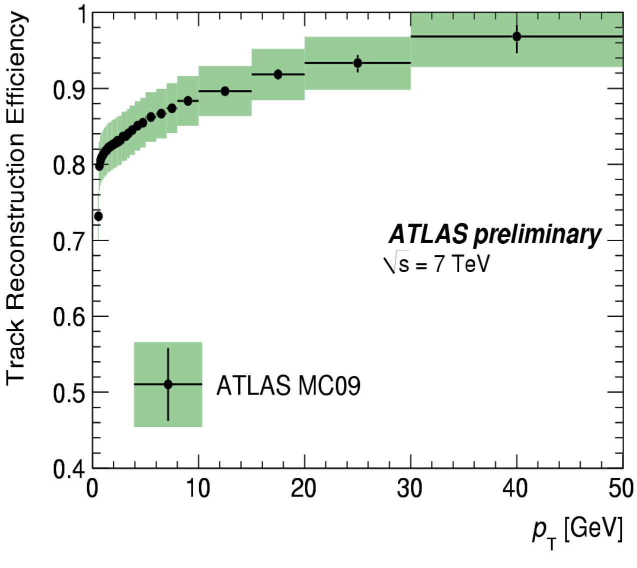

Figure 4.7. Track reconstruction efficiency as a function of p_T.

The number of tracks were also corrected as given by,

$$w_{trk}(p_T, \eta) = \frac{1}{\epsilon(p_T, \eta)} \times (1 - f_{sec}(p_T)) \times (1 - f_{okr}(p_T, \eta)) \tag{4.13}$$

where, f_{sec} are the fraction of secondary tracks arising from non-primary sources like converted photons or decay of long lived particles determined from Monte Carlo simulations. The f_{okr} is the fraction of primary particles that are outside the kinematic range, also determined from Monte Carlo. A detailed explanation of the methodology of the correction procedure is given in reference [2]

4.3.4 Systematic Uncertainties

For each of the calculations of efficiency and the corrections systematic uncertainties were estimated. A summary of the systematic uncertainties associated with event selection is presented in table 4.1. The systematic uncertainties on charged particle multiplicity is summarized in 4.1. Distributions of charged particle multiplicities incorporate these systematic uncertainties.

Table 4.1. Systematic uncertainty on the number of events N_{events}

Trigger Efficiency	0.2%
Vertex reconstruction efficiency	<0.1 %
Track reconstruction efficiency	0.8%
Monte Carlo tune differences	0.4%
Total uncertainty on N_{events}	1.2%

Table 4.2. Systematic uncertainty on $(1/N_{events}).(dN_{ch}/d\eta)$ at $\eta = 0$

Track reconstruction efficiency	3.8%
Trigger and vertex efficiency	<0.1 %
Secondary fraction	0.1 %
Total uncertainty onN_{events}	- 0.9%
Total uncertainty on $(1/N_{events}).(dN_{ch}/d\eta)$ at $\eta = 0$	2.9%

4.3.5 Charged Particle Distributions

The multiplicity of charged tracks measured in the Minimum Bias data at $\sqrt{s} =$ 7 TeV with corresponding Monte Carlo predictions is shown in figure 4.8. The same plot for $\sqrt{s} = 0.9$ TeV [44] is shown in figure 4.9 with corresponding Monte Carlo predictions.

Figure 4.10 shows the corrected multiplicity distributions for both $\sqrt{s} = 7$ TeV [45] and $\sqrt{s} = 0.9$ TeV with all associated errors. Subsequent tests of KNO scaling and fits for multiplicity distributions are performed on the distributions obtained in this figure.

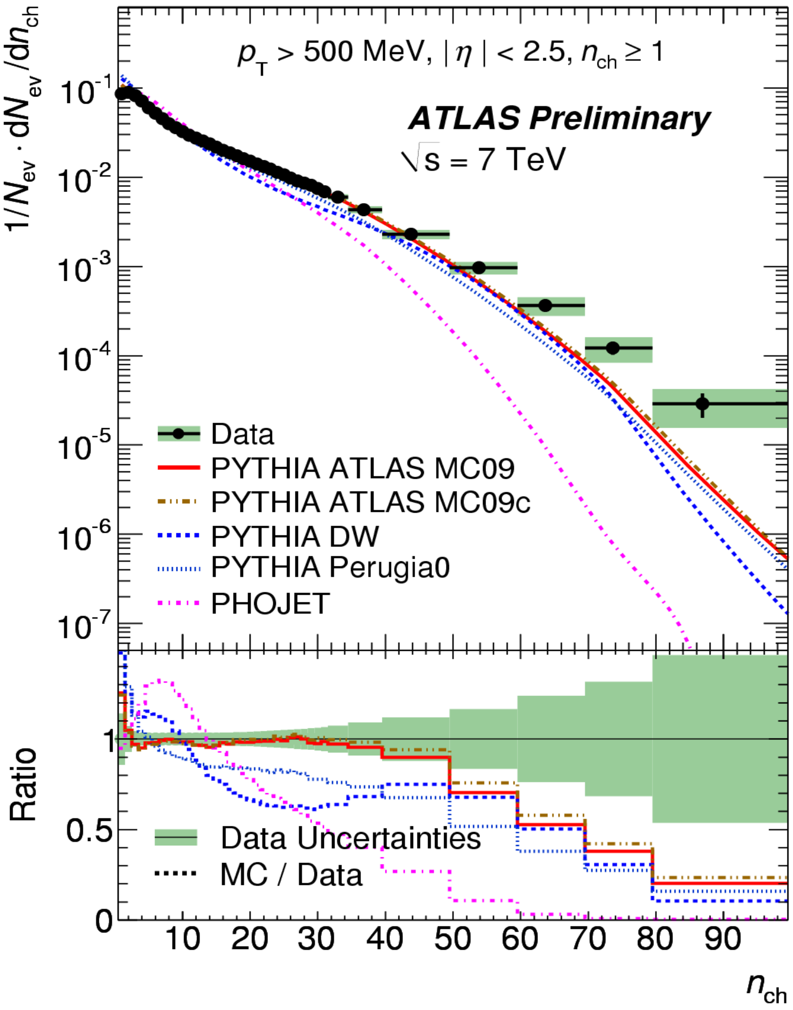

Figure 4.8. Multiplicity distribution for charged particles for $\sqrt{s} = 7$ TeV.

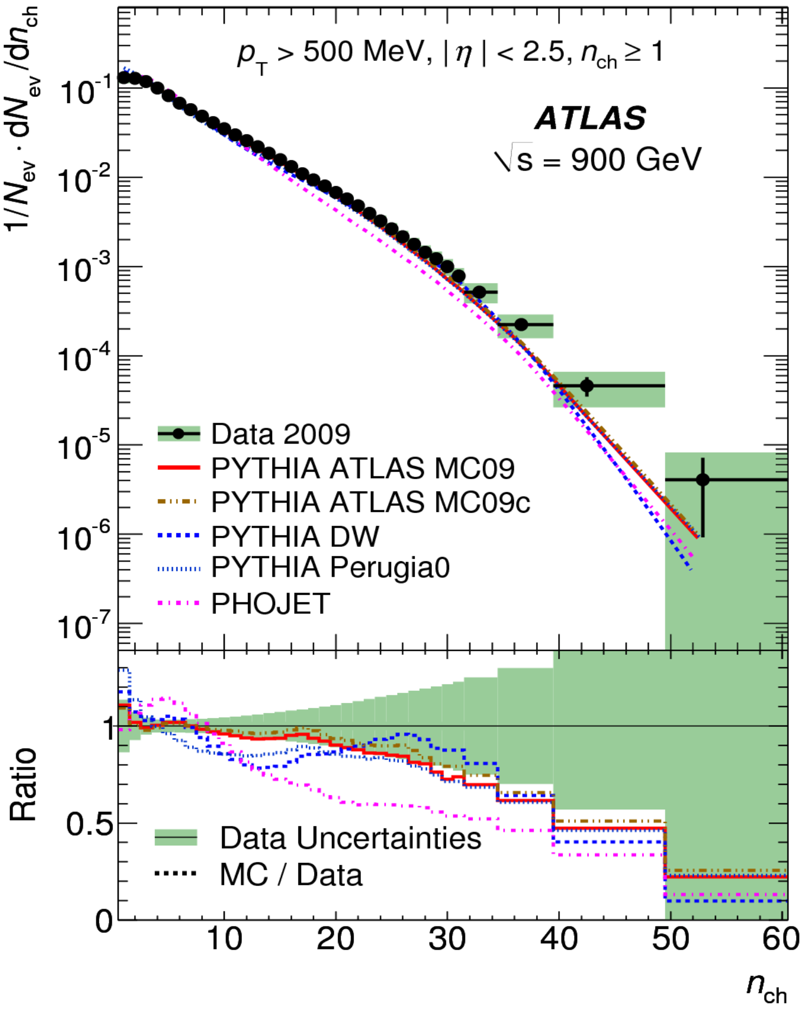

Figure 4.9. Multiplicity distribution for charged particles for $\sqrt{s} = 0.9$ TeV.

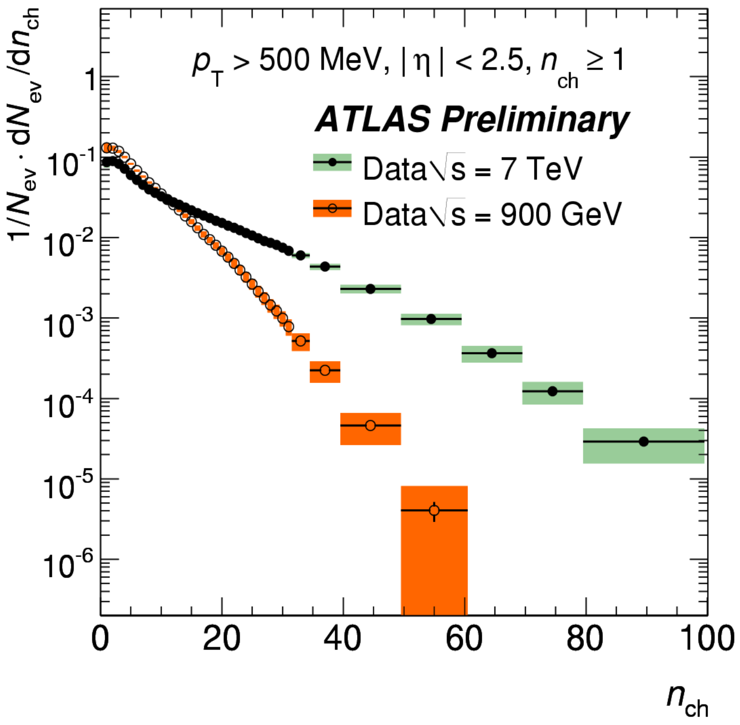

Figure 4.10. Comparison of Multiplicity distribution for charged particles for $\sqrt{s} = 7$ TeV and $\sqrt{s} = 0.9$ TeV..

4.4 Koba-Nielsen-Olsen Scaling

The multiplicity distribution up to a leading order in $\ln(s)$ is given by 4.10. Using 4.10 the central moments can be expressed as,

$$C_q = \frac{\langle n^q \rangle}{\langle n \rangle^q} = \int_0^\infty z^q \Psi(z) \mathrm{d}z = \mathrm{const}(s), \tag{4.14}$$

with the the dispersion defined as, $D = \sqrt{\langle n^2 \rangle - \langle n \rangle^2}$. The average multiplicity ratio can then be shown to be energy-independent:

$$\frac{D}{\langle n \rangle} = \sqrt{C_2 - 1} = \mathrm{const}(s). \tag{4.15}$$

The factorial moments $F_q = \langle n(n-1)\cdots(n-q+1)\rangle / \langle n \rangle^q$ of the KNO distribution however is depend on the energy, e.g.

$$F_2 = C_2 - 1/\langle n \rangle, \tag{4.16}$$

tending to independence of the energy at asymptotically high energy, $\langle n \rangle \to \infty$. Figure 4.11 , 4.12 and 4.13 show the KNO scaling for pseudorapidity intervals of $|\eta| < 0.5$, $|\eta| < 1.0$ and $|\eta| < 2.5$ respectively for both center of mass energy of $\sqrt{s} = 0.9$ TeV and $\sqrt{s} = 7$ TeV. Violation of KNO scaling is clearly apparent in the distributions with the violation being prominent after $z \sim 2.5$. For the pseudorapidity intervals of 2.5 and 1 the deviation is not as clear as in 0.5. A clear violation of KNO scaling is observed for $|\eta| < 0.5$.

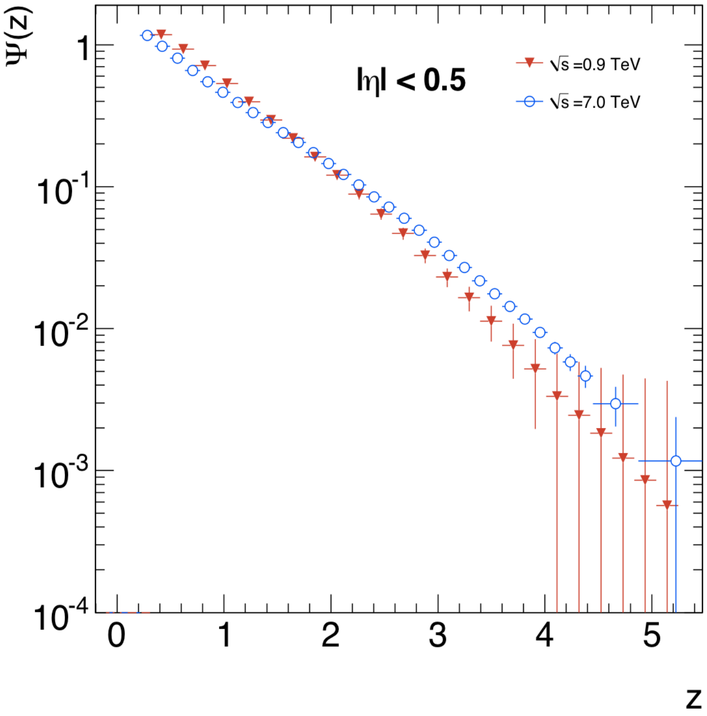

Figure 4.11. KNO distribution for $\sqrt{s} = 0.9$ TeV and $\sqrt{s} = 7$ TeV for $|\eta| < 0.5$.

4.5 Negative Binomial Fits of the Multiplicity Distribution

The Negative Binomial Distribution gives the probability of k'th success after n failures and $k-1$ successes and can be expressed as,

$$P_{p,k}^{NBD}(n) = \binom{n+k-1}{n}(1-p)^n p^k \tag{4.17}$$

To perform a fit the combinatorial coefficients are evaluated as Gamma functions, with,

$$\binom{n+k-1}{n} = \frac{(n+k-1)!}{n!(k-1)!} = \frac{\Gamma(n+k)}{\Gamma(n+1)\Gamma(k)} \tag{4.18}$$

with the mean $\bar{n}$ of the distribution related to p by, $p^{(-1)} = 1 + \bar{n}/k$. The 'clan model' describes the underlying production of particles by a cascading mechanism. In this

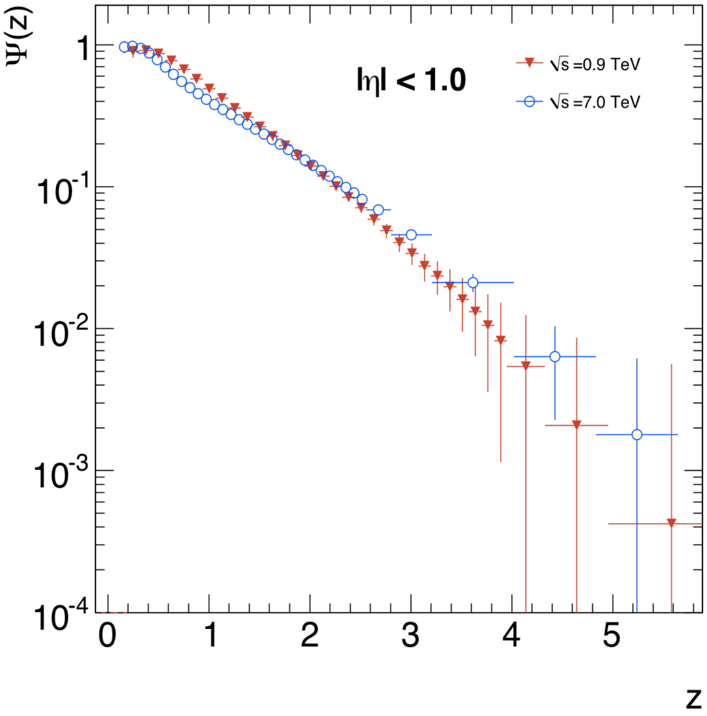

Figure 4.12. KNO distribution for $\sqrt{s} = 0.9$ TeV and $\sqrt{s} = 7$ TeV for $|\eta| < 1.0$.

scenario particles produce additional particles through fragmentation and decay. A ‘clan’ being the cluster of particles produced by an originally produced particle. The production of a clan is governed by the Poisson distribution $P(N, \bar{N})$ where $\bar{N}$ is the average number of clans. To obtain the probability of n_c particles in a given clan two assumptions are made. Firstly, it is assumed that lack of particles indicate a lack of clans or $F_c(0) = 0$ and the production of particles with probability $\tilde{p}$ is proportional to the number of particles already existing, giving,

$$\tilde{p}n_c = \frac{(n_c + 1)F_c(n_c + 1)}{F_c(n_c)} \tag{4.19}$$

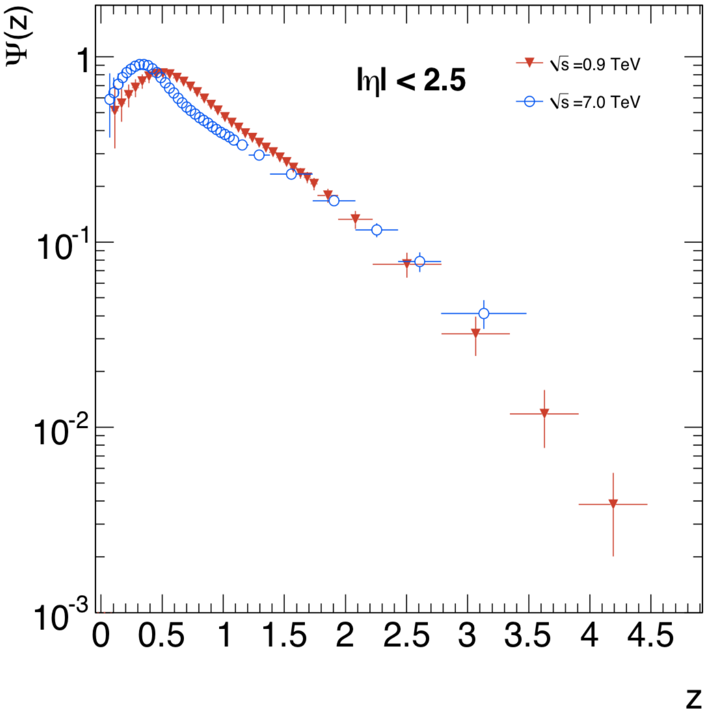

Figure 4.13. KNO distribution for $\sqrt{s} = 0.9$ TeV and $\sqrt{s} = 7$ TeV for $|\eta| < 2.5$.

and upon further iterations,

$$F_c(n_c) = F_c(1)\frac{\tilde{p}^{n_c-1}}{n_c} \tag{4.20}$$

Accounting for the distribution of the clans and the distribution of particles within the clans the multiplicity distribution can be written as,

$$P(n) = \sum_{N=1}^{n} P(N, \bar{N}) \sum^{n_i} F_c(n_1)F_c(n_2)\ldots F_c(n_N) \tag{4.21}$$

with the second sum running over all possible n_i such that $n = \sum_{i=1}^{N} n_i$. Equation 4.21 is the Negative Binomial distribution after the following transformations, $\bar{n} = \bar{N}F_c(1)/(1-\tilde{p})$ and $k = \bar{N}F_c(1)/\tilde{p}$ are made. A fit of the multiplicity distribution with a negative binomial distribution according to the ‘clan’ model of particle production yields the average number of clans as,

$$\bar{N} = k \ln \left(1 + \frac{\bar{n}}{k}\right) \tag{4.22}$$

and the average multiplicity within a clan as,

$$\bar{n}_c = \frac{k}{\bar{n}} \ln \left[\left(1 + \frac{\bar{n}}{k}\right)\right]^{-1} \tag{4.23}$$

with the $\bar{n}$ and k obtained from the fit of the data with the Negative Binomial distribution. Figures 4.14 and 4.15 show the Negative binomial fitted to ATLAS data for $\sqrt{s} = 0.9$ TeV for different intervals of η. Table 4.3 summarizes the fit parameters obtained from the fit as well as the cluster quantities obtained from equations 4.22 and 4.23. Figure 4.15 shows the dependence of the fit parameters and number of cluster and particles per cluster as a function of $\sqrt{s}$.

The number of clusters are dependent on the center of mass energy and the number of particles per cluster increases with the mean multiplicity parameter. The parameter $1/k$ varies its dependence on $\sqrt{s}$ as the η range changes. As observed the k-parameter changes with energy thereby violating KNO scaling.

4.6 Double Negative Binomial Fits of the Multiplicity Distribution

The χ^2/n.d.f. for the Negative Binomial fits from 4.3 indicate that the the Negative Binomial distribution (does not fit the data well. A combination of two NBDs give a better fit for the observed multiplicity distribution. This has been explained by considering the multiplicity distribution as a sum of soft and ‘semi-hard’ processes with the production of ‘mini-jets’. The two components come from

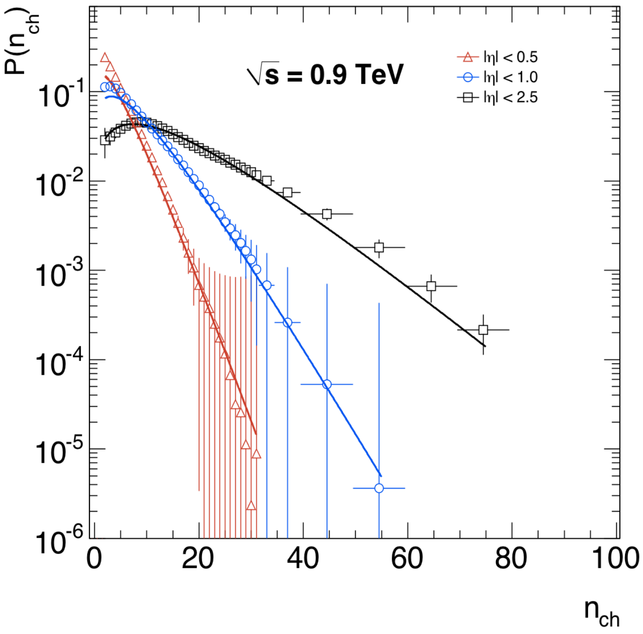

Figure 4.14. Charged particle multiplicities for $|\eta| < 2.5$, 1.0 and 0.5 for $\sqrt{s} = 0.9$ TeV with Negative Binomial fits.

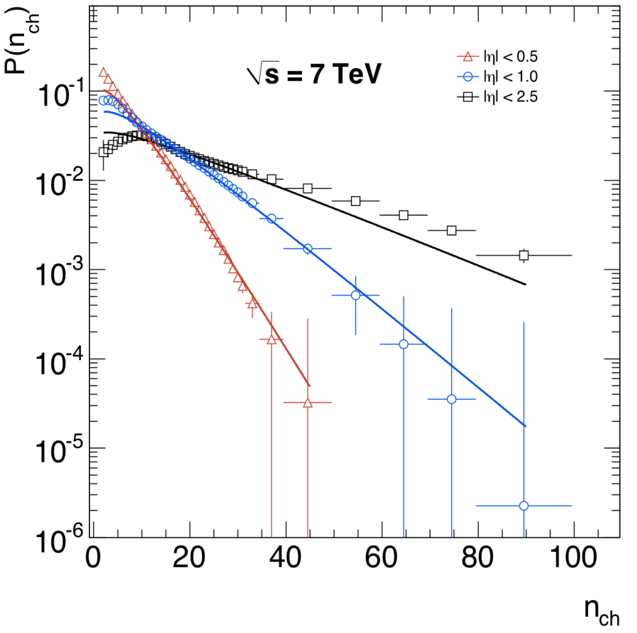

Figure 4.15. Charged particle multiplicities for $|\eta| < 2.5$, 1.0 and 0.5 for $\sqrt{s} = 7$ TeV with Negative Binomial fits.

Table 4.3. The parameters of the NBD fits to the charged-particle multiplicity distribution measured by ATLAS.

$\sqrt{s}$	η-region	k	$\bar{n}$	$N_{\rm cl}$	n_c	χ^2/n.d.f.*
900 GeV	$\lvert\eta\rvert < 2.5$	2.0 ± 0.1	16.0 ± 0.2	4.4 ± 0.2	3.6 ± 0.2	32.6/35
	$\lvert\eta\rvert < 1.0$	2.0 ± 0.1	7.4 ± 0.1	3.1 ± 0.3	2.4 ± 0.2	59.3/32
	$\lvert\eta\rvert < 0.5$	1.8 ± 0.1	3.8 ± 0.1	2.1 ± 0.1	1.9 ± 0.1	105.8/30
7 TeV	$\lvert\eta\rvert < 2.5$	1.18 ± 0.01	22.2 ± 0.3	3.5 ± 0.3	6.3 ± 0.6	111.7/35
	$\lvert\eta\rvert < 1.0$	1.34 ± 0.04	12.7 ± 0.1	3.2 ± 0.1	4.0 ± 0.1	121.6/35
	$\lvert\eta\rvert < 0.5$	1.47 ± 0.05	6.3 ± 0.1	2.5 ± 0.1	2.6 ± 0.1	156.8/31

* number of degrees of freedom.

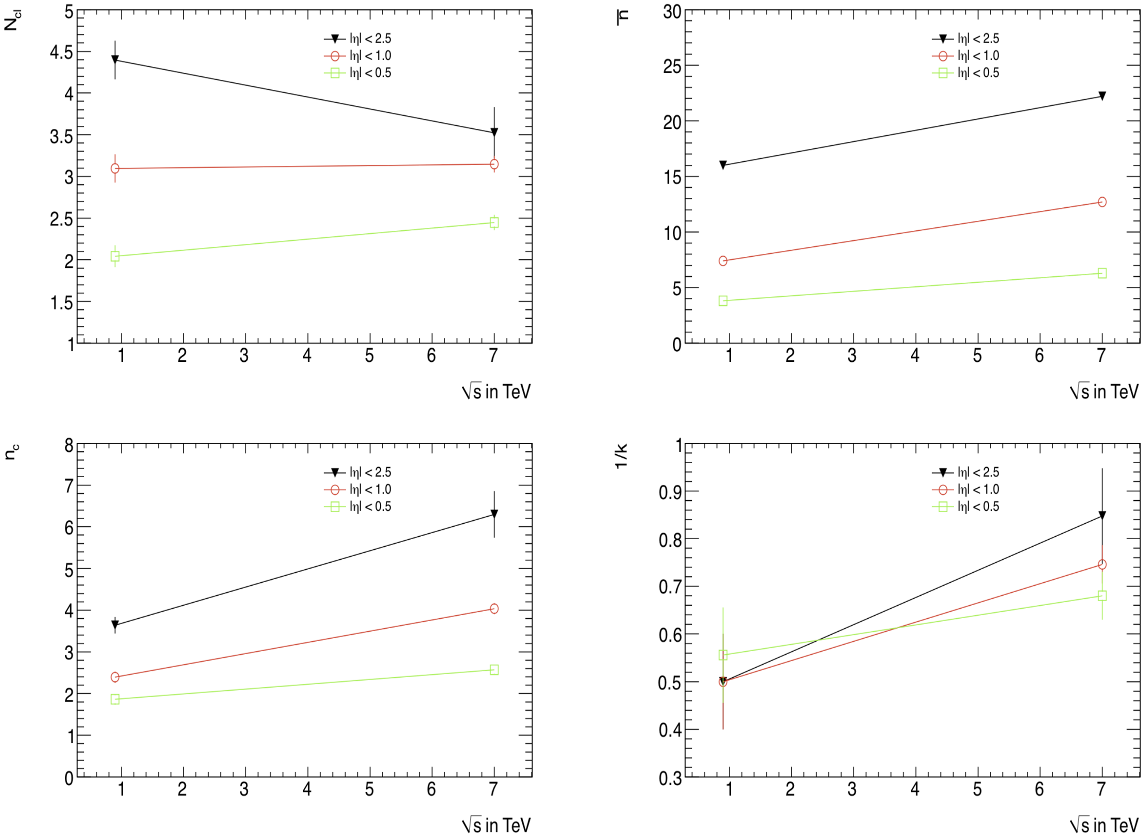

Figure 4.16. Negative binomial fit parameters as a function of $\sqrt{s}$.

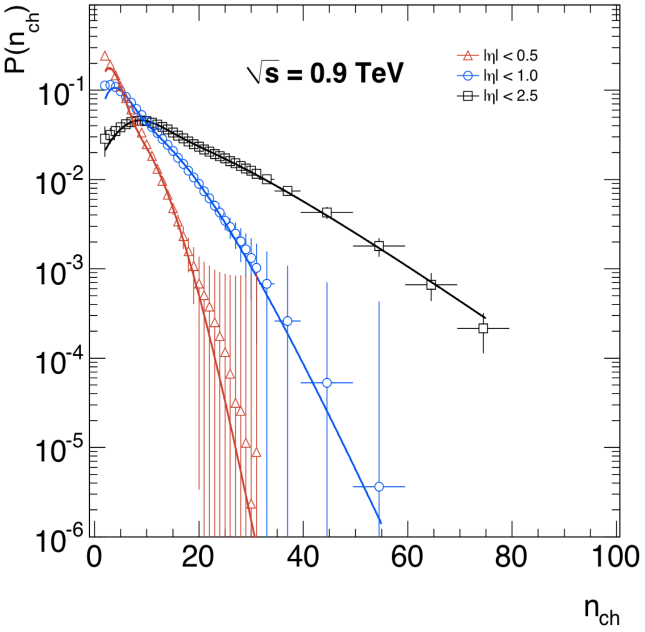

Figure 4.17. Charged particle multiplicities for $|\eta| < 2.5$, 1.0 and 0.5 for $\sqrt{s} = 0.9$ TeV with Double Negative Binomial fits.

independent events and do not belong two different particle production mechanisms within the same event. The double negative binomial distribution is given by,

$$P(n) = \alpha_{soft} \times P^{NBD}_{\bar{n}_{soft},k_{soft}}(n) + (1 - \alpha_{soft}) \times P^{NBD}_{\bar{n}_{semi-hard},k_{semi-hard}}(n) \qquad (4.24)$$

The double negative binomial fits to $\sqrt{s} = 0.9$ TeV and $\sqrt{s} = 7$ TeV multiplicity data for different η intervals is shown in figures 4.17 and 4.18. Table 4.4 lists all the soft and semi-hard parameters obtained from the double negative binomial fit. The χ^2/n.d.f. value indicates that the two component fit gives a better description of the data than the single negative binomial fit.

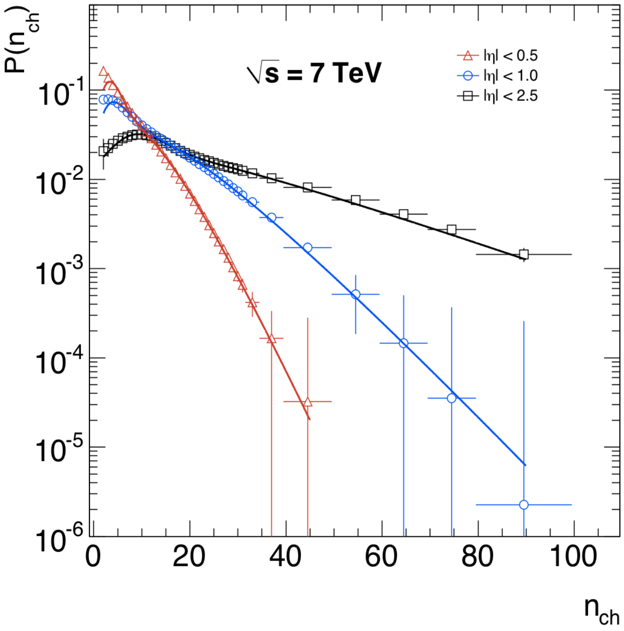

Figure 4.18. Charged particle multiplicities for $|\eta| < 2.5$, 1.0 and 0.5 for $\sqrt{s} = 7$ TeV with Double Negative Binomial fits.

Table 4.4. The parameters of the two-component NBD fits to the charged-particle multiplicity distribution measured by ATLAS.

$\sqrt{s}$	η-region	α_{soft}	k_1	k_2	$\bar{n}_1$	$\bar{n}_2$	χ^2/n.d.f.*
900 GeV	$|\eta| < 2.5$	0.1 ± 0.1	22.5 ± 34.9	2.0 ± 0.1	9.7 ± 0.7	18.4 ± 1.2	3.2/32
	$|\eta| < 1.0$	0.5 ± 0.1	10.6 ± 3.6	4.6 ± 0.5	4.4 ± 0.2	11.0 ± 0.2	9.3/29
	$|\eta| < 0.5$	0.74 ± 0.06	130 ± 106	13.9 ± 9.6	3.2 ± 0.2	8.2 ± 0.9	22.8/25
7 TeV	$|\eta| < 2.5$	0.12 ± 0.04	12.1 ± 8.3	1.4 ± 0.1	10.9 ± 0.5	30.0 ± 2.1	2.6/32
	$|\eta| < 1.0$	0.28 ± 0.07	9.3 ± 5.9	2.3 ± 0.4	4.7 ± 0.3	15.0 ± 0.9	12.1/32
	$|\eta| < 0.5$	0.42 ± 0.04	120 ± 110	3.3 ± 0.4	3.6 ± 0.2	9.3 ± 0.4	22.7/28

* number of degrees of freedom.

CHAPTER 5

SUSY SEARCHES IN DIJET AND MULTIJET CHANNELS

5.1 Introduction

Supersymmetry (SUSY) as described in chapter two is one of the primary candidates for physics beyond the standard model. SUSY elegantly solves the Higgs hierarchy problem as well as given R-parity conservation provides a natural candidate for a dark matter particle. The various SUSY breaking scenarios give rise to various event topologies. The primary objective of SUSY searches in hadron collision physics is to identify typical detector signatures that discriminate a SUSY like ‘signal’ event from a known Standard Model event. This chapter describes SUSY searches with ATLAS data for events with two or more jets and high missing transverse energy in the final state. Techniques to identify a SUSY signal in such channels are described with data as well as Monte Carlo simulations. In the next few sections detailed studies of variables constructed discriminate possible SUSY signals from Standard Model background performed in Monte Carlo is presented. In the last section of the chapter example plots of such discriminating variables on ATLAS data is presented. Although, no hint of SUSY has been observed in the data analyzed for this study the methods and variables explored in Monte Carlo are validated by the data.

5.2 SUSY Scenarios And Monte Carlo Simulations

To find new physics one must look in the right places. The Minimal Supersymmetric Standard Model is the minimal extension to the Standard model and is a well studies model. The MSSM Lagrangian can be written in terms of the sum of the

SUSY Lagrangian and the soft SUSY breaking term. Given the MSSM parameter space is of ∼124 dimensions, many different scenarios of SUSY breaking is postulated at a scale in between the electroweak and the GUT (grand unified theory) scale such that the parameters of MSSM unify to give a much smaller phase space. Depending on the scenario and mechanism of SUSY breaking the (s)particle mass spectrum at the electroweak scale can vary substantially. This gives numerous possible topologies to explore for searches. One of the scenarios that has been studied extensively is the gravity mediated SUSY breaking or SUGRA. A more simplified version of SUGRA where the parameter space is reduced to five is called mSUGRA. The mSUGRA breaking scenario has five parameters given by,

- m_0 : the common scalar mass at the GUT scale

- $m_{\frac{1}{2}}$: the common gaugino mass at the GUT scale

- A_0 : the common soft trilinear SUSY breaking parameter at the GUT scale

- $\tan\beta$: the ratio of Higgs vacuum expectation values at the electroweak scale

- the sign of $\mu = \pm 1$: the sign of the Higgsino mass term

The masses of the particles and their couplings at the electroweak scale are calculated by using the renormalization group equations. Figure 5.1 shows the running mSUGRA masses as function of energy scale.

Most ATLAS studies in SUSY is based on the mSUGRA model, since it has been studied extensively. Even though mSUGRA is the most studied, models like gauge mediated SUSY breaking or anomaly mediated SUSY breaking is also explored

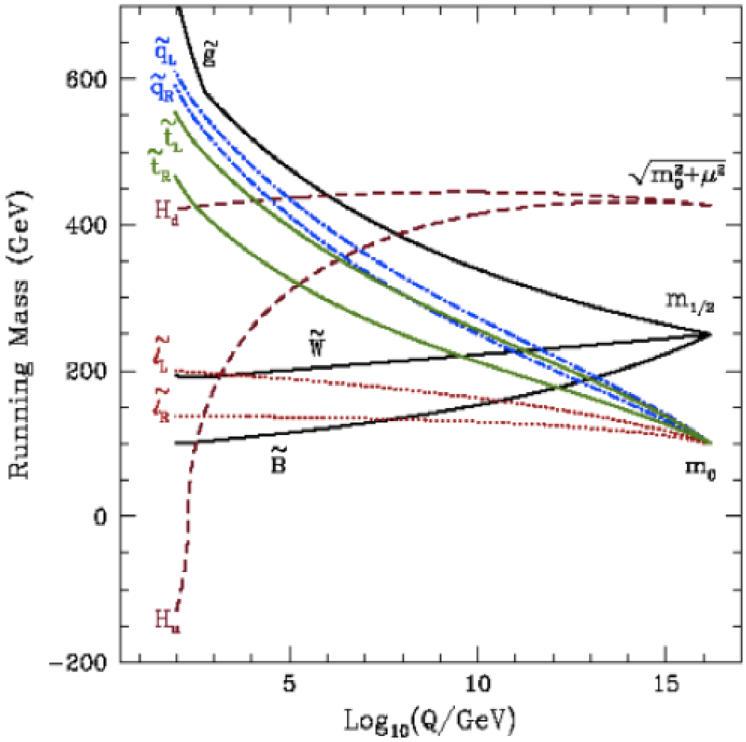

Figure 5.1. mSUGRA particle mass extrapolations from the GUT scale.

in ATLAS. To study any of the many SUSY scenarios Monte Carlo for the signal is generated. The SUSY mass spectrum in ATLAS is generated by ISAJET (cite arXiv:hep-ph/0312045v1 here). ISAJET is a multi purpose event generator for high energy physics with support for generating SUSY sparticle spectra for many different scenarios. ISAJET generated SUSY spectrum is then used in the ATLAS full generation, simulation and reconstruction chain to obtain MC data-sets for ATLAS. A HERWIG (cite) interface for ISAJET is used in ATLAS for event generation, which is coupled with JIMMY (cite) to add showering and initial and final state radiative processes. This output is used in GEANT4 for full detector simulation process. A typical SUSY analysis is performed on derived physics data after reconstruction.

The primary focus of ATLAS studies have been for the mSUGRA scenario. Several benchmark points in the mSUGRA parameter space had been chosen for detailed study at the LHC. Figure 5.2 shows the mSUGRA $m_0 - m_{1/2}$ plane with $\tan\beta = 2, 10$ and $\mu = \pm 1$. The dashed circular lines show masses of squarks while the green horizontal lines show the gluino masses. The dark gray regions represent regions that are already excluded by experiments or are theoretically not allowed. Of the benchmark points selected for investigations in ATLAS, those in the lower $m_0 - m_{1/2}$ range are easily accessible for early ATLAS runs. [46] [47] Although the mSUGRA parameter space is still quite vast many constraints have already been applied to it from other experiments. The LEP2 experiment constrained the, mass of the Standard Model like Higgs $m_h > 114.4$ GeV, the mass of the wino $m_{\tilde{w}_1} > 103.5$ GeV and the mass of the selectron $m_{\tilde{e}_{L,R}} > 99$ GeV for $m_{\tilde{l}} - m_{\tilde{Z}_1} > 10$ GeV. The branching fraction of b-particle decays to strange and photon is limited to $3.25 \pm 0.54 \times 10^{-4}$ by the BELLE, CLEO and ALEPH experiments. The muons magnetic moment g-factor can be written as, $a_\mu = (g-2)_\mu/2$ with a constraint on $\Delta a_\mu = 27.1 \pm 9.4) \times 10^{-10}$ from the Muon g-2 collaboration implying that $\Delta a_\mu^{SUSY} \propto \frac{m_\mu^2 \mu M_i \tan\beta}{M_{SUSY}^4}$. The WMAP constraint on the mass-energy density of cold dark matter $\Omega_{CDM} h^2 = 0.113 \pm 0.009$ limits the possible R-parity conserved SUSY scenarios. [48]

The point SU4 is one of the 'low-mass' points that is not in an excluded region of parameter space selected for early studies in ATLAS. The parameters for SU4 are shown in table 5.1. The mass spectrum for SU4 that is obtained from ISAJET is shown in figure 5.3. As is evident the masses of the gluinos and squarks are well below the TeV scale, with the $\tilde{t}_1$ mass being 206.04 GeV and the $\tilde{g}$ mass at 413.37 GeV. This makes the SU4 point easily accessible in early ATLAS data. [49]

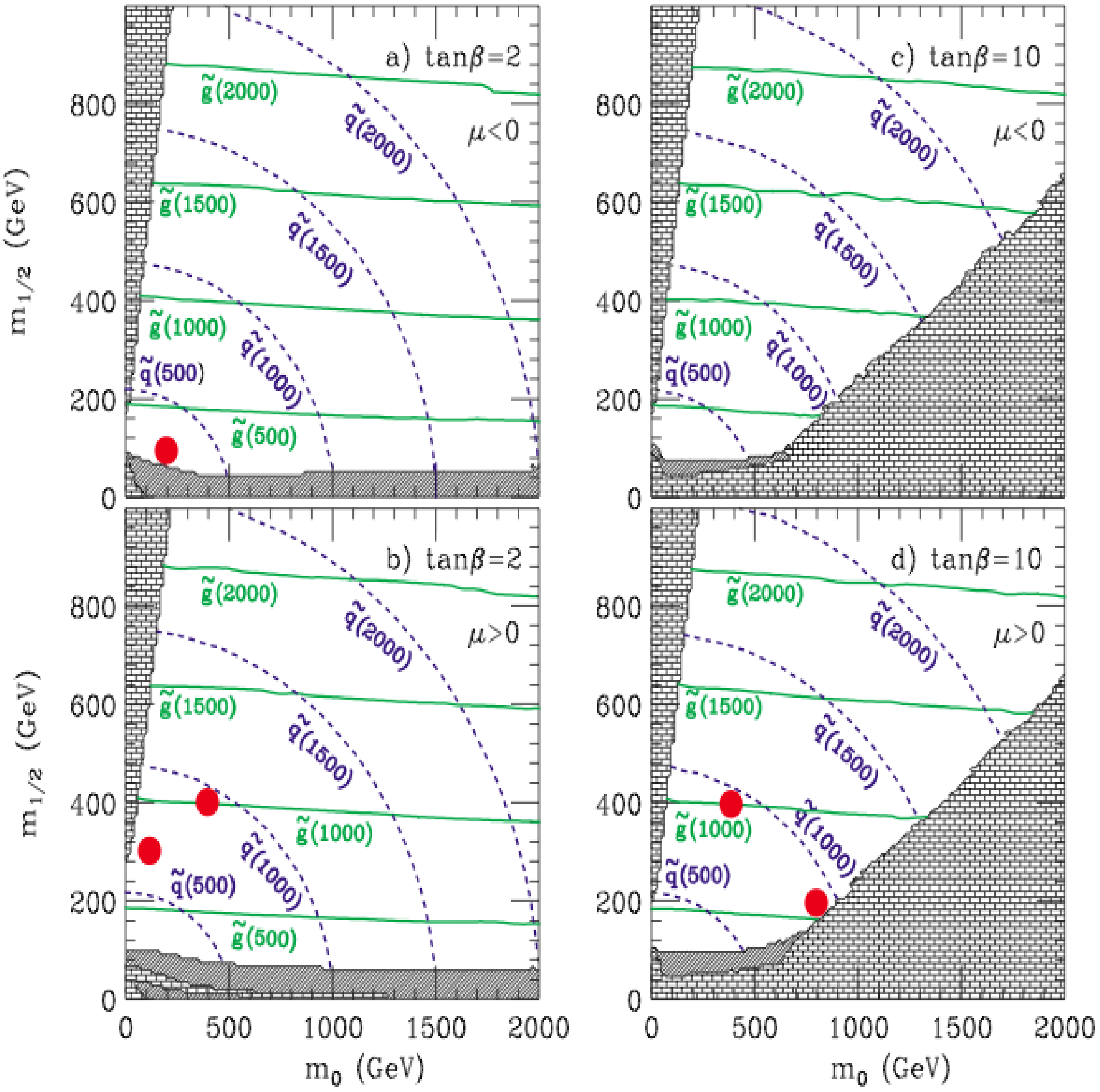

Figure 5.2. mSUGRA contour in $m_0 - m_{1/2}$ plane for $A_0 = 0$.

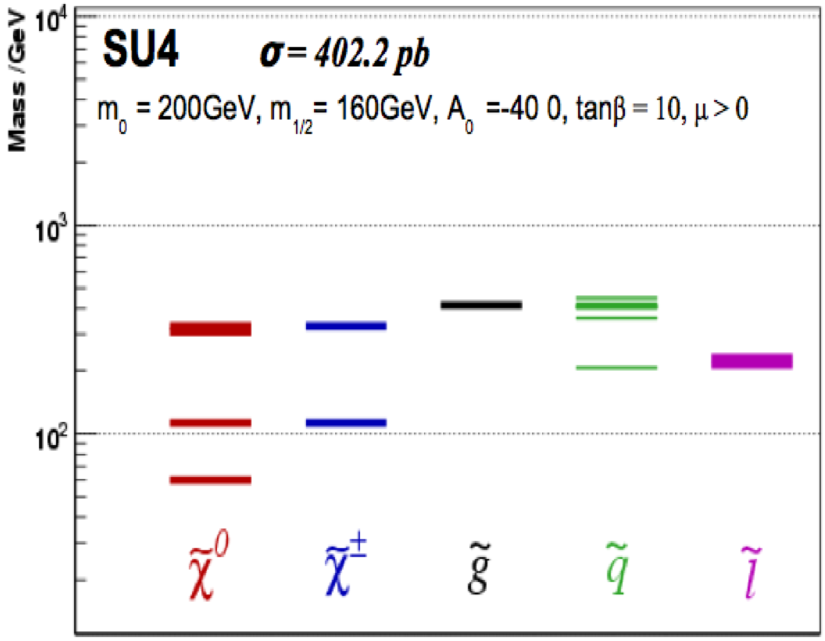

Figure 5.3. Particle Mass Spectra Obtained For mSUGRA Point SU4.

5.3 Standard Model Background Monte Carlo

Supersymmetry being a purely theoretical conjecture all studies on SUSY is performed in Monte Carlo. Monte Carlo simulations at $\sqrt{s} = 10$ TeV is used for the results presented. Although the data taken is at $\sqrt{s} = 7$ TeV the conclusions obtained are not significantly different as shown in other studies.

Table 5.1. mSUGRA Parameters Defining The Point SU4

Point	m_0 (GeV)	$m_{\frac{1}{2}}$ (GeV)	A_0 (GeV)	tan(β)	$sign(\mu)$	σ NLO (pb)	σ(10 TeV) (pb)	σ(7 TeV) (pb)
Low Mass SU4	200	160	-400	10	+	402.19	107.6	60.0

Monte Carlo samples were used to simulate the standard model background for this study. QCD jets were simulated using the ALPGEN (cite) matrix element calculator combined with event generation using PYTHIA (cite). The showering and initial and final state radiation is simulated using the HERWIG and JIMMY generators respectively. Samples for top, Z and W processes were produced using PYTHIA and their cross sections were weighted by the event generation efficiency. Table 5.2 shows a summary of the QCD (referred to as 'AlpJetsAll' for all jets produced using ALPGEN), top (anti-top), W and Z production with associated jets with all possible and diboson (W^+W^- and Z^0Z^0) processes with their corresponding cross sections. All possible decay channels of each of the above processes were considered and their cross sections were incorporated to in the cross sections shown.

Table 5.2. Monte Carlo Simulated Standard Model Background Cross Sections

Background Sample	σ [pb]
QCD	1.7×10^6
$t\bar{t}$ (top-pair)	202.85
W/Z + Jets	8.1×10^4
Di-Boson ($W^+W^-, W^\pm Z^0, Z^0Z^0$)	48.83

5.4 Di-jet And Multi-jet SUSY Searches

The different models and the largeness of the parameter space for each Supersymmetric model yields many different (s)particle production scenarios at the LHC. Such particle productions and the resulting topologies are dependent on the model of SUSY being explored. However, all such topologies can be grouped together based on the detector signature for any such event, since all SUSY particles are unstable and must decay into a subsequent lighter particle through a cascade of intermediate particle production. If R-parity conserved SUSY is considered, one SUSY particle will remain that cannot decay any further and is thus termed the 'Lightest Supersymmetric Particle' or LSP. This in turn gives two main ways to look for SUSY or in general any particle production beyond the Standard Model with heavy particles subsequently decaying into lighter ones via cascades.

It is possible to look for detector signatures typical of SUSY like events without the knowledge of the detailed particle production mechanism. These final state signatures can be enumerated as,

- E_T^{Miss} + N jets, with $N \in \mathbb{N}$: signature with multiple jets with associated missing transverse energy (due to the production of a stable neutral weakly interacting particle)
- $1l + E_T^{Miss}$ + N jets : signature with exactly one lepton (electron or muon) with multiple jets and associated missing transverse energy
- $2l(OS) + E_T^{Miss}$ + N jets : signature with exactly two leptons of opposing signs (charges) with multiple jets and missing transverse energy
- $2l(SS) + E_T^{Miss}$ + N jets : signature with exactly two leptons of same sign (charge) with multiple jets and missing transverse energy
- $3l + E_T^{Miss}$ + N jets : exactly three leptons with multiple jets and associated missing transverse energy
- $Nl + E_T^{Miss}$ + N jets : multiple leptons with multiple jets and associated missing transverse energy

with many of the signatures listed above, a special identification of jets as B-jets (originating from the bottom quark) can also be performed. The above list constitute the 'inclusive' SUSY search channels. The primary SUSY search strategy in ATLAS consist of the inclusive channels described above.

In addition to looking at the inclusive detector signatures towards a general search for SUSY there are searches that focus on the exact particle production mechanism and their decay signatures. Such 'exclusive' searches may or may not be model dependent. Although the inclusive searches may incorporate the exclusive signature, the exclusive searches have the advantage of exploring in detail some special decay mechanisms or specific kinematic constraints that can provide better discrimination between signal and Standard Model background than the inclusive searches.

This study focuses on the exclusive signature where two particles (squarks or gluinos) are produced in the collision event, which consequently decay into jets and missing transverse energy. Thus the search presented here is focused on the exclusive di-jet with associated missing transverse energy channel. Multiple jets are treated as coming from two original jets and a combinatorial mechanism is described that treats multi-jet scenarios as part of exclusive di-jet cases. As the detector signature corresponds to the inclusive case of multiple jets and leptons the study performed is equally valid for an inclusive search.

5.4.1 Event Selection And Cuts

Simple kinematic and fiducial preselection cuts were made on signal and background Monte Carlo. The variables and the corresponding preselection cuts are listed in table 5.3. The first two kinematic cuts were applied to the highest and second highest p_T jets to select high energy jets in events that are free from detector resolution effects. The variable H_T is the sum of the p_Ts of the jets and a cut of 300 GeV was made for maximal trigger efficiency of signal as well as for selecting events that provide good separation between signal and background in kinematic variables discussed later. The trigger study was based on trigger efficiencies obtained for the the jet energy (JE) based trigger. Figure 5.4 (cite) shows the turn on curve for the

Table 5.3. Preselection Cuts On Signal And Background Monte Carlo

Variable Description	Cut
jet with highest transverse momentum	$p_T^{j1} > 150$ GeV
jet with second highest transverse momentum	$p_T^{j2} > 50$ GeV
pseudorapidity of jets (1 and 2)	$\eta^{j1,j2} < 2.5$
sum of the jets' transverse momenta	$H_T = \sum_i^N p_T^{ji} > 300$ GeV
electron veto	$N^{el(tight)} = 0$ where $p_T^{el} > 10$ GeV
muon veto	$N^{\mu(isolated)} = 0$ where $p_T^{\mu} > 10$ GeV

JE triggers. From the turn on curves it is seen that the total jet energy trigger (JE100 or JE120) of thresholds 100 GeV and 120GeV respectively attain ∼99% efficiency at the jet energy sum of around 300 GeV. This makes the $H_T > 300$ GeV cut particularly important. Although, this study is done with the 300 GeV cut on H_T higher cuts up to 500 GeV were explored in other studies without a significant loss in signal efficiency. The H_T cut thus gives a leeway to select higher thresholds in trigger in case higher than recordable rates are obtained with lower trigger thresholds. Electrons were identified using the 'tight' identification criteria based on shower shapes int he electromagnetic calorimeter requiring a nominal isolation of energy in the cluster and matching inner detector tracks. Muons were identified using statistical track matching algorithms using muon chamber and inner detector tracks. Events with both electrons and muons identified as above with a transverse energy of 10 GeV or more were rejected for this study. The efficiency of SU4 signal after all the preselection cuts was calculated to be 0.47. The analysis was performed for the dijet scenario and multijet scenarios separately. Figure 5.5 shows the H_T distribution for events where exactly two jets were selected, whereas figure 5.6 shows the H_T distribution where more than two jets were selected in the event. No cuts except the lepton veto had been made. The plots show the SU4 signal in red marks while the QCD

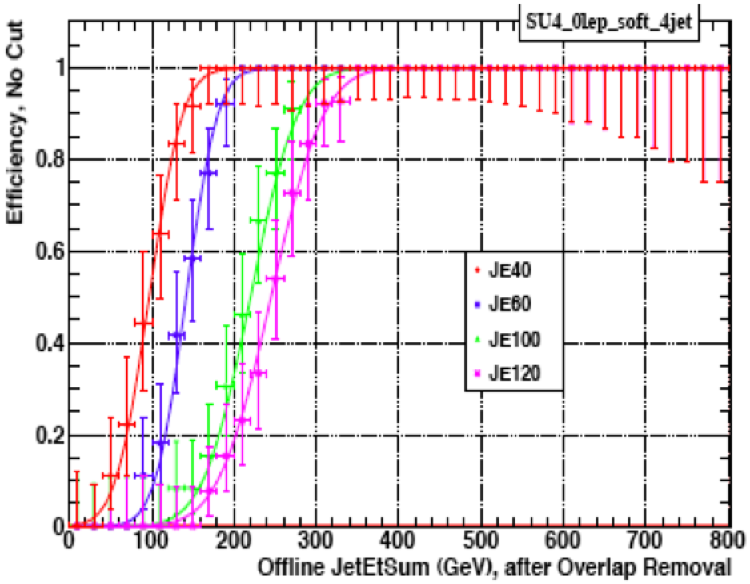

Figure 5.4. Trigger Turn On Curve For JE.

background is shown in blue. The H_T cut is not an effective discriminant between signal and background as is evident but helps in selecting events with predominantly hard scattering activity with possible heavy particle production is present.

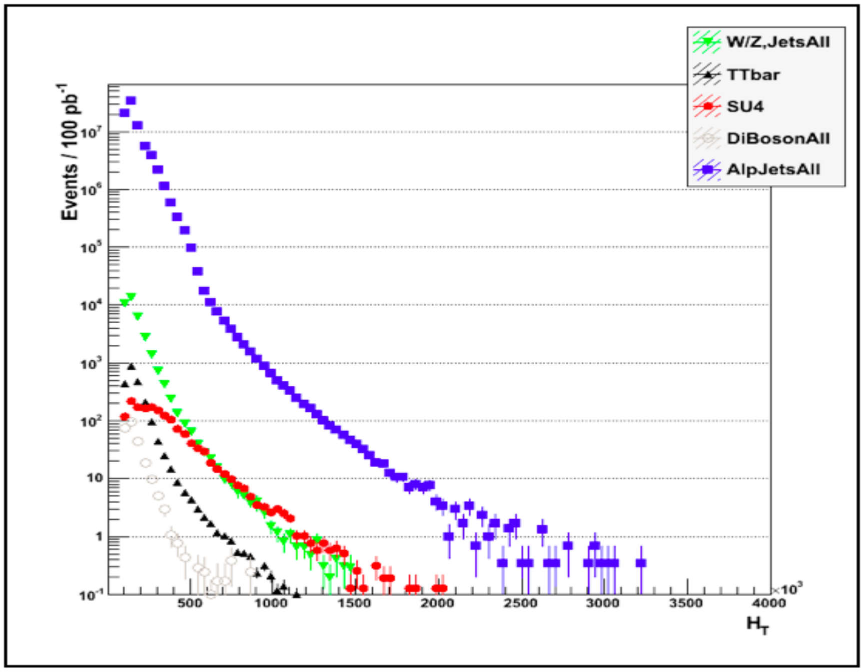

Figure 5.5. H_T Distribution For the Di-jet Case.

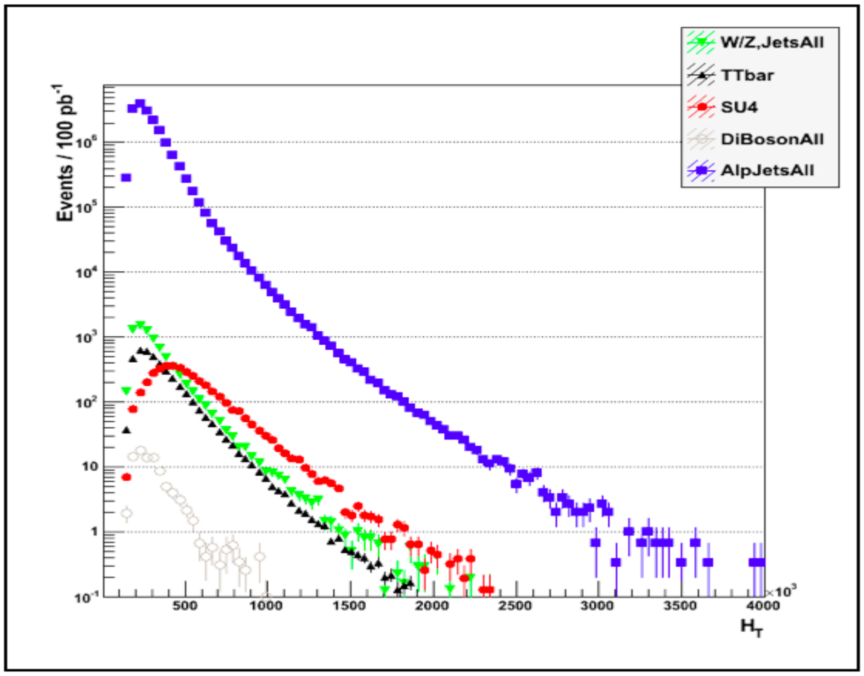

Figure 5.6. H_T Distribution For the Multi-jet Case.

5.4.2 Kinematic And Topological Variables

Topological variables particularly useful for the exclusive di-jet, multi-jet searches were explored in this study. It was assumed that during the initial period of data taking variables based on accurate colorimetric behavior such as E_T^{miss} would be poorly modeled and particular focus was given to kinematic variables that did not depend on the performance of the detector in terms of the jet resolution but were constructed out of the specific topologies of the events.

Table 5.4 shows the variables that were constructed for this analysis, followed by brief explanation for the motivation behind constructing each of the topological variables. The definition of missing transverse energy is also shown for completeness.

Table 5.4. Topological Variables Used For Di-jet Multi-jet Study

Variable	Symbol	Expression
Missing transverse energy	E_T^{Miss}	$\sqrt{(-\sum_{clus} E_x)^2 + (-\sum_{clus} E_y)^2}$
Sum of the p_T of selected jets	H_T	$\sum_i p_T^{j_i}$
Missing transverse energy using only jets	$\vec{H}_T^{miss}$	$-\sum_i \vec{p}_T^{j_i}$
Difference in p_T of the two jets	ΔH_T	$p_T^{j_1} - p_T^{j_2}$
Ratio of H_T^{miss} constructed with $p_T^{jet} > 50$ GeV and $p_T^{jet} > 30$ GeV	$R(H_T)$	$\frac{H_T^{miss}(JetP_T > 50GeV)}{H_T^{miss}(JetP_T > 30GeV)}$
Difference in ϕ of the two jets, where j_1 and j_2 are effective jets for $N^j > 2$	$\Delta\phi(j_1, j_2)$	$\phi(j_1) - \phi(j_2)$
Ratio of second jet transverse energy and two jet transverse mass	α_T	$\frac{H_T - \Delta H_T}{2M_T(j_1,j_2)} = \frac{E_T^{j2}}{M_T(j_1,j_2)}$

All the topological variables are constructed after a kinematic cut on $p_T^j > 50$ GeV and fiducial cut in pseudorapidity of $\eta^j > 2.5$ is made. In constructing the topological variables the di-jet and multi-jet cases were treated with equal footing. For events where more than two jets passed the initial kinematic preselection cuts, the jets were combined to form two 'pseudo-jets' or 'effective-jets' such that the ΔH_T between the resulting two pseudo-jets was minimized.

The variable α_T (cite) was constructed to give discrimination between the predominant background, QCD, as evident from figure 5.5, and the signal SU4. The construction of α_T ensures that for well measured QCD events $\alpha_T = 0.5$. The reasoning for this is as follows. The expression for α_T can be written as,

$$\begin{aligned}\alpha_T &= \frac{E_T^{j2}}{M_T} \\ &= \frac{H_T - \Delta H_T}{2M_T} \\ &= \frac{1 - \left(\frac{\Delta H_T}{H_T}\right)}{2\sqrt{1 - \left(\frac{H_T^{miss}}{H_T}\right)^2}}\end{aligned} \tag{5.1}$$

where, the expression for transverse mass (M_T) of the two jets(pseudo-jets) is written in terms of ΔH_T, H_T^{miss} and H_T. The expression for M_T is given as,

$$\begin{aligned}M_T^2 &\equiv (p_{T1}^{\mu} + p_{T2}^{\mu})(p_{\mu T1} + p_{\mu T2}) \\ &= 4E_{T1}E_{T2}sin^2(\frac{\delta\phi}{2}) \\ &= 2sin(\frac{\delta\phi}{2})\sqrt{E_{T1}E_{T2}}\end{aligned} \tag{5.2}$$

Using the definition of H_T and H_T^{miss} one obtains,

$$\begin{aligned}H_T^2 &= (P_{T1} + P_{T2})^2 \\ &= P_{x1}^2 + P_{y1}^2 + P_{x2}^2 + P_{y2}^2 + 2\sqrt{P_{x1}^2 + P_{y1}^2}\sqrt{P_{x2}^2 + P_{y2}^2}\end{aligned} \tag{5.3}$$

and,

$$\begin{aligned}(H_T^{miss})^2 &= (\vec{P}_{T1} + \vec{P}_{T2}).(\vec{P}_{T1} + \vec{P}_{T2}) \\ &= P_{x1}^2 + P_{x2}^2 + P_{y1}^2 + P_{y2}^2 + 2(P_{x1}P_{x2} + P_{y1}P_{y2}) \qquad (5.4)\end{aligned}$$

Subtracting the right hand side of equation 5.4 from the right hand side of equation 5.3 gives,

$$\begin{aligned}H_T^2 - (H_T^{miss})^2 &= 2\sqrt{P_{x1}^2 + P_{y1}^2}\sqrt{P_{x2}^2 + P_{y2}^2} - 2(P_{x1}P_{x2} - P_{x1}P_{x2}) \\ &= 2P_{T1}P_{T2}(1 - cos\delta\theta) \\ &= M_T^2 \qquad (5.5)\end{aligned}$$

This shows the validity of writing the right hand side of equation 5.2. The exclusive topology of the di-jet events and multi-jet events is distinctly different for the signal versus the QCD background. Referring to figure 5.7 it can be seen that for a QCD di-jet event the jets produced are back-to-back, i.e. the azimuthal angle between the two jets is π radians. Also the transverse energy of the two jets are the same for well measured jets. In case of multi-jets the ‘pseudo-jets’ are constructed such that ΔH_T between them ∼0 giving 1 in the numerator in equation 5.1. However, for the SUSY like event the recoiling invisible particles make the azimuthal angle between the two jets less than π radians. Also the two jet transverse momenta do not have to be equal. This gives values of $\alpha_T > 0.5$ for SUSY like topologies. The other variables constructed are H_T^{miss} and $\Delta\phi$. In early ATLAS data the missing transverse energy is constructed using cell information in the topological clusters found in the calorimeter. It is defined as, $E_T^{miss} \equiv \sqrt{(E_X^{miss})^2 + (E_Y^{miss})^2}$ where, $E_X^{miss} \equiv -\sum_{i=1}^{N_{cell}} E_i \sin\theta_i \cos\phi_i$ and $E_Y^{miss} \equiv -\sum_{i=1}^{N_{cell}} E_i \sin\theta_i \sin\phi_i$. This makes the E_T^{miss} variable sensitive to noise

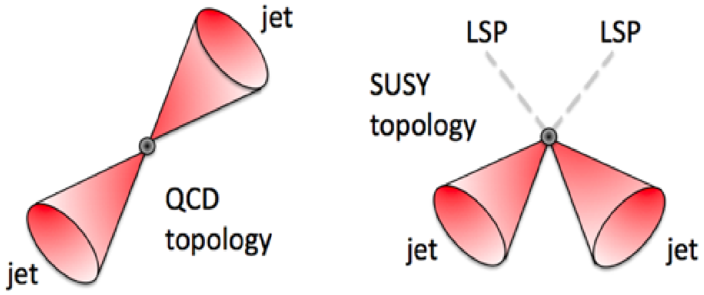

Figure 5.7. Diagrammatic representation of the difference in topologies for QCD events and SUSY events.

in the calorimeter cells, cracks in the detector geometry including un-instrumented regions as well as regions of the detector with not nominal voltages or dead connecting fibers. Moreover, fakes coming from cosmics, beam halo muons and punch throughs can also contribute to the missing E_T making it a difficult variable to clearly trust in early data. The variable H_T^{miss} avoids these problems by constructing the missing transverse energy out of only the high p_T activity in an event. The $\Delta\phi$ is also a good substitute for E_T^{miss} as explained earlier. It is clear that α_T, H_T^{miss} and $\Delta\phi$ are correlated variables that depend on the presence of invisible particles recoiling against the jets. The advantage of using α_T and $\delta\phi$ is that both of these variables are dimensionless and thus depend minimally on the resolution and energy scale. All the variables however assume that the jet response of the detector is uniform and linear. In the rest of this section study of each of these variables will be presented as an alternative to E_T^{miss} to discriminate a SUSY signal over background.

5.4.3 Distributions Of Topological Variables And E_T^{miss}

In this section distributions of the topological variables and E_T^{miss} comparing SU4 and Standard Model background is presented. For all the plots, preselection cuts described in 5.3 has been made including the H_T cut of 300 GeV.

Figures 5.8 and 5.9 show the E_T^{miss} distribution for signal, in red, and each of the Standard Model backgrounds for the dijet case and the multijet case respectively. Figures 5.10 and 5.11 show the H_T^{miss} distribution for signal, in red, and each of the Standard Model backgrounds for the dijet case and the multijet case respectively. Figures 5.12 and 5.13 show the $\Delta\phi$ distribution for signal, in red, and each of the Standard Model backgrounds for the dijet case and the multijet case respectively. Figures 5.14 and 5.15 show the α_T distribution for signal, in red, and each of the Standard Model backgrounds for the dijet case and the multijet case respectively.

It can be seen that H_T^{miss} gives a cleaner discrimination between signal and background. The delta phi distribution works well for the dijet scenario, with the distribution peaking at π whereas it does not perform well for the multijet since the construction of 'pseudo-jets' is such that ΔH_T is minimized but $\Delta\phi$ is not maximized. The α_T distribution gives remarkable discrimination between signal and QCD background with the QCD distribution, shown in blue, falls off sharply at ~ 0.5. The maximum contribution to $\alpha_T > 0.5$ arises from events with the Z boson produced with associated jets where the Z decays into two neutrinos. This constitutes a real irreducible background to SUSY and an estimation for this from ATLAS data is presented in chapter 6.

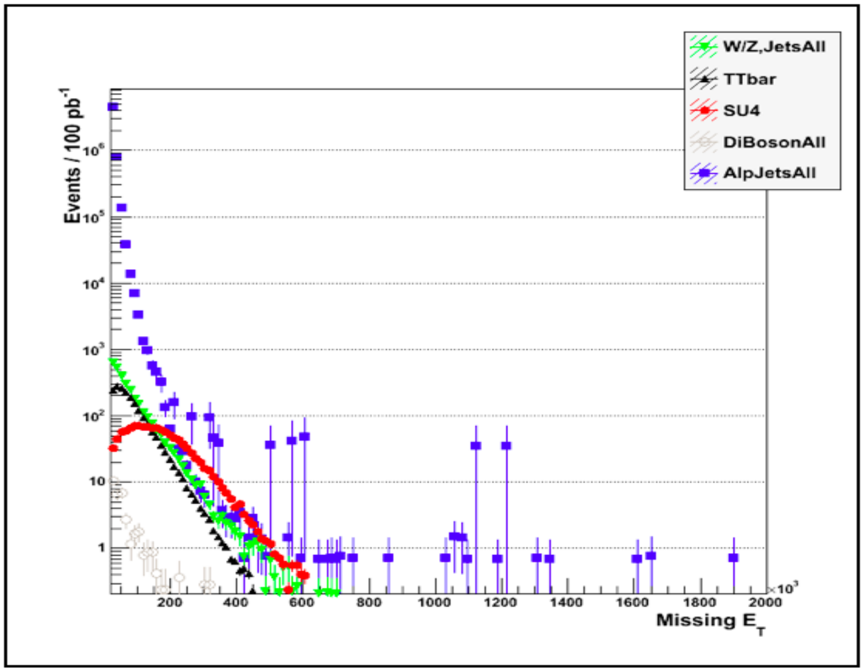

Figure 5.8. E_T^{miss} Distribution For the Di-jet Case.

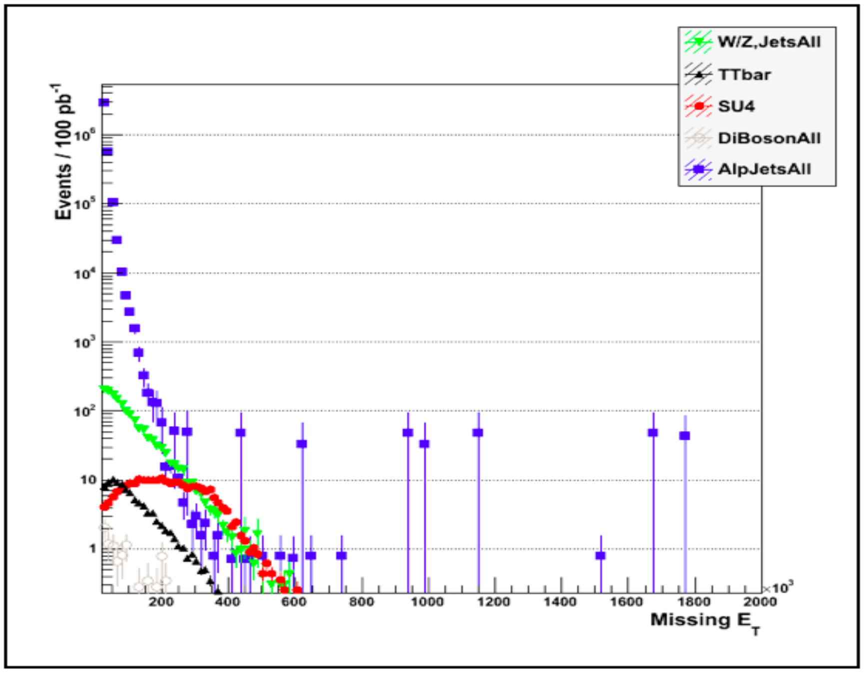

Figure 5.9. E_T^{miss} Distribution For the Multi-jet Case.

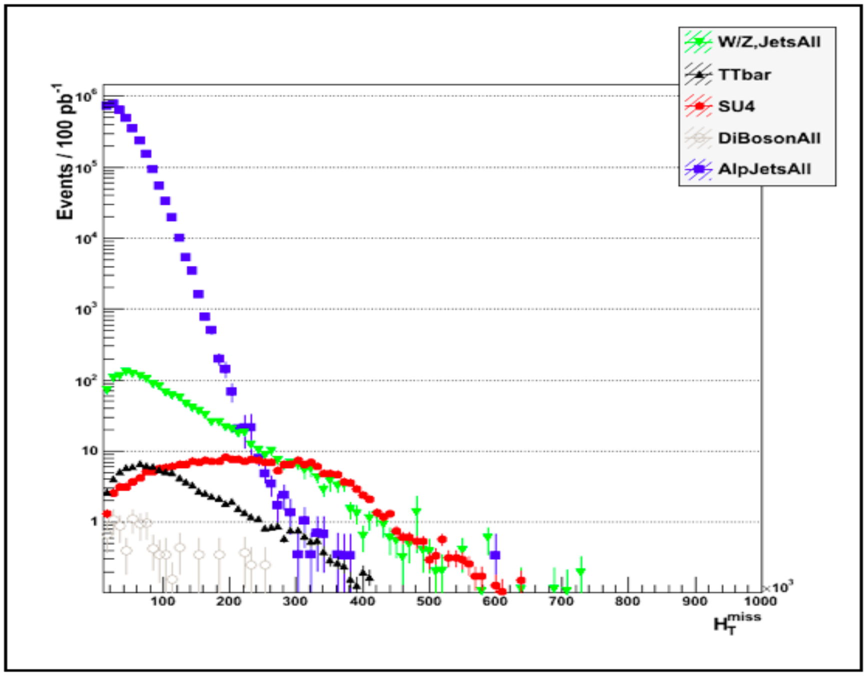

Figure 5.10. H_T^{miss} Distribution For the Di-jet Case.

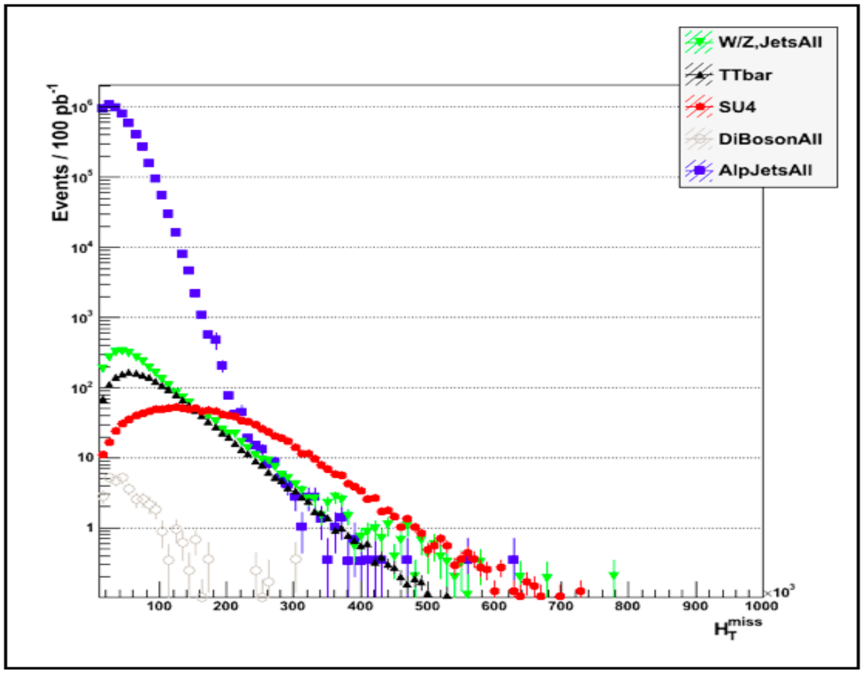

Figure 5.11. H_T^{miss} Distribution For the Multi-jet Case.

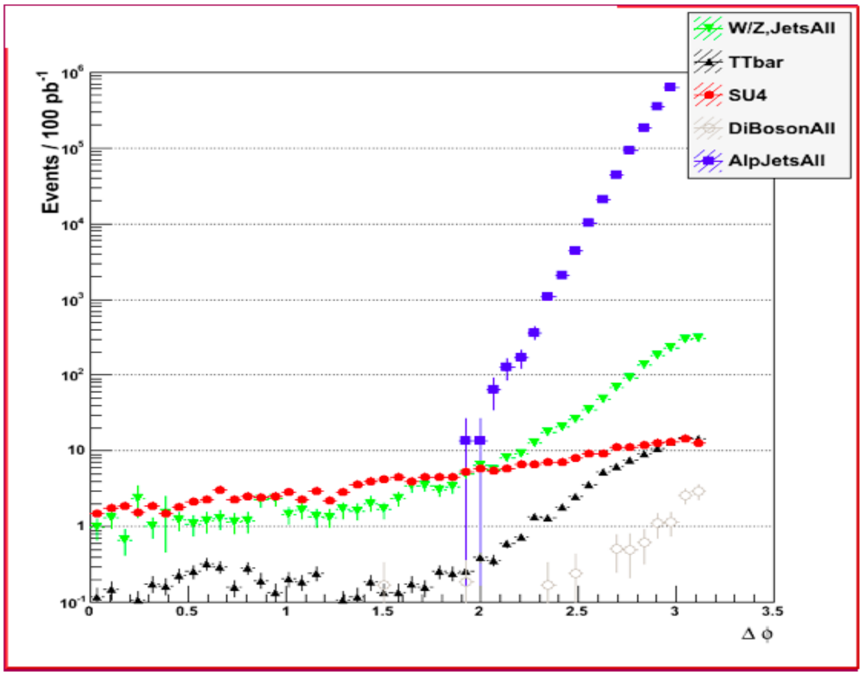

Figure 5.12. $\Delta\phi$ Distribution For the Di-jet Case.

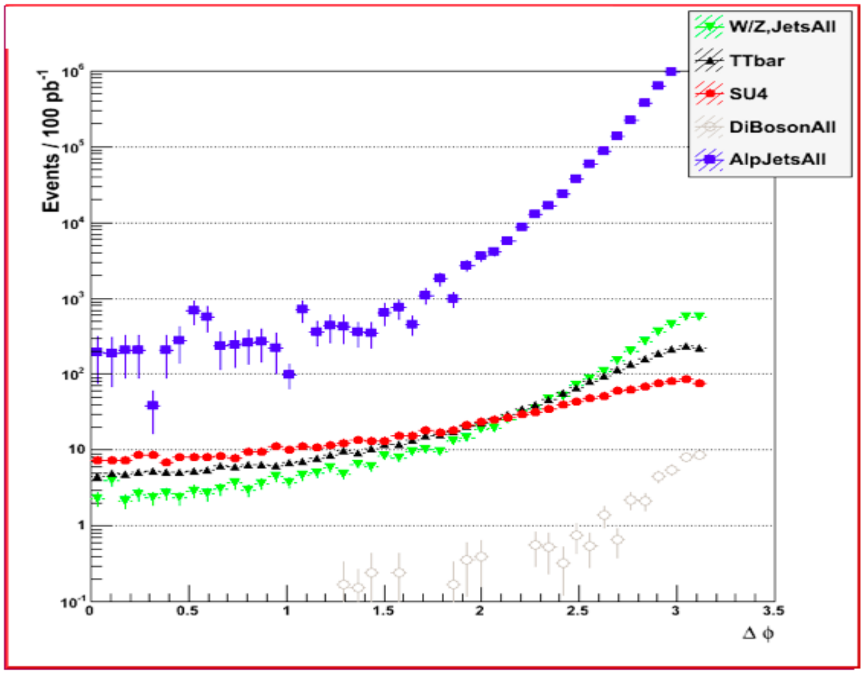

Figure 5.13. $\Delta\phi$ Distribution For the Multi-jet Case.

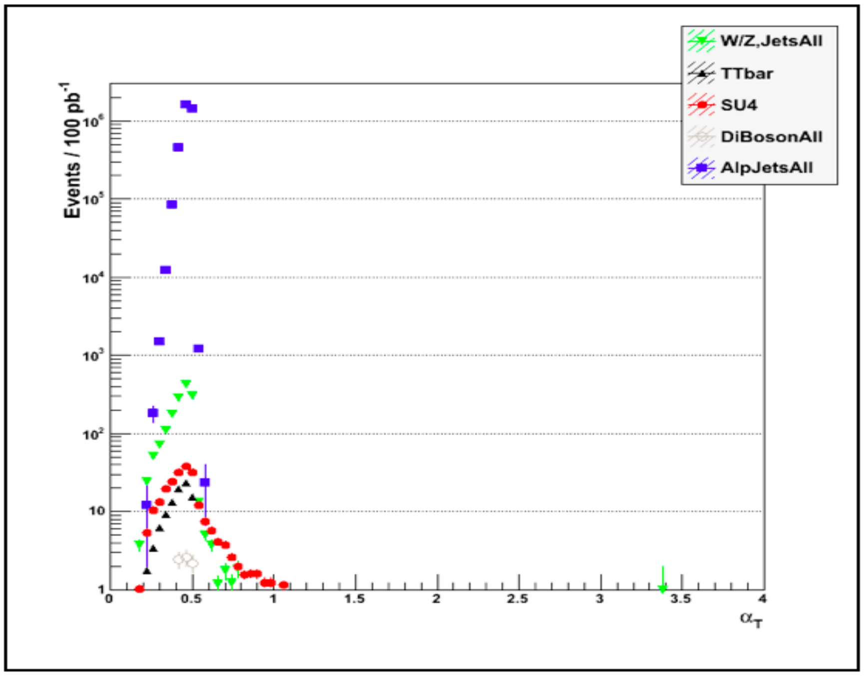

Figure 5.14. α_T Distribution For the Di-jet Case.

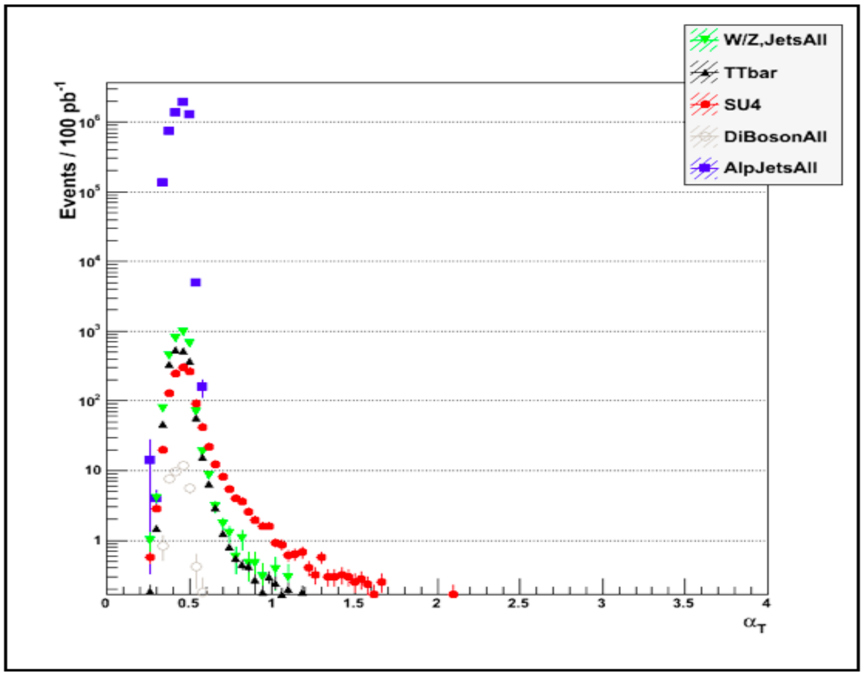

Figure 5.15. α_T Distribution For the Multi-jet Case.

5.4.4 Cut Optimizations And Significance Calculations

Cuts in each of the four variables were optimized to obtained maximum significance for discovering the SUSY signal over background. In each of the variables cuts were made on a sliding scale with the significance of discovery calculated as a function of the cut according to the following definition,

$$\mathcal{S} = \frac{S}{\sqrt{S+B}} \tag{5.6}$$

where $\mathcal{S}$ is the significance of discovering the signal with S number of signal events and B number of background events after a cut is made.

To obtain a cleaner signal yield from the E_T^{miss} distribution one further cut is made. A metric R is calculated in the plane of the two dimensional scatter distribution is made in the transverse plane in the azimuthal angle between the highest p_T jet and the E_T^{miss} vector versus the azimuthal angle between the second highest p_T jet and the E_T^{miss} vector given as,

$$\mathcal{R} = \sqrt{\left(\Delta\phi\left(\vec{E}_T^{miss}, \vec{p}_T^{j1}\right)\right)^2 + \left(\Delta\phi\left(\vec{E}_T^{miss}, \vec{p}_T^{j2}\right)\right)^2} \tag{5.7}$$

The distribution of $\mathcal{R}$ is shown for QCD and SU4 in figure 5.16 before any cut is made on top. It is clear due to the specific angular correlation between jets in QCD and E_T^{miss} arising from mostly fakes and detector miss-measurements the jet p_T vectors point in the same direction as the E_T^{miss} vector in the transverse plane. In SUSY however this relation does not hold. Thus a cut on $\mathcal{R} > 0.5$ substantially cuts out QCD events compared with SU4 events as shown in the distribution at the bottom.

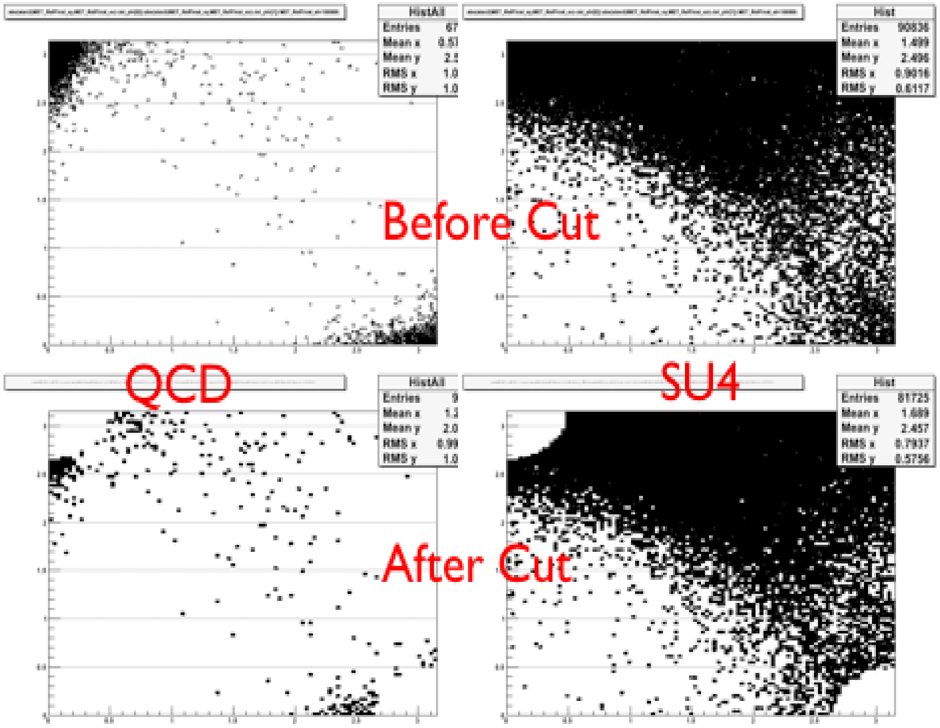

Figure 5.16. Distribution of $\mathcal{R}$ for QCD and SU4 before and after cut.

After the cut on $\mathcal{R}$ the significance $\mathcal{S}$ is plotted versus cut in E_T^{miss}. The distribution is shown in figure 5.17 for the di-jet and the multi-jet case. A peak in significance is clearly visible with $\mathcal{S} = 7.7$ for the di-jet case at a cut of 175 GeV and $\mathcal{S} = 14.0$ for the same cut of 175 GeV. Thus the cut of $E_T^{miss} > 175$ GeV is used to discriminate signal from background.

For each of the variables H_T^{miss}, $\Delta\phi$ and α_T one further cut is made as part of the selection cut to reduce contribution from softer jets. The distribution of $R(H_T)$ as defined in 5.4 is made and shown in figure 5.18 and 5.19 for the dijet and multijet cases. A plot of the significance as a function of a cut in $R(H_T)$ is shown in figure 5.20 for the dijet case (left) and the multijet case (right) is shown. An optimal cut of $R(H_T) < 1.25$ is made. This in turn suppresses 25% of the contribution to H_T^{miss}

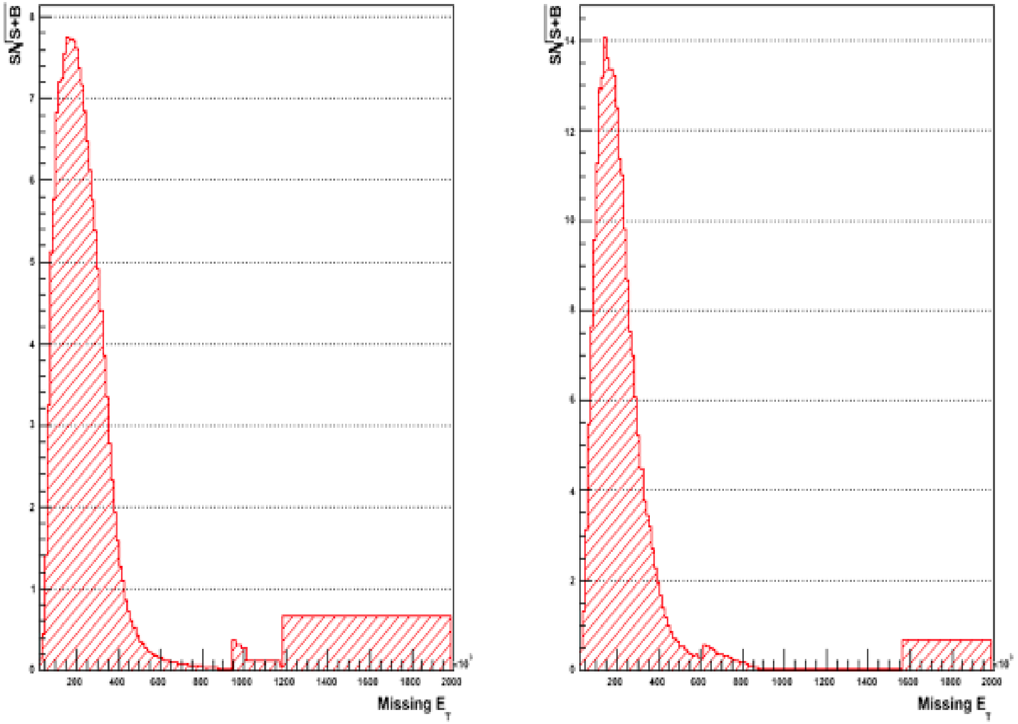

Figure 5.17. Distribution of $\mathcal{S}$ as a function of cut in E_T^{miss} for dijet (left) and multijet (right) cases.

due to low p_T jets. Similar plots of significance as a function of H_T^{miss}, $\Delta\phi$ and α_T is shown in figures 5.21, 5.22 and 5.23 respectively. The significance $\mathcal{S}$ for H_T^{miss} is maximum for value of 220 GeV with $\mathcal{S} = 7.7$ for the dijet and $\mathcal{S} = 13.8$ in the multijet case for H_T^{miss}, $\mathcal{S} = 6.4$ and $\mathcal{S} = 2.6$ for a cut of $\Delta\phi < 1.8$ for the dijet and multijet cases respectively and $\mathcal{S} = 5.45$ and $\mathcal{S} = 7.9$ for a cut of $\alpha_T > 0.52$ for the di-jet and the multi-jet cases respectively.

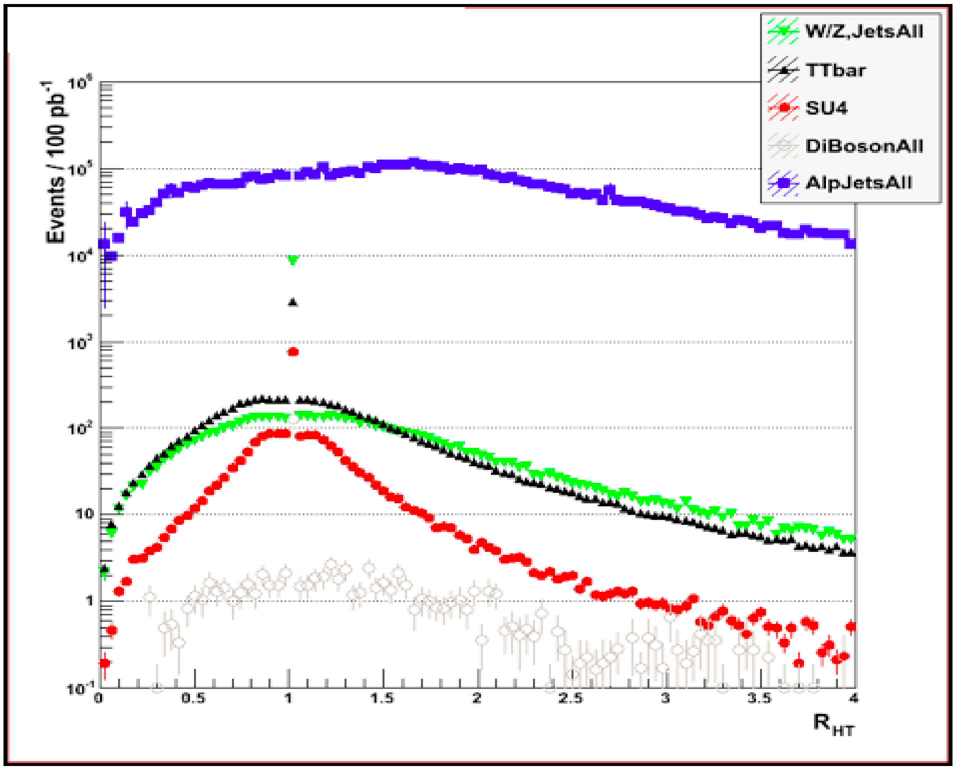

Figure 5.18. Distribution of $R(H_T)$ for the dijet case.

5.4.5 Event Counts And Discovery Significance With Optimized Cuts

The final count results for each of the cuts on the variables explored is summarized in this section with the discovery significance given for SU4 as a signal. Table 5.5 shows the cut flow values for SU4 and background for cuts in each of the variables in the dijet case.

Table 5.6 shows the cut flow values for SU4 and background for cuts in each of the variables in the multijet channel. Finally table 5.7 shows the final significance for SU4 signal for separate cuts in each of the variables for the di-jet and the multi-jet case.

From the results it is seen that E_T^{miss} seems to have slightly better performance than any of the topological variables explored as is expected. However, this assumed

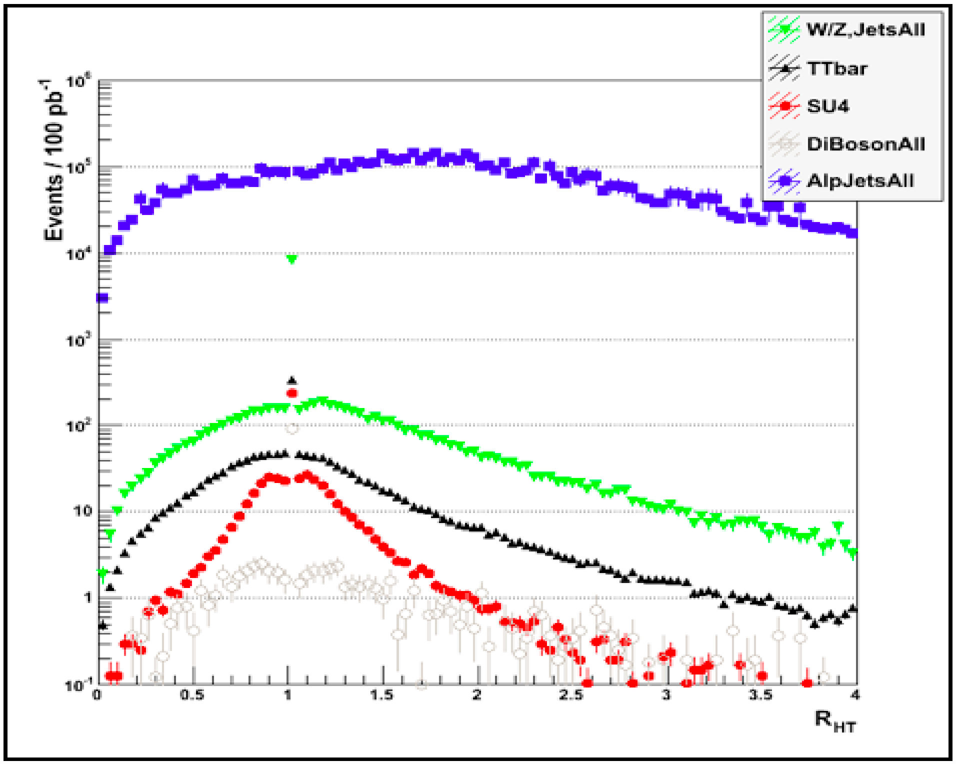

Figure 5.19. Distribution of $R(H_T)$ for multi-jet case.

that E_T^{miss} performs perfectly as assumed in data. Each of the variables H_T^{miss}, $\Delta\phi$ and α_T are independently useful to obtain significant discrimination between SUSY and Standard Model background.

5.5 Distribution Of Topological Variables In Data

After studies in Monte Carlo is performed initial plots of kinematic variables are made on data. To perform the plots on data event and object selection and object cleaning is done. The next sections describe the procedure of pre-selecting events for a SUSY analysis as well as the cleaning cuts that are applied to jets, leptons and missing transverse energy before final distributions are made. No cuts or final counts for signal are shown on data, but for comparison the Monte Carlo distributions

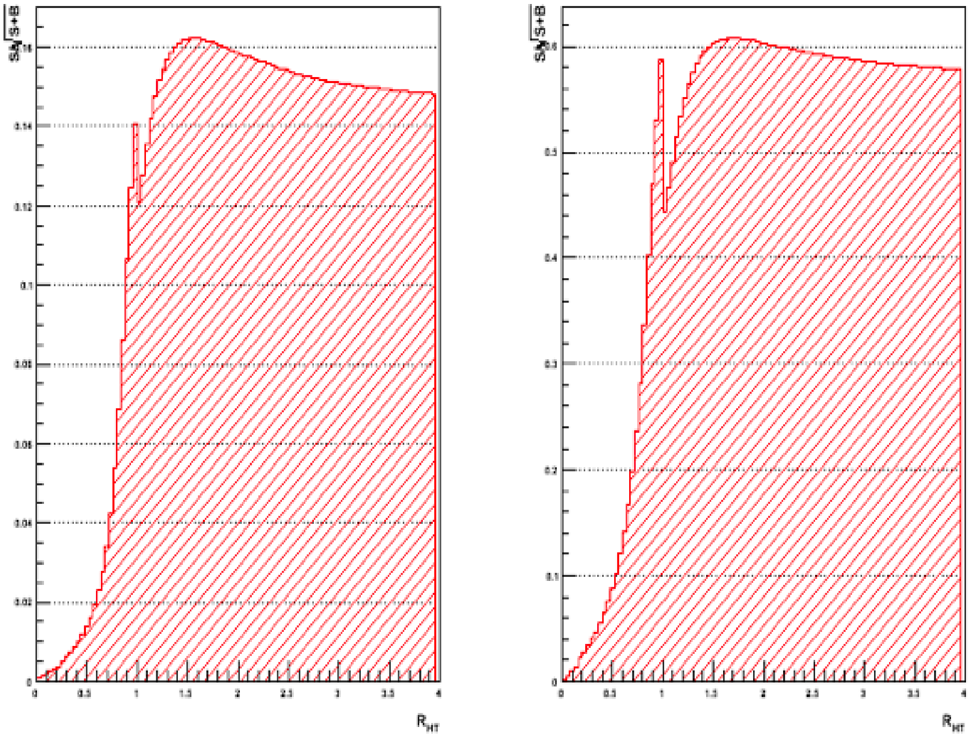

Figure 5.20. Significance vs.cut on $R(H_T)$ for di-jet and multi-jet cases.

Table 5.5. Cut flow for signal and background for di-jet scenario

	SIGNAL	BACKGROUND			
	SU4	QCD	Top	WZ+Jets	Di-bosons
Preselection	237.75	3573418.02	96.83	1488.22	9.89
E_T^{miss} Cut	133.27	22.39	11.25	122.50	0.95
H_T^{miss} Cut	91.13	0.66	6.53	59.66	0.30
$\Delta\phi$ Cut	69.62	0.0	4.49	41.39	0.28
α_T Cut	52.33	0.0	2.90	28.93	6.72

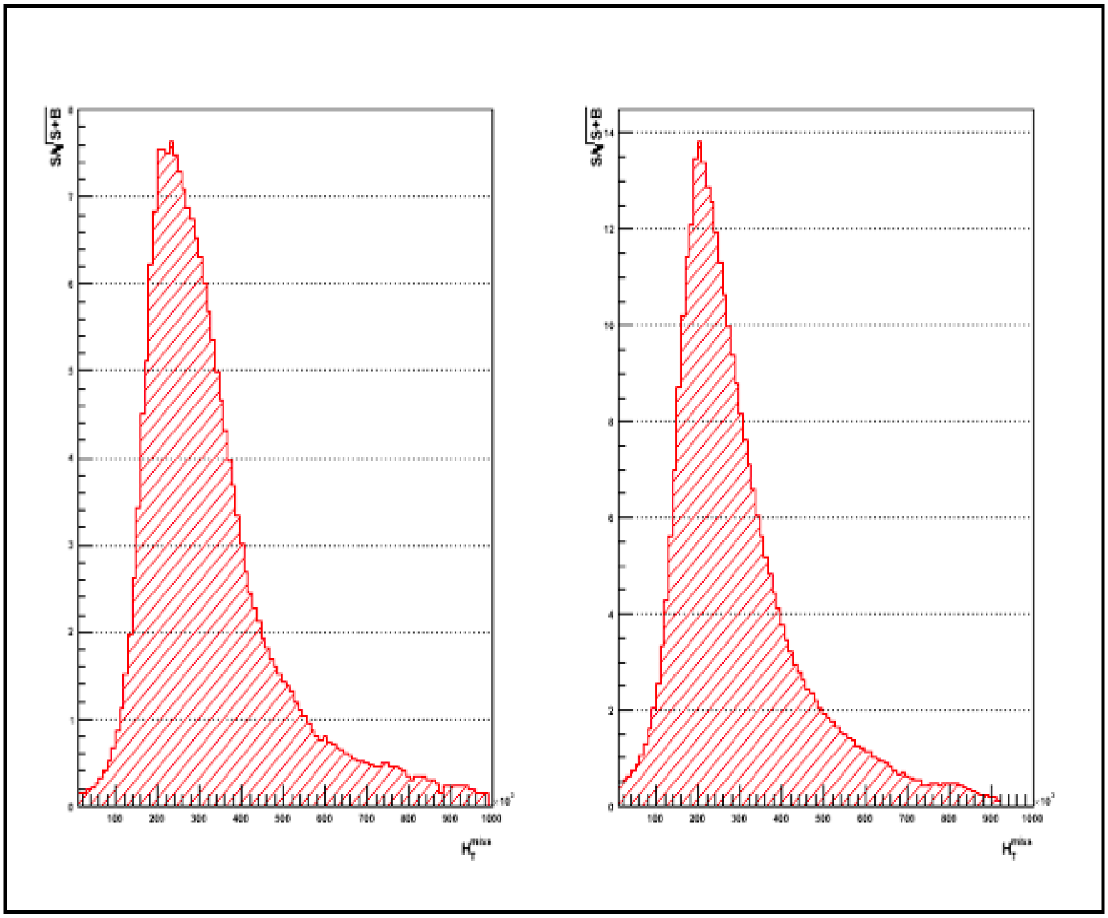

Figure 5.21. Significance vs.cut on (H_T^{miss}) for di-jet and multi-jet cases.

Table 5.6. Cut flow for signal and background for multi-jet scenario

	SIGNAL	BACKGROUND			
	SU4	QCD	Top	WZ+Jets	Di-bosons
Preselection	1165.29	5461456.81	1904.63	3035.947	36.16
E_T^{miss} Cut	406.817	147.81	105.18	158.15	0.82
H_T^{miss} Cut	189.29	9.03	36.92	52.16	0.57
$\Delta\phi$ Cut	269.81	9363.97	191.45	114.79	1.19
α_T Cut	120.58	14.87	31.96	42.70	0.19

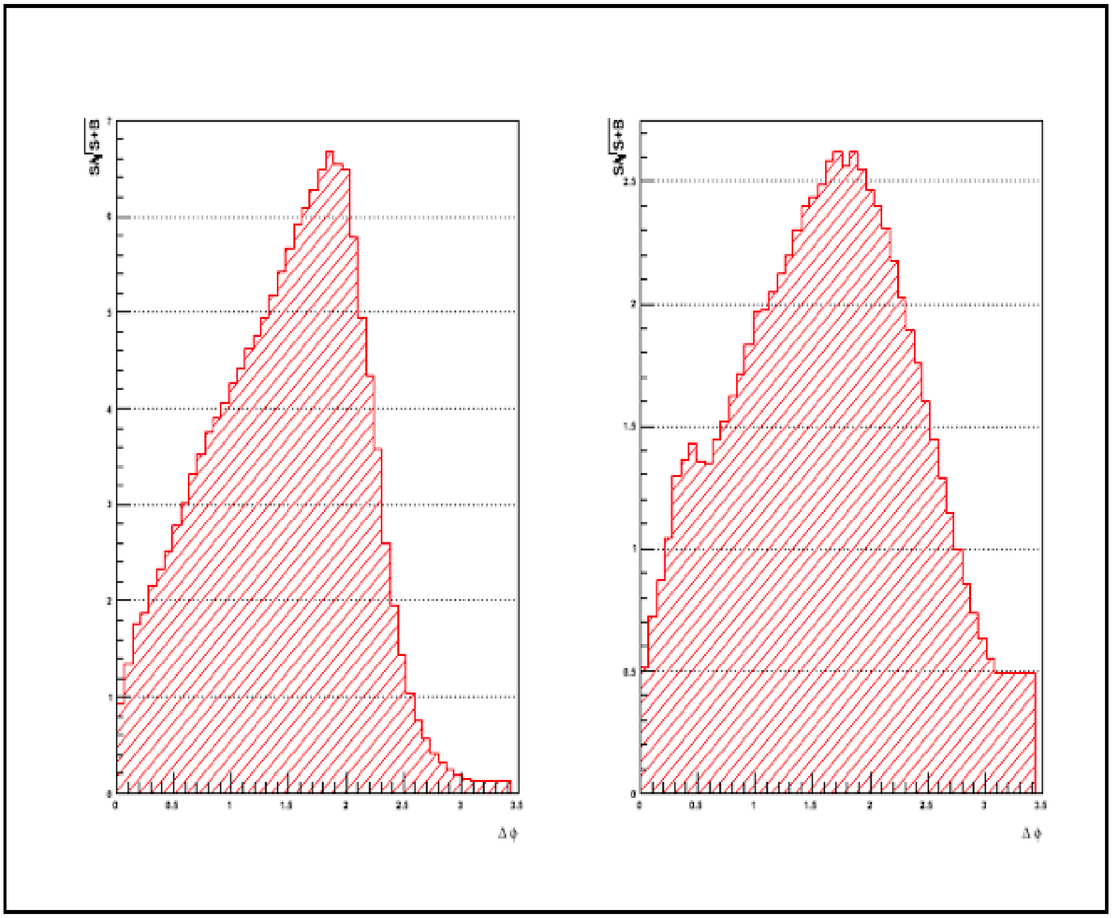

Figure 5.22. Significance vs.cut on $\Delta\phi$ for di-jet and multi-jet cases.

Table 5.7. Significance of discovering SU4 for each of the cuts in E_T^{miss} and topological variables for the di-jet and multi-jet cases

	Di-Jet	Multi-jet
E_T^{miss}	7.81	14.21
H_T^{miss}	7.24	11.13
$\Delta\phi$	6.47	2.7
α_T	5.48	8.31

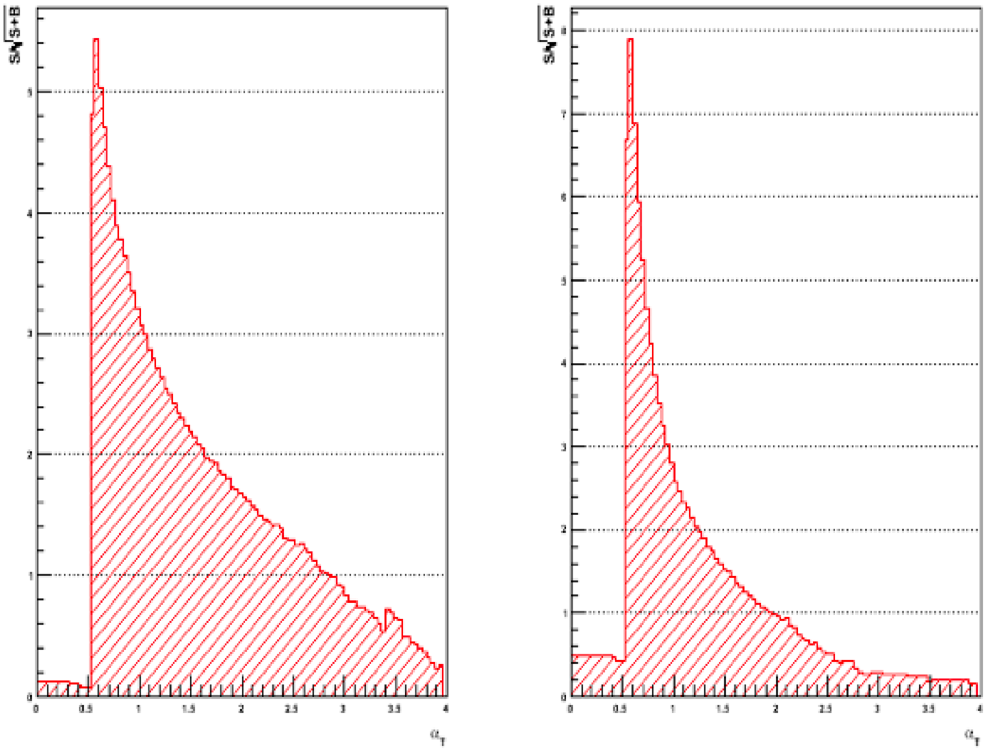

Figure 5.23. Significance vs.cut on α_T for di-jet and multi-jet cases.

for all the relevant background for each of the Standard Model processes are shown separately. Distribution of the kinematic variables for the SU4 signal point is shown with 10 times magnification for emphasis and clarity.

5.5.1 Object Selection for SUSY in Data

For the dijet and multijet study the primary objects required were jets and missing transverse energy. All relevant object selection cuts on Monte Carlo were equivalent to ones made on data. The jets were selected according to the following criteria:

- Jets were reconstructed using the AntiKt algorithm with topological clusters in the calorimeter with maximum distance between jet-core and constituent cluster (R) at 0.4
- Jets at electromagnetic scale were used without global cell weights being applied
- All jets were required to have a transverse momentum greater than 20 GeV
- All jets were required to be within a speudorapidity range of less than or equal to 2.5
- Good jets were selected using jet cleaning cuts that veto-ed noisy cells in the calorimeter, cosmic and beam halo muons.

The missing transverse energy was calculated using the following definitions,

$$\vec{E}_T^{Miss} \equiv \left(\vec{E}_X^{Miss}, \vec{E}_Y^{Miss}\right) \tag{5.8}$$

with,

$$E_T^{Miss} \equiv \sqrt{\left(E_X^{Miss}\right)^2 + \left(E_Y^{Miss}\right)^2} \tag{5.9}$$

The E_X^{Miss} and E_Y^{Miss} were defined as,

$$\begin{aligned} E_X^{Miss} &\equiv -\sum_{i=1}^{N_{cell}} E_i \sin\theta_i \cos\phi_i \\ E_Y^{Miss} &\equiv -\sum_{i=1}^{N_{cell}} E_i \sin\theta_i \sin\phi_i \end{aligned} \tag{5.10}$$

A cut of 30 GeV was applied on selecting the missing transverse energy. For the dijet, multijet study no corrections for electrons or muons were applied to the missing transverse energy.

5.5.2 Event Selection for SUSY in Data

Events were selected from data with requirement on stable LHC beam, optimal high voltage conditions, nominal field values for the solenoid and toroid magnets with subdetectors measuring electrons, muons and jets with correct momentum and energy. The trigger requirements were calorimeter based jet triggers with a event filter level threshold of 75 GeV along with a missing transverse energy threshold of 20 GeV. A good collision candidate event was selected by requiring at least one primary vertex with greater than four tracks. If more than two such primary vertexes were found a reweighting of events was done to correct for pileup. After removing electrons and muons that were in a cone of 0.4 of jets all events with an electron or muon with transverse energy greater than 10 GeV were rejected.

Distributions of the topological variables for the dijet channel is made after all the object selection cuts and the event selections were applied. The distributions presented are for $6.84pb^{-1}$ of data at $\sqrt{s} = 7$ TeV. Figure 5.24 shows the distribution of H_T in data. Figure 5.25 shows the distribution of H_T^{Miss} in data. Figure 5.26 shows the distribution of $\Delta\phi$ in data. Figure 5.27 shows the distribution of α_T in data. Figure 5.28 shows the distribution of E_T^{Miss} in data.

5.6 Conclusions

In this chapter methods to search for Supersymmetry in the dijet and multijet channels were described. Several topological and kinematic variables were explored as alternative discriminating variables to missing transverse energy with studies optimizing cuts for a low mass mSUGRA point. Distributions of these variables were also shown with early ATLAS data compared with Monte Carlo predictions of signal

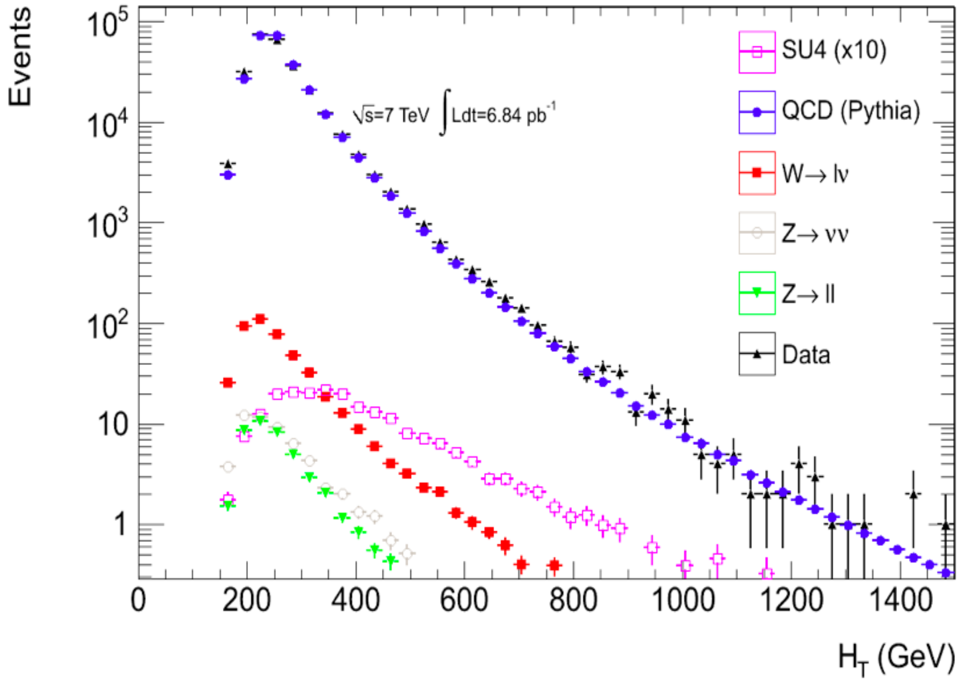

Figure 5.24. Distribution of H_T for dijets in data.

and background. The Monte Carlo seems to agree reasonably well with data for the luminosity shown. No excess above Standarc Model predictions were observed.

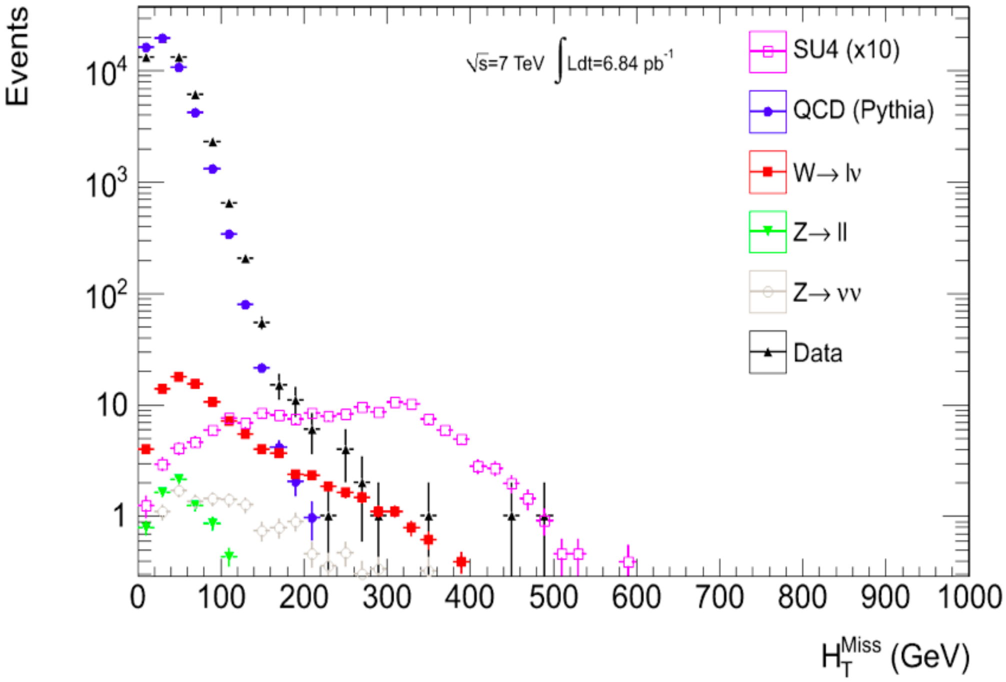

Figure 5.25. Distribution of H_T^{Miss} for dijets in data.

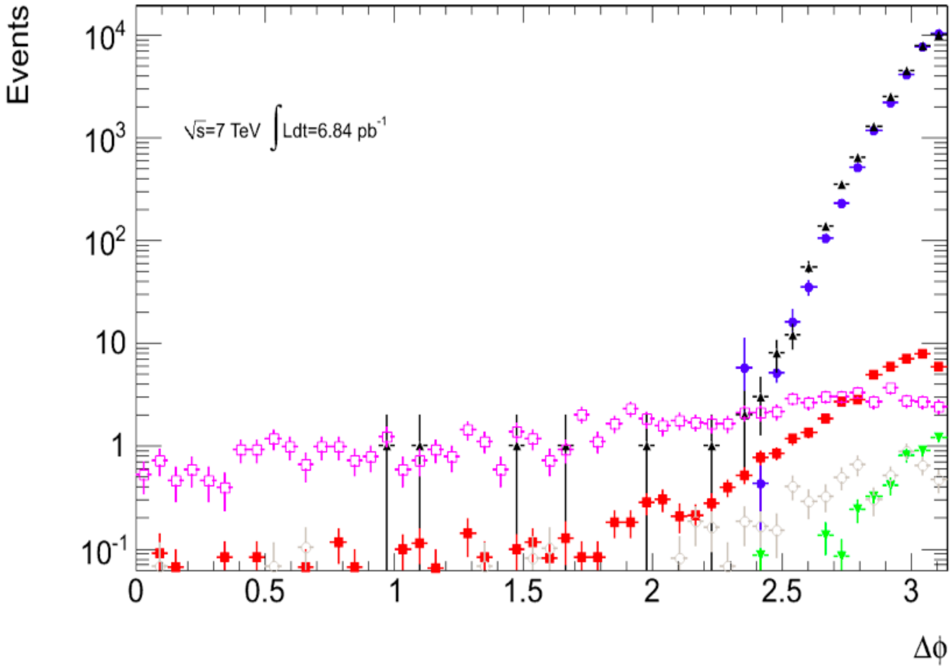

Figure 5.26. Distribution of $\Delta\phi$ for dijets in data.

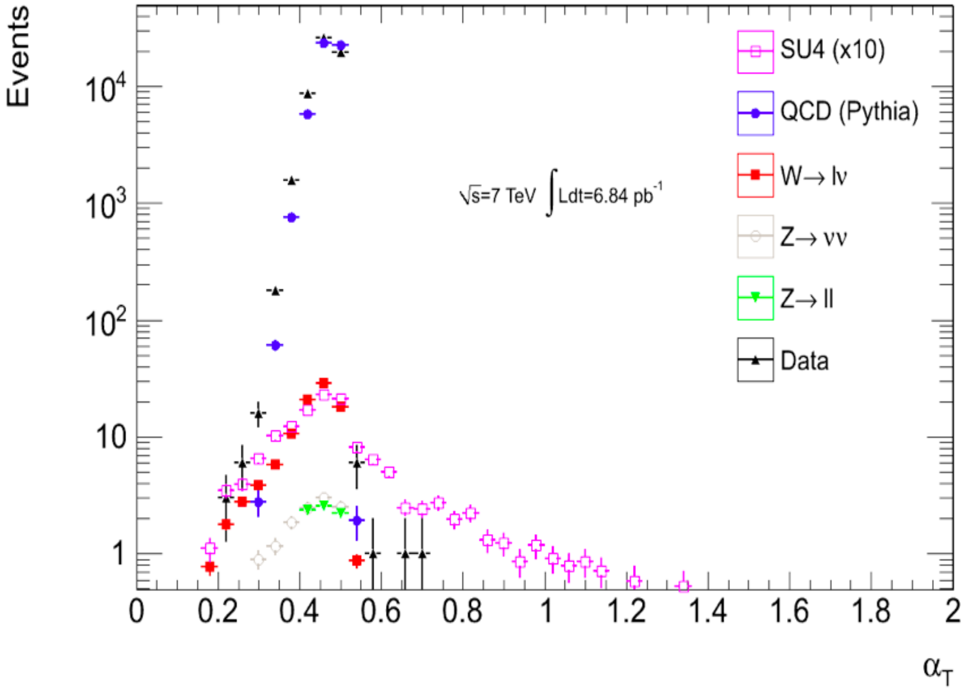

Figure 5.27. Distribution of α_T for dijets in data.

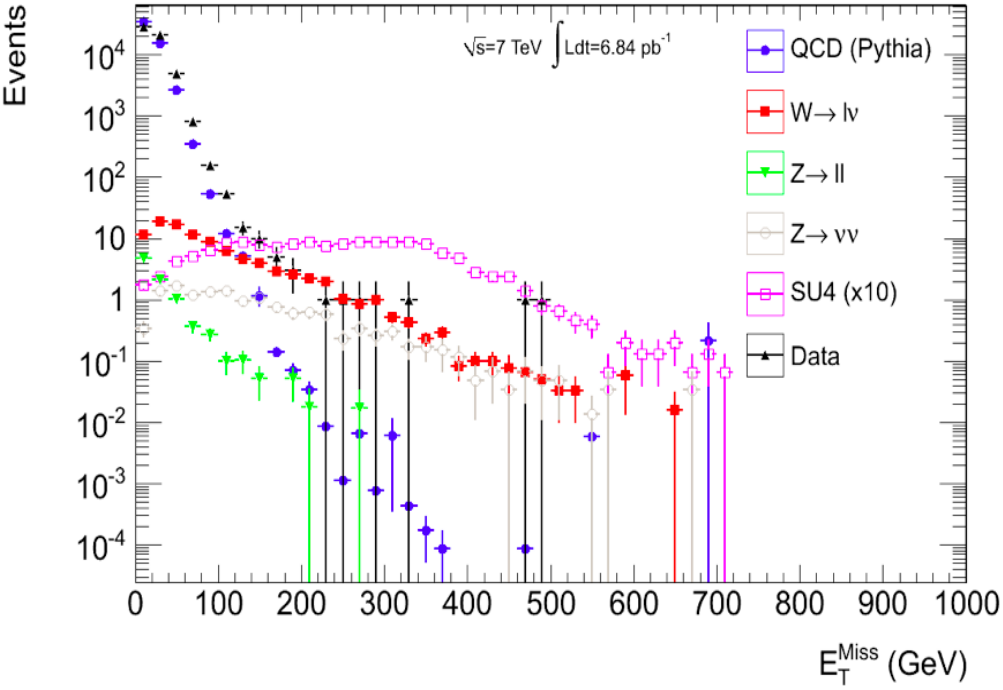

Figure 5.28. Distribution of E_T^{Miss} for dijets in data.

CHAPTER 6

Z + JETS BACKGROUND ESTIMATION FROM DATA

6.1 Introduction

Production of the Z boson with associated jets, where the Z decays into two neutrinos constitute an irreducible background towards SUSY searches involving multiple jets with missing transverse momentum. The Z can decay into the invisible neutrino with a branching fraction, $\Gamma_i/\Gamma = (20 \pm 0.06)\%$ making this as one of the primary decay modes of the Z particle. The detector signature for this decay mode consists of missing transverse energy from the undetected neutrinos and associated jet production. As this detector signature is indistinguishable form the signal signatures explored in multijet SUSY searches, these events constitute a background that are irreducible. Thus a data driven background estimation technique for this channel has been developed.

6.2 $Z \rightarrow \nu\nu$ + Jets Estimation Using γ + Jets Events

The detector signature of Z boson production with associated jets with the Z decaying into two neutrinos is presence of missing transverse energy with multiple jets. As such it is impossible to actually 'isolate' such events from other QCD like events as well as many new physics signatures which require high missing transverse energy as a discriminating signature. This makes it necessary to estimate the contribution of $Z \rightarrow \nu\nu + Jets$ towards the missing transverse energy with multiple jets signature using data driven techniques. The Feynman diagram for the production mechanism of the Z with associated jets is shown in figure 6.1. [50]

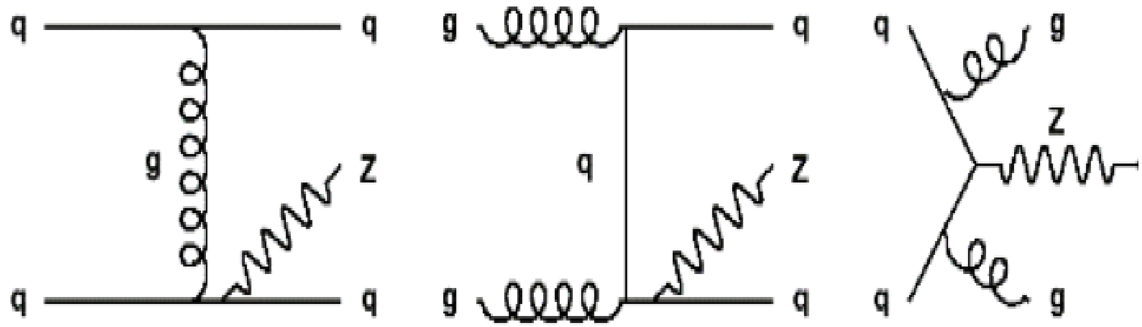

Figure 6.1. Feynman diagram for Z production with associated Jets.

One method to estimate this contribution has been to measure the contribution from $Z \rightarrow ll + Jets$ where the ll are either e^+e^- or $\mu^+\mu^-$ and using the electrons' or muons' transverse momentum contribution towards the missing transverse energy weighted with the appropriate ratio of branching fractions. However, the branching fraction of $Z \rightarrow e^+e^-$ and $Z \rightarrow \mu^+\mu^-$ is approximately $\Gamma_i/\Gamma = (3.363 \pm 0.004)\%$ each. Thus this method for estimating background for initial ATLAS data will be statistically limited for high transverse momentum regions. Also the ratio for $Z \rightarrow l^+l^-$ to the f $Z \rightarrow \nu\nu$ is alway at most ~ 0.3 times the ratio of f γ to f $Z \rightarrow \nu\nu$. Subsequently, a method to estimate the missing transverse momentum spectrum using photon events has been developed.

The process of $pp \rightarrow Z(\nu\nu)+$ Jets and $pp \rightarrow \gamma+$ Jets from a hard proton proton collision is the same except for the mass of the Z and the vertex factor associated theoretical couplings as represented by figure 6.2. This in turn ensures that the ratio $\frac{Z(\nu\nu)+Jets}{\gamma+Jets}$ should stabilize at high values of transverse momenta. This ratio is then used to scale the $\gamma+$ Jets distributions from data to estimate the $Z(\nu\nu)+$ Jets contribution. The plot for the ratio $\frac{Z(\nu\nu)+Jets}{\gamma+Jets}$ is shown as a function of the transverse momentum for 'true' bosons produced using PYTHIA as well as ALPGEN

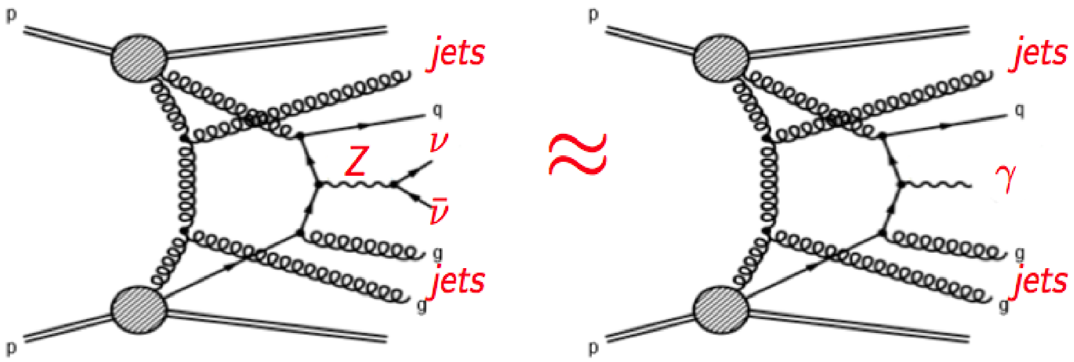

Figure 6.2. Photon and Z production with associated Jets.

Monte Carlo generators, in figure 6.3. The plot 6.3 shows that for large values of the transverse momentum the ratio stabilizes at a constant value. A clean photon distribution obtained from early ATLAS data convoluted with this ratio obtained from Monte Carlo then yields the missing transverse momentum distribution.

6.3 Pure Photon Distribution from Data

To extrapolate the missing transverse energy distribution from the direct photon distribution a ‘clean’ or ‘pure’, well identified sample of photons must be extracted from data. The rest of this section will describe the process of selecting a ‘pure’ photon sample from early ATLAS data. [51]

6.3.1 Prompt Photon Production Mechanism

‘Prompt’ or ‘direct’ photons are produced in ATLAS predominantly as QCD processes. The primary production mechanisms for production of photons are Compton scattering, quark-anti-quark annihilation processes and fragmentations. Feynman diagrams for each of these processes are shown in figure 6.4. The dominant process is the quark-gluon process at lower transverse energy (E_T) with Compton scattering

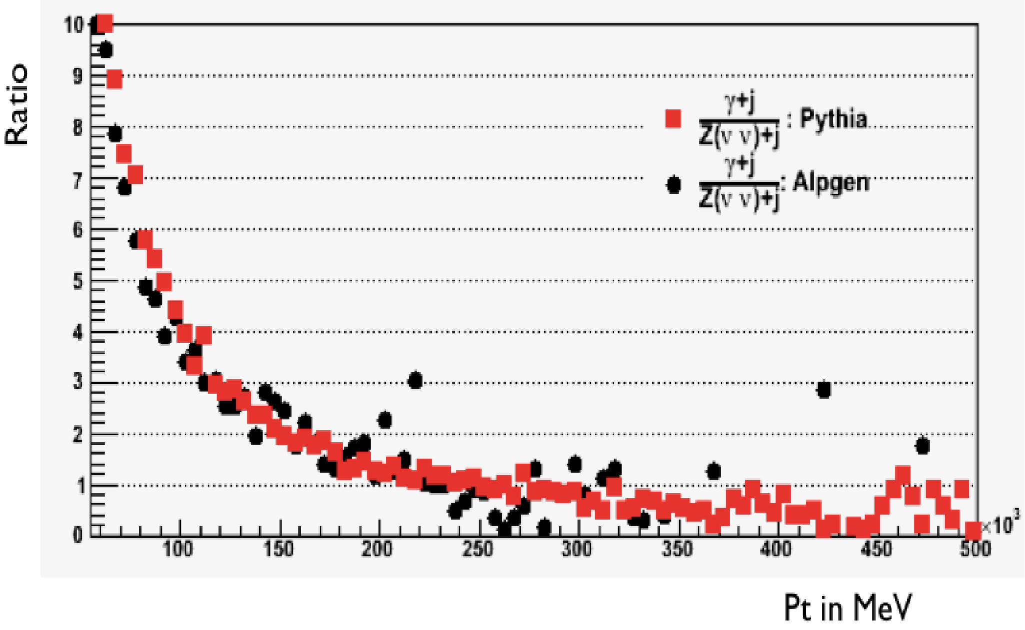

Figure 6.3. $\frac{Z(\nu\nu)+Jets}{\gamma+Jets}$ as a function of transverse momentum.

dominating at higher (E_T). Although all the above processes are relevant for photon production, keeping in mind that the goal of the analysis is to emulate the production of the Z boson, the fragmentation processes need to be suppressed when considering the ratio of γ + Jets versus Z + Jets production. As the expected cross section for direct photon production at the LHC is considerably higher than previous experiments due to higher center of mass energy of collisions, ∼30 times higher than at the Tevatron, a study of direct photon cross section using Monte Carlo was performed. An ab initio isolation requirement was introduced [51] to suppress the fragmentation processes. Such an isolation criterion has been shown in general to not affect the factorization properties in the calculations. The isolation criteria is also useful to distinguish photons that are produced via the decays of pion opposed to the ones that are directly produced. Figure 6.5 shows the results for cross section calculation at next-to-leading order (NLO) QCD, at $\sqrt{s}$ = 7TeV using the JETPHOX (program

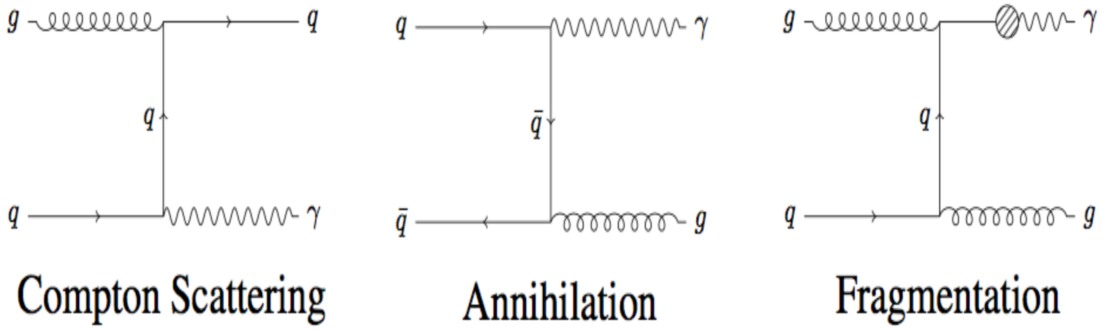

Figure 6.4. Prompt photon production processes..

with CTEQ6.6 PDF as the parton distribution function. [52] The uncertainties shown in figure 6.5 are calculated by considering the uncertainties of the PDF, as well as variations due to the scale and isolation criteria.

6.3.2 Event selection in Data

Events are selected for this analysis from data according to the criteria described as follows. Firstly, stable LHC beam conditions are required with nominal fields from the magnet systems. A detector quality selection where the calorimeters and the inner detector are fully operational and give good quality of reconstructed objects is required.

The trigger selection for this analysis is based on level-1 hardware trigger with an initial granularity of $\eta \times \phi = 0.1 \times 0.1$ such that more than 5 GeV of transverse energy is available in two of the four trigger channels in an electromagnetic cluster of size 0.2×0.2. The nominal transverse energy threshold required at the end of the high level trigger chain is 10 GeV. A loose (loser than the offline selection) photon identification criterion is also required. These requirements essentially form the 'EF_g10_loose' trigger of ATLAS, where 'EF' stands for event filter or the highest level of the trigger

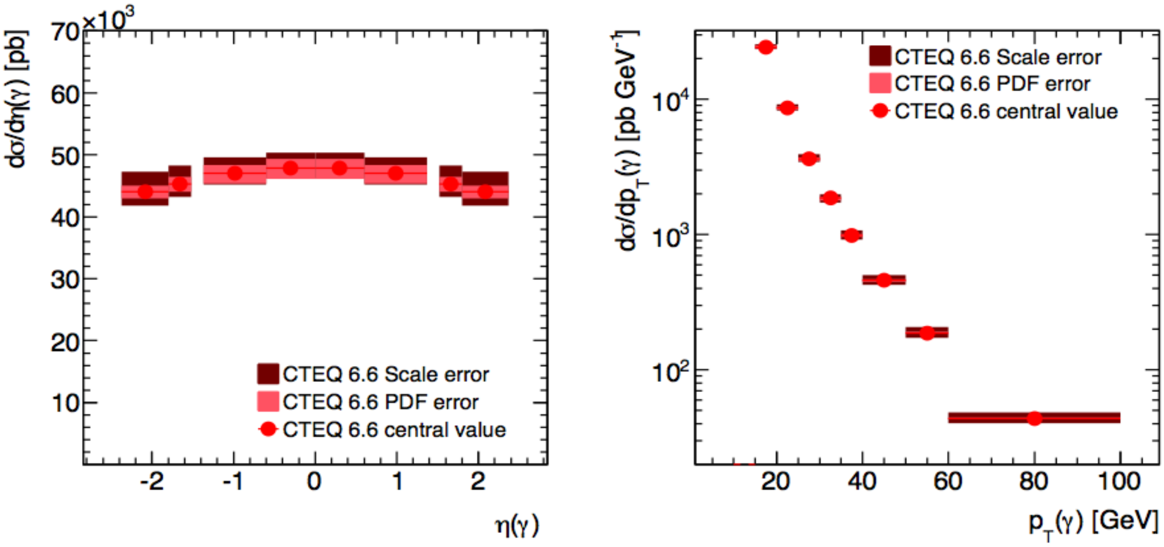

Figure 6.5. Theoretical predictions for the differential cross section for prompt photon production as a function of η and p_T of the photons at $\sqrt{s} = 7$TeV.

system. After the trigger selections an efficiency of 100% is achieved for $E_T^\gamma > 15$ GeV and $|\eta| < 1.81$. The periods of ATLAS data used for the analysis is from period A to period E4 where no prescales were used on the EF_g10_loose trigger. Table 6.1 shows the different run periods of ATLAS with the corresponding range of run numbers for periods A to E. The total Luminosity of data used for analysis after the above selections correspond to $(8.8 \pm 1.0) \times 10^2 nb^{-1}$. From the beginning of period E4 the ATLAS data was divided in steams of given triggers. The 'egamma' stream consisting of all the level 1 triggers based on the electromagnetic calorimeter was used for this analysis. A summary of the runs with the corresponding luminosity breakdown is shown for some run and the total in table 6.2. A primary vertex requirement is also used to select events from collisions and reduce non collision background. To this end the average beam spot is compared with the reconstructed vertex with three or more associated tracks. The efficiency of this is 99% and with the non-collision background contributing less than 1%. Thus this contribution is ignored.

Table 6.1. List of ATLAS run periods, corresponding run-numbers and integrated luminosity

Period	Sub-range	Run Range	Luminosity (nb^{-1})
A	none	152166-153200	0.4
B	B1-B2	153565-155160	9
C	C1	155228-155697	
	C2	156682	9.5
D	D1-D6	158045-159224	320
E	E1	160387-160479	144
	E2	160530	96
	E3	160613-160879	272
	E4	160899-160980	133

6.3.3 Events selection in Monte Carlo

The Monte Carlo samples used for this analysis were generated using the PYTHIA generator at $\sqrt{s} = 7$ TeV, described in chapter one. The full GEANT simulation of the ATLAS detector was performed on the generated events using ATLAS geometry corresponding to the database ATLAS-GEO-10-00-00.

The primary samples used for this analysis correspond to simulated direct photon samples and and dijet background samples with a filter on one jet. A sample of Z boson production with associated decays is also used for studying theoretical ratios of Z boson and photon production with associated jets. A summary of the samples with the relevant details is shown in table 6.3. An initial filter on the transverse momentum of the parton ($\hat{p}_T$) is used to generate the PYTHIA Monte Carlo samples used. The sample (105802) has a filter on production of at least one jet whereas the sample (108087) has a filter on production of at least one photon. Similar cuts and selections to data are made on Monte Carlo for comparison with data. The Monte Carlo is scaled such that an equivalent luminosity of the data ($0.88pb^{-1}$) is represented

Table 6.2. Run by run Luminosity information summary

Run Number	Good LBs	Bad LBs	Luminosity delivered nb^{-1}	Luminosity live fraction corrected nb^{-1}	Luminosity prescale corrected nb^{-1}	Lumi weighted live fraction (%)	Lumi weighted prescale
152166	47	48	0.00734313	0.00291795	0.00291795	39.74	1.0
152214	43	0	0.00323667	0.00323431	0.00323431	99.93	1.0
152221	163	0	0.0210465	0.0210317	0.0210317	99.93	1.0
152345	80	0	0.016125	0.0161162	0.0161162	99.95	1.0
152409	589	4	0.0800099	0.0793812	0.0793812	99.21	1.0
152441	359	4	0.0682389	0.0671911	0.0671911	98.46	1.0
...	...	...	...	...	...	...	...
Total	12124	127	897.267709	877.62489	877.62489	97.81	1.0

Table 6.3. Monte Carlo Samples used for photon study

Data Set	Process	σ [pb]	Filter	Filter cut [GeV]	Filter Efficiency	Events	Lumi $[pb^{-1}]$	Generator
105802	QCD	1.148×10^9	1 jet	17	0.08.62	48931022	0.494	PYTHIA
108087	γ-jet	2.250×10^5	1γ	17	0.470	4994464	47.2	PYTHIA

in the Monte Carlo samples in distributions after the cross section reported by the generator is scaled by the efficiencies of the corresponding filters used in the samples.

6.3.4 Photon Object Selection From Data

After events pass the selection criteria described above photon objects are subjected to addisional quality selection. A sliding window of clusters in the calorimeter are matched to tracks. If no tracks are found the cluster is considered to be a reconstructed photon. If a reconstructed vertex of converted tracks is matched to the clusters the candidates are considered to be converted photons. [53] The unconverted photon candidates correspond to a cluster size of 3×7 cells in $\eta \times \phi$ in the electromagnetic barrel and a size of 5×5 in the end-caps. To obtain a clean sample of direct photons several kinematic, fiducial and calorimeter based cuts are used. A detail description of the photon selection method is itemized :

- A kinematic cut of 15 GeV $< p_T^{\gamma}$ to obtain $\sim 100\%$ trigger efficiency in data.
- A fiducial cut on the pseudorapidity calculated using the second sampling of the detector of $|\eta| < 1.37$ and $1.52 \leq |\eta| < 2.37$ is used. This analysis further looks at the fiducial regions described in table 6.4 with each region characterizing a design specific region of the detector. The region of $1.37 \leq |\eta| < 1.52$ corresponds to the 'crack' region of the calorimeter, where the service cables are and thus is a poor photon reconstruction region. Only the outer wheel of the end-cap EM calorimeter is considered while the inner wheel ($2.5 \leq |\eta| < 3.2$) as well as the forward calorimeter (FCAL) region ($3.1 \leq |\eta| < 4.9$) are not included due to poorly understood detector effects with the collected luminosity for this study.

Table 6.4. Monte Carlo Samples used for photon study

Fiducial regions	Detector region
$0.00 \leq \|\eta\| < 0.60$	Material in front of EM Calorimeter
$0.60 \leq \|\eta\| < 1.37$	Rest of the Barrel
$1.52 \leq \|\eta\| < 1.81$	Endcap
$1.81 \leq \|\eta\| < 2.37$	Endcap

- Regions of the calorimeter, that have inactive regions due to malfunctions in optical connectors have been studied to measure the effect of this on photon reconstruction. Figure 6.6 shows a map of the first layer of the calorimeter with

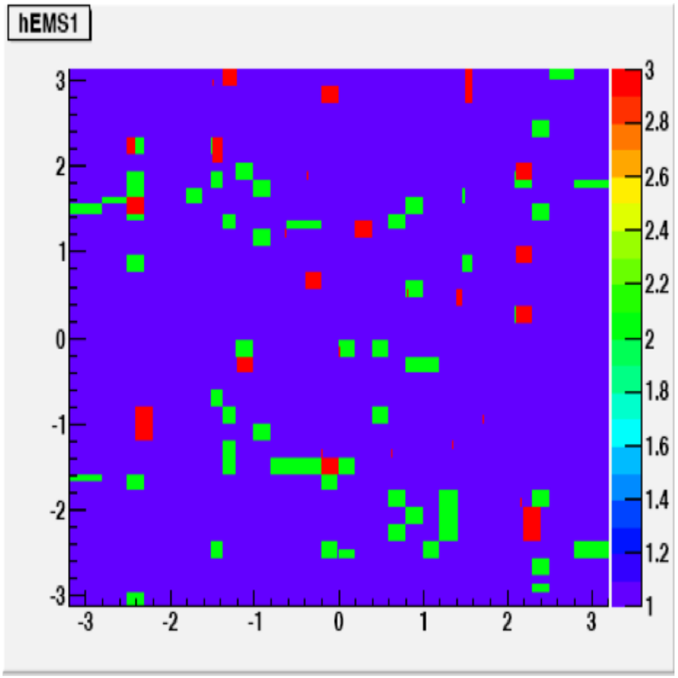

Figure 6.6. $\eta - \phi$ map of the first layer of the electromagnetic calorimeter showing the state of optical connectors and high voltages.

red showing inactive regions and green with not nominal high voltage conditions, and blue showing fully functioning regions of the detector in the $\eta - \phi$ plane of the detector. For each run a database of conditions for the optical connectors and detector voltages are stored. Thus any cluster that contained a dead optical link (OTX) or a dead cell is rejected from being considered.

- A trigger selection is made on data requiring level 1 calorimeter based trigger, with a electromagnetic energy threshold of 10 GeV at the event filter level. The selection is performed in the data stream of electron-gamma (EGamma) for later runs as described earlier.
- At least one primary vertex is required in the event to have at least 3 inner detector tracks associated with it

6.3.5 Photon Identification

After photons are pre-selected from data there are still substantial number of QCD jets containing pions that decay into two photons present in the selection. To distinguish photons produced directly from the collision as opposed to photons from pion decays photon identification algorithms have been developed based on the shower shape variables. The shower shape variables, or discriminating variables (DVs) are grouped in three primary categories:

- hadronic leakage
- variables using the second longitudinal compartment (middle layer) of the electromagnetic calorimeter
- variables using the first longitudinal compartment (strip layer) of the electromagnetic calorimeter

The cuts on the discriminating variables are made such that maximum background rejection can be obtained in each fiducial region in the pseudorapidity of the detector. Three identification levels (IDs) are used : ‘loose’, ‘tight’ and ‘robust-tight’ based on variations in cuts. The ’robust-tight’ selection is used in this analysis for the extraction of purity of photons from data. [54]

6.3.5.1 Cut Flow With Photon Identification

Table 6.5 shows the ‘cut-flow’ of some typical runs for each of the event and object selections described above. Although the table lists only a few runs, a cut by cut extraction of photons yield for each run was performed to extract the photons for this analysis and cross checked with other analyses performed. The three rows correspond to the photon IDs, loose, tight and robust tight. The first column gives the number of photons obtained from the photon container after kinematic and fiducial cuts for preselection. The second column (GRL) lists the number of photons obtained after good events were selected using good luminosity blocks, and optimal data reconstruction flags were passed. The third column (Vtx) shows the number of photons obtained after the requirement of at least one primary vertex is made. The fourth column shows the number of photons after trigger selection at event filter, is applied. The fifth column shows the number of photons after the cleaning is performed for bad optical connectors and voltages in the detector. The sixth column is the intersection of the GRL and Trig cut, the seventh the intersection of the sixth cut with the primary vertex selection and the eighth column the intersection of all the cuts. As is evident from the example runs for some runs the final yield is zero whereas for some other runs a large number of photon yield is obtained.

6.3.5.2 Photon Identification Variables And Cuts

The photon identification variables are constructed out of shower shapes variables after careful study is made to discriminate regions of pure photons versus fakes. The discriminating variables based on the hadronic leakage criteria are:

- R_{had_1} : The ratio of transverse energy (E_T) in the first sampling of the hadronic (Tile) calorimeter to the transverse energy (E_T) of the Electromagnetic cluster in the fiducial range in pseudorapidity given as, $|\eta| < 0.8$ and $|\eta| < 1.37$. Figure 6.7 shows the R_{had_1} distribution in data and Monte Carlo.

- R_{had} : The ratio of transverse energy (E_T) in all the hadronic calorimeter to the transverse energy (E_T) of the Electromagnetic cluster measures in the fiducial

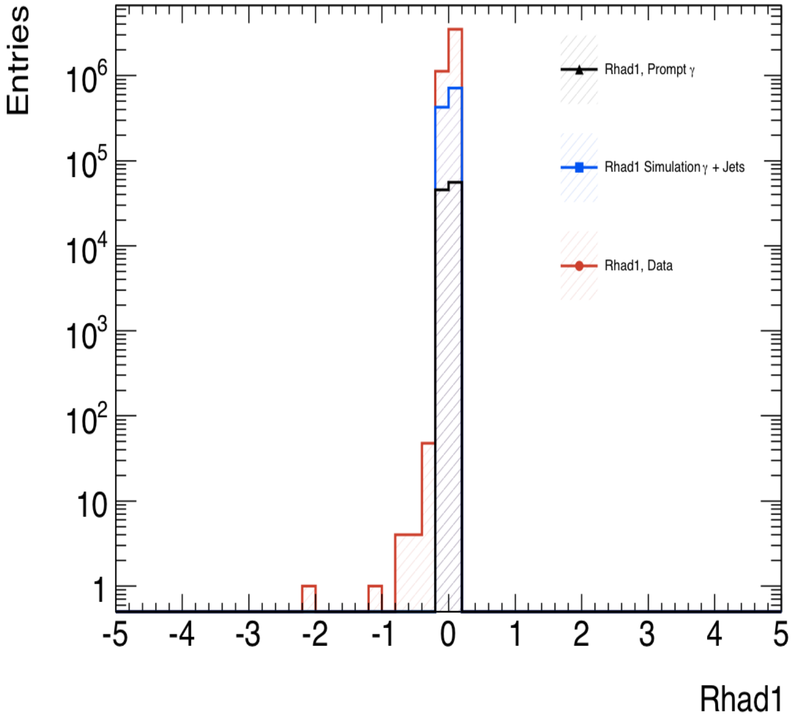

Figure 6.7. R_{had_1} distribution for data and Monte Carlo.

range in pseudorapidity given as, $|\eta| < 0.8$ and $|\eta| < 1.37$ Figure 6.7 shows the R_{had} distribution in data and Monte Carlo.

The discriminating variables based on the electromagnetic middle layer are given by the following shower shape variables:

- R_η: Ration in η of cell energies in 3×7 versus 7×7 cells. Figure 6.9 shows the distribution of R_η in data versus Monte Carlo.

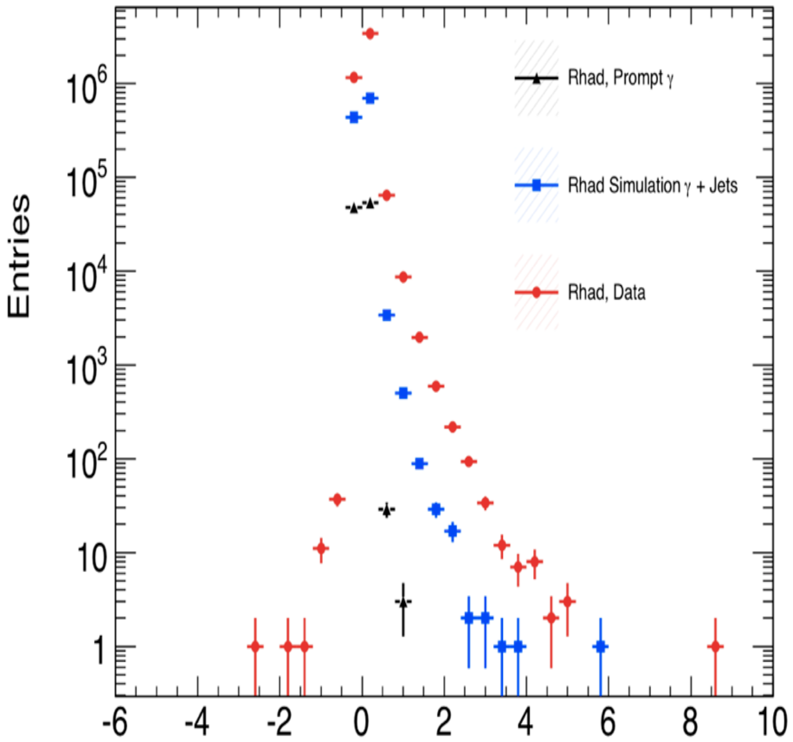

Figure 6.8. R_{had} distribution for data and Monte Carlo.

- w_{η_2} : The lateral width of the shower. Figure 6.10 shows the distribution of w_{η_2} in data versus Monte Carlo.

- R_{ϕ} : Ratio of ϕ of cell energies in 3×3 and 3×7 cells. Figure 6.11 shows the distribution of R_{ϕ} in data and Monte Carlo.

The discriminating variables based on the electromagnetic strip layer are given by the following shower shape variables:

- w_{S_3} : The shower width of three strips around the maximum strip. Figure 6.12 shows the w_{S_3} distribution in data and Monte Carlo.

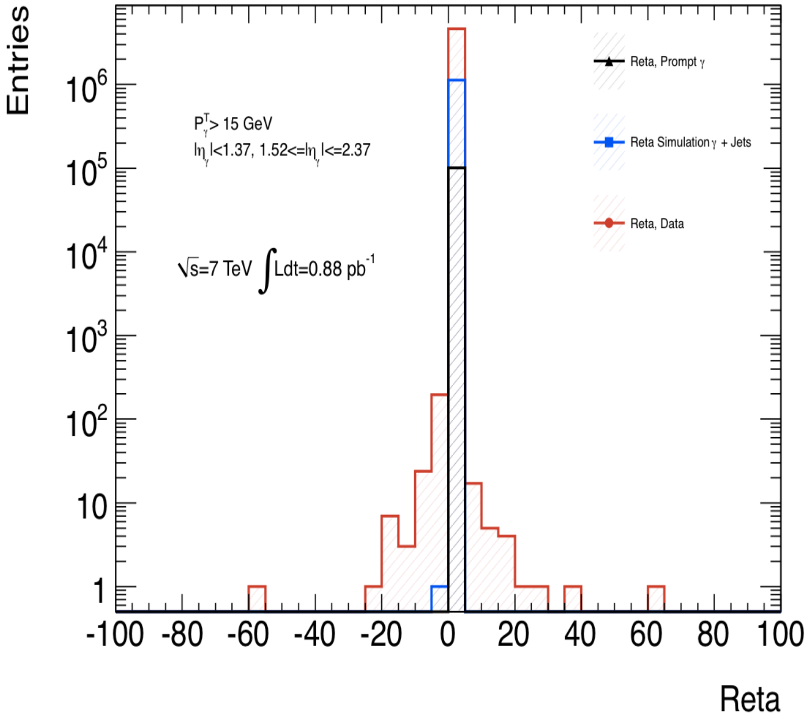

Figure 6.9. R_η distribution for data and Monte Carlo.

- $w_{s_{tot}}$: The total lateral shower width. Figure 6.13 shows the $w_{s_{tot}}$distribution of in data and Monte Carlo.

- F_{side} : The fraction of energy outside the core of three central strips but within seven strips. Figure 6.14 shows the F_{side} distribution in data and Monte Carlo.

- ΔE : The difference in energy of the strip with the second largest energy deposit and the energy of the strip with the smallest energy deposit between the two leading strips. Figure 6.15 shows the ΔE distribution in data and Monte Carlo.

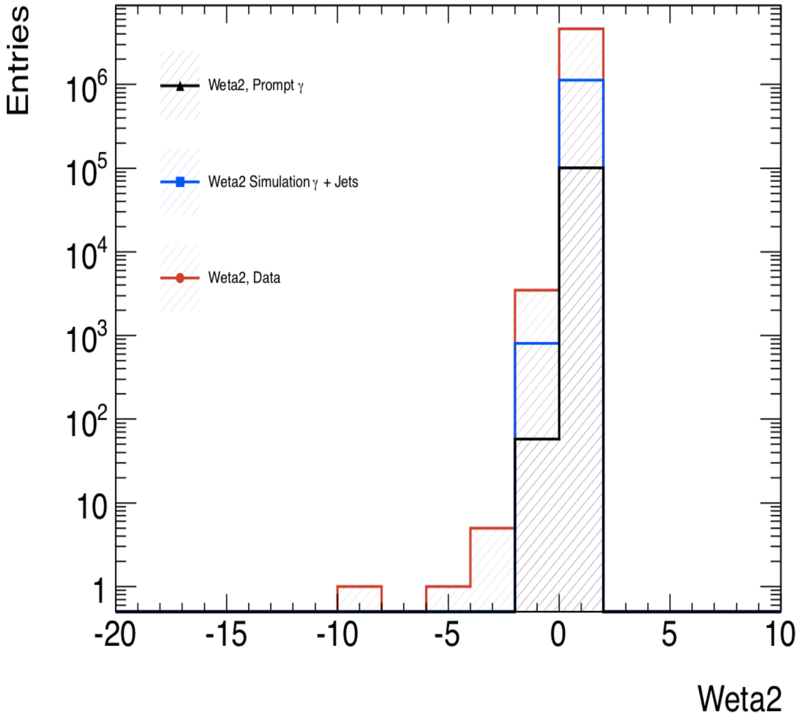

Figure 6.10. $w_{\eta 2}$ distribution for data and Monte Carlo.

- E_{ratio} : The ratio of the difference in energy associated with the largest and the second largest energy deposits over the sum of these energies. Figure 6.16 shows the E_{ratio} distribution in data and Monte Carlo.

Cuts in each of the discriminating variables are optimized to obtain maximum discrimination between true direct photons and fakes. All discrepancies between data and Monte Carlo is treated in each fiducial region as well as kinematic ranges and 'loose' or 'tight' ID tags are assigned to each photon depending on passage of these cuts.

The discrepancy between data and Monte Carlo is particularly pronounced in the R_{η} and $w_{\eta 2}$ variables and cuts in these two variables were relaxed by the difference

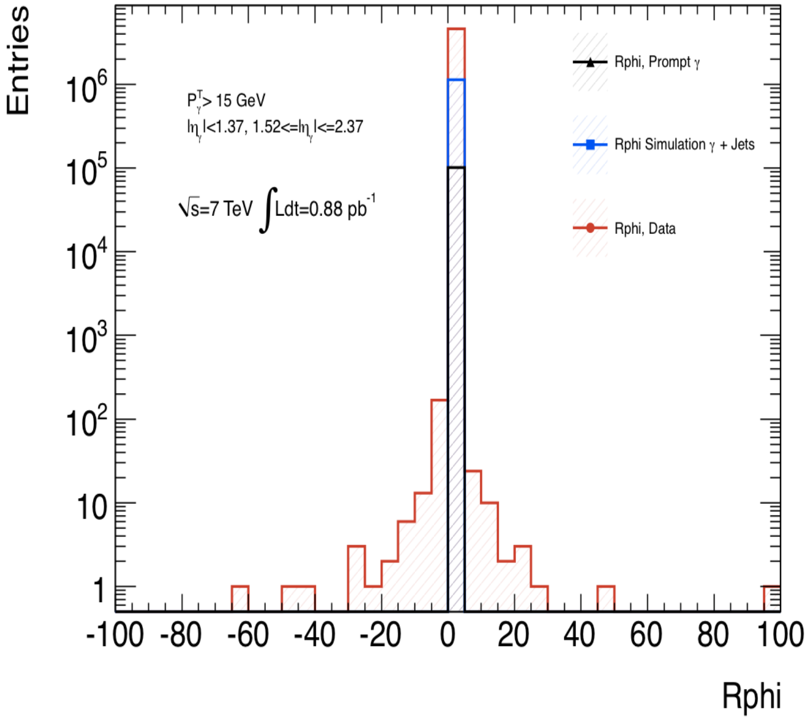

Figure 6.11. R_ϕ distribution for data and Monte Carlo.

in the mean of the distributions in data and Monte Carlo for photons that already passed the 'loose' ID cut. The ID tag thus obtained with looser selection than 'tight' is the 'robust-tight' ID for photons. For the purity calculation of photons in this analysis the robust-tight ID selection has been used. The table 6.6 shows a summary of the variables used to construct each of the 'loose', 'tight' and 'robust-tight' ID selections.

6.3.6 Photon Isolation Energy

The prompt photon signal should be more isolated from hadronic activities than photon signals arising from π^0 and other neutral hadron decays as well as photons arising from fragmentation processes and bremsstrahlung radiation. A post recon-

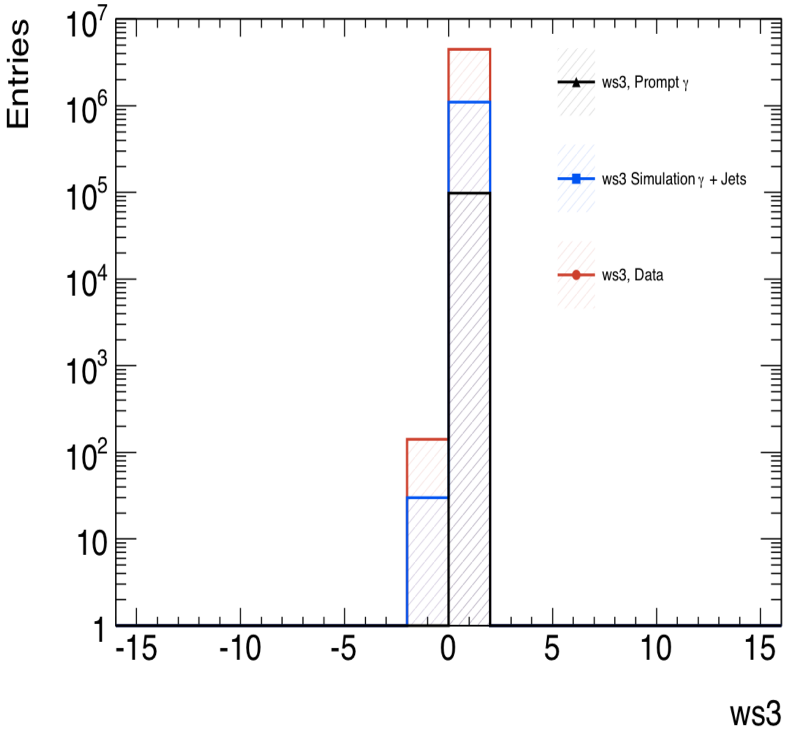

Figure 6.12. w_{S_3} distribution for data and Monte Carlo.

struction isolation variable is required to be robust enough to be linked to the parton level isolation cuts discussed earlier. The isolation variable is also used to suppress the contributions from soft jet activities as well as pileup.

The isolation variable is calculated using a fixed cone of radius 0.4 in the $\eta - \phi$ space using both the electromagnetic and the hadronic calorimeter contributions as represented in the figure 6.17. The isolation criterion can be given as,

$$E_T^{isolation}(R) < \epsilon_f E_T^{\gamma} \tag{6.1}$$

with the isolation energy within the cone of R = 0.4 is required to be less than a fraction of the transverse energy of the photon. The energy contribution due to leakage from outside a region of 5 × 7 in cells is estimated using single particle

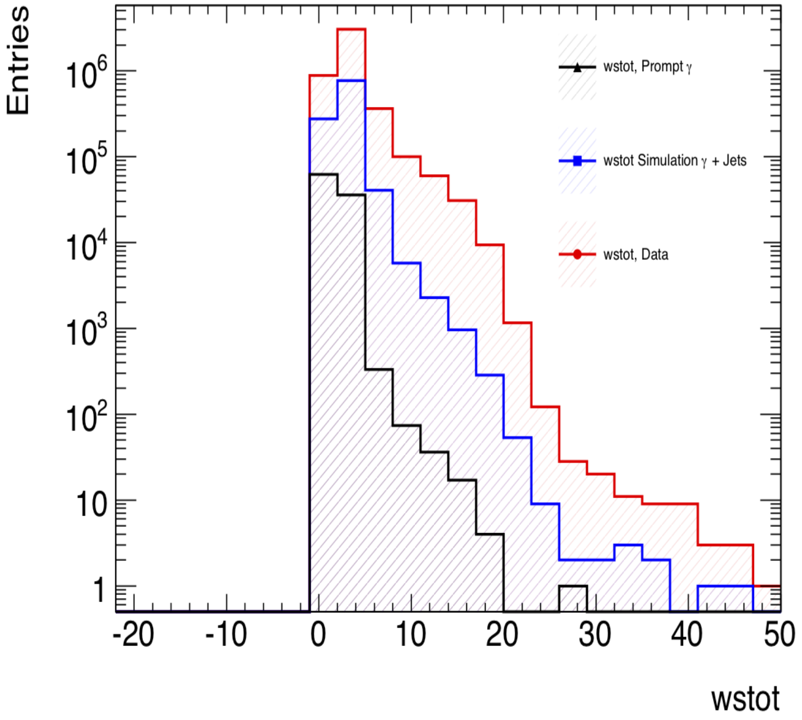

Figure 6.13. $w_{s_{tot}}$ distribution for data and Monte Carlo.

Monte Carlo simulations and this energy is subtracted from the energy measured in the isolation cone defined above. The plot of the energy leakage calculated using true photons versus the transverse energy of the photons is shown in figure 6.18 (cite http://cdsweb.cern.ch/record/1296264 http://cdsweb.cern.ch/record/1296262). Figure 6.19 shows the isolation distribution using the corrected isolation variable in data and Monte Carlo with simulated prompt photons and Monte Carlo with photons and jets mixed. The same distribution is shown in figure 6.20 with the 'robust-tight' (henceforth referred to as 'tight') photon identification requirement.

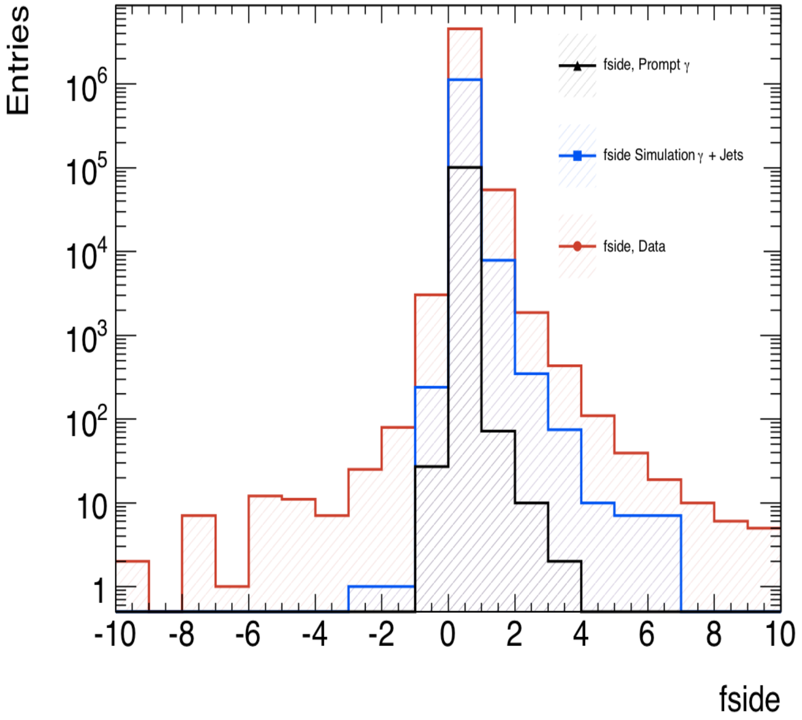

Figure 6.14. F_{side} distribution for data and Monte Carlo.

6.3.7 Jet Selection And Cleaning From Data

To estimate the $Z(\nu\nu)$ + jets contribution to SUSY the extraction of the ratio of Z + jets versus γ + jets needed to be performed in bins of the associated jet multiplicity. To do so a clean sample of jets needed to be selected in data in accordance with the cuts applied to investigate SUSY. For this analysis jets reconstructed using the AntiKt algorithm (cite arXiv:1009.5908v2 [hep-ex]) that uses topological clusters in calorimeter with the jet-core and constituent cluster distance of 0.4 has been used. Due to effects originating from calorimeter noise as well as jets originating from fragmentation processes the following cleaning and selection cuts were performed on jets and the jets were rejected:

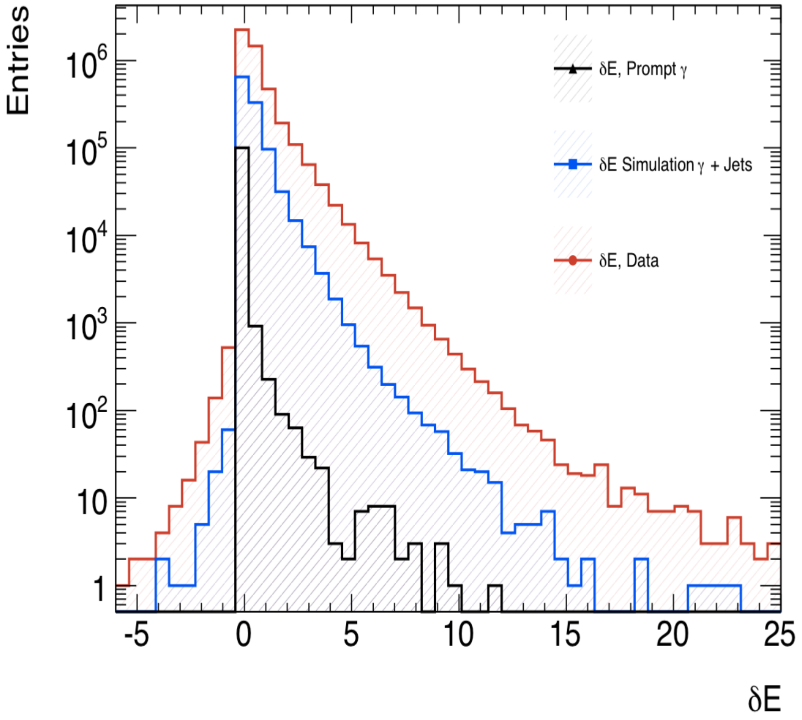

Figure 6.15. ΔE distribution for data and Monte Carlo.

- A signal is considered consistent with sporadic noise in the hadronic endcap calorimeter if the fraction of energy in the hadronic endcap calorimeter is larger than 0.8 and the number of cells containing 90% of the energy is less than six.

- A veto is applied depending on the correlation between the fraction of the energy contained in the hadronic endcap calorimeter and the fraction of the jet energy in the LAr calorimeter cells flagged as problematic. This occurs when the noise as described above coincides with real energy deposition in the cells.

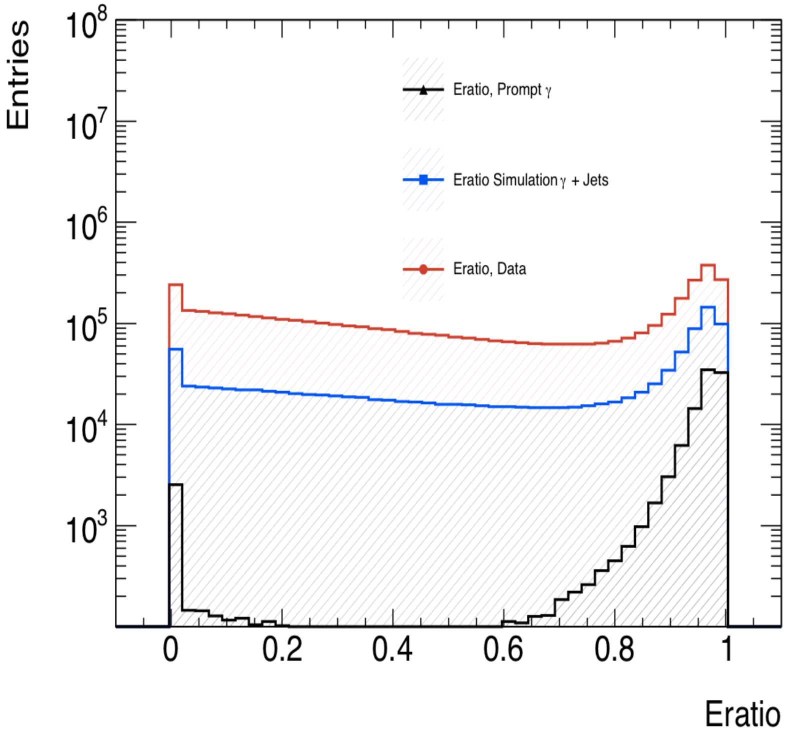

Figure 6.16. E_{ratio} distribution for data and Monte Carlo.

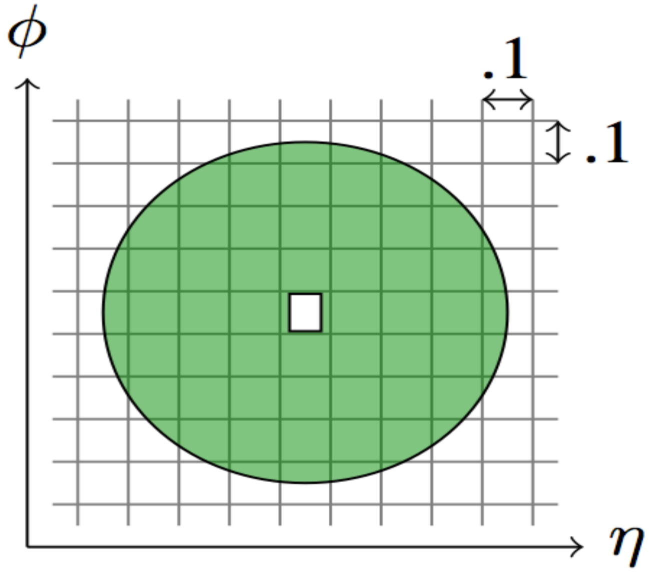

Figure 6.17. Isolation Energy Measured In $\eta - \phi$ Space With Radius =4.

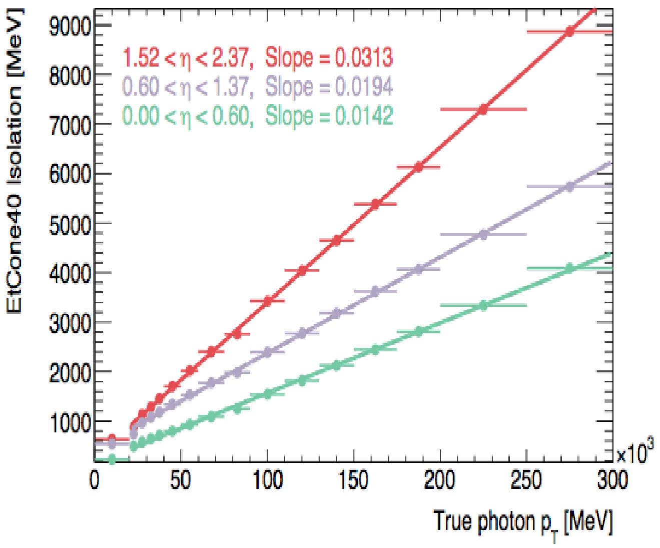

Figure 6.18. Isolation Energy Measured In $\eta - \phi$ Space With Radius =4.

- A jet with energy-squared-weighted time difference of more than 50 ns from the expected mean value is rejected.

- A jet with the electromagnetic fraction larger than 0.95 with a pulse shape distinctly different from the expected signal consistent with noise in the electromagnetic calorimeter is rejected.

- A jet with 90% of the energy in fewer than six cells and less than 5% of the total energy in the electromagnetic calorimeter is considered to be originating from a cosmic ray or a beam halo muon and are rejected.

After the above cuts are made different kinematic and fiducial cuts on jets are made depending on the signal for which the background estimation is being performed. After the selection of jets, the surviving jets and photons are compared for

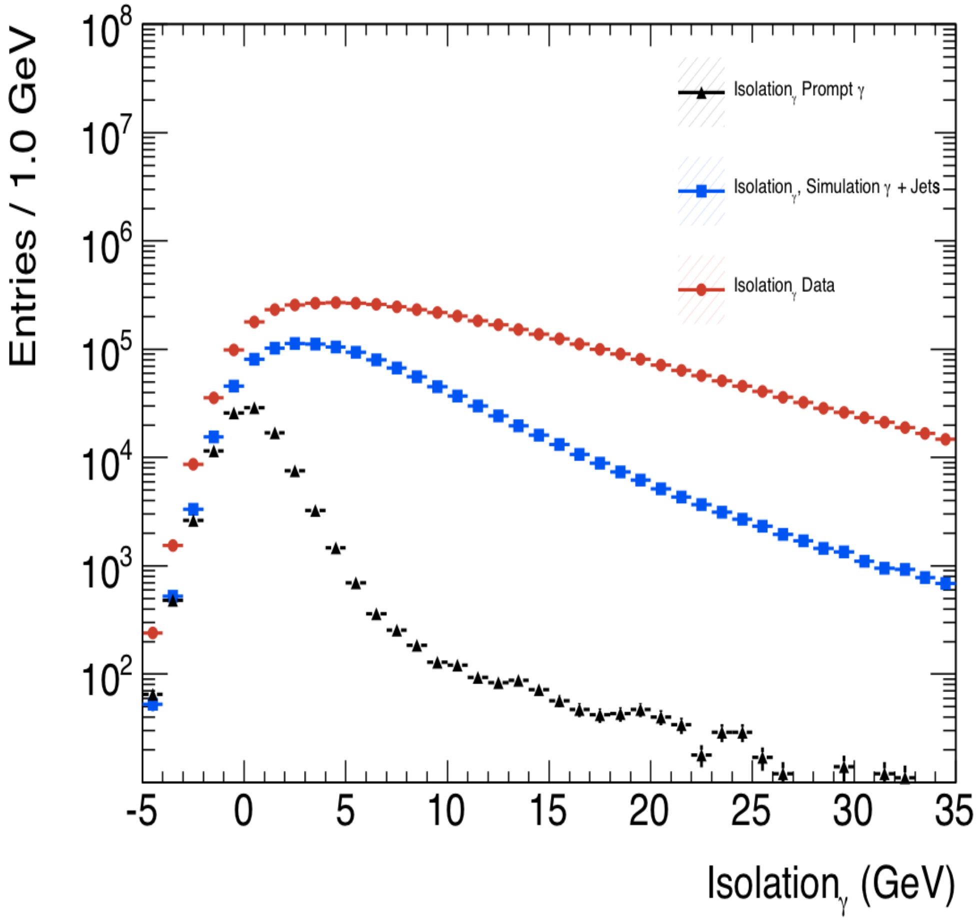

Figure 6.19. Isolation Energy In Data and Monte Carlo Without ID Cut.

overlap. If a jet is found within a cone of 0.4 of a selected photon, this jet is also rejected.

6.3.8 Photon Distributions For Exclusive Jet Selections

After the above selections are made distributions of photons are obtained for each of the jet multiplicities of 1, 2, 3 and greater than or equal to 4 jets. In this section distributions obtained for the photon transverse momentum (energy) in data for photons without purity selections and photons with the tight ID requirement as

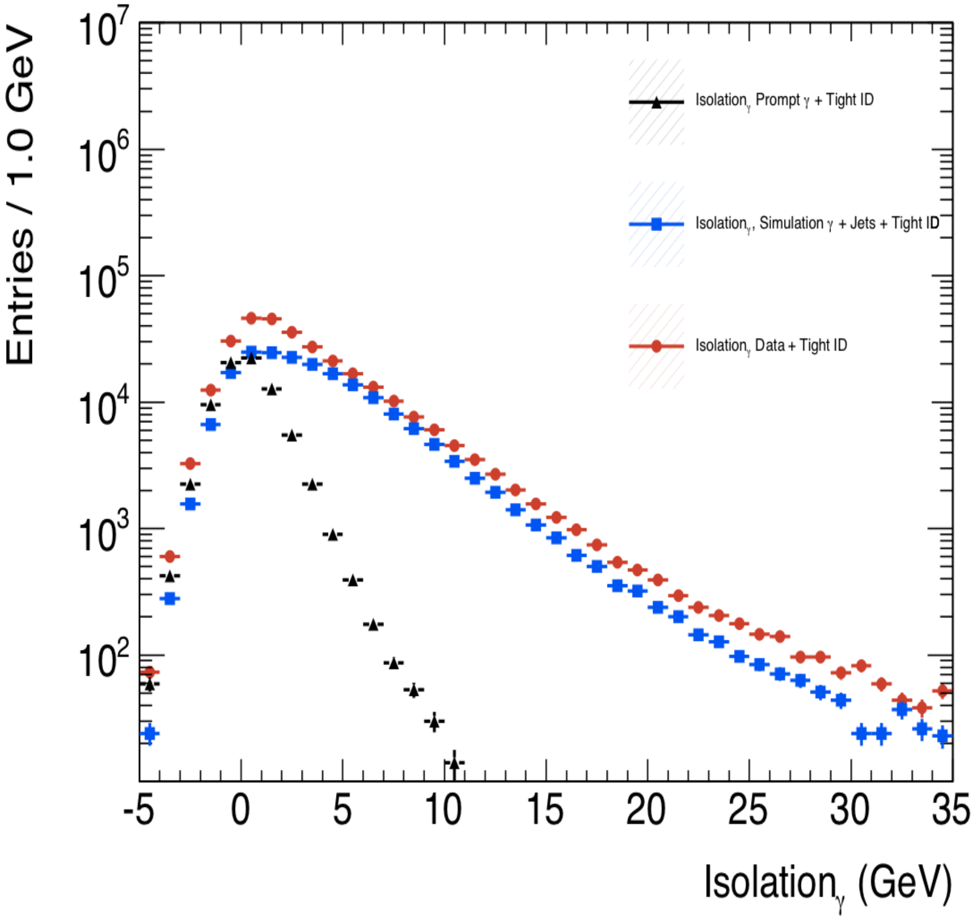

Figure 6.20. Isolation Energy In Data and Monte Carlo With Tight ID Cut.

well as an isolation energy cut of less than 3 GeV are shown for each of the selected jet multiplicity bins.

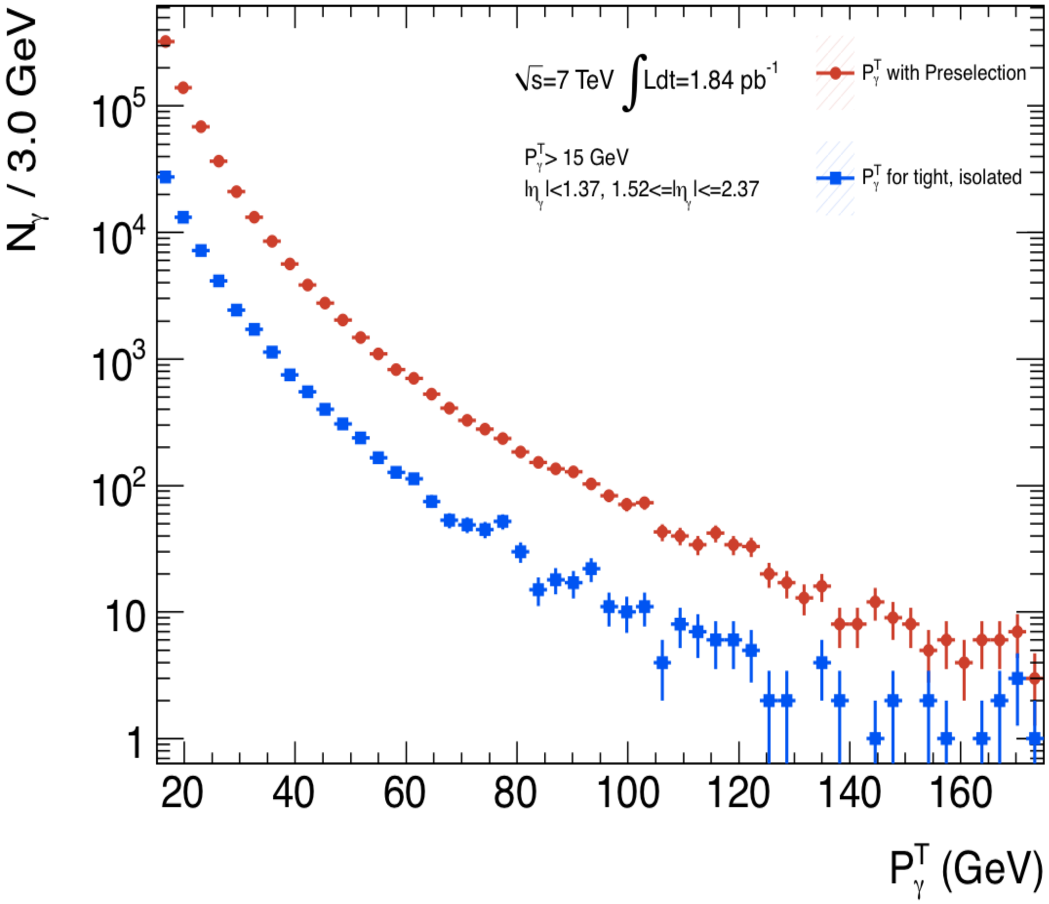

Figure 6.21. Inclusive Photon p_T Distribution In Data For Preselected and Pure Photons .

Figure 6.21 shows the distribution of photons, preselected from data after fiducial and kinematic cuts in red compared with the photons obtained after the above requirements and tight ID and isolation requirements, as a function of the ph ton transverse momentum. No selection on jets have been made.

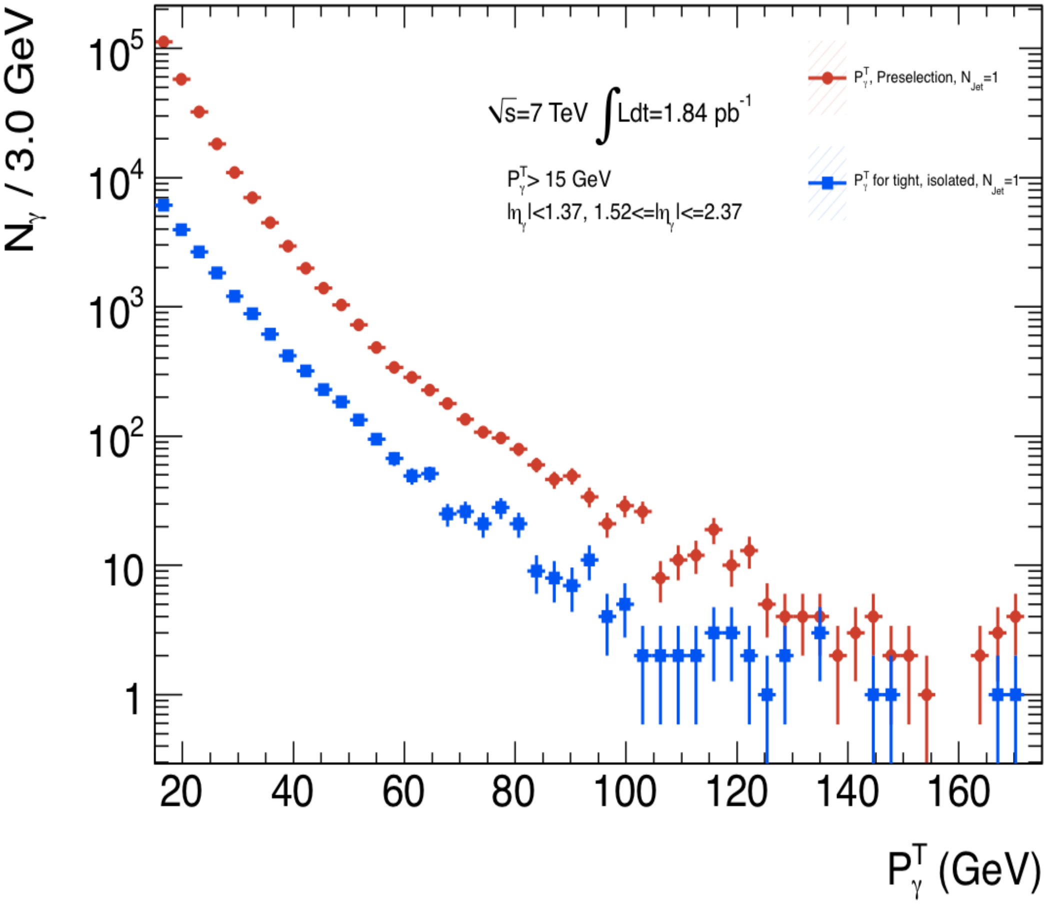

Figure 6.22. Photon p_T Distribution In Data For Preselected and Pure Photons After Selecting One Exclusive Jet.

Figure 6.22 shows the distribution of photons, preselected from data after fiducial and kinematic cuts in red compared with the photons obtained after the above requirements and tight ID and isolation requirements, as a function of the ph ton transverse momentum after requiring exactly ONE jet that passes all jet cleaning and selection criteria.

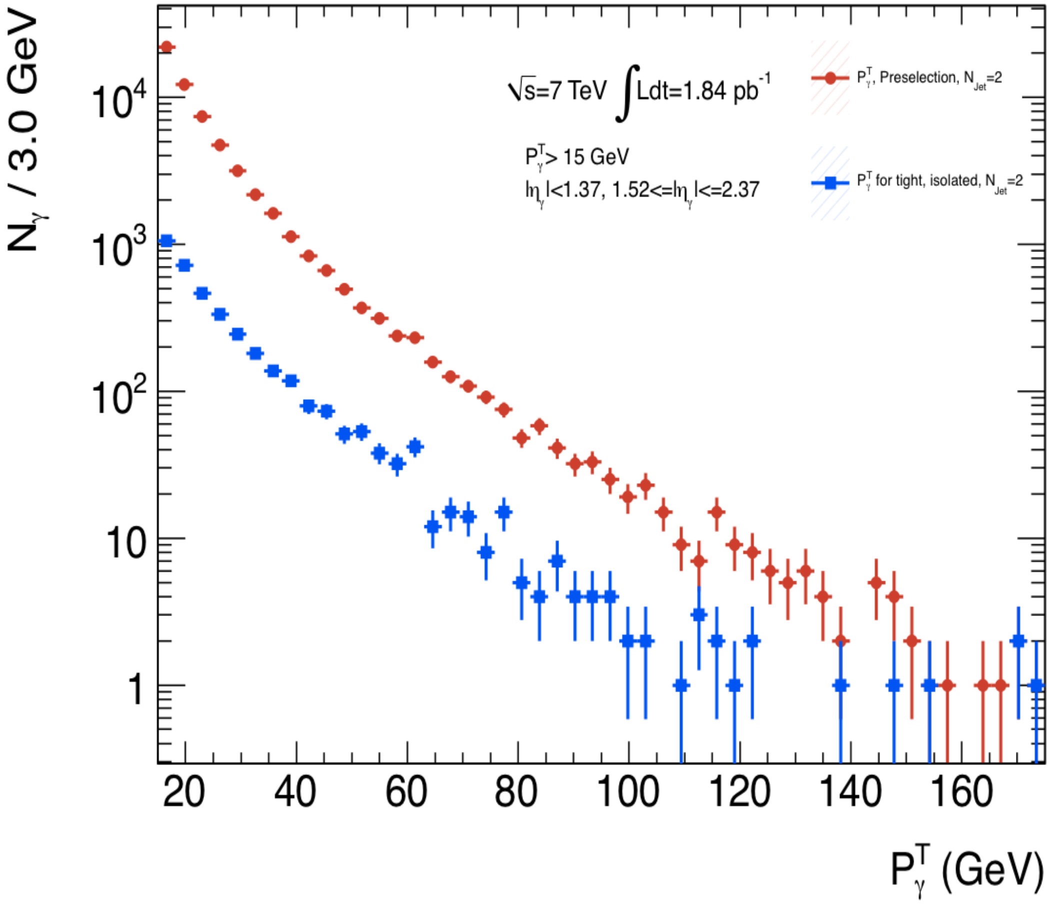

Figure 6.23. Photon p_T Distribution In Data For Preselected and Pure Photons After Selecting Two Exclusive Jets.

Figure 6.23 shows the distribution of photons, preselected from data after fiducial and kinematic cuts in red compared with the photons obtained after the above requirements and tight ID and isolation requirements, as a function of the photon transverse momentum after requiring exactly TWO jets that passes all jet cleaning and selection criteria.

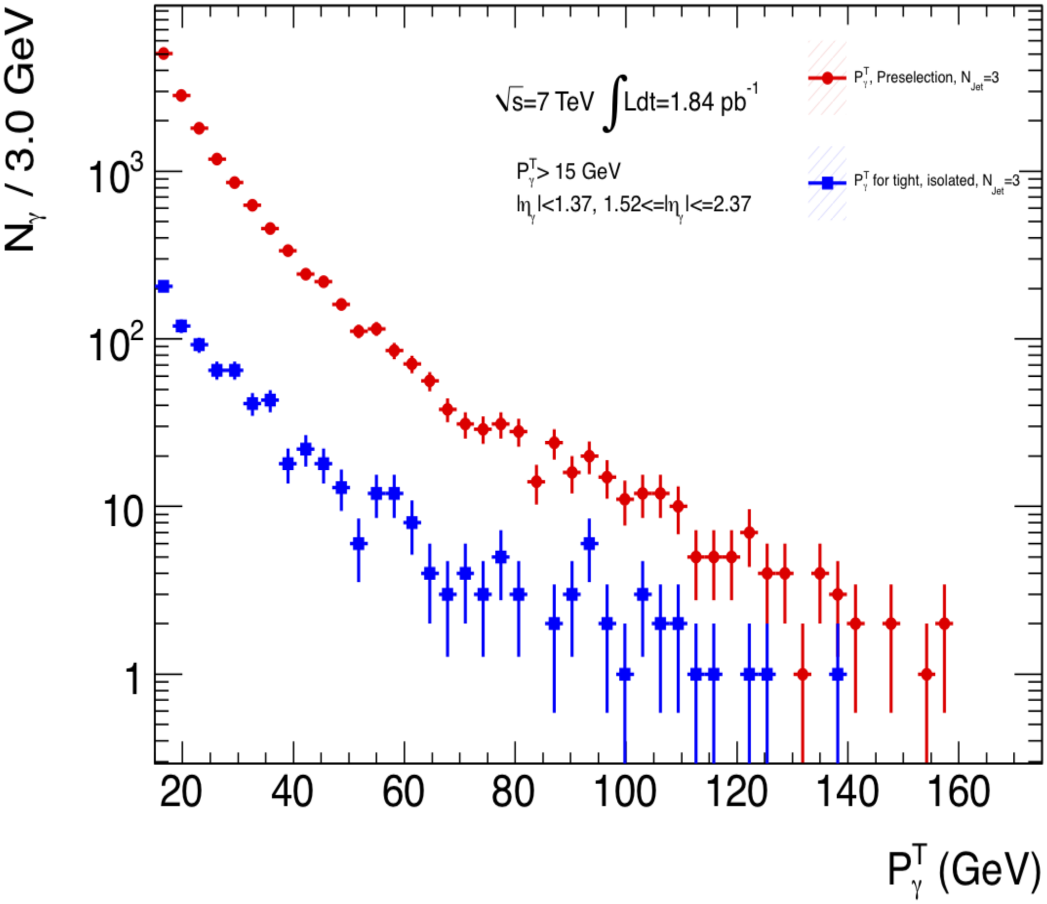

Figure 6.24. Photon p_T Distribution In Data For Preselected and Pure Photons After Selecting Three Exclusive Jets.

Figure 6.24 shows the distribution of photons, preselected from data after fiducial and kinematic cuts in red compared with the photons obtained after the above requirements and tight ID and isolation requirements, as a function of the photon transverse momentum after requiring exactly THREE jets that passes all jet cleaning and selection criteria.

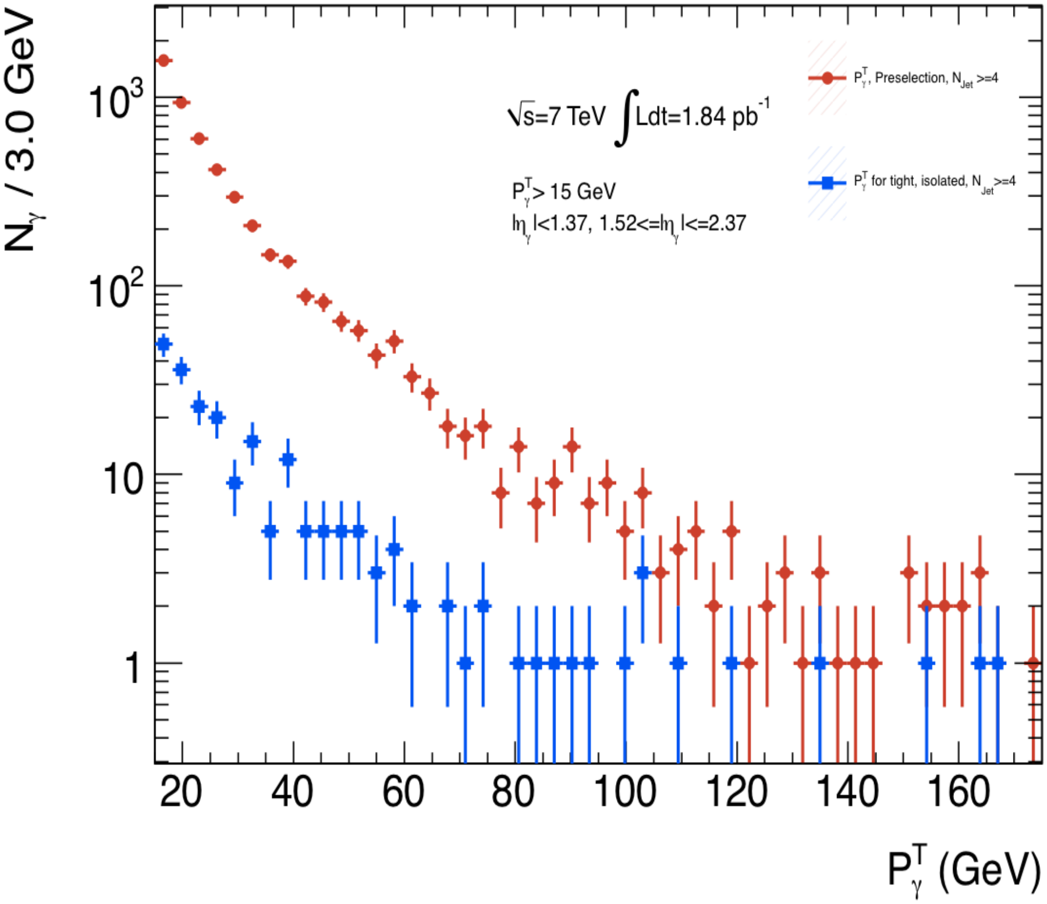

Figure 6.25. Photon p_T Distribution In Data For Preselected and Pure Photons After Selecting Four Or More Exclusive Jets.

Figure 6.25 shows the distribution of photons, preselected from data after fiducial and kinematic cuts in red compared with the photons obtained after the above requirements and tight ID and isolation requirements, as a function of the photon transverse momentum after requiring FOUR OR MORE jets that passes all jet cleaning and selection criteria.

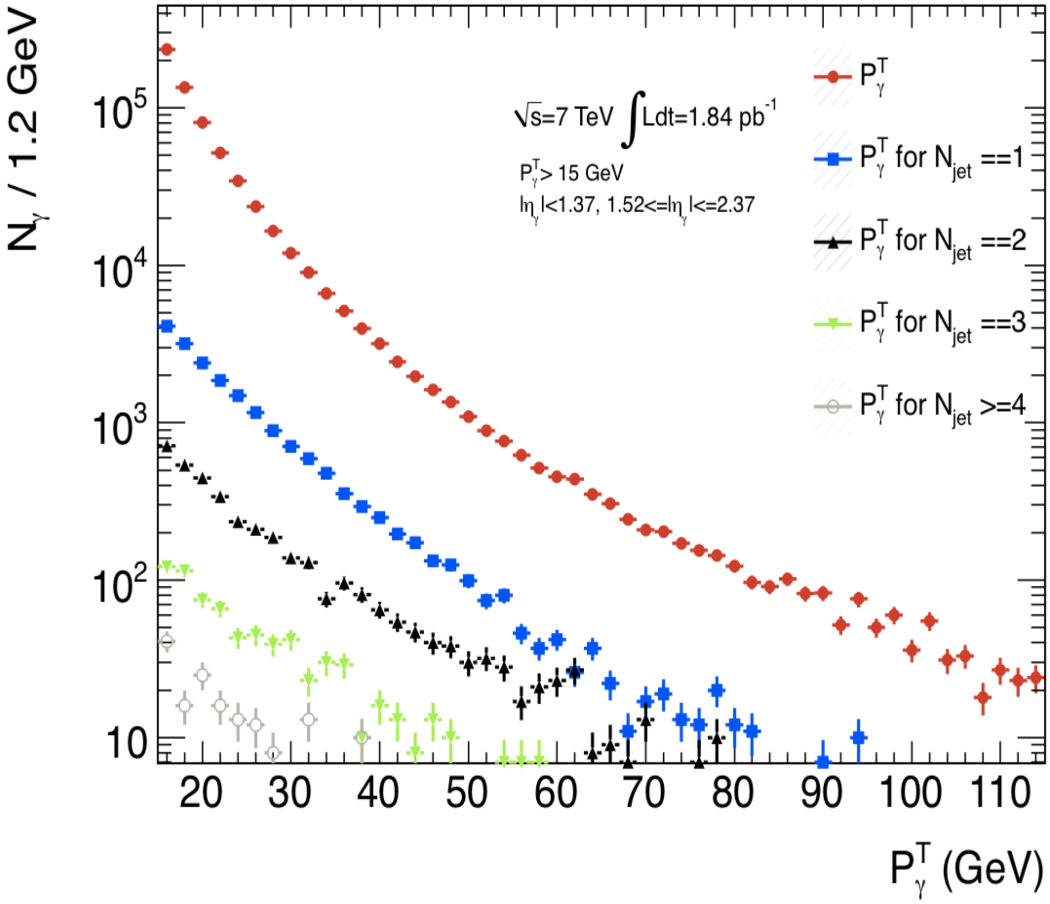

Figure 6.26. Photon p_T Distribution In Data For Preselected and Pure Photons For All Jet Selections .

Figure 6.26 shows the distribution of photons obtained after the fiducial, kinematic as well as tight ID and isolation requirements are made, as a function of the photon transverse momentum for all the different selections shown before.

6.3.9 Isolated Prompt Photon Yield

To obtain isolated prompt photons the following selections are defined in line with the previously defined cuts:

- Signal region : photons passing the tight (robust-tight) ID selection criterion as well as an isolation energy of $E_T^{isolation} < 3$ GeV
- Background region : photons that fail both the tight ID and have an isolation energy of $E_T^{isolation} > 5$ GeV

To obtain a pure photon signal yields and purity a counting method is used. Due to lack of statistics the following η and p_T ranges are defined :

- η ranges : $|\eta_{S2}| < 0.6$ (little material in front of EM calo), $0.6 \leq |\eta_{S2}| < 1.37$ (rest of barrel), $1.52 \leq |\eta_{S2}| < 1.8$ and $1.8 \leq |\eta_{S2}| < 2.37$ (endcap)
- p_T ranges : [15,20), [20,25), [25,30), [30,35), [35,40), [40,50), [50,60), [60,100) all measured in GeV

6.4 Photon Purity Measurements From Data

Once a spectrum of tight, isolated photons are obtained, one needs an estimate of the purity of the sample so obtained. This requires estimating the background that still passes the tight and isolation cuts. To do this a data driven counting technique is applied. Given that isolation and tight ID are uncorrelated variables (based on different detector observables) a side-band method involving rectangular cuts on the ID and isolation variable to extract photon purity is applied.

6.4.1 The Counting or Side-Band Method For Pure Photon Yield Extraction

As in figure 6.27 a signal region (A) versus three background regions (B, C, D) are defined such that:

- Region A contains photons that pass the tight ID selection as well as an isolation cut of $E_T^{\gamma} < 3$ GeV
- Region B contains photons that pass the tight ID selection but has an isolation cut of $E_T^{\gamma} > 5$ GeV
- Region C contains photons that fail the tight ID selection but has an isolation cut of $E_T^{\gamma} < 3$ GeV
- Region D contains photons that fail the tight ID selection and has an isolation cut of $E_T^{\gamma} > 5$ GeV

This renders a region A rich in signal with regions B, C and D rich in background. Now the background contribution in region A (N_A^{bkg}) can be expressed as,

$$\frac{N_A^{bkg}}{N_B^{bkg}} = \frac{N_C^{bkg}}{N_D^{bkg}} \tag{6.2}$$

Now, as B, C and D are background rich regions the following assumption is made,

$$\begin{aligned} N_B^{bkg} &= N_B^{obs} \\ N_C^{bkg} &= N_C^{obs} \\ N_D^{bkg} &= N_D^{obs} \end{aligned} \tag{6.3}$$

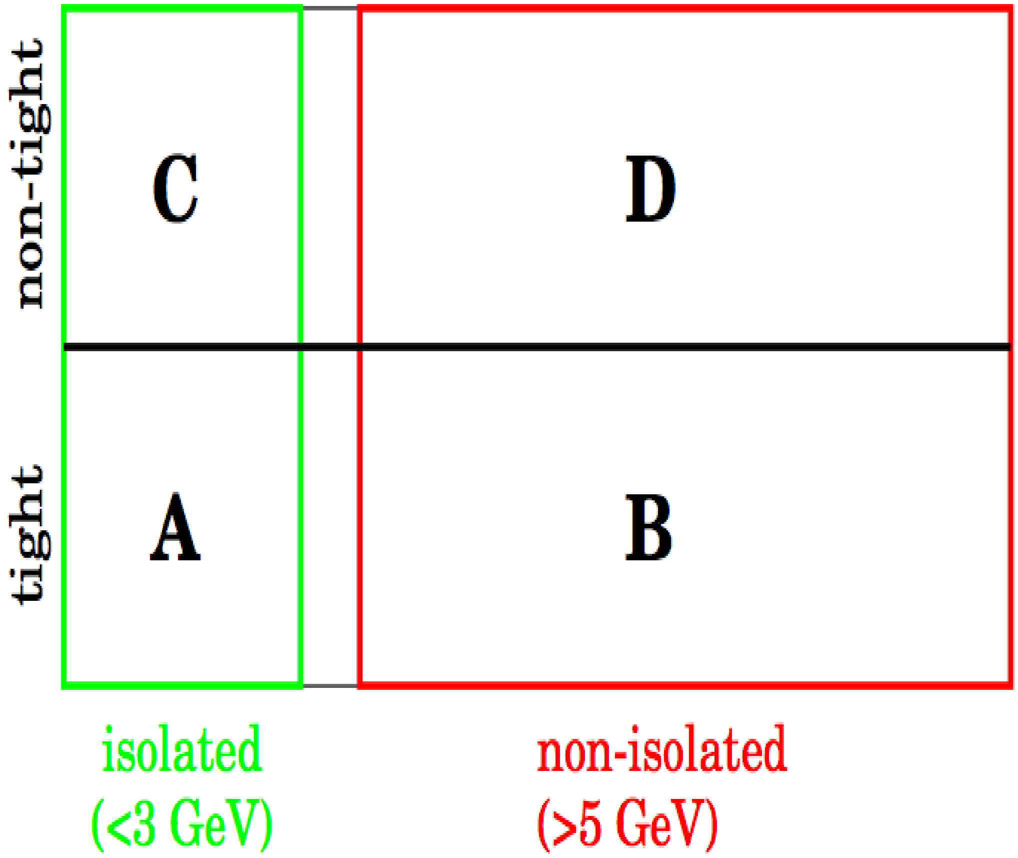

Figure 6.27. Diagrammatic Representation Of the Sideband Method.

The pure signal yield in region A can be defined as,

$$N_A^{sig} = N_A^{obs} - N_A^{bkg} \tag{6.4}$$

Now combining equations 6.2 and 6.3 gives the pure photon signal yield N_A^{sig} as,

$$N_A^{sig} = N_A^{obs} - N_B^{obs} \times \frac{N_C^{obs}}{N_D^{obs}} \tag{6.5}$$

The purity of the photon sample in signal region can be defined as,

$$P^{\gamma}_{signal} = 1 - \left(\frac{N^{obs}_{B}}{N^{obs}_{A}} \frac{N^{obs}_{C}}{N^{obs}_{D}} \right) \tag{6.6}$$

The signal yield and purity is calculated for each of the fiducial regions in each bin of the photon transverse momentum for each multiplicity of jets and is reported in the next section.

6.4.2 Purity Results From Side-Band Counting Method

The signal yield (N^{sig}_{A}) and purity (P^{γ}_{signal}) of the photon from data was obtained using the sideband counting method described in the previous section. The results for each jet bin including the inclusive jet bin is given below. Table 6.7 shows the signal yield for the inclusive jets.

The errors shown are only statistical while table 6.8 shows the purity of signal for the inclusive jet case.

The results are shown for each bin of transverse momentum and pseudorapidity as in table 6.4. Figures, 6.28, 6.30, 6.32, 6.34 show the signal purity for each of the pseudorapidity bins for the inclusive jet selections. Figures 6.29, 6.31, 6.33 and 6.35 show the photon yield after the tight and isolation requirements in each pseudorapidity interval for all inclusive jets.

Table 6.9 and 6.10 show the yield and the purity numbers for each fiducial cut in each transverse momentum bin for one exclusively selected jet.

Table 6.11 and 6.12 show the yield and the purity numbers for each fiducial cut in each transverse momentum bin for two exclusively selected jets.

Table 6.13 and 6.14 show the yield and the purity numbers for each fiducial cut in each transverse momentum bin for three exclusively selected jets.

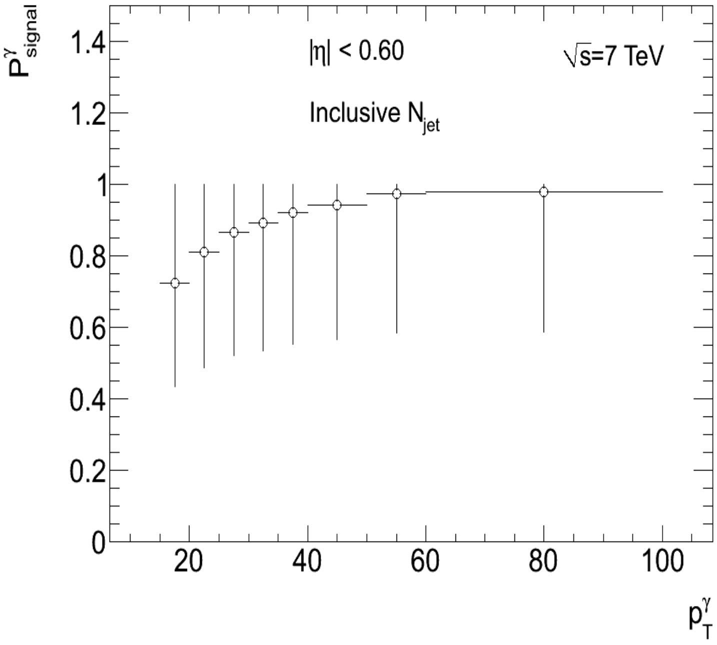

Figure 6.28. Photon Purity With Inclusive Jets For $|\eta| < 0.60$.

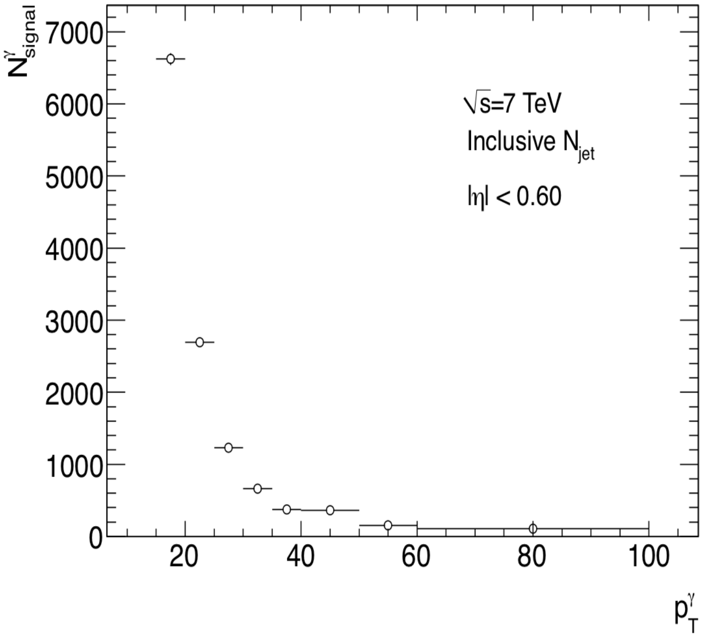

Figure 6.29. Photon Yield With Inclusive Jets For $|\eta| < 0.60$.

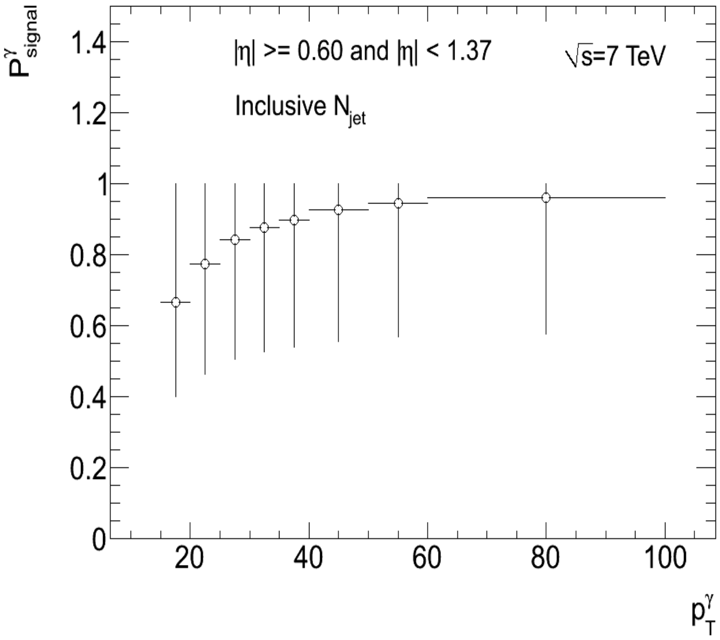

Figure 6.30. Photon Purity With Inclusive Jets For $0.60 <= |\eta| < 1.37$.

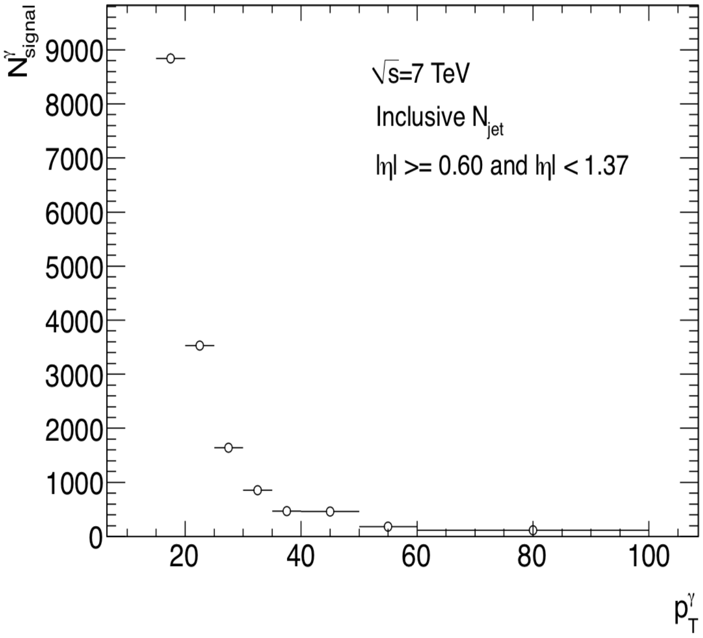

Figure 6.31. Photon Yield With Inclusive Jets For $0.60 <= |\eta| < 1.37$.

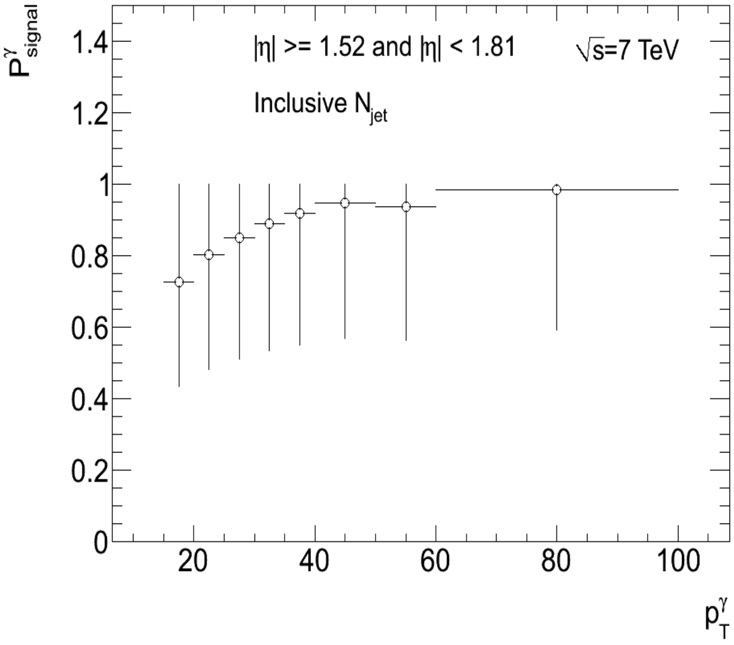

Figure 6.32. Photon Purity With Inclusive Jets For 1.52 <= $|\eta| < 1.81$.

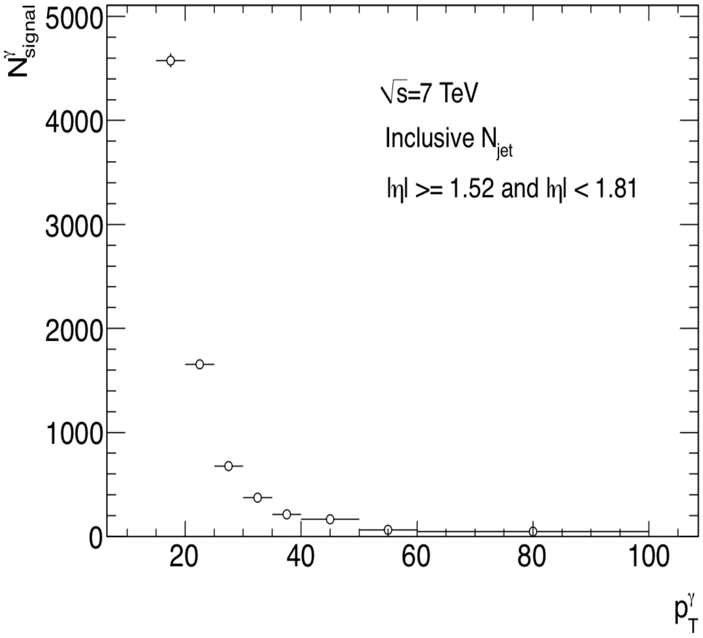

Figure 6.33. Photon Yield With Inclusive Jets For 1.52 <= $|\eta| < 1.81$.

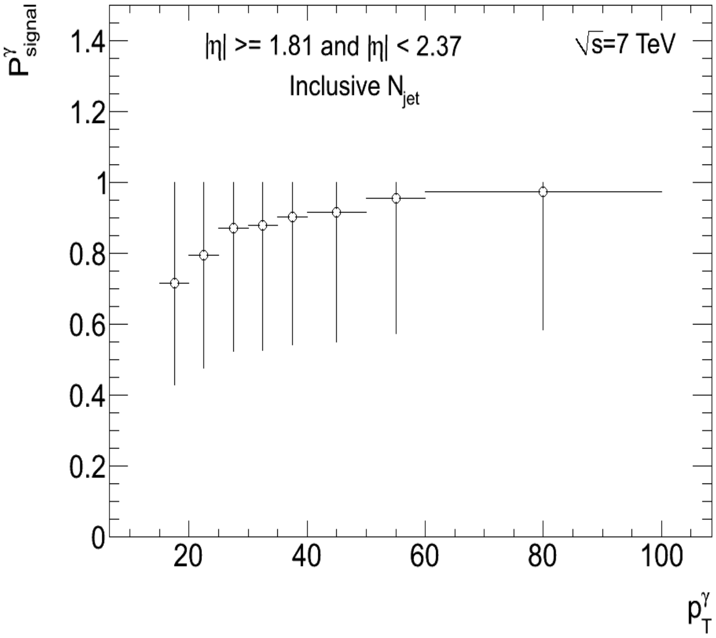

Figure 6.34. Photon Purity With Inclusive Jets For 1.81 <= $|\eta|$ < 2.37 .

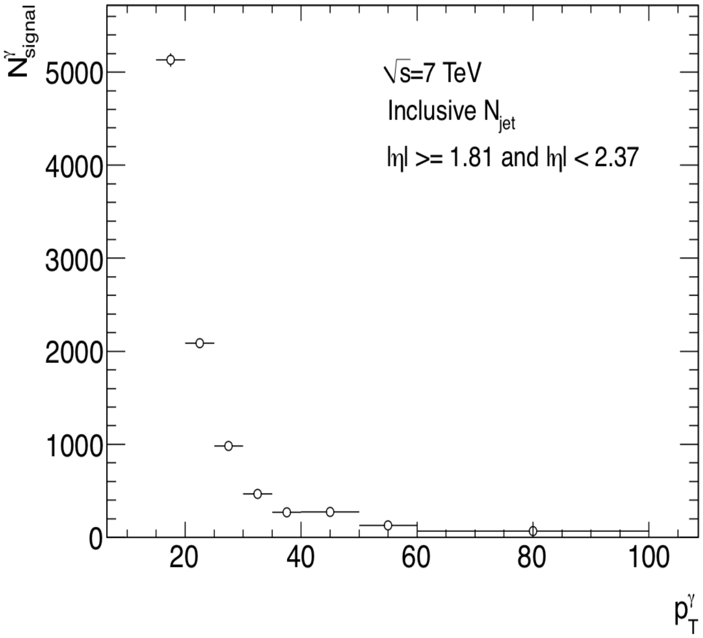

Figure 6.35. Photon Yield With Inclusive Jets For 1.81 <= $|\eta|$ < 2.37 .

Tables 6.15 and 6.16 show the yield and the purity numbers for each fiducial cut in each transverse momentum bin for four or more selected jets.

6.5 Pure Photon Signal Yield From Side-Band Method

The signal yield calculated in the previous section gives the total number of signal photons. The purity gives the fraction of the selected tight isolated signal that is faked by the background. The 'true' signal yield is then calculated by,

$$\frac{N^{\gamma}_{signal}}{\Delta p^{\gamma}_{T}} = P^{\gamma}_{signal} \times \frac{N^{sig}_{A}}{\Delta p^{\gamma}_{T}} \tag{6.7}$$

Table 6.17 shows the total yield for pure photons per bin of transverse momentum and pseudorapidity, given by the signal yield multiplied by the corresponding purity of the signal for the inclusive jet case. Table 6.18 shows the true signal yield for the pure photons per bin of transverse momentum and pseudorapidity after an exclusive selection of one jet. Table 6.19 shows the true signal yield for the pure photons per bin of transverse momentum and pseudorapidity after an exclusive selection of two jets. Table 6.20 shows the true signal yield for the pure photons per bin of transverse momentum and pseudorapidity after an exclusive selection of three jets. Table 6.21 shows the true signal yield for the pure photons per bin of transverse momentum and pseudorapidity after a selection of four or more jets.

6.6 Photon Efficiency Measurement

The 'true' photon yield needs to be unfolded for all the detector level selections and cuts that have been applied to data to obtain the 'true' photon distribution. In this analysis, the efficiencies are all estimated by using Monte Carlo truth information in the full range of pseudorapidity. The photon yield can be written as,

$$\Delta N^{reco} = \left(\int \mathcal{L}\mathrm{d}x\right)\epsilon_{trigger}\epsilon_{ID}\epsilon_{reco}\Delta P_T^{true}\left(\frac{\Delta N^{isolated}}{\Delta E_T^{true}}\right) \tag{6.8}$$

where, the left hand side of 6.8 can be given as,

$$\begin{aligned} \Delta N^{reco} &= P^{\gamma}_{signal}N_A^{signal} \\ &= N^{\gamma}_{signal} \end{aligned} \tag{6.9}$$

in accordance with 6.7. The final number to be obtained is the last term in equation 6.8. For that each of the efficiencies are defined and determined as follows.

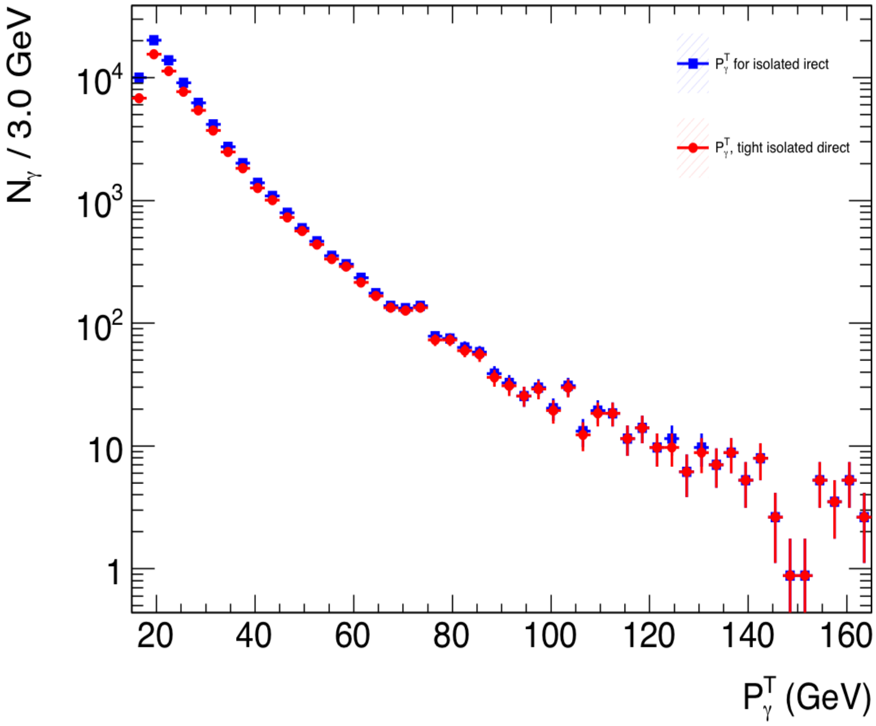

Figure 6.36. Isolated p_T^γ with and without tight ID selection.

6.6.1 Photon Identification Efficiency

The photon identification efficiency is determined from Monte Carlo using the following definition,

$$\epsilon_{ID} \equiv \frac{\mathrm{d}N^\gamma(E_{T,reco}^{isolation} < 3GeV, tight - ID)/\mathrm{d}E_{T,reco}^\gamma}{\mathrm{d}N^\gamma(E_{T,reco}^{isolation} < 3GeV)/\mathrm{d}E_{T,reco}^\gamma} \tag{6.10}$$

Figure 6.36 shows the distribution of reconstructed photon transverse momentum with tight-ID as well as isolation selections compared with photon transverse momentum with isolation selection.

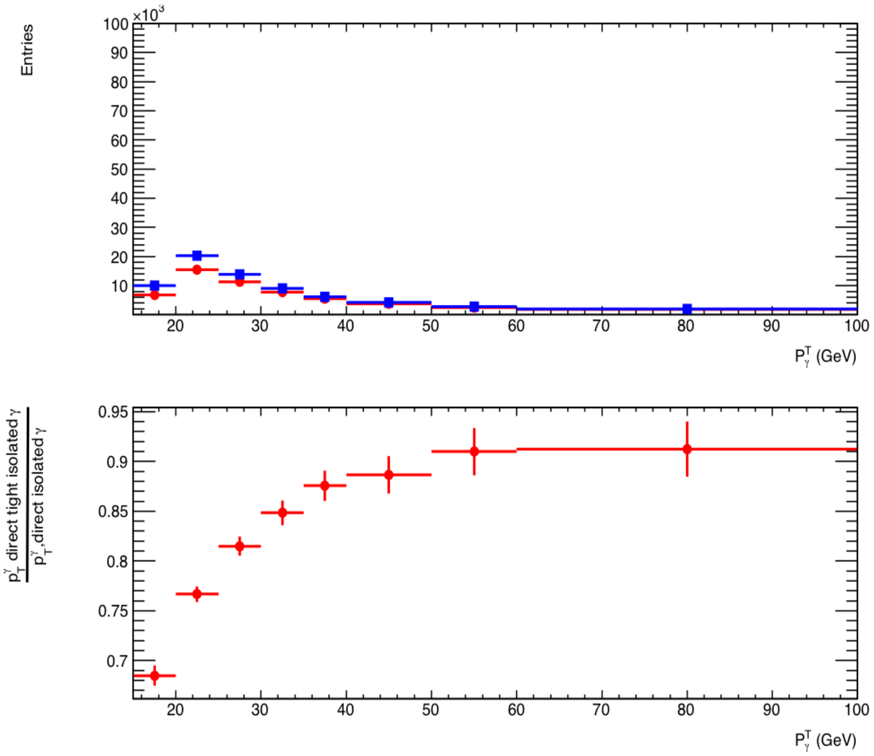

Figure 6.37. Isolated p_T^γ with and without tight ID selection re-binned with efficiency per bin.

Figure 6.37 shows the same plot as above re-binned in the bins of transverse momentum of the photon together with the photon ID efficiency calculated for each bin.

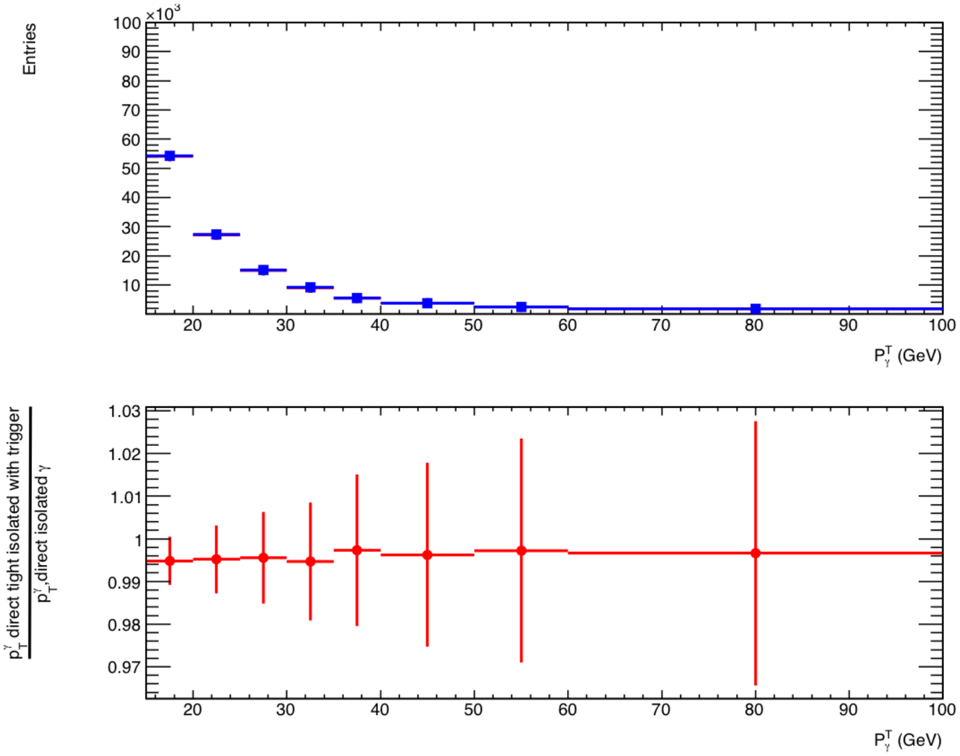

Figure 6.38. Isolated p_T^γ with tight ID and trigger compared to the same selection without trigger showing efficiency per bin.

6.6.2 Photon Trigger Efficiency

The photon trigger efficiency is measured using data with photons that pass the ID and the isolation requirements. The trigger efficiency can be defined as,

$$\epsilon_{Trigger} \equiv \frac{\mathrm{d}N^\gamma(E_{T,reco}^{isolation} < 3GeV, tight - ID, trigger)/\mathrm{d}E_{T,reco}^\gamma}{\mathrm{d}N^\gamma(E_{T,reco}^{isolation} < 3GeV, tight - ID)/\mathrm{d}E_{T,reco}^\gamma} \tag{6.11}$$

The trigger selection in data and Monte Carlo was consistent with the event filter level electromagnetic trigger with a threshold of 10 GeV. The figure 6.38

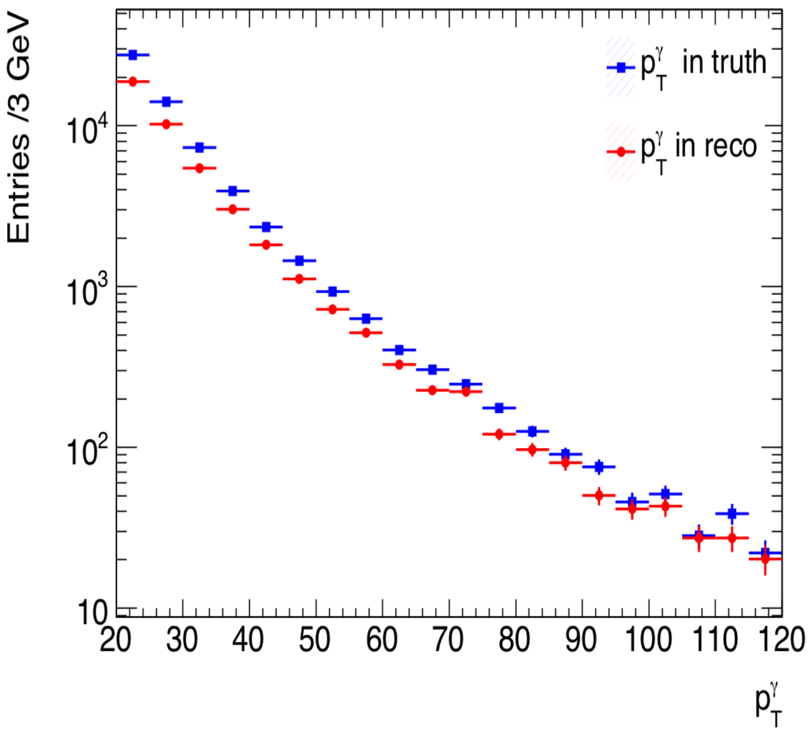

Figure 6.39. True p_T^γ with reconstruction level isolation compared with true p_T^γ with truth level isolation.

6.6.3 Photon Reconstruction Efficiency

The photon reconstruction efficiency is measured on signal Monte Carlo as a function of the true photon transverse momentum. The reconstruction efficiency is defined as,

$$\epsilon_{reco} \equiv \frac{\mathrm{d}N^\gamma(E_{T,reco}^{isolation} < 3GeV)/\mathrm{d}E_{T,true}^\gamma}{\mathrm{d}N^\gamma(E_{T,true}^{isolation} < 5GeV)/\mathrm{d}E_{T,true}^\gamma} \tag{6.12}$$

The efficiencies of the dead optical connection, material defects in the detector, pileup are all folded in the reconstruction efficiency. Figure 6.39 shows the reconstructed photon transverse momentum distribution against the true photon transverse momentum.

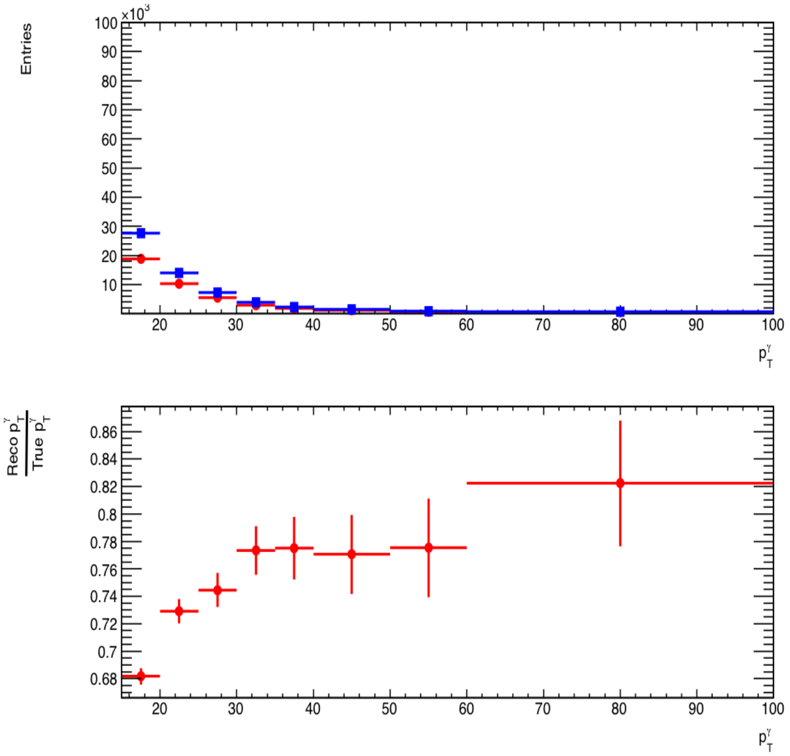

Figure 6.40. True p_T^γ with reconstruction level isolation compared with true p_T^γ with truth level isolation showing reconstruction efficiencies per bin.

Figure 6.40 shows the comparison of the true transverse momentum distribution in signal Monte Carlo with a reconstruction level isolation cut of 3 GeV compared with the true transverse momentum distribution of the photon with an isolation selection of 5 GeV on the true photon.

Table 6.5. Photon yield after every cut for some typical runs

	No Cuts	GRL	Vtx	Trig	OTX	GRL $\cap$ Trig	Grl $\cap$ Trig $\cap$ Vtx	Grl $\cap$ Trig $\cap$ Vtx
Run Number : 153200								
Loose	13	12	12	12	12	12	12	11
Tight	0	0	0	0	0	0	0	0
Robust	1	1	1	1	1	1	1	1
Run Number : 153565								
loose	1005	959	954	950	945	950	947	890
tight	214	210	210	209	199	209	209	194
Robust	257	251	251	250	242	250	250	235
Run Number : 153599								
loose	112	0	80	80	105	0	0	0
tight	29	0	23	22	29	0	0	0
Robust	33	0	27	26	33	0	0	0
Run Number : 154810								
loose	203	171	174	171	189	171	171	160
tight	43	38	38	38	40	38	38	35
Robust	52	44	44	44	47	44	44	39
Run Number : 154810								
loose	203	171	174	171	189	171	171	160
tight	43	38	38	38	40	38	38	35
Robust	52	44	44	44	47	44	44	39
Run Number : 154813								
loose	397	318	393	396	373	317	317	294
tight	68	59	68	68	63	59	59	54
Robust	81	70	81	81	76	70	70	65

Table 6.6. Summary of Discriminating Variables Used For Photon ID

Variable	loose	tight	robust-tight
η	-	✓	✓
R_{had_1}	✓	✓	✓
R_{had}	✓	✓	✓
R_η	✓	✓	loosen cut
w_{η_2}	✓	✓	loosen cut
R_ϕ	-	✓	✓
w_{S_3}	-	✓	✓
$w_{s_{tot}}$	-	✓	✓
F_{side}	-	✓	✓
ΔE	-	✓	✓
E_{ratio}	-	✓	✓

Table 6.7. Signal yield for Inclusive N_{jet}

P_T range [GeV]	$\|\eta\| < 0.60$	$0.60 \leq \|\eta\| < 1.37$	$1.52 \leq \|\eta\| < 1.81$	$1.81 \leq \|\eta\| < 2.37$
$15 \geq p_T^\gamma < 20$	6622.25 ± 81.38	8842.68 ± 94.04	4577.15 ± 67.65	5130.35 ± 71.63
$20 \geq p_T^\gamma < 25$	2693.45 ± 51.9	3528.26 ± 59.4	1654.17 ± 40.67	2084.79 ± 45.66
$25 \geq p_T^\gamma < 30$	1230.55 ± 35.08	1637.78 ± 40.47	676.63 ± 26.01	980.45 ± 31.31
$30 \geq p_T^\gamma < 35$	666.17 ± 25.81	851.87 ± 29.19	374.73 ± 19.36	465.62 ± 21.58
$35 \geq p_T^\gamma < 40$	376.57 ± 19.41	471.45 ± 21.71	213.89 ± 14.62	269.81 ± 16.43
$40 \geq p_T^\gamma < 50$	362.0 ± 19.03	461.51 ± 21.48	166.47 ± 12.9	272.18 ± 16.5
$50 \geq p_T^\gamma < 60$	155.49 ± 12.47	178.59 ± 13.36	62.8 ± 7.92	128.73 ± 11.35
$60 \geq p_T^\gamma < 100$	107.54 ± 10.37	112.44 ± 10.6	47.26 ± 6.87	64.21 ± 8.01

Table 6.8. Purity estimate for Inclusive N_{jet}

P_T range [GeV]	$\lvert\eta\rvert < 0.60$	$0.60 \leq \lvert\eta\rvert < 1.37$	$1.52 \leq \lvert\eta\rvert < 1.81$	$1.81 \leq \lvert\eta\rvert < 2.37$
$15 \geq p_T^\gamma < 20$	0.72 ± 0.29	0.67 ± 0.27	0.72 ± 0.29	0.71 ± 0.29
$20 \geq p_T^\gamma < 25$	0.81 ± 0.32	0.77 ± 0.31	0.8 ± 0.32	0.79 ± 0.32
$25 \geq p_T^\gamma < 30$	0.87 ± 0.35	0.84 ± 0.34	0.85 ± 0.34	0.87 ± 0.35
$30 \geq p_T^\gamma < 35$	0.89 ± 0.36	0.87 ± 0.35	0.89 ± 0.36	0.88 ± 0.35
$35 \geq p_T^\gamma < 40$	0.92 ± 0.37	0.9 ± 0.36	0.92 ± 0.37	0.9 ± 0.36
$40 \geq p_T^\gamma < 50$	0.94 ± 0.38	0.92 ± 0.37	0.95 ± 0.38	0.92 ± 0.37
$50 \geq p_T^\gamma < 60$	0.97 ± 0.39	0.94 ± 0.38	0.94 ± 0.37	0.95 ± 0.38
$60 \geq p_T^\gamma < 100$	0.98 ± 0.39	0.96 ± 0.38	0.98 ± 0.39	0.97 ± 0.39

Table 6.9. Signal yield for $N_{jet} = 1$

P_T range [GeV]	$\lvert\eta\rvert < 0.60$	$0.60 \leq \lvert\eta\rvert < 1.37$	$1.52 \leq \lvert\eta\rvert < 1.81$	$1.81 \leq \lvert\eta\rvert < 2.37$
$15 \geq p_T^\gamma < 20$	1565.52 ± 39.57	2098.74 ± 45.81	1113.46 ± 33.37	1015.06 ± 31.86
$20 \geq p_T^\gamma < 25$	958.69 ± 30.96	1291.07 ± 35.93	583.39 ± 24.15	647.96 ± 25.46
$25 \geq p_T^\gamma < 30$	603.52 ± 24.57	785.68 ± 28.03	297.36 ± 17.24	385.12 ± 19.62
$30 \geq p_T^\gamma < 35$	355.84 ± 18.86	462.62 ± 21.51	179.01 ± 13.38	227.88 ± 15.1
$35 \geq p_T^\gamma < 40$	217.17 ± 14.74	250.65 ± 15.83	101.4 ± 10.07	130.95 ± 11.44
$40 \geq p_T^\gamma < 50$	218.89 ± 14.79	274.3 ± 16.56	101.16 ± 10.06	141.04 ± 11.88
$50 \geq p_T^\gamma < 60$	78.83 ± 8.88	110.62 ± 10.52	33.48 ± 5.79	70.44 ± 8.39
$60 \geq p_T^\gamma < 100$	55.86 ± 7.47	63.69 ± 7.98	25.76 ± 5.08	28.97 ± 5.38

Table 6.10. Purity estimate for $N_{jet} = 1$

P_T range [GeV]	$\lvert\eta\rvert < 0.60$	$0.60 \leq \lvert\eta\rvert < 1.37$	$1.52 \leq \lvert\eta\rvert < 1.81$	$1.81 \leq \lvert\eta\rvert < 2.37$
$15 \geq p_T^\gamma < 20$	0.7 ± 0.28	0.64 ± 0.26	0.72 ± 0.29	0.68 ± 0.27
$20 \geq p_T^\gamma < 25$	0.79 ± 0.32	0.77 ± 0.31	0.78 ± 0.31	0.77 ± 0.31
$25 \geq p_T^\gamma < 30$	0.86 ± 0.34	0.85 ± 0.34	0.85 ± 0.34	0.86 ± 0.34
$30 \geq p_T^\gamma < 35$	0.88 ± 0.35	0.87 ± 0.35	0.88 ± 0.35	0.87 ± 0.35
$35 \geq p_T^\gamma < 40$	0.92 ± 0.37	0.88 ± 0.35	0.91 ± 0.36	0.9 ± 0.36
$40 \geq p_T^\gamma < 50$	0.94 ± 0.38	0.93 ± 0.37	0.95 ± 0.38	0.9 ± 0.36
$50 \geq p_T^\gamma < 60$	0.96 ± 0.38	0.95 ± 0.38	0.93 ± 0.37	0.95 ± 0.38
$60 \geq p_T^\gamma < 100$	0.98 ± 0.39	0.98 ± 0.39	0.99 ± 0.4	0.97 ± 0.39

Table 6.11. Signal yield for $N_{jet} = 2$

P_T range [GeV]	$\lvert\eta\rvert < 0.60$	$0.60 \leq \lvert\eta\rvert < 1.37$	$1.52 \leq \lvert\eta\rvert < 1.81$	$1.81 \leq \lvert\eta\rvert < 2.37$
$15 \geq p_T^\gamma < 20$	284.04 ± 16.85	408.16 ± 20.2	218.38 ± 14.78	226.29 ± 15.04
$20 \geq p_T^\gamma < 25$	181.52 ± 13.47	220.4 ± 14.85	112.13 ± 10.59	121.57 ± 11.03
$25 \geq p_T^\gamma < 30$	129.23 ± 11.37	145.96 ± 12.08	57.31 ± 7.57	79.25 ± 8.9
$30 \geq p_T^\gamma < 35$	67.11 ± 8.19	90.93 ± 9.54	35.24 ± 5.94	41.12 ± 6.41
$35 \geq p_T^\gamma < 40$	58.06 ± 7.62	74.46 ± 8.63	38.13 ± 6.18	30.08 ± 5.48
$40 \geq p_T^\gamma < 50$	56.28 ± 7.5	79.52 ± 8.92	26.32 ± 5.13	39.53 ± 6.29
$50 \geq p_T^\gamma < 60$	35.77 ± 5.98	39.22 ± 6.26	19.33 ± 4.4	28.55 ± 5.34
$60 \geq p_T^\gamma < 100$	25.8 ± 5.08	29.24 ± 5.41	8.82 ± 2.97	19.57 ± 4.42

Table 6.12. Purity estimate for $N_{jet} = 2$

P_T range [GeV]	$\lvert\eta\rvert < 0.60$	$0.60 \leq \lvert\eta\rvert < 1.37$	$1.52 \leq \lvert\eta\rvert < 1.81$	$1.81 \leq \lvert\eta\rvert < 2.37$
$15 \geq p_T^\gamma < 20$	0.77 ± 0.31	0.72 ± 0.29	0.78 ± 0.31	0.8 ± 0.32
$20 \geq p_T^\gamma < 25$	0.83 ± 0.33	0.78 ± 0.31	0.85 ± 0.34	0.84 ± 0.34
$25 \geq p_T^\gamma < 30$	0.91 ± 0.36	0.83 ± 0.33	0.84 ± 0.34	0.86 ± 0.34
$30 \geq p_T^\gamma < 35$	0.91 ± 0.36	0.89 ± 0.36	0.88 ± 0.35	0.86 ± 0.34
$35 \geq p_T^\gamma < 40$	0.94 ± 0.37	0.93 ± 0.37	0.95 ± 0.38	0.86 ± 0.34
$40 \geq p_T^\gamma < 50$	0.94 ± 0.38	0.92 ± 0.37	0.94 ± 0.38	0.94 ± 0.38
$50 \geq p_T^\gamma < 60$	0.97 ± 0.39	0.96 ± 0.38	0.97 ± 0.39	0.95 ± 0.38
$60 \geq p_T^\gamma < 100$	0.99 ± 0.4	0.97 ± 0.39	0.98 ± 0.39	0.98 ± 0.39

Table 6.13. Signal yield for $N_{jet} = 3$

P_T range [GeV]	$\|\eta\| < 0.60$	$0.60 \leq \|\eta\| < 1.37$	$1.52 \leq \|\eta\| < 1.81$	$1.81 \leq \|\eta\| < 2.37$
$15 \geq p_T^\gamma < 20$	53.82 ± 7.34	72.02 ± 8.49	44.73 ± 6.69	38.93 ± 6.24
$20 \geq p_T^\gamma < 25$	35.18 ± 5.93	45.1 ± 6.72	13.03 ± 3.61	22.37 ± 4.73
$25 \geq p_T^\gamma < 30$	23.03 ± 4.8	42.07 ± 6.49	9.78 ± 3.13	17.04 ± 4.13
$30 \geq p_T^\gamma < 35$	20.23 ± 4.5	23.48 ± 4.85	11.52 ± 3.39	10.18 ± 3.19
$35 \geq p_T^\gamma < 40$	10.94 ± 3.31	15.79 ± 3.97	4.62 ± 2.15	12.25 ± 3.5
$40 \geq p_T^\gamma < 50$	13.34 ± 3.65	18.03 ± 4.25	6.78 ± 2.6	13.96 ± 3.74
$50 \geq p_T^\gamma < 60$	11.8 ± 3.44	11.27 ± 3.36	0.92 ± 0.96	4.9 ± 2.21
$60 \geq p_T^\gamma < 100$	8.89 ± 2.98	13.67 ± 3.7	5.0 ± 2.24	4.8 ± 2.19

Table 6.14. Purity estimate for $N_{jet} = 3$

P_T range [GeV]	$\|\eta\| < 0.60$	$0.60 \leq \|\eta\| < 1.37$	$1.52 \leq \|\eta\| < 1.81$	$1.81 \leq \|\eta\| < 2.37$
$15 \geq p_T^\gamma < 20$	0.71 ± 0.28	0.73 ± 0.29	0.81 ± 0.33	0.78 ± 0.31
$20 \geq p_T^\gamma < 25$	0.86 ± 0.34	0.81 ± 0.32	0.77 ± 0.31	0.83 ± 0.33
$25 \geq p_T^\gamma < 30$	0.82 ± 0.33	0.88 ± 0.35	0.82 ± 0.33	0.95 ± 0.38
$30 \geq p_T^\gamma < 35$	0.92 ± 0.37	0.87 ± 0.35	0.89 ± 0.35	0.93 ± 0.37
$35 \geq p_T^\gamma < 40$	0.91 ± 0.36	0.93 ± 0.37	0.92 ± 0.37	0.94 ± 0.38
$40 \geq p_T^\gamma < 50$	0.95 ± 0.38	0.95 ± 0.38	0.97 ± 0.39	0.93 ± 0.37
$50 \geq p_T^\gamma < 60$	0.98 ± 0.39	0.94 ± 0.38	0.92 ± 0.37	0.98 ± 0.39
$60 \geq p_T^\gamma < 100$	0.99 ± 0.4	0.98 ± 0.39	1.0 ± 0.4	0.96 ± 0.38

Table 6.15. Signal yield for $N_{jet} >= 4$

P_T range [GeV]	$\|\eta\| < 0.60$	$0.60 \leq \|\eta\| < 1.37$	$1.52 \leq \|\eta\| < 1.81$	$1.81 \leq \|\eta\| < 2.37$
$15 \geq p_T^\gamma < 20$	9.44 ± 3.07	20.53 ± 4.53	7.99 ± 2.83	18.75 ± 4.33
$20 \geq p_T^\gamma < 25$	5.65 ± 2.38	9.15 ± 3.03	4.85 ± 2.2	13.93 ± 3.73
$25 \geq p_T^\gamma < 30$	2.07 ± 1.44	14.28 ± 3.78	1.93 ± 1.39	1.47 ± 1.21
$30 \geq p_T^\gamma < 35$	1.39 ± 1.18	8.37 ± 2.89	3.95 ± 1.99	3.63 ± 1.9
$35 \geq p_T^\gamma < 40$	1.9 ± 1.38	3.33 ± 1.83	7.0 ± 2.65	2.0 ± 1.41
$40 \geq p_T^\gamma < 50$	4.86 ± 2.2	6.52 ± 2.55	3.0 ± 1.73	1.38 ± 1.17
$50 \geq p_T^\gamma < 60$	2.0 ± 1.41	3.0 ± 1.73	2.96 ± 1.72	4.93 ± 2.22
$60 \geq p_T^\gamma < 100$	4.86 ± 2.21	3.0 ± 1.73	2.0 ± 1.41	1.0 ± 1.0

Table 6.16. Purity estimate for $N_{jet} >= 4$

P_T range [GeV]	$\lvert\eta\rvert < 0.60$	$0.60 \leq \lvert\eta\rvert < 1.37$	$1.52 \leq \lvert\eta\rvert < 1.81$	$1.81 \leq \lvert\eta\rvert < 2.37$
$15 \geq p_T^\gamma < 20$	0.73 ± 0.29	0.79 ± 0.32	0.8 ± 0.32	0.89 ± 0.36
$20 \geq p_T^\gamma < 25$	0.81 ± 0.32	0.76 ± 0.31	0.69 ± 0.28	0.93 ± 0.37
$25 \geq p_T^\gamma < 30$	0.69 ± 0.28	0.95 ± 0.38	0.97 ± 0.39	0.73 ± 0.29
$30 \geq p_T^\gamma < 35$	0.7 ± 0.28	0.93 ± 0.37	0.99 ± 0.39	0.91 ± 0.36
$35 \geq p_T^\gamma < 40$	0.95 ± 0.38	0.83 ± 0.33	1.0 ± 0.4	1.0 ± 0.4
$40 \geq p_T^\gamma < 50$	0.97 ± 0.39	0.93 ± 0.37	1.0 ± 0.4	0.69 ± 0.28
$50 \geq p_T^\gamma < 60$	1.0 ± 0.4	1.0 ± 0.4	0.99 ± 0.39	0.99 ± 0.39
$60 \geq p_T^\gamma < 100$	0.97 ± 0.39	1.0 ± 0.4	1.0 ± 0.4	1.0 ± 0.4

Table 6.17. Final Signal Yield For Inclusive N_{jet}

P_T range [GeV]	$\|\eta\| < 0.60$	$0.60 \leq \|\eta\| < 1.37$	$1.52 \leq \|\eta\| < 1.81$	$1.81 \leq \|\eta\| < 2.37$
$15 \geq p_T^\gamma < 20$	4783.4 ± 81.38	5887.14 ± 94.04	3317.02 ± 67.66	3666.32 ± 71.63
$20 \geq p_T^\gamma < 25$	2183.82 ± 51.9	2723.98 ± 59.4	1325.07 ± 40.67	1653.87 ± 45.66
$25 \geq p_T^\gamma < 30$	1065.62 ± 35.08	1376.96 ± 40.47	575.16 ± 26.01	853.72 ± 31.31
$30 \geq p_T^\gamma < 35$	594.09 ± 25.81	745.06 ± 29.19	333.55 ± 19.36	409.07 ± 21.58
$35 \geq p_T^\gamma < 40$	346.71 ± 19.41	422.55 ± 21.72	196.34 ± 14.63	243.46 ± 16.43
$40 \geq p_T^\gamma < 50$	341.26 ± 19.03	426.84 ± 21.49	157.46 ± 12.91	249.43 ± 16.5
$50 \geq p_T^\gamma < 60$	151.1 ± 12.48	168.75 ± 13.37	58.86 ± 7.93	122.76 ± 11.35
$60 \geq p_T^\gamma < 100$	105.13 ± 10.38	108.06 ± 10.61	46.54 ± 6.89	62.48 ± 8.02

Table 6.18. Final Signal Yield For $N_{jet} = 1$

P_T range [GeV]	$\|\eta\| < 0.60$	$0.60 \leq \|\eta\| < 1.37$	$1.52 \leq \|\eta\| < 1.81$	$1.81 \leq \|\eta\| < 2.37$
$15 \geq p_T^\gamma < 20$	1095.59 ± 39.57	1344.12 ± 45.81	804.54 ± 33.37	695.24 ± 31.86
$20 \geq p_T^\gamma < 25$	757.7 ± 30.96	989.83 ± 35.93	456.22 ± 24.16	501.62 ± 25.46
$25 \geq p_T^\gamma < 30$	516.65 ± 24.57	667.35 ± 28.03	251.92 ± 17.25	329.59 ± 19.63
$30 \geq p_T^\gamma < 35$	311.88 ± 18.87	404.57 ± 21.51	157.09 ± 13.38	198.97 ± 15.1
$35 \geq p_T^\gamma < 40$	199.0 ± 14.74	220.44 ± 15.84	91.8 ± 10.08	117.45 ± 11.45
$40 \geq p_T^\gamma < 50$	205.63 ± 14.8	254.19 ± 16.57	96.55 ± 10.07	126.7 ± 11.88
$50 \geq p_T^\gamma < 60$	75.78 ± 8.89	105.5 ± 10.52	31.14 ± 5.8	67.05 ± 8.4
$60 \geq p_T^\gamma < 100$	54.75 ± 7.48	62.4 ± 7.99	25.52 ± 5.09	27.97 ± 5.4

Table 6.19. Final Signal Yield For $N_{jet} = 2$

P_T range [GeV]	$\|\eta\| < 0.60$	$0.60 \leq \|\eta\| < 1.37$	$1.52 \leq \|\eta\| < 1.81$	$1.81 \leq \|\eta\| < 2.37$
$15 \geq p_T^\gamma < 20$	217.47 ± 16.86	295.39 ± 20.21	170.31 ± 14.78	180.95 ± 15.05
$20 \geq p_T^\gamma < 25$	151.14 ± 13.48	172.26 ± 14.85	95.24 ± 10.59	101.93 ± 11.03
$25 \geq p_T^\gamma < 30$	117.62 ± 11.37	121.74 ± 12.09	48.3 ± 7.58	68.27 ± 8.91
$30 \geq p_T^\gamma < 35$	60.87 ± 8.2	81.06 ± 9.54	31.04 ± 5.95	35.22 ± 6.42
$35 \geq p_T^\gamma < 40$	54.37 ± 7.63	69.3 ± 8.64	36.35 ± 6.19	25.85 ± 5.5
$40 \geq p_T^\gamma < 50$	52.79 ± 7.51	73.52 ± 8.92	24.75 ± 5.14	37.21 ± 6.3
$50 \geq p_T^\gamma < 60$	34.58 ± 5.99	37.52 ± 6.27	18.69 ± 4.41	27.16 ± 5.36
$60 \geq p_T^\gamma < 100$	25.6 ± 5.1	28.5 ± 5.42	8.65 ± 3.0	19.14 ± 4.44

Table 6.20. Final Signal Yield For $N_{jet} = 3$

P_T range [GeV]	$\|\eta\| < 0.60$	$0.60 \leq \|\eta\| < 1.37$	$1.52 \leq \|\eta\| < 1.81$	$1.81 \leq \|\eta\| < 2.37$
$15 \geq p_T^\gamma < 20$	38.11 ± 7.34	52.4 ± 8.49	36.38 ± 6.7	30.32 ± 6.25
$20 \geq p_T^\gamma < 25$	30.19 ± 5.94	36.32 ± 6.72	9.98 ± 3.62	18.53 ± 4.74
$25 \geq p_T^\gamma < 30$	18.95 ± 4.81	36.87 ± 6.5	7.97 ± 3.14	16.12 ± 4.14
$30 \geq p_T^\gamma < 35$	18.6 ± 4.51	20.43 ± 4.86	10.2 ± 3.41	9.43 ± 3.21
$35 \geq p_T^\gamma < 40$	9.97 ± 3.33	14.66 ± 3.99	4.27 ± 2.18	11.54 ± 3.52
$40 \geq p_T^\gamma < 50$	12.72 ± 3.67	17.11 ± 4.26	6.56 ± 2.63	12.99 ± 3.75
$50 \geq p_T^\gamma < 60$	11.61 ± 3.46	10.58 ± 3.38	0.85 ± 1.03	4.8 ± 2.25
$60 \geq p_T^\gamma < 100$	8.78 ± 3.01	13.34 ± 3.72	5.0 ± 2.27	4.61 ± 2.22

Table 6.21. Final Signal Yield For $N_{jet} >= 4$

P_T range [GeV]	$\|\eta\| < 0.60$	$0.60 \leq \|\eta\| < 1.37$	$1.52 \leq \|\eta\| < 1.81$	$1.81 \leq \|\eta\| < 2.37$
$15 \geq p_T^\gamma < 20$	6.86 ± 3.09	16.22 ± 4.54	6.39 ± 2.84	16.74 ± 4.34
$20 \geq p_T^\gamma < 25$	4.57 ± 2.4	6.98 ± 3.04	3.36 ± 2.22	12.94 ± 3.75
$25 \geq p_T^\gamma < 30$	1.43 ± 1.46	13.6 ± 3.8	1.86 ± 1.44	1.08 ± 1.25
$30 \geq p_T^\gamma < 35$	0.97 ± 1.21	7.78 ± 2.92	3.89 ± 2.03	3.29 ± 1.94
$35 \geq p_T^\gamma < 40$	1.81 ± 1.43	2.78 ± 1.86	7.0 ± 2.68	2.0 ± 1.47
$40 \geq p_T^\gamma < 50$	4.72 ± 2.24	6.08 ± 2.58	3.0 ± 1.78	0.95 ± 1.2
$50 \geq p_T^\gamma < 60$	2.0 ± 1.47	3.0 ± 1.78	2.92 ± 1.77	4.85 ± 2.25
$60 \geq p_T^\gamma < 100$	4.73 ± 2.24	3.0 ± 1.78	2.0 ± 1.47	1.0 ± 1.08

6.7 Final Photon Distribution From Data

Referring back to equation 6.8 it can be seen that the left hand side is given by the yield values obtained in tables 6.17, 6.18, 6.19, 6.20 and 6.21 for each of the inclusive and 1, 2, 3 and greater than or equal to 4 jets cases. From the right hand side, each of the efficiencies have been measured. The efficiencies are all measured for the inclusive jet case and have been applied to all the jet bins. This is based on the assumption that the efficiencies are related entirely to the photon objects and selection on jets do not change the efficiencies by large factors. The final numbers obtained are for normalized luminosity values and the corrections to each luminosty at which the final photon numbers are to be calculated must be applied.

Table 6.22 shows the final yield of photons for the inclusive jets bin given for each interval of pseudorapidity.

Table 6.23 shows the final yield of photons for the one selected jet bin given for each interval of pseudorapidity.

Table 6.24 shows the final yield of photons for the two selected jet bin given for each interval of pseudorapidity.

Table 6.25 shows the final yield of photons for the three selected jet bin given for each interval of pseudorapidity

Table 6.26 shows the final yield of photons for the four or more selected jet bin given for each interval of pseudorapidity.

Figure 6.41 shows the final photon distribution for the inclusive jets case for each of the four pseudorapidity bins. 6.42 shows the total number of photons for all the combined pseudorapidity bins.

Figures 6.43, 6.44, 6.45, 6.46 show the final photon distributions for each of the pseudorapidity intervals for the 1, 2, 3, and 4 or more jets case. Figures 6.47, 6.48,

Table 6.22. Final photon numbers for inclusive N_{jet}

P_T range [GeV]	$\|\eta\| < 0.60$	$0.60 <= \|\eta\| < 1.37$	$1.52 <= \|\eta\| < 1.81$	$1.81 <= \|\eta\| < 2.37$
$15 >= p_T^\gamma < 20$	7246.21 ± 81.38	8918.24 ± 94.04	5024.85 ± 67.66	5553.99 ± 71.63
$20 >= p_T^\gamma < 25$	2961.44 ± 51.9	3693.94 ± 59.4	1796.91 ± 40.67	2242.78 ± 45.66
$25 >= p_T^\gamma < 30$	1350.82 ± 35.08	1745.48 ± 40.47	729.09 ± 26.01	1082.2 ± 31.31
$30 >= p_T^\gamma < 35$	725.34 ± 25.81	909.67 ± 29.19	407.24 ± 19.36	499.44 ± 21.58
$35 >= p_T^\gamma < 40$	413.59 ± 19.41	504.06 ± 21.72	234.22 ± 14.63	290.42 ± 16.43
$40 >= p_T^\gamma < 50$	402.54 ± 19.03	503.49 ± 21.49	185.73 ± 12.91	294.21 ± 16.5
$50 >= p_T^\gamma < 60$	170.25 ± 12.48	190.13 ± 13.37	66.32 ± 7.93	138.31 ± 11.35
$60 >= p_T^\gamma < 100$	120.84 ± 10.38	124.21 ± 10.61	53.5 ± 6.89	71.82 ± 8.02

Table 6.23. Final photon numbers for $N_{jet} = 1$

P_T range [GeV]	$\lvert\eta\rvert < 0.60$	$0.60 <= \lvert\eta\rvert < 1.37$	$1.52 <= \lvert\eta\rvert < 1.81$	$1.81 <= \lvert\eta\rvert < 2.37$
$15 >= p_T^\gamma < 20$	1659.68 ± 39.57	2036.17 ± 45.81	1218.78 ± 33.37	1053.2 ± 31.86
$20 >= p_T^\gamma < 25$	1027.5 ± 30.96	1342.29 ± 35.93	618.67 ± 24.16	680.24 ± 25.46
$25 >= p_T^\gamma < 30$	654.93 ± 24.57	845.95 ± 28.03	319.34 ± 17.25	417.8 ± 19.63
$30 >= p_T^\gamma < 35$	380.78 ± 18.87	493.96 ± 21.51	191.8 ± 13.38	242.92 ± 15.1
$35 >= p_T^\gamma < 40$	237.39 ± 14.74	262.96 ± 15.84	109.5 ± 10.08	140.1 ± 11.45
$40 >= p_T^\gamma < 50$	242.55 ± 14.8	299.83 ± 16.57	113.88 ± 10.07	149.45 ± 11.88
$50 >= p_T^\gamma < 60$	85.38 ± 8.89	118.86 ± 10.52	35.09 ± 5.8	75.55 ± 8.4
$60 >= p_T^\gamma < 100$	62.93 ± 7.48	71.73 ± 7.99	29.34 ± 5.09	32.15 ± 5.4

Table 6.24. Final photon numbers for $N_{jet} = 2$

P_T range [GeV]	$\|\eta\| < 0.60$	$0.60 <= \|\eta\| < 1.37$	$1.52 <= \|\eta\| < 1.81$	$1.81 <= \|\eta\| < 2.37$
$15 >= p_T^\gamma < 20$	329.44 ± 16.86	447.47 ± 20.21	258.0 ± 14.78	274.11 ± 15.05
$20 >= p_T^\gamma < 25$	204.95 ± 13.48	233.59 ± 14.85	129.16 ± 10.59	138.23 ± 11.03
$25 >= p_T^\gamma < 30$	149.09 ± 11.37	154.32 ± 12.09	61.23 ± 7.58	86.54 ± 8.91
$30 >= p_T^\gamma < 35$	74.32 ± 8.2	98.97 ± 9.54	37.9 ± 5.95	43.0 ± 6.42
$35 >= p_T^\gamma < 40$	64.86 ± 7.63	82.67 ± 8.64	43.37 ± 6.19	30.84 ± 5.5
$40 >= p_T^\gamma < 50$	62.27 ± 7.51	86.73 ± 8.93	29.19 ± 5.14	43.89 ± 6.3
$50 >= p_T^\gamma < 60$	38.96 ± 5.99	42.28 ± 6.27	21.06 ± 4.41	30.61 ± 5.36
$60 >= p_T^\gamma < 100$	29.43 ± 5.1	32.76 ± 5.42	9.94 ± 3.0	22.01 ± 4.44

Table 6.25. Final photon numbers for $N_{jet} = 3$

P_T range [GeV]	$\|\eta\| < 0.60$	$0.60 <= \|\eta\| < 1.37$	$1.52 <= \|\eta\| < 1.81$	$1.81 <= \|\eta\| < 2.37$
$15 >= p_T^\gamma < 20$	57.74 ± 7.34	79.37 ± 8.49	55.11 ± 6.7	45.93 ± 6.25
$20 >= p_T^\gamma < 25$	40.94 ± 5.94	49.26 ± 6.72	13.53 ± 3.62	25.13 ± 4.74
$25 >= p_T^\gamma < 30$	24.02 ± 4.81	46.73 ± 6.5	10.11 ± 3.14	20.44 ± 4.14
$30 >= p_T^\gamma < 35$	22.71 ± 4.51	24.94 ± 4.86	12.45 ± 3.41	11.51 ± 3.21
$35 >= p_T^\gamma < 40$	11.9 ± 3.33	17.49 ± 3.99	5.09 ± 2.18	13.76 ± 3.52
$40 >= p_T^\gamma < 50$	15.0 ± 3.67	20.18 ± 4.26	7.74 ± 2.63	15.32 ± 3.75
$50 >= p_T^\gamma < 60$	13.08 ± 3.46	11.92 ± 3.38	0.96 ± 1.03	5.4 ± 2.25
$60 >= p_T^\gamma < 100$	10.09 ± 3.01	15.34 ± 3.72	5.75 ± 2.27	5.3 ± 2.23

Table 6.26. Final photon numbers for $N_{jet} = 4$

P_T range [GeV]	$\|\eta\| < 0.60$	$0.60 <= \|\eta\| < 1.37$	$1.52 <= \|\eta\| < 1.81$	$1.81 <= \|\eta\| < 2.37$
$15 >= p_T^\gamma < 20$	10.39 ± 3.09	24.57 ± 4.54	9.67 ± 2.84	25.36 ± 4.34
$20 >= p_T^\gamma < 25$	6.19 ± 2.4	9.47 ± 3.04	4.56 ± 2.22	17.55 ± 3.75
$25 >= p_T^\gamma < 30$	1.81 ± 1.47	17.24 ± 3.8	2.36 ± 1.44	1.37 ± 1.25
$30 >= p_T^\gamma < 35$	1.18 ± 1.21	9.49 ± 2.92	4.75 ± 2.03	4.01 ± 1.94
$35 >= p_T^\gamma < 40$	2.15 ± 1.43	3.31 ± 1.86	8.35 ± 2.68	2.39 ± 1.47
$40 >= p_T^\gamma < 50$	5.57 ± 2.24	7.17 ± 2.58	3.54 ± 1.78	1.12 ± 1.21
$50 >= p_T^\gamma < 60$	2.25 ± 1.47	3.38 ± 1.78	3.29 ± 1.77	5.47 ± 2.25
$60 >= p_T^\gamma < 100$	5.43 ± 2.24	3.45 ± 1.78	2.3 ± 1.47	1.15 ± 1.08

6.49, 6.50 show the final photon distributions for all of the fiducial pseudorapidity interval for the 1, 2, 3, and 4 or more jets case.

The final results for missing transverse energy can thus be obtained by scaling each of the final photon distributions by the theoretical factors, and using the corresponding luminosity of the samples.

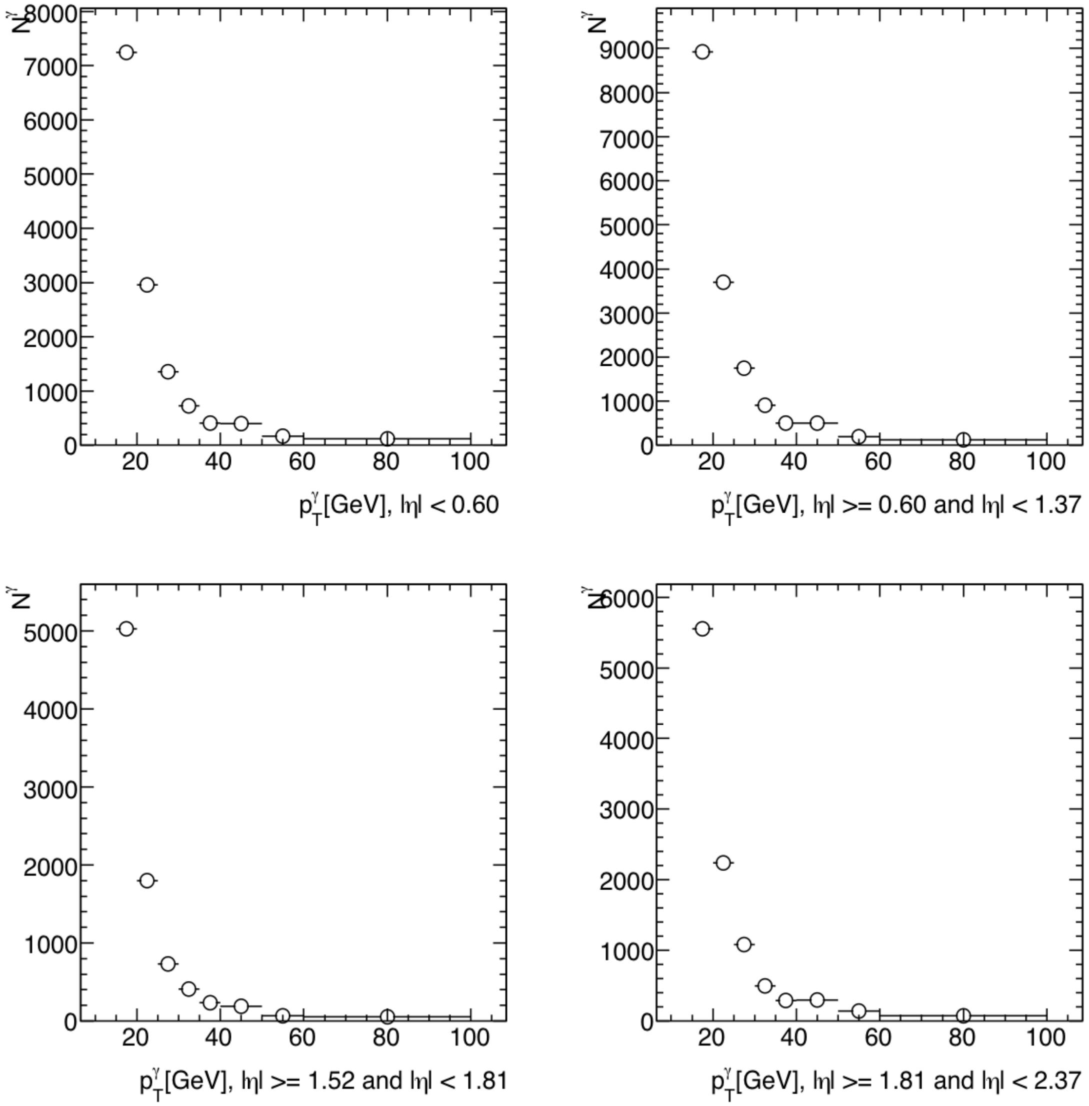

Figure 6.41. Number of photons as a function of p_T^γ for each η interval with inclusive jets.

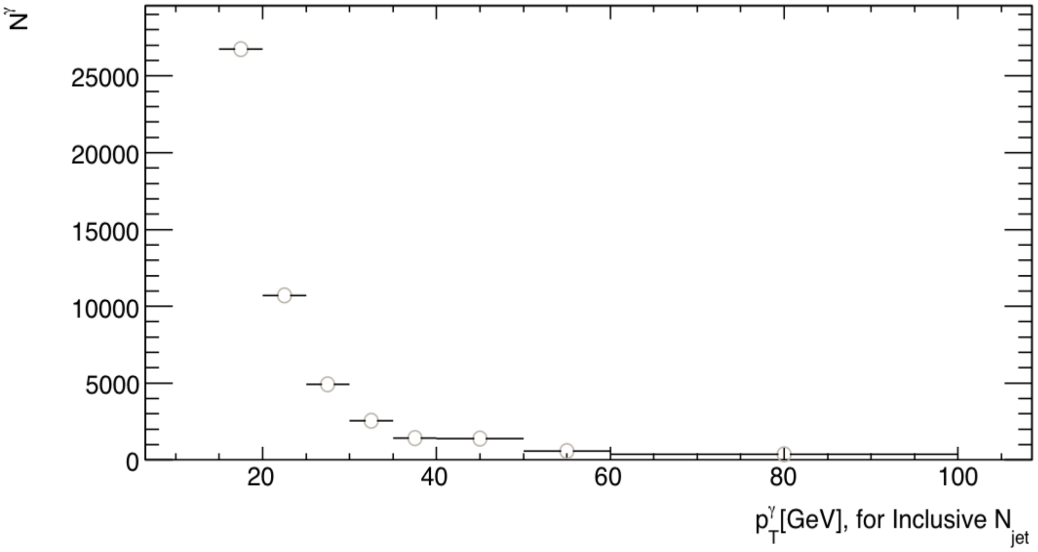

Figure 6.42. Number of photons as a function of p_T^γ for all η intervals with inclusive jets.

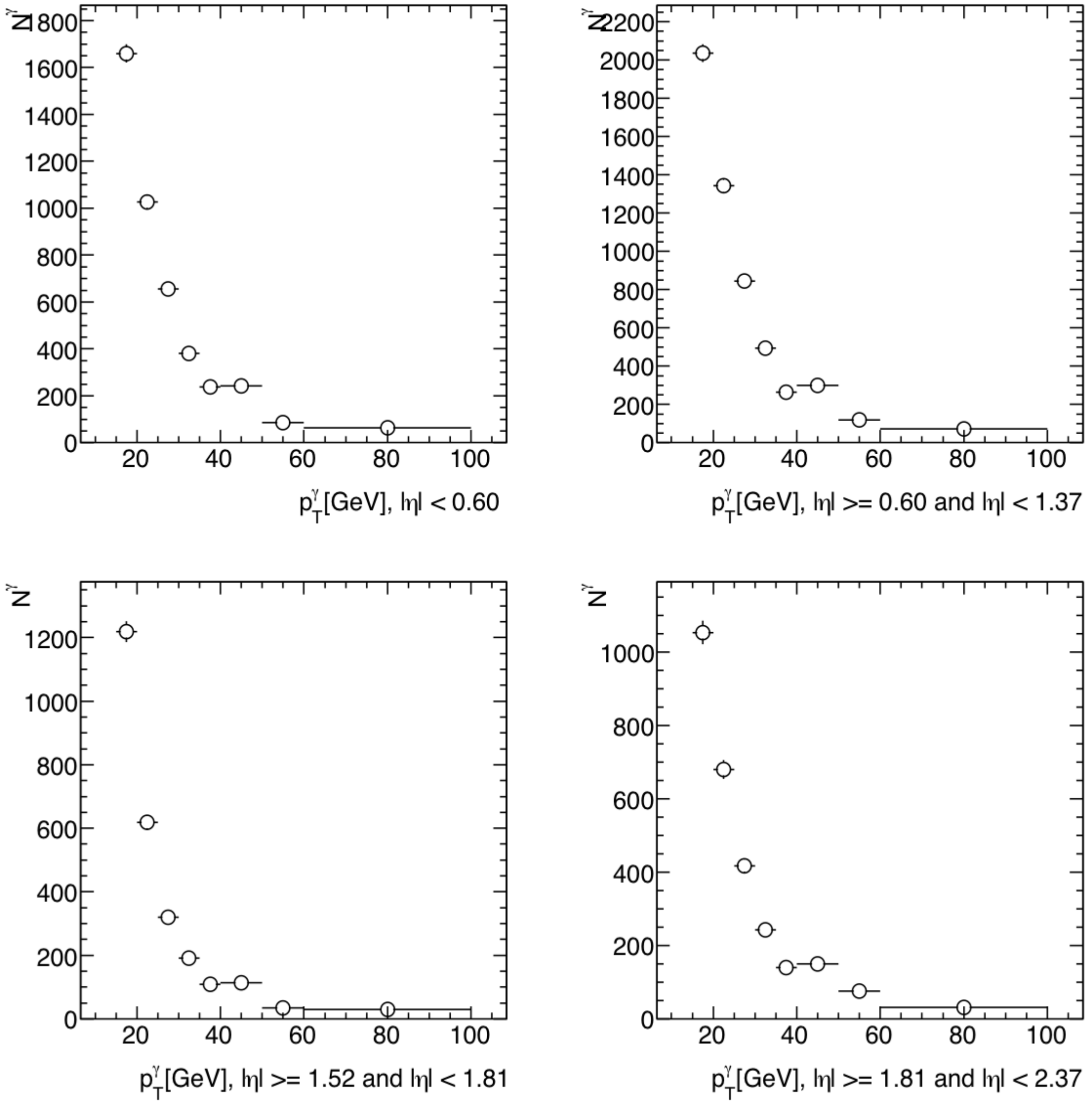

Figure 6.43. Number of photons as a function of p_T^{γ} for $N_{jet} = 1$.

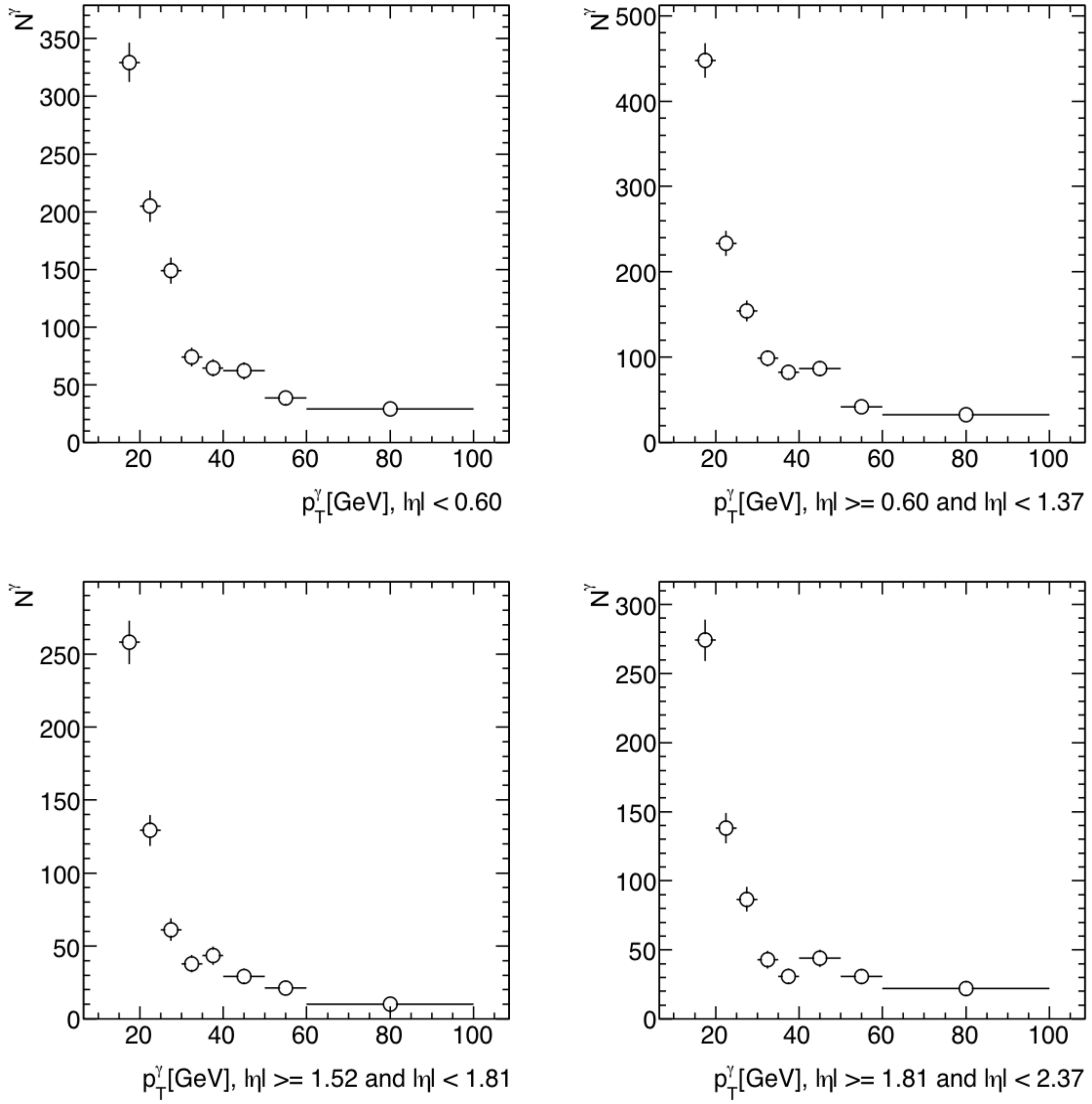

Figure 6.44. Number of photons as a function of p_T^{γ} for $N_{jet} = 2$.

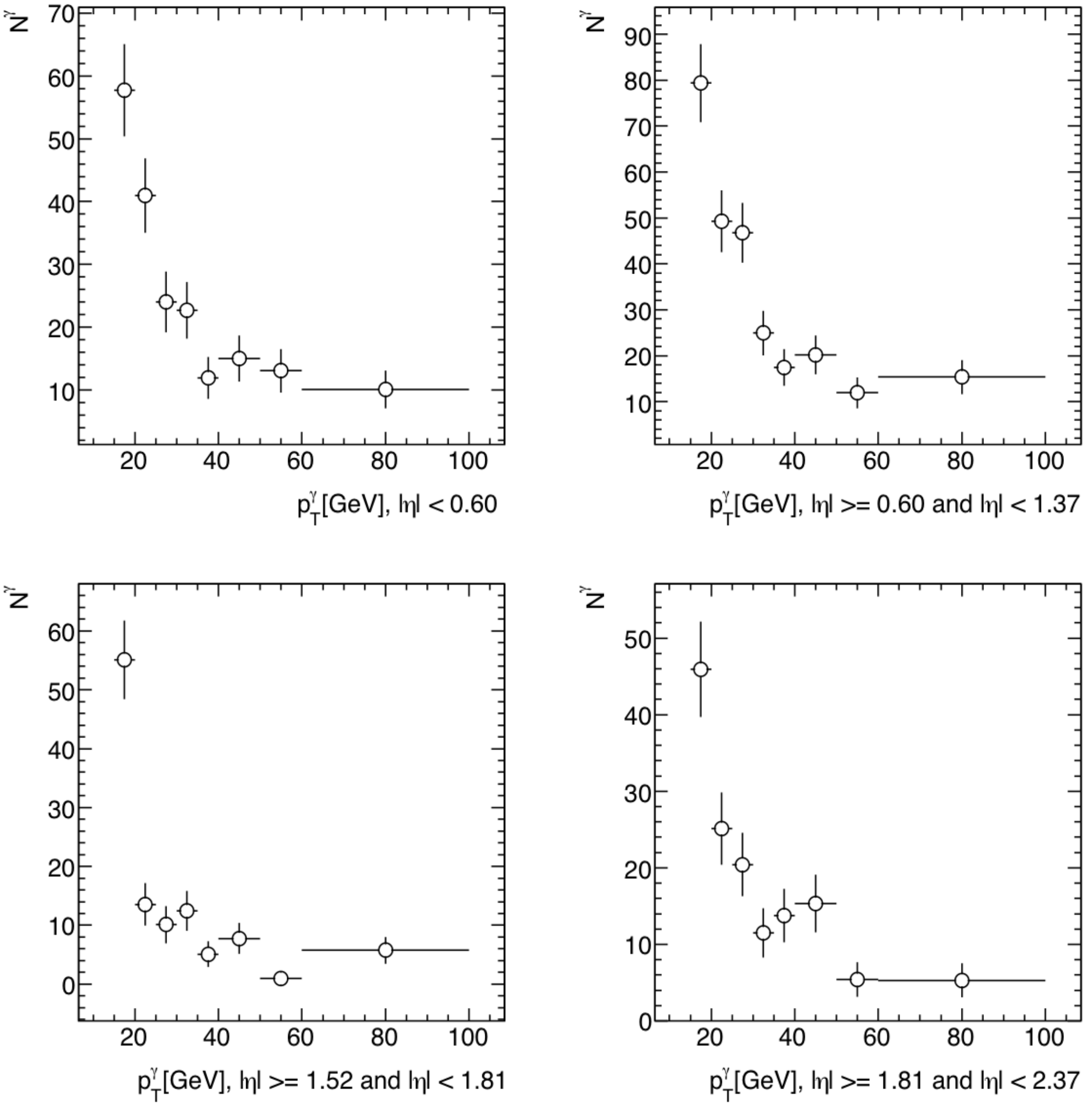

Figure 6.45. Number of photons as a function of p_T^{γ} for $N_{jet} = 3$.

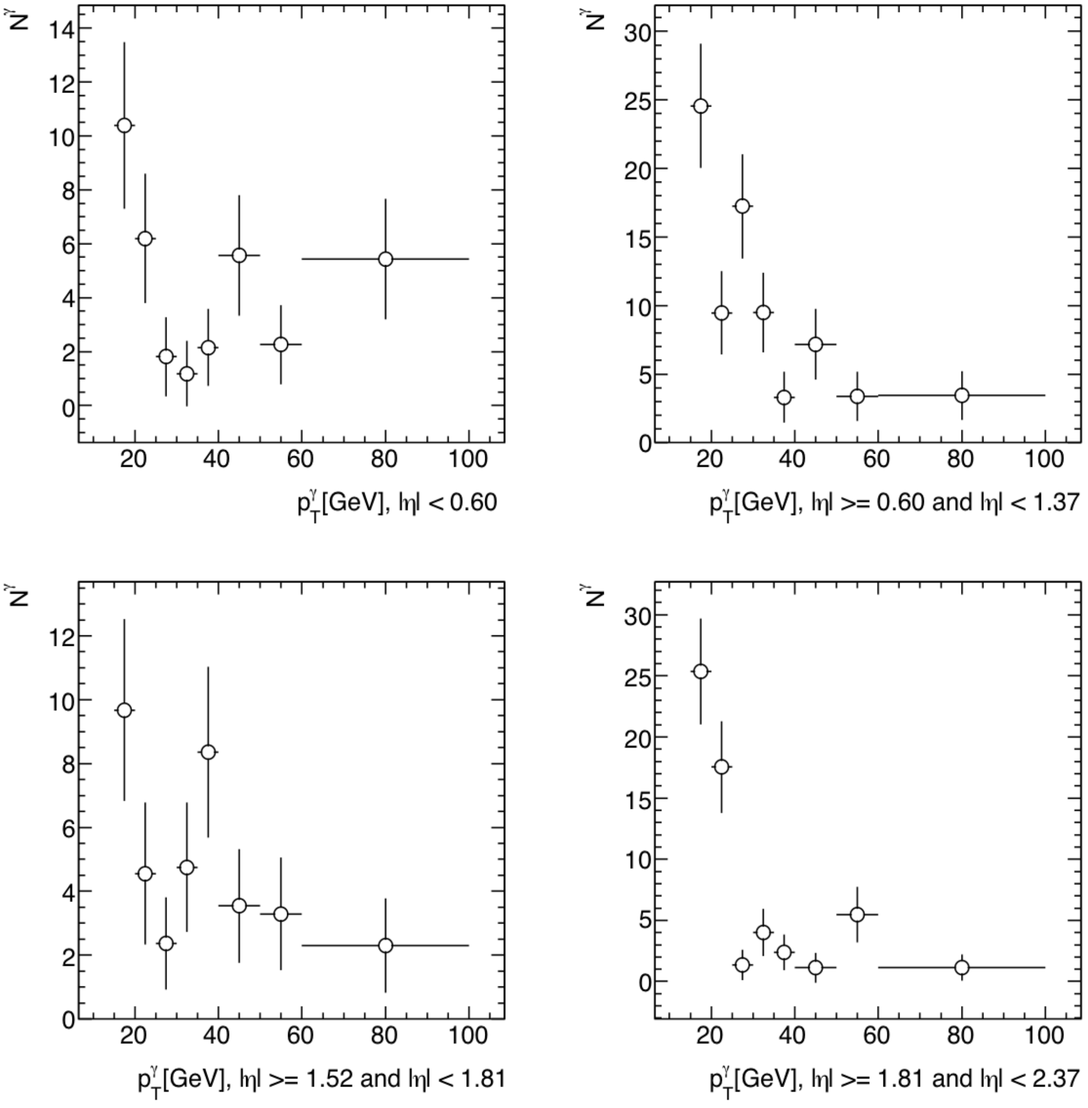

Figure 6.46. Number of photons as a function of p_T^{γ} for $N_{jet} >= 4$.

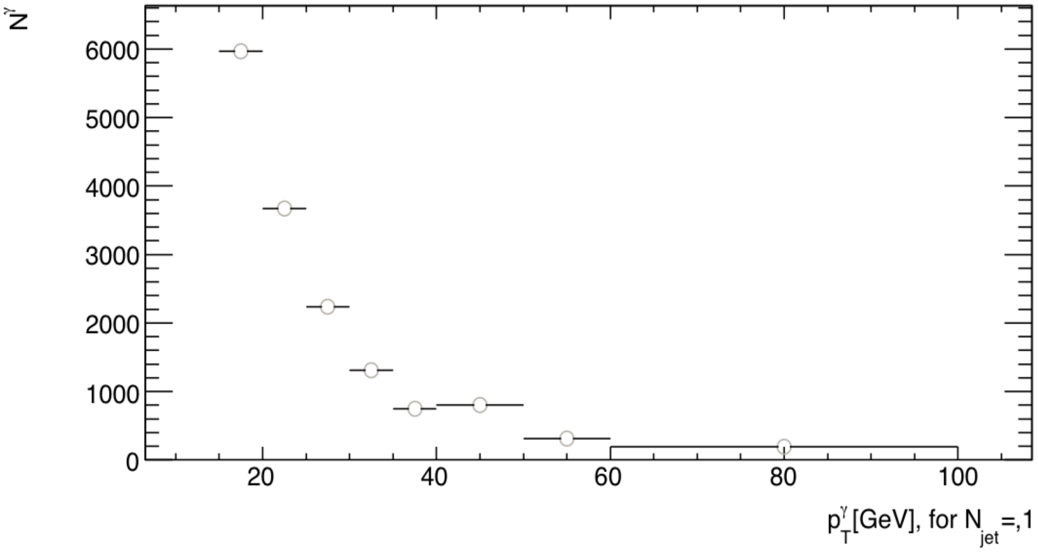

Figure 6.47. Number of photons as a function of p_T^{γ} for all η intervals for $N_{jet} = 1$.

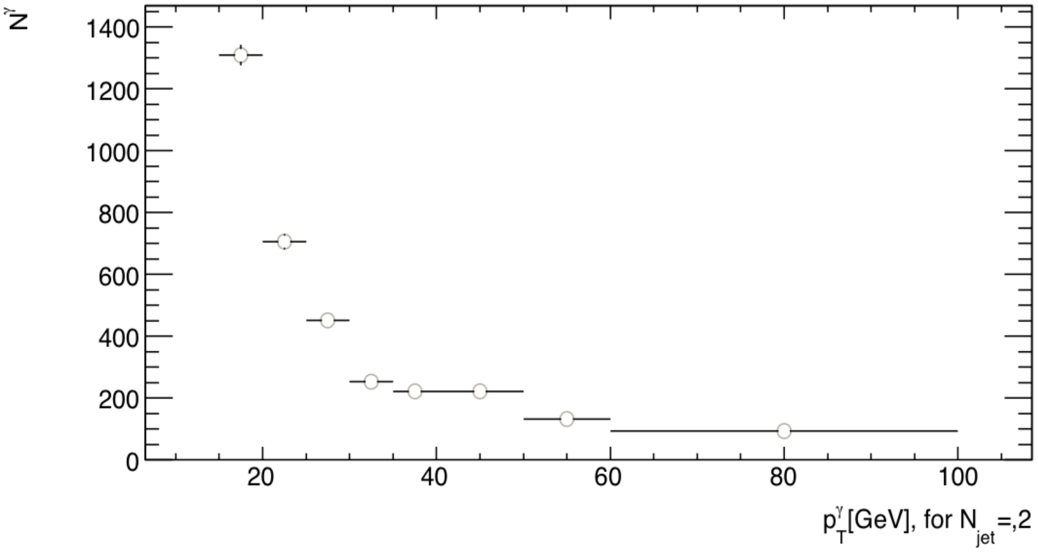

Figure 6.48. Number of photons as a function of p_T^{γ} for all η intervals for $N_{jet} = 2$.

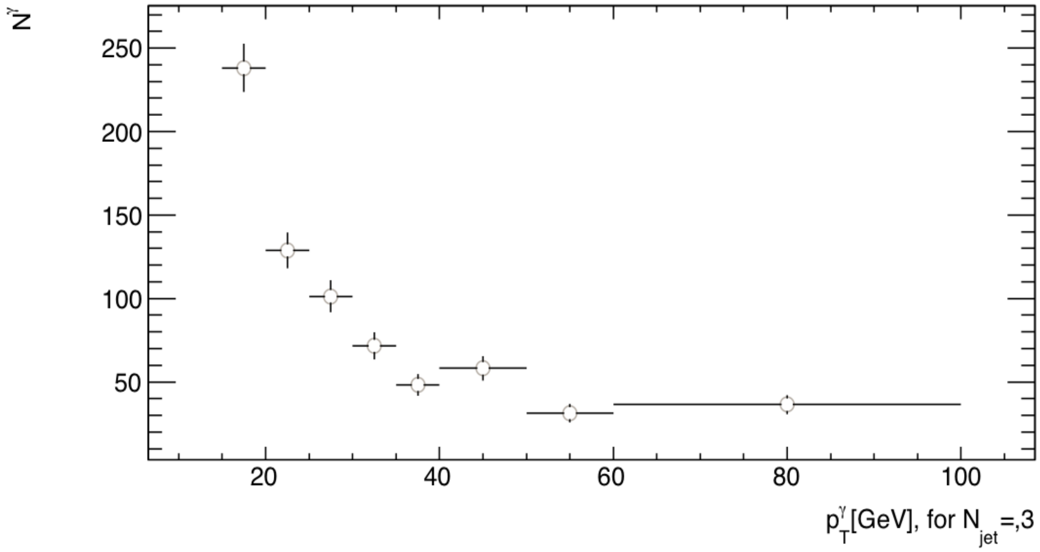

Figure 6.49. Number of photons as a function of p_T^γ for all η intervals for $N_{jet} = 3$.

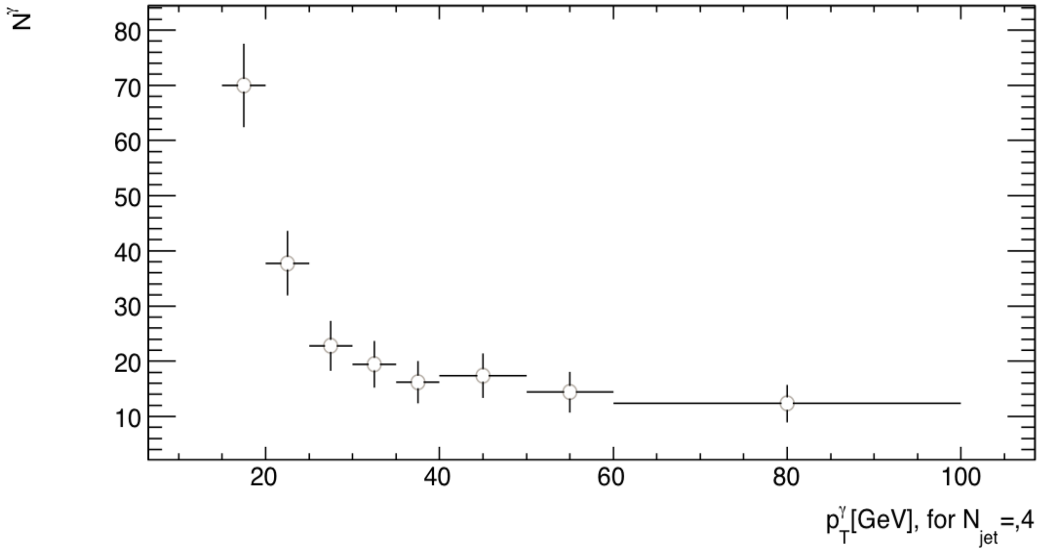

Figure 6.50. Number of photons as a function of p_T^γ for all η intervals for $N_{jet} >= 4$.

CHAPTER 7

CONCLUSIONS

7.1 A Good Start For LHC Physics

The ATLAS experiment at the Large Hadron Collider at the time of this writing (November 2010) has collected ∼45 pico-barns of data with a better than expected performance in the final few months of the year 2010. With the new data, ATLAS has performed many studies of the performance of the detector and physics. Initial results have been promising and further analyses to understand the physics of the Standard Model at higher than before collision energies are underway.

7.2 The Scope Of The Studies Presented

The studies presented here comprise of several years of work before and since the start of the LHC. Initial work on the commissioning and calibration of the ATLAS detector, specially the Tile Calorimeter was presented in chapter 3. Study of early data from ATLAS including minimum bias data with $\sqrt{s} = 900$ GeV and 7 TeV was presented in chapter 4. A mostly Monte Carlo based study to search for Supersymmetry and other new physics in the dijet and multijet channels was explored in chapter 5. A detailed study using $\sqrt{s} = 7$ TeV data for the irreducible background estimation of $Z(\nu\nu)$ plus jets using photons plus jets sample is studied in chapter 6.

Each of the studies performed required understanding of specific subsections of the detector. Investigations of scaling effects in soft QCD required detailed study of soft processes. A good understanding of the inner detector with accurate modelling of the detector using Monte Carlo was performed to obtain multiplicity distributions from data. All detector effects were unfolded to achieve generality of results. Binomial and negative binomial fits to multiplicity distributions were presented.

For the study of SUSY searches in the dijet and multijet channels a robust understanding of jets and missing transverse energy was required. This in turn required a good understanding of the hadronic calorimeter. The installation, testing and calibration of the intermediate tile calorimeter was performed towards this purpose. Several alternative kinematic and topological variables to missing transverse energy to search for Supersymmetry was also presented.

The estimation of $Z \rightarrow \nu\nu$ + jets background from γ + jets events was presented in detail. The understanding of photons required a good understanding of the electromagnetic calorimeter with fine precision. Shower shape variables were studied to give optimal photon identification. Monte Carlo simulations were tuned to the data to extract detector efficiencies. The first estimate of photon counts in exclusive jet bins using ATLAS data was performed in this study with results tabulated for reference. Systematic errors were closely investigated and high systematic errors were assumed for estimations that require cross check studies. This method also provided the first study in ATLAS of standard model backgrounds to SUSY using data driven technique.

7.3 Outlook

Although a variety of studies involving many detector sub systems and physics was presented in this thesis, due to the deadline of graduation a much lower luminosity available at the beginning of the LHC run was used for studies in this dissertation. Thus one of the first steps in the future will be to incorporate the total luminosity to obtain more robust numbers. A thorough investigation of the data to perform the search outlined via Monte Carlo studies to search for SUSY in the dijet and multijet channels using alternative kinematic and topological variables to missing transverse energy will be the primary focus of study in the future. The results of such studies will depend on what mother nature has in store for physicists to discover.

REFERENCES

[1] The LHC Experiment. (2008) LHC The Guide. [Online]. Available: http://cdsmedia.cern.ch/img/CERN-Brochure-2008-001-Eng.pdf

[2] J. Wenninger, “The LHC Machine,” Lecture, CERN, June 2009.

[3] The ATLAS Collaboration: G. Aad, E. Abat, B. Abbott, J. Abdallah, A. A. Abdelalim, A. Abdesselam, O. Abdinov, B. Abi, M. Abolins, H. Abramowicz, and et al., “Expected Performance of the ATLAS Experiment - Detector, Trigger and Physics,” *ArXiv e-prints*, Dec. 2009.

[4] G. Aad *et al.*, “The ATLAS Experiment at the CERN Large Hadron Collider,” *JINST*, vol. 3, p. S08003, 2008. [Online]. Available: http://www-library.desy.de/cgi-bin/spiface/find/hep/www?irn=7955545

[5] The ATLAS Collaboration. (2010) ATLAS Fact Sheet. [Online]. Available: http://atlas.ch/fact_sheets.html

[6] H. J. Kim, “Search for standard model higgs particle in two photons final state at atlas,” Ph.D. dissertation, Univ. of Texas at Arlington, Texas, 2010.

[7] The ATLAS Collaboration, “The ATLAS Inner Detector commissioning and calibration,” *ArXiv e-prints*, Apr. 2010.

[8] G. Aad *et al.*, “Readiness of the ATLAS Liquid Argon Calorimeter for LHC Collisions,” *Eur. Phys. J. C*, 2010, long author list - awaiting processing.

[9] “Readiness of the ATLAS Tile Calorimeter for LHC collisions,” 2010, long author list - awaiting processing.

[10] Peter Speckmayer, “Energy Measurement of Hadrons with the CERN ATLAS Calorimeter,” Ph.D. dissertation, eingereicht an der Technischen Universitat Wien Fakultat fur Physik, Gex, May 2008.

[11] “Commissioning of the ATLAS Muon Spectrometer with Cosmic Rays,” *Eur. Phys. J. C*, 2010.

[12] G. Aad *et al.*, “Expected Performance of the ATLAS Experiment - Detector, Trigger and Physics,” 2009.

[13] *ATLAS computing: Technical Design Report*, ser. Technical Design Report ATLAS. Geneva: CERN, 2005, revised version submitted on 2005-06-20 16:33:46.

[14] S. Agostinelli *et al.*, “GEANT4: A simulation toolkit,” *Nucl. Instrum. Meth.*, vol. A506, pp. 250–303, 2003.

[15] The ATLAS Collaboration. (1998) ATLAS Technical Design Report. [Online]. Available: http://atlas.web.cern.ch/Atlas/GROUPS/PHYSICS/TDR/TDR.html

[16] T. Sjostrand, S. Mrenna, and P. Z. Skands, “PYTHIA 6.4 Physics and Manual,” *JHEP*, vol. 05, p. 026, 2006.

[17] G. Corcella *et al.*, “HERWIG 6.5 release note,” 2002.

[18] M. L. Mangano, M. Moretti, F. Piccinini, R. Pittau, and A. D. Polosa, “ALPGEN, a generator for hard multiparton processes in hadronic collisions,” *JHEP*, vol. 07, p. 001, 2003.

[19] H. W. Baer, F. E. Paige, S. D. Protopopescu, and X. Tata, “Simulating supersymmetry with isajet 7.0 / isasusy 1.0; rev. version,” no. SSCL-441. SSCL-P-441, p. 18 p, Jun 1993.

[20] S. Frixione and B. R. Webber, “The MC@NLO 3.4 Event Generator,” 2008.

[21] R. project. (2010) Root. [Online]. Available: http://root.cern.ch/drupal/

[22] F. Halzen and A. D. Martin, *Quarks and Leptons : An introductory course in Modern Particle Physics*. USA: John Wiley and Sons, 1984.

[23] WMAP. (2010) Wilkinson microwave anisotropy probe. [Online]. Available: http://map.gsfc.nasa.gov/

[24] COBE. (2010) Cosmic background explorer. [Online]. Available: http://lambda.gsfc.nasa.gov/product/cobe/

[25] M. E. Peskin and D. V. Schroeder, *An Introduction to Quantum Field Theory*. Westview Press, 1995.

[26] M. P. Khanna, *Introduction to Particle Physics*. New Delhi: Printice Hall of India, 2004.

[27] A. Das and T. Ferbel, *Introduction to Nuclear and Particle Physics*. USA: John Wiley and Sons, 1994.

[28] A. Zee, *Quantum Field Theory in a Nutshell*. Hyderabad: University Press (India), 2003, reprinted by arrangement with Princeton University Press, USA.

[29] P. Langacker, "Structure of the Standard Model," *ArXiv High Energy Physics - Phenomenology e-prints*, Apr. 2003.

[30] A. Signer, "Topical Review: ABC of SUSY," *Journal of Physics G Nuclear Physics*, vol. 36, no. 7, pp. 073 002–+, July 2009.

[31] H. Murayama, "Supersymmetry Phenomenology," in *Particle Physics*, G. Senjanović & A. Y. Smirnov, Ed., 2000, pp. 296–+.

[32] B. Bajc. (2010) A Short Introduction to Supersymmetry. [Online]. Available: http://www-f1.ijs.si/ bajc/susy.pdf

[33] "Muon Performance in Minimum Bias pp Collision Data at $\sqrt{s} = 7$ TeV with ATLAS," CERN, Geneva, Tech. Rep. ATLAS-CONF-2010-036, Jul 2010.

[34] G. Aad, "Measurement of inclusive jet and dijet cross sections in proton-proton collisions at 7 tev centre-of-mass energy with the atlas detector.

oai:cds.cern.ch:1295801," CERN, Geneva, Tech. Rep. arXiv:1009.5908. CERN-PH-EP-2010-034, Sep 2010, preliminary entry.

[35] "Jet energy scale and its systematic uncertainty for jets produced in proton-proton collisions at $\sqrt(s) = 7$ tev and measured with the atlas detector," CERN, Geneva, Tech. Rep. ATLAS-CONF-2010-056, Jul 2010.

[36] "Performance of the missing transverse energy reconstruction and calibration in proton-proton collisions at a center-of-mass energy of 7 tev with the atlas detector," CERN, Geneva, Tech. Rep. ATLAS-CONF-2010-057, Jul 2010.

[37] The ATLAS Collaboration, "Readiness of the ATLAS Tile Calorimeter for LHC collisions," *ArXiv e-prints*, July 2010.

[38] K. Anderson, T. Del Prete, E. Fullana, J. Huston, C. Roda, and R. Stanek, "Tilecal: The hadronic section of the central atlas calorimeter," 2009.

[39] H. Brown, "ITC Calibration Using Cosmic and Cesium Analyses," Talk, ATLAS, September 2010.

[40] R. Field, "Towards an understanding of hadron hadron collisions," Lecture, CMS, 2009.

[41] M. Deile and for the TOTEM Collaboration, "Diffraction and Total Cross-Section at the Tevatron and the LHC," *ArXiv High Energy Physics - Experiment e-prints*, Feb. 2006.

[42] J. Fiete Grosse-Oetringhaus and K. Reygers, "TOPICAL REVIEW: Charged-particle multiplicity in proton-proton collisions," *Journal of Physics G Nuclear Physics*, vol. 37, no. 8, pp. 083 001–+, Aug. 2010.

[43] M. A. Leyton, "Minimum bias measurements with the atlas detector at the cern large hadron collider," Ph.D. dissertation, University of California, Berkeley, Berkeley, 2009.

[44] G. Aad, "Charged-particle multiplicities in pp interactions at $\sqrt{s} = 900$ GeV measured with the ATLAS detector at the LHC. oai:cds.cern.ch:1249427," *Phys. Lett. B*, vol. 688, no. arXiv:1003.3124. CERN-PH-EP-2010-004. 1, pp. 21–42. 40 p, Apr 2010, comments: 40 pages (pages 24-40 appendix with ATLAS collaboration author list), 4 figures.

[45] "Charged particle multiplicities in pp interactions at sqrt(s) = 7 tev measured with the atlas detector at the lhc," CERN, Geneva, Tech. Rep. ATLAS-CONF-2010-024, Jul 2010.

[46] "Early supersymmetry searches in channels with jets and missing transverse momentum with the atlas detector," CERN, Geneva, Tech. Rep. ATLAS-CONF-2010-065, Jul 2010.

[47] "Early supersymmetry searches with jets, missing transverse momentum and one or more leptons with the atlas detector," CERN, Geneva, Tech. Rep. ATLAS-CONF-2010-066, Jul 2010.

[48] H. Baer, "Supersymmetry at the LHC," Lecture, Florida State University, 2006.

[49] G. Aad, *Expected performance of the ATLAS experiment: detector, trigger and physics*. Geneva: CERN, 2009.

[50] T. Sandoval, "Z $\rightarrow \nu\nu$ + jets Background Estimation from γ +jets," Talk, University of Cambridge, 2010.

[51] S. Catani, M. Fontannaz, J. P. Guillet, and E. Pilon, "Cross-section of isolated prompt photons in hadron hadron collisions," *JHEP*, vol. 05, p. 028, 2002.

[52] B. Blair, F. Bucci, S. Chekanov, M. Stockton, and M. Tripiana, "Theoretical predictions for measurements of the inclusive isolated photon cross section in pp collisions at $\sqrt{s} = 7$ tev," CERN, Geneva, Tech. Rep. ATL-COM-PHYS-2010-805, Oct 2010.

[53] "Electron and photon reconstruction and identification in atlas: expected performance at high energy and results at 900 gev," CERN, Geneva, Tech. Rep. ATLAS-CONF-2010-005, Jun 2010.

[54] "Evidence for prompt photon production in p p collisions at $\sqrt{s} = 7$ tev with the atlas detector," CERN, Geneva, Tech. Rep. ATLAS-CONF-2010-077, Jul 2010.

BIOGRAPHICAL STATEMENT

Rishiraj Pravahan was born in Calcutta (Kolkata) on September 24 1976, to Mr Bijoy Kumar Srivastava and Ms Prabha Srivastava. He attended St. Xavier's Collegiate School, Calcutta for primary and La Martiniere for Boys, Calcutta for secondary education. After attending one year of college in St Xavier's he moved to University of Missouri Kansas City in the United States for a year before again transferring to University of Texas at Arlington (UTA). He graduated with a bachelor's degree in Physics with honors from UTA in May 2000 and a master's degree in Physics by May 2001. He started a PhD program in Johns Hopkins University in 2001 studying theoretical particle physics but did not finish due to ill health. After recovery, he joined the UTA Physics department to continue his doctoral studies. He was posted permanently at CERN in April 2006 for installation and calibration of the Tile Calorimeter of the ATLAS detector. This dissertation is the culmination of his work at CERN. He currently resides in Geneva with his girlfriend Ima-Karina Narvaez and dog Mukhosh.